Title
Consequences of non-trivial band topology in condensed matter systems

Author
Hosur, Pavan Ramakrishna

Publication Date
2012

Peer reviewed|Thesis/dissertation

Consequences of Non-Trivial Band Topology in Condensed Matter Systems

By

Pavan Ramakrishna Hosur

A dissertation submitted in partial satisfaction
of the requirements of the degree of

Doctor of Philosophy

in

Physics

in the
Graduate Division
of the

University of California, Berkeley

Committee in charge:

Professor Ashvin Vishwanath, Chair
Professor Joel Moore,
Professor Birgitta Whaley

Spring 2012

Abstract

Consequences of Non-Trivial Band Topology in Condensed Matter Systems

by

Pavan Ramakrishna Hosur

Doctor of Philosophy in Physics

University of California, Berkeley

Professor Ashvin Vishwanath, Chair

The commonly adopted classification of the electronic phases of matter as metals, insulators, semimetals, semiconductors and superconductors can be refined by studying the topological properties of the band structure in these phases. This unveils a rich and diverse substructure, and helps to conclude the existence of *topological phases* – phases whose properties are robust against perturbations, possibly with the requirement that the perturbations preserve certain symmetries. In this dissertation, several topological phases are studied, and predictions are made for some unusual physical phenomena involving these phases. Some of these phenomena may be observable using current experimental techniques. Topological phases often carry unconventional surface states; experimental signatures for the surface states of a *strong topological insulator* are presented as well.

We begin by systematically discussing the gapped phases, including some topological insulators and topological superconductors, proximate to a three-dimensional Dirac node. Studying topological defects in these phases reveals interesting duality relations between them, which provide potential routes for unconventional or non-Landau-Ginzburg-Wilson continuous phase transitions between them. Topological textures, on the other hand, can lead to very different physics, and we show that a bulk superconductor vortex in a topological insulator – a texture with a non-trivial Hopf index – acts like a fermion. As a corollary, we show that if the vortex string is terminated by a surface, the resulting dangling end traps a Majorana zero mode. The Majorana mode is found to be stable against doping the topological insulator, provided the doping is below a critical value set by Berry phase properties of the Fermi surface of the doped insulator. Importantly, several existing superconductors such as Cu-doped Bi_2Se_3 and $TlBiTe_2$ are predicted to host surface Majorana modes. In the absence of superconductivity, the surface of a topological insulator has gapless, spin-momentum locked states. This locking leads to an interesting response to circularly polarized radiation, with the dominant photocurrent being tied to the Berry curvature of the surface bands.

Having studied several theoretical and experimental implications of gapped topological phases, we turn our attention towards a gapless topological phase – the Weyl semimetal. We investigate transport in this phase in the presence of Coulomb interactions or disorder at finite temperature, and compare our results to experimental data on the candidate Weyl semimetal $Y_2Ir_2O_7$, finding encouraging agreement.

Contents

1 Introduction to band structure topology **1**
- 1.1 Topological band structures . . . 2
  - 1.1.1 Quantum Hall effect (class A, $d = 2$) . . . 5
  - 1.1.2 Quantum spin Hall effect (class AII, $d = 2$) . . . 5
  - 1.1.3 Spinless $p_x + ip_y$ superconductor (class D, $d = 2$) . . . 7
  - 1.1.4 Spinful $p_x + ip_y$ superconductor (class A, $d = 2$) . . . 8
  - 1.1.5 Kitaev wire (class D, $d = 1$) . . . 8
- 1.2 Band structure singularities . . . 9
  - 1.2.1 Fermi surface . . . 9
  - 1.2.2 Weyl points . . . 9

2 Review of topological insulators **13**
- 2.1 Quantum spin Hall effect in three dimensions . . . 13
- 2.2 Effective field theory and axion electrodynamics . . . 14
- 2.3 Exotic phenomena . . . 15
  - 2.3.1 Majorana modes in surface superconductors . . . 15
  - 2.3.2 Half-integer quantum hall effect . . . 16
  - 2.3.3 Image magnetic monopole . . . 17
- 2.4 Real materials . . . 17

3 Chiral topological insulators, superconductors and other competing orders in three dimensions **21**
- 3.1 Introduction . . . 21
- 3.2 Cubic lattice Dirac model . . . 23
  - 3.2.1 Continuum limit . . . 24
  - 3.2.2 Transformation to normal form . . . 25
- 3.3 Chiral topological insulator: Protected surface states . . . 27
  - 3.3.1 Protected surface states . . . 27
  - 3.3.2 Physical picture . . . 29
  - 3.3.3 Stability of nodes and the $\mathbb{Z}$-cTI . . . 32
  - 3.3.4 Application to spin-orbit $\mathbb{Z}_2$ topological insulators . . . 33
- 3.4 Chiral topological insulator: Electromagnetic response . . . 36
  - 3.4.1 Derivation of the theta term . . . 37
- 3.5 Chiral topological insulator with spin . . . 41
- 3.6 Singlet topological superconductors . . . 42

3.7 Toward physical realization . . . 43
3.8 Topological defects and dualities . . . 46
3.8.1 VBS and Neel . . . 46
3.8.2 $O(6)$ vectors of order parameters and the WZW term . . . 48
3.8.3 Non-linear sigma model with WZW term . . . 50
3.9 Conclusions . . . 54

4 Fermionic Hopf solitons and Berry phase in topological surface superconductors 57
4.1 Model and Hopf Texture . . . 58
4.2 Hopf Solitons are Fermions . . . 60
4.2.1 Connections to 3D non-Abelian statistics . . . 63
4.3 A Two Dimensional Analog . . . 64
4.4 Effective Theory and Topological Term . . . 65
4.5 Calculation of Topological Term . . . 66
4.5.1 Calculating S_{topo} in $D = 3 + 1$: . . . 67
4.5.2 Long Exact Sequence in Homotopy Theory . . . 69
4.6 Physical Consequences . . . 71
4.7 Conclusions . . . 72

5 Majorana modes at the ends of superconductor vortices in doped topological insulators 73
5.1 Introduction . . . 73
5.1.1 The Problem . . . 74
5.1.2 Vortex as a 1D topological SC . . . 75
5.1.3 VPT in a lattice model . . . 76
5.2 Continuum model: Analytical solution . . . 77
5.3 General Fermi surface Berry phase condition . . . 78
5.3.1 Vortex modes and the Berry phase of the Fermi surface . . . 79
5.4 Candidate materials . . . 88
5.4.1 $Cu_xBi_2Se_3$ . . . 88
5.4.2 $TlBiTe_2$, Bi_2Te_3 under pressure and $Pd_xBi_2Te_3$ . . . 90
5.4.3 MZMs from trivial insulators . . . 90

6 Circular photogalvanic effect on topological insulator surface states: Berry curvature dependent response 93
6.1 Introduction . . . 93
6.2 Symmetry considerations for the CPGE . . . 96
6.3 Helicity-dependent direct photocurrent . . . 97
6.3.1 Results . . . 97
6.3.2 Physical process . . . 100
6.3.3 Calculation in brief . . . 100
6.3.4 Calculation in detail . . . 102
6.4 Optical spin injection . . . 103
6.5 CPGE at oblique incidence . . . 104

6.6 Conclusions . . . 105

7 Charge transport in Weyl semimetals **107**
7.1 Introduction . . . 107
7.2 The Model . . . 109
7.2.1 Renormalization of couplings . . . 109
7.3 Conductivity with Interactions . . . 110
7.4 Conductivity with impurities . . . 115
7.5 Experiments . . . 116
7.6 Conclusions . . . 117
7.7 Appendix . . . 117
7.7.1 The Collision Operator and the 'Leading Log' Approximation . . . 117
7.7.2 Conductivity with Disorder . . . 120

Acknowledgements

First and foremost, I wish to express my deepest gratitude to my adviser Ashvin Vishwanath for accepting me into his research group, walking me through the initial phases of my PhD and calmly guiding me through the later ones. This helped me evolve from a wide-eyed fresh college graduate with a fascination for physics into a researcher with a somewhat sharper eye for spotting novel physical phenomena and identifying the physical machinery required to understand them. I also want to thank Ashvin for regularly suggesting research problems that were not only exciting and intellectually stimulating, but were also cutting-edge and important to the condensed matter physics community as a whole. Finally, I would like to thank him for his initiatives such as setting up collaborations with experimentalists, encouraging me to visit schools and conferences and urging me to write a single-author paper, each of which should have positive impact on my academic career.

I am grateful to each and every one of my collaborators for the collaborations and the numerous insightful discussions we had, which made the research more enjoyable. More specifically, I wish to thank Shinsei Ryu for patient and detailed explanations on various topics during our collaboration and also afterwards, Ying Ran for including me into an exciting project that he was involved in, Pouyan Ghaemi, Roger Mong and Siddharth Parameswaran for bringing a tremendous amount of energy and enthusiasm into the projects I worked with them on (I must thank my office mates Yi Zhang, Itamar Kimchi and Yi-Zhuang You for bearing with the pandemonium that sometimes broke in the office during these projects), and collaborators in the group of Dan Stamper-Kurn – Gyu-Boong Jo, Jennie Guzman, Claire Thomas and Dan Stamper-Kurn himself – for educating me in the basic experimental aspects of the physics of cold atoms and optical lattices.

Besides my collaborators mentioned above, my other coworkers – Yi Zhang, Ari Turner, Tarun Grover, Itamar Kimchi, Yi-Zhuang You, Jonas Kjäll, Jens Bardarson, Gil Young Cho, Vasudha Shivamoggi, Yuan-Ming Lu, Jerome Cayssol – have been wonderful company in my doctoral journey. On top of the engaging academic discussions I have had with them, the conducive and stimulating environment they created buoyed me too. The help and advice I have received from them, especially from Siddharth Parameswaran and Tarun Grover, on peripherally academic matters such as job applications, research statements etc. has been invaluable. Discussions with visitors to Berkeley and co-attendees at various schools, workshops and conferences have been highly enlightening.

Among my non-academic acquaintances, I have greatly enjoyed the company of my friends in Berkeley and elsewhere. With my roommates Sudeep Juvekar, Sudeep Kamath and Kartik Ganapathi, in Berkeley and college friends Hitesh Changlani, Ranjan Das and Anurag Setty, I have engaged in countless absorbing non-academic conversations, which have often helped

me decompress after long days of academic colloquy. The dance teams I have been on while in Berkeley also were welcome change from the rigors of academics and are an important reason behind the mushrooming of my social circle here.

I am obligated to Prof. Ashvin Vishwanath, Prof. Joel Moore, Prof. Joseph Orenstein and Prof. Birgitta Whaley for taking time out from their busy schedules to be on my qualifying exam committee, and to Prof. Ashvin Vishwanath, Prof. Joel Moore and Prof. Birgitta Whaley for agreeing to be on my thesis committee. I am also thankful to the journals Physical Review B and Physical Review Letters for allowing me to use my papers published in these journals in my thesis.

Finally, I am thankful to my family for granting me uninhibited freedom to pursue my goals in the profession of my choice, for being forever optimistic about my success which often raised my spirits as well and for thoroughly pampering me on my annual trips home. Last but not the least, I am indebted to my father for inspiring me to pursue science in the first place.

Chapter 1

Introduction to band structure topology

The earliest classification of the forms of matter we see around us, typically presented to us in our early school days, consists of *solids*, *liquids* and *gases*. High school physics textbooks and experience later teach us that solids can be further classified based on their electronic properties as *conductors* and *insulators*. Solid state physics courses in college add *semiconductors*, *semimetals* and *superconductors* to that list, and explain the basic physics that governs the electronic properties of these phases. More precisely, as long as the electrons in a solid are non-interacting, solids with partially filled bands are shown to be metals or conductors while those with no partially filled bands and a gap between the valence and the conduction bands are insulators or semiconductors. If the gap is extremely small or vanishing or if there is a very small overlap between the valence and the conduction bands, the material is semimetallic. Superconductors are argued to be the fate of a metal cooled to extremely low temperatures.

However, vast quantitative as well as qualitative differences between the properties of materials within a single category are often observed. For instance, some insulators have conducting surfaces (e.g. *topological insulators*) while others do not. Moreover, the surface conduction is stable against perturbations as well as deformations in the band structure as long as the underlying symmetries of the system are preserved and the system remains insulating after the deformations. Similarly, interactions and certain perturbations can gap out some semimetals and turn them insulating but not others (e.g. *Weyl semimetals*). These observations call for further refinement in the classification of solids, especially one that explains why the properties of some phases are robust to certain deformations, interactions and perturbations. In other words, an understanding for why some phases are topological while other are not, is required. The study of the *topology* of the bands provides a powerful unifying framework for accomplishing this task.

Topology shows up in two distinct ways in the band structures of non-interacting Hamiltonians depending on whether the spectrum is gapped or gapless. In systems with gapped band structures, which include insulators and most superconductors, the wavefunctions wind non-trivially across the Brillouin zone in the topological phases, as described in Sec. 1.1. What constitutes a non-trivial winding depends strongly on the symmetries and the dimensionality of the system under consideration, thus, revealing a rich substrucutre within the insulating and superconducting phases. On the other hand, gapless band structures contain topological objects in momentum space which can be characterized by the winding of the

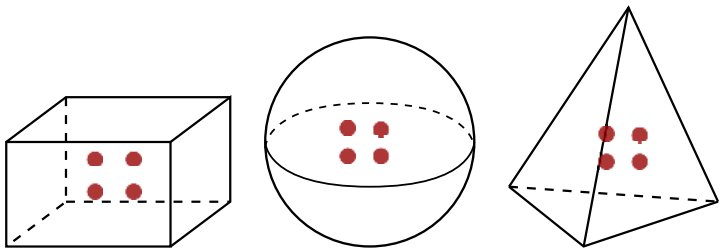

Figure 1.1.1: Gaussian surfaces of different shapes but the same topology and the same enclosed charge. The electric flux piercing each surface is the same and thus, is a topological invariant.

Green's function around the object, as exemplified in Sec. 1.2.

A key feature of topological media is that they typically have unconventional surface states which, in many cases, cannot exist independently of the bulk phase in one lower dimension. For instance, the two dimensional surface of a three dimensional topological insulator hosts pseudorelativistic electrons and cannot exist as an independent two dimensional system. Because of this intimate surface-bulk connection and because the surface is usually more accessible than the bulk, experiments usually probe the surface states in order to identify the bulk topological phase. The surface states are also extremely valuable from a practical point of view, since the unconventional properties bestowed upon them by the non-trivial bulk topology may be exploited to design novel electronic devices.

1.1 Topological band structures

The role topology plays in the band structures of gapped non-interacting Hamiltonians is analogous to its manifestation in an early example of topology in physics – Gauss's law in electrostatics.

Gauss's law states that the total electric flux piercing a closed surface is determined only by the charge enclosed by it and is independent of its shape or the precise charge distribution. Thus, the total flux through each surface in Figure 1.1.1 is four units. For gapped non-interacting lattice Hamiltonians, the analog of the Gaussian surface is the Brillouin zone, and different Gaussian surfaces correspond to different Brillouin zones in the extended zone scheme or to different bands in the reduced zone scheme. The electric charge, then, maps to an appropriate *topological invariant* whose exact form depends on the symmetries of the system under consideration. This topological invariant can be written as an integral over the Brillouin zone of an appropriate field derived from the Bloch functions of the occupied bands, analogous to how the electric charge enclosed by a Gaussian surface is equal to an integral of the electric field over it. The analogy is generalizable to continuum Hamiltonians, defined over all of momentum space, as well, provided the points at infinity are identified. This identification compactifies momentum space to the topological equivalent of a sphere, which, being a closed surface, permits the application of (analogs of) Gauss's law.

Next, assuming every charge that exists in the universe is inside a Gaussian surface, the only way to change the amount of charge enclosed by a single surface is by fusing it with another Gaussian surface, moving charges across the junction and pinching the junction off

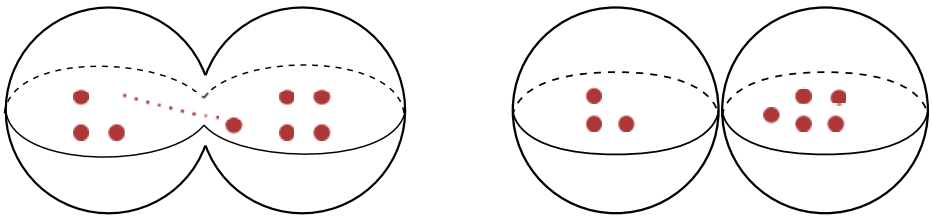

Figure 1.1.2: If charges can only exist inside Gaussian surfaces, the only way charge can be transferred from one surface to another is by fusing the surfaces together, passing charge across the neck of the resultant dumbbell and separating the spheres again.

Band structure entity	Gauss's law analog
Topological invariant, ν	Enclosed electric charge, Q
Some function f of the Bloch functions $u_{\boldsymbol{k}}$	Electric field, $\boldsymbol{E}$
Brillouin zone	Gaussian surface
$\nu = \oint_{\boldsymbol{k}\in \mathrm{BZ}} f\left[u_{\boldsymbol{k}}\right]$	$Q = \frac{1}{4\pi}\oint \boldsymbol{E}\cdot \mathrm{d}\boldsymbol{S}$
Changing ν requires band-touching	Changing Q requires Gaussian surfaces to touch

Table 1.1: Band structure entities and their Gauss's law analogs

to get the original surfaces back, as illustrated in Figure 1.1.2. Similarly, for band structures, topological invariants can only be defined for Brillouin zones wavefunctions in the extended zone scheme or equivalently, for bands in the more common reduced zone scheme. Analogous to exchanging charges between Gaussian surfaces, changing the topological invariant necessarily requires two sets of Brillouin zone wavefunctions or equivalently, two bands to touch and exchange quanta of the invariant. Thus, the system becomes gapless as it is tuned across a topological phase transition. Table 1.1 contains a list of analogies between Gauss's law in electrostatics and topological phenomena in non-interacting band structures.

An important consequence of the gaplessness of band structures as they are tuned across a topological phase transition is the existence of protected gapless states on the surface of a topological insulator or superconductor. If a topological insulator or superconductor is placed next to a topologically trivial one, including vacuum, the phases on the two sides of the interface are topologically distinct. Thus, gapless states exist at the interface and survive in the presence of weak perturbations as long as certain basic symmetries of the system are preserved by the perturbations. The number of such protected surface states is intimately tied to the value of the bulk topological invariant. These surface states are very important from a practical point of view as well as they are more easily accessible to many experimental probes than the bulk states and hence, help in identifying the topology of the bulk bands without requiring the bulk bands to be probed directly. Moreover, the surface states fully determine the low energy physics in the presence of a bulk gap and hence, are the only ones relevant for transport. And finally, the surface states of many topological phases display various unusual phenomena that ordinary quasiparticle states do not. These phenomena may be of interest both from a fundamental as well as a practical point of view.

As mentioned earlier, the precise form of the topological invariant in terms of the Bloch functions depends on the symmetry properties of the system of interest. Table 1.2 lists the

System	Cartan nomenclature	TRS	PHS	SLS	$d=1$	$d=2$	$d=3$
Standard (Wigner-Dyson)	A (unitary)	0	0	0	–	$\mathbb{Z}$	–
	AI (orthogonal)	+1	0	0	–	–	–
	AII (symplectic)	−1	0	0	–	$\mathbb{Z}_2$	$\mathbb{Z}_2$
Chiral (sublattice)	AIII (chiral unitary)	0	0	1	$\mathbb{Z}$	–	$\mathbb{Z}$
	BDI (chiral orthogonal)	+1	+1	1	$\mathbb{Z}$	–	–
	CII (chiral symplectic)	−1	−1	1	$\mathbb{Z}$	–	$\mathbb{Z}_2$
BdG	D	0	+1	0	$\mathbb{Z}_2$	$\mathbb{Z}$	–
	C	0	−1	0	–	$\mathbb{Z}$	–
	DIII	−1	+1	1	$\mathbb{Z}_2$	$\mathbb{Z}_2$	$\mathbb{Z}$
	CI	+1	−1	1	–	–	$\mathbb{Z}$

Table 1.2: The ten possible classes of single-particle Hamiltonians classified in terms of the presence or absence of time-reversal symmetry (TRS), particle-hole symmetry (PHS) and sublattice symmetry (SLS), and the sets of their topologically distinct quantum ground states in spatial dimensions $d = 1$, $d = 2$ and $d = 3$. In columns 3-5, 0 denotes the absence of a symmetry and ± 1 denotes the value to which the (anti-unitary, in case of TRS and PHS) symmetry operator squares, if present. In columns 6-8, – denotes the absence of any topologically nontrivial ground states, $\mathbb{Z}_2$ denotes two kinds of topologically distinct ground states, while $\mathbb{Z}$ indicates that the topologically distinct ground states can be labeled by the set of integers. (See [119])

classes of non-interacting Hamiltonians classified using their symmetry properties, and the sets of topologically distinct gapped phases each class of Hamiltonians may have in one, two and three spatial dimensions [119]. The only physical symmetries used in the classification process are time-reversal symmetry (TRS) and particle-hole symmetry (PHS), since these are the only ones generic to random, disordered systems. Thus, crystal symmetries, which are in general absent in disordered systems, are not considered. The sublattice symmetry (SLS) in Table 1.2 is defined as the product of TRS and PHS. The ten classes are obtained as follows: both time-reversal and particle-hole conjugation are anti-unitary operations and hence, can either be absent, or be present and square to either $+1$ or -1. This gives 9 classes of Hamiltonians. The tenth class, AIII is one where both TRS and PHS are broken but their product, the SLS, is preserved.

In the last three columns, while '–' denotes the absence of any topologically non-trivial phases, $\mathbb{Z}(\mathbb{Z}_2)$ indicates that the topologically distinct ground states can be labeled by the set of integers (integers modulo 2). This table contains several well-known phases. We briefly review some topological phases in one and two dimensions below, and review the $\mathbb{Z}_2$ phase in class AII in $d = 3$, famously called the 'Strong Topological Insulator', in more detail in Chapter 2.

1.1.1 Quantum Hall effect (class A, $d = 2$)

The most famous example of a topological phase of non-interacting electrons is the Integer Quantum Hall insulator, which results when a two-dimensional electron gas is subjected to a large perpendicular magnetic field. The spectrum of this system is discrete and consists of highly degenerate states known as Landau levels. If ν Landau levels are filled, the Hall conductivity is quantized to be $\nu e^2/h$, and this value has been experimentally found to be extremely robust against disorder [133]. While the bulk is insulating, the edge carries exactly ν gapless states, as expected for a topological phase from the previous discussion. A phase transition between two insulating phases with different ν takes place through a critical point at which the bulk becomes gapless.

The integer quantum Hall insulator has a lattice analog known as the Chern insulator. In this phase, there is no external magnetic field, but time-reversal symmetry is broken by effects such as complex hopping amplitudes between sites or magnetic ordering [50]. The number of gapless edge states and the Hall conductivity (in units of e^2/h) are both ν [55], where $\nu \in \mathbb{Z}$ is the total Chern number of the occupied bands. Also known as the TKNN integer [130], it is the total Berry curvature of the occupied bands integrated over the Brillouin zone:

$$\nu = \frac{1}{2\pi} \sum_{n \in \text{OCC}} \int_{\boldsymbol{k} \in \text{B.Z.}} \mathrm{d}k_x \mathrm{d}k_y \mathcal{F}_n(\boldsymbol{k}) \,, \; \mathcal{F}_n(\boldsymbol{k}) = i \left\langle \partial_{k_x} u_n(\boldsymbol{k}) | \partial_{k_y} u_n(\boldsymbol{k}) \right\rangle + \text{h.c.} \tag{1.1.1}$$

where $|u_n(\boldsymbol{k})\rangle$ is the Bloch function at $\boldsymbol{k}$ in the n^{th} band. The edge states of a quantum Hall system or Chern insulator are chiral, that is, they only disperse one way. Since there are no states available to backscatter into, an impurity at the edge cannot localize the edge state. Thus, the edge states are protected against disorder.

1.1.2 Quantum spin Hall effect (class AII, $d = 2$)

The quantum spin Hall effect, in the simplest situation, can be thought of as two copies of the quantum Hall effect – one for each spin – with opposite magnetic fields or time-reversal breaking effects. Since both spin and magnetic field get flipped under time-reversal, this system is time-reversal symmetric. The edge now carries a pair of counter-propagating states, with spin up moving one way and spin down, the other. Such states, where spin is locked to the direction of motion, are known as *helical* states. An effective Hamiltonian for such states is of the form

$$H_{\text{eff}} = v_F \sigma_z k_z \tag{1.1.2}$$

where v_F is a velocity, the edge is taken to be along z and σ_z is chosen as the quantization direction for the spins. In the presence of weak disorder, these states clearly cannot backscatter into each other and localize if the disorder cannot flip the spin. However, Kane and Mele showed in 2005 that the stability is much stronger: the edge states and indeed, the insulating bulk, are stable as long as time-reversal symmetry is preserved [74]. If S_z is not conserved, the form of H_{eff} in (1.1.2) survives, but σ_z now represents spin tied to orbital degrees of freedom. Thus, only time-reversal symmetry breaking perturbations such as magnetic impurities and magnetic ordering can potentially localize the edge states. The proof of this argument comes from Kramer's theorem which says that

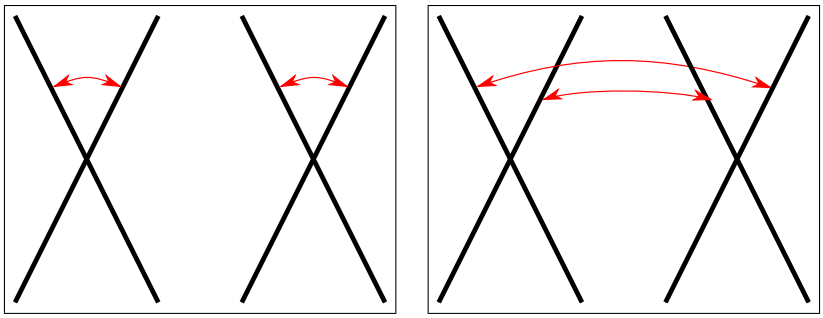

Figure 1.1.3: Two potential backscattering processes when there are two pairs of counter-propagating edge states, each pair centred at a time-reversal invariant momentum. While the process shown on the left is forbidden by time-reversal symmetry, the one on the right is not and localization by non-magnetic disorder is possible.

1. in a time-reversal symmetric fermionic system (such that $\mathcal{T}^2 = -1$), every state is doubly degenerate:

$$\text{If } \mathcal{T}H\mathcal{T}^{-1} = H \text{ and } H|\psi\rangle = E|\psi\rangle \text{ , then } H\left(\mathcal{T}|\psi\rangle\right) = E\left(\mathcal{T}|\psi\rangle\right) \text{ and } \langle\psi|\mathcal{T}\psi\rangle = 0 \tag{1.1.3}$$

   and

2. the two degenerate states in a Kramer's pair cannot scatter into each other to first order in a time-reversal symmetric perturbation:

$$\text{If } \mathcal{T}V\mathcal{T}^{-1} = V \text{ , then } \langle\psi|V|\mathcal{T}\psi\rangle = 0 \tag{1.1.4}$$

Both these statements can be easily proven using the property $\mathcal{T}^2 = -1$, which is true for fermionic systems. Note, however, that time-reversal symmetry cannot prevent the counter-propagating pairs of edge states from localizing if there is an even number of such pairs, as illustrated in Figure 1.1.3. Thus, only an odd number of linearly dispersing or *Diraclike* edge nodes are protected, which suggests a $\mathbb{Z}_2$ classification of time-reversal invariant insulators in two dimensions.

The topological invariant $\nu \in \mathbb{Z}_2$ takes values 0 for an ordinary insulator or 1 for a topologically non-trivial insulator or the quantum spin Hall insulator. It can be written in terms of the Bloch functions $u(\boldsymbol{k})$ as [34]

$$\nu = \frac{1}{2\pi}\sum_{n\in\text{OCC}}\left[\oint_{\partial(\text{half BZ})} \mathrm{d}\boldsymbol{k}\cdot\boldsymbol{\mathcal{A}}_n(\boldsymbol{k}) - \int_{\boldsymbol{k}\in(\text{half BZ})} \mathrm{d}k_x\mathrm{d}k_y\boldsymbol{\mathcal{F}}_n(\boldsymbol{k})\right] \bmod 2 \tag{1.1.5}$$

where $\boldsymbol{\mathcal{A}}_n(\boldsymbol{k}) \equiv i\left\langle u_n(\boldsymbol{k})\left|\boldsymbol{\nabla}_{\boldsymbol{k}}\right|u_n(\boldsymbol{k})\right\rangle$ is the Berry connection of the n^{th} band at $\boldsymbol{k}$ and the integrals involve only a continuous half of the Brillouin zone. Note that time-reversal transforms $\boldsymbol{k}$ to $-\boldsymbol{k}$, so the states over the entire Brillouin zone are, in fact, involved in the definition of ν.

There is another equivalent way of defining ν [35]. Define a matrix w that measures the overlap between Bloch states $|u_{\{n\}}(\boldsymbol{k})\rangle$ and the time-reversals of their Kramer's conjugates

$|u_{\{\bar{n}\}}(-\boldsymbol{k})\rangle$: $w_{\bar{n}n}(\boldsymbol{k}) = \langle u_{\bar{n}}(-\boldsymbol{k})\,|\mathcal{T}|\,u_n(\boldsymbol{k})\rangle$. In two-dimensions, there are exactly four time-reversal invariant momenta (TRIMs) in the Brillouin zone, that is, $\boldsymbol{k}$-points which are the same as $-\boldsymbol{k}$. At each of these points, w can be shown to be anti-symmetric, which allows a *Pfaffian* – the square root of the determinant upto a sign – to be defined for w. The topological invariant ν turns out to be related to the product of the sign of the Pfaffian over all TRIMs and all occupied bands

$$(-1)^{\nu} = \prod_{\boldsymbol{k}\in TRIM} \prod_{n\in \text{OCC}} \text{sign}\left[\text{Pf}\left(w_{\bar{n}n}(\boldsymbol{k})\right)\right] \tag{1.1.6}$$

A tremendous simplification occurs when the lattice has inversion symmetry [35]. Then, the states at the TRIMs have well-defined parities, and the sign of $\text{Pf}(w)$ turns out to equal the parity eigenvalue, upto an overall gauge. Since parity eigenvalues are supplied by routine band structure calculations, the determination of the $\mathbb{Z}_2$ topological characteristic of a time-reversal symmetric insulator is greatly facilitated. Helped by this observation, the quantum spin Hall effect has been observed in HgTe/CdTe quantum wells [81].

1.1.3 Spinless $p_x + ip_y$ superconductor (class D, $d = 2$)

The spinless $p_x + ip_y$ superconductor is a spin-triplet superconductor that can be thought of as the superconducting version of the spin-polarized or spinless integer quantum Hall system. In this phase, the superconducting pairing amplitude couples to the $S_z^{\text{total}} = +1$ (or -1) component of the angular momentum of a pair of spin-½ electrons, and is complex and momentum dependent. Its momentum dependence is such that while its magnitude is always non-zero, hence giving a gapped phase since the gap is proportional to the magnitude, its phase winds by 2π around the origin. Explicitly, the pairing term that enters the BdG Hamiltonian in momentum space is of the form

$$\Delta_0 c^{\dagger}_{\boldsymbol{p}\uparrow} c^{\dagger}_{-\boldsymbol{p}\uparrow}(p_x + ip_y) + \text{h.c.} \tag{1.1.7}$$

The topological invariant ν, as for the Chern insulator, is the Chern number of the occupied Bogoliubov-deGennes (BdG) bands, and for an ordinary metallic Fermi surface in the absence of pairing is simply the winding number of the phase of the pairing amplitude around the origin. The number of chiral edge states is also equal to ν. However, in contrast to the integer quantum Hall state, they carry of BdG quasiparticles rather than ordinary electrons. Another difference, compared to the Chern insulator, is that the BdG Hamiltonian has a built-in particle-hole symmetry which is absent in the Chern insulator. As a result of this additional symmetry, the spinless $p_x + ip_y$ superconductor falls into the D class in Table 1.2. A remarkable property of the spinless $p_x + ip_y$ superconductor is that the core of a vortex in this phase traps a *Majorana zero mode* [114] – a fermionic state which is its own anti-particle. In the language of second quantization, their creation and annihilation operators are the same, upto a gauge transformation, i.e.,

$$c^{\dagger} \equiv c \implies c \text{ is a Majorana fermion} \tag{1.1.8}$$

Majorana fermions, first predicted by Ettore Majorana in 1931, have intrigued high-energy physicists for decades, but have evaded experimental detection thus far. Among condensed

matter systems, these states can appear in superconductors, and are expected to exhibit remarkable properties such as immunity against arbitrary local noise and non-Abelian exchange statistics [95]. Majorana modes will be discussed in some more detail in Chapter 5.

1.1.4 Spinful $p_x + ip_y$ superconductor (class A, $d = 2$)

A close cousin of the spinless $p_x + ip_y$ superconductor is the spinful $p_x + ip_y$ superconductor. In contrast to the spinless $p_x + ip_y$ superconductor, the pairing couples to the $S_z^{\text{total}} = 0$ component of the angular momentum of a pair of electrons, so that the corresponding pairing term in the BdG Hamiltonian is of the form

$$\Delta_0 \left(c^\dagger_{\boldsymbol{p}\uparrow} c^\dagger_{-\boldsymbol{p}\downarrow} + c^\dagger_{\boldsymbol{p}\downarrow} c^\dagger_{-\boldsymbol{p}\uparrow} \right) (p_x + ip_y) \tag{1.1.9}$$

A unique property of this phase is that it supports *half-quantum vortices* – vortices that trap a magnetic flux of $h/4e$ – and protected Majorana modes at their cores. The topological invariant has the same expression in terms of the Bloch states as for the spinless $p_x + ip_y$ superconductor. There are several candidate systems for this phase, namely, the superfluid A phase of He-3 confined to a thin slab [9, 8], Sr_2RuO_4 [73], and, from a rather different context, the Moore-Read state which is a candidate ground state for the 5/2 fractional quantum Hall effect [95].

1.1.5 Kitaev wire (class D, $d = 1$)

The Kitaev wire is the simplest example of a topological superconductor. While Majorana modes appear in vortices in $p_x + ip_y$ superconductors, the Kitaev wire provides an example of a system where Majorana modes appear directly as the edge states of a topological phase. It consists of spin-polarized electrons hopping on a one-dimensional chain under the influence of p-wave pairing. The real space Hamiltonian is [78]

$$H_{\text{Kitaev}} = \sum_i \left(-t c_i^\dagger c_{i+1} + \Delta c_i c_{i+1} - \frac{\mu}{2} c_i^\dagger c_i \right) + \text{h.c.} \tag{1.1.10}$$

Kitaev showed that if $|\mu| > t$, the resulting phase is topologically trivial with no edge modes. On the other hand, $|\mu| < t$ gives a topological superconductor with a protected Majorana mode at each end of the chain [78]. The topological invariant $\nu \in \mathbb{Z}_2$ is the Berry phase – the integral of the Berry connection – around the one-dimensional Brillouin zone modulo π [129]:

$$\nu = \oint \mathrm{d}k A(k) \bmod \pi \tag{1.1.11}$$

Several theoretical proposals involving topological insulator or spin-orbit coupled semiconductor quantum wires in a heterostructure with an s-wave superconductor have been made for realizing this phase [92, 24]. The Majorana mode discussed in Chapter 5 falls in this class as well. Very recently, Mourik *et. al.* reported experimental evidence for a system Majorana modes [99], and the particular realization of Majorana modes there is in the same class as the Kitaev wire.

1.2 Band structure singularities

The second way in which topology appears in band Hamiltonians is in the form of topological defects in momentum space. These defects occur at points where the band structure becomes gapless and are analogous to real space topological defects such as domain walls, vortices and hedgehogs, where an order parameter has a non-trivial winding around the defect and vanishes at the defect. Like real space topological defects, topological defects in momentum space can be combined by moving them in momentum space while keeping their total topological quantum number conserved.

On a finite system, band structure singularities result in peculiar surface states. Whereas gapped topological phases carry dispersing surface states, gapless topological phases host dispersionless or *flat* bands on their surface. The flatness of these bands is protected by the topological nature of the bulk band structure and cannot be removed as long as the topological objects in the bulk band structure survive.

One crucial manner in which the topological nature of gapless band structures is different from that of gapped ones is that the former is not immune arbitrary disorder. Since the topological entities occur in momentum space, it is vital that momentum be a good quantum number. Thus, perturbations that break translational symmetry can potentially gap out the topological defects.

We now briefly review two common instances of band structure singularities and their associated flat surface bands.

1.2.1 Fermi surface

The ordinary Fermi surface in metals is the analog of a vortex in $(\omega, \boldsymbol{k})$ space [132]. In this space and assuming a single band for simplicity, a Fermi surface is represented by the $\omega = \epsilon(\boldsymbol{k}) = 0$ and the inverse Green's function $G^{-1}(i\omega, \boldsymbol{k}) = i\omega - \epsilon(\boldsymbol{k})$ vanishes. Away from the Fermi surface, G^{-1} is non-vanishing and its phase winds by 2π around a loop pierced by the Fermi surface, as illustrated in Figure 1.2.1. In more complex systems with multiple bands, the winding number can be any non-zero integer. However in all cases, this winding cannot be changed continuously to zero, which makes the Fermi surface robust to perturbative interactions. The stability of the Fermi surface against perturbative interactions is at the heart of Landau's Fermi liquid theory – the effective low energy theory of systems with a Fermi surface – and the above picture of G^{-1} winding around points on the Fermi surface provides a natural explanation for the phenomenon.

In a finite geometry, the surface of the system has a dispersionless or flat region in momentum space and this region is precisely the projection of the bulk Fermi surface onto the surface. While the correspondence between a topological object in the bulk – the Fermi surface – and a flat band on the surface may seem fairly obvious in the current example, the next example of Weyl points gives a more surprising result.

1.2.2 Weyl points

Weyl points are points in three-dimensional band structures where a pair of non-degenerate bands accidentally touch, as depicted in Figure 1.2.2. Near each such point, the Hamiltonian

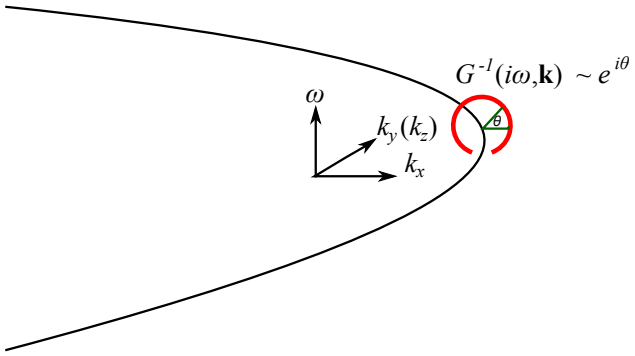

Figure 1.2.1: The phase of the Green's function inverse for a single band changes by 2π around a small loop (red circle) penetrated by the Fermi surface (black curve). The loop is drawn in the ω-k_x plane; the k_y and k_z axes are equivalent as far as the winding of G^{-1} is concerned and are therefore superimposed for convenience.

resembles the Hamiltonian for the Weyl fermions that are well-known in particle physics literature:

$$H_{\text{Weyl}} = \sum_{i,j\in\{x,y,z\}} v_{ij} k_i \sigma_j \tag{1.2.1}$$

where v_{ij} have dimensions of velocity, k_i is the momentum relative to the Weyl point and σ_i are Pauli matrices in the basis of the bands involved. Thus, this phase is known as a Weyl semimetal.

Based on (1.2.1), each Weyl point in a Weyl semimetal can be characterized by a *chirality quantum number* χ defined as $\chi = \text{sgn}[\det(v_{ij})]$. The physical significance of the chirality is that each Weyl point acts as a source of unit Chern flux, just like a magnetic monopole acts as a source of unit magnetic flux in real space, and the chirality is the "magnetic charge" corresponding to the the Chern flux. Nielsen and Ninomiya [103] showed that the number of Weyl points in a band structure must be even with half of each chirality.

An immediate consequence of the form of H_{Weyl} is that the Weyl points are topological objects in momentum space. Since all three Pauli matrices have been used up in H_{Weyl}, there is no matrix that anticommutes with H_{Weyl} and can gap out the spectrum. The only way a Weyl point can be destroyed is by annihilating it with another Weyl point of opposite chirality, either by explicitly moving the Weyl points in momentum space and merging them or by allowing for scattering to occur between different Weyl nodes. The latter requires the violation of translational invariance; thus, given a band structure, the Weyl nodes are stable to arbitrary perturbations as long as translational invariance is preserved. Disorder, in general, does not preserve this symmetry; however, if the disorder is smooth, many properties of the Weyl semimetal that rely on the topological nature of the band structure should are expected to survive.

Clearly, the topological stability of the Weyl nodes requires that the touching bands be non-degenerate. For degenerate bands, terms that mix states within a degenerate subspace can in general gap out the spectrum. Thus, the Weyl semimetal phase necessarily breaks at least one out of time-reversal and inversion symmetries, as the presence of both will make each state doubly degenerate. For the same reason, a Dirac node, which can be thought of

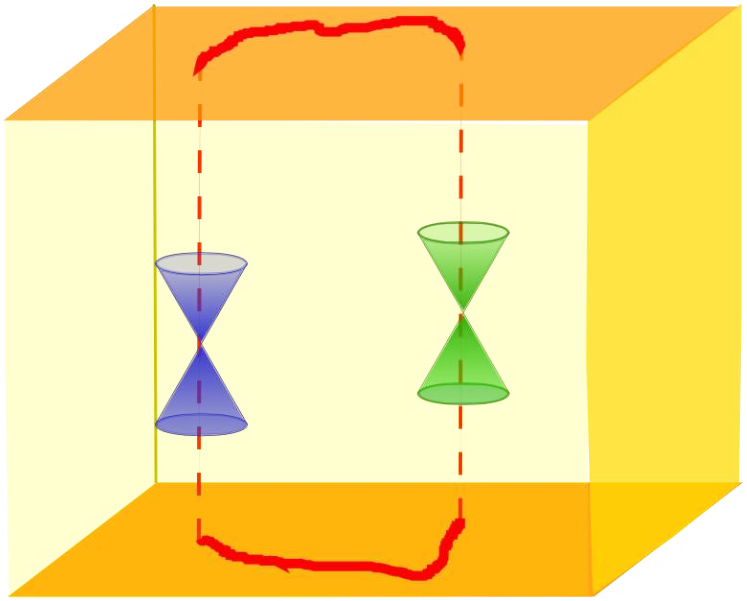

Figure 1.2.2: Weyl semimetal with a pair of Weyl nodes of opposite chirality (denoted by different colors green and blue) in a slab geometry. The surface has unusual Fermi arc states (shown by red curves) that connect the projections of the Weyl points on the surface.

as two degenerate Weyl nodes, can be gapped out by various mass terms. This is described in detail in Chapter 3.

The Fermi surface of a Weyl semimetal on a slab consists of unusual states known as Fermi arcs. The Fermi arcs are like a two dimensional Fermi surface, except that the two dimensional Fermi surface is broken into two parts (for the simplest case with exactly two Weyl nodes) and one part is localized on the top surface while the other is localized on the bottom surface. On each surface, the Fermi arc connects the projection of the bulk Weyl nodes onto the surface, as shown in Figure 1.2.2. A simple way to understand the presence of Fermi arcs is by recalling that the Weyl points are sources of Chern flux. Each two dimensional slice in momentum space perpendicular to the line joining the Weyl nodes can be thought of as a Chern insulator, and the Chern numbers of two slices on either side of a Weyl node differ by one. Thus, if the slices in the region far away from the Weyl nodes have Chern number 0, the Chern number of the slices between the Weyl nodes must be 1 (or -1) and so on. The Fermi arcs, then, are simply the edge states of the Chern insulators.

In summary, there are two broad ways in which topology manifests itself in the spectra of non-interacting band Hamiltonians. For gapped Hamiltonians, a topological phase exists when the Bloch wavefunctions of the occupied bands form non-trivial topological textures across the Brillouin zone. The exact class of textures that is stable against perturbations depends on the symmetries and the dimensionality of the system. Gapless Hamiltonians, on the other hand, can be characterized by topological invariants by focusing only on the states near the gapless region. The latter manifestation of topology in band structures is, in some sense, less stable than the former because it requires translational invariance and is thus not

oblivious to disorder. Both classes of topological phases are associated with unconventional states on the surface of a finite system – dispersing Dirac, Weyl or Majorana modes for gapped phases and flat bands for gapless phases.

In the next chapter, the physics of a famous gapped topological phase – the strong topological insulator – will be briefly introduced and reviewed. Some novel phenomena associated with this phase as well as some material realizations will be mentioned.

Chapter 2

Review of topological insulators

In the last half of a decade, the buzzword that has perhaps stolen the greatest amount of limelight in condensed matter physics is *topological insulators*. Two examples of insulators with non-trivial band topology, hence topological insulators according to the definition, were touched upon in the previous chapter. This section does a brief review of the phase that is colloquially called the *topological insulator* and is the one that has actually captured most of the attention. This is the three-dimensional insulator with time-reversal symmetry – class AII according to Table 1.2 – which has a non-trivial $\mathbb{Z}_2$ topological invariant. Henceforth, unless otherwise mentioned, the term 'topological insulator' will be used to refer to this particular realization of an insulating topological phase. It is closely related to the quantum spin Hall state; thus, the latter is often also termed the 'two-dimensional topological insulator'.

2.1 Quantum spin Hall effect in three dimensions

In 2006, a natural generalization of the quantum spin Hall effect to three dimensions was found [96, 117, 38]. It was realized that there are four $\mathbb{Z}_2$ invariants – ν_0, ν_1, ν_2 and ν_3 – for time-reversal symmetric insulators in three dimensions and for a stack of quantum spin Hall systems, $(\nu_1\nu_2\nu_3)$ are the Miller indices for the stacking direction and $\nu_0 = 0$. While stacking quantum spin Hall systems produces an insulating topological phase with at least one of $\nu_{1,2,3} = 1$, the resulting phase can be shown to host an even number of surface Dirac nodes which, as depicted in Figure 1.1.3, are not immune to arbitrary disorder even in the presence of time-reversal symmetry and can potentially be localized. Thus, this phase is termed as a *weak topological insulator* and the indices $(\nu_1\nu_2\nu_3)$ are known as weak indices.

In contrast, a *strong topological insulator* or simply, topological insulator, is the true three-dimensional extension of the quantum spin Hall state. The surface carries an odd number of Dirac nodes and non-magnetic disorder cannot localize all of them. The $\mathbb{Z}_2$ invariant $\nu_0 = 1$, and can be written in terms of the Pfaffians of an anti-symmetric matrix at the *eight* time-reversal invariant points, analogous to (1.1.6). For inversion symmetric systems, ν_0 reduces, as for the quantum spin Hall system, to

$$(-1)^{\nu_0} = \prod_{\boldsymbol{k}\in TRIM} \prod_{n\in \mathrm{OCC}} P_{n\boldsymbol{k}} \tag{2.1.1}$$

where $P_{n\boldsymbol{k}}$ is the parity eigenvalue of the Kramer's pair at the time-reversal invariant momentum $\boldsymbol{k}$ in the n^{th} band. This parity criterion is the one that has been used to identify all the topological insulators known so far. Besides being based on a quantity that is available from routine band structure calculations, it is also related to the concept of *band inversion*, which helps in identifying topological insulators as well.

In ordinary insulators, the valence and conduction bands are typically made up of atomic orbitals of opposite parities. While inversion takes $\boldsymbol{k}$ to $-\boldsymbol{k}$, the time-reversal invariant momenta remain unchanged under inversion and hence, the Bloch states at these points have definite parity eigenvalues which are equal to the parities of the atomic orbitals the respective bands are composed of. Thus, the right hand side of (2.1.1) equals 1, giving $\nu_0 = 1$. On the other hand, if some term in the Hamiltonian (typically spin-orbit coupling) causes the Kramer's pair in the valence band at one (or an odd number) out of the eight points to exchange places with the pair in the conduction band at the same momentum, the right hand side of (2.1.1) equals -1, hence, $\nu_0 = 1$, which describes a topological insulator. This exchange of places between conduction and valence band states at a time-reversal invariant momentum is termed as *band inversion* in the literature.

In the simplest case, the surface of a topological insulator hosts a single Dirac node and can be described by the effective Hamiltonian

$$H_{\text{surf}} = v_F \boldsymbol{\sigma} \cdot \boldsymbol{k} \tag{2.1.2}$$

where v_F is a velocity, $\boldsymbol{k}$ is the two-dimensional momentum in the surface Brillouin zone and $\sigma_{x,y}$ are Pauli matrices representing electron spin. H_{surf} is identical to the Hamiltonian for massless relativistic fermions in $2+1$ dimensional spacetime provided the velocity v_F is thought of as an effective "speed-of-light". This phenomenon also occurs in graphene; however, the Pauli matrices in graphene operate on the sublattice index of the underlying honeycomb lattice, there is an additional spin degeneracy and there are two Dirac nodes in the Brillouin zone. This effective surface theory (2.1.2) reveals two crucial properties of topological insulators:

1. The phase requires spin-orbit coupling, which is evident from the fact that on the surface, spin is maximally coupled to momentum. In the absence of spin-orbit coupling, the surface states would be doubly degenerate which would result in an even number of Dirac nodes which, as discussed earlier, are not topologically protected.

2. The Berry phase picked up by quasiparticles around a surface Fermi surface is π, since the spin direction rotates by 2π as an electron travels around a surface Fermi surface.

Having reviewed the physics of topological insulators in terms of properties of its band structure, we now approach this phase from different point of view and review the theory of its response to electromagnetic fields.

2.2 Effective field theory and axion electrodynamics

An effective field theory is a theory written in terms of the low energy and low momentum degrees of freedom only, after smearing out the physics occurring at short length (or large

momentum) and short time (or large energy) scales. If the effective theory involves external fields such as electromagnetic fields, it describes the response of the system to small electric and magnetic fields. For instance, the effective field theory for ordinary time-reversal invariant insulators coupled to electromagnetic perturbations is given by the action

$$S_0 = \frac{8}{\pi}\int \mathrm{d}x^3\mathrm{d}t\left(\epsilon\boldsymbol{E}^2 - \mu^{-1}\boldsymbol{B}^2\right) \tag{2.2.1}$$

to lowest order in $\boldsymbol{E}$ and $\boldsymbol{B}$, where ϵ and μ are the dielectric constant and the permeability of the insulator, and $\boldsymbol{E}$ and $\boldsymbol{B}$ are the dynamic electric and magnetic fields inside the insulator. The usual set of Maxwell's equations of electrodynamics descend from S_0. Note that S_0 does not contain any fermion fields, as they are gapped and thus relevant only at energies larger than the energy gap. S_0 can be derived by minimally coupling fermions in the insulator to electromagnetic fields and integrating over the fermion fields in the resulting path integral in imaginary time. (2.2.1) also implies that the electric polarization (magnetization), given by $\delta S/\delta\boldsymbol{E}$ ($\delta S/\delta\boldsymbol{B}$), is proportional to $\boldsymbol{E}(\boldsymbol{B})$.

In contrast, the effective electromagnetic action for topological insulators is $S_{\mathrm{TI}} = S_0 + S_\theta$, where[1]

$$S_\theta = \frac{\theta}{2\pi}\frac{e^2}{hc}\int \mathrm{d}^3x\mathrm{d}t\boldsymbol{E}\cdot\boldsymbol{B} \tag{2.2.2}$$

and

$$\theta = \pi \tag{2.2.3}$$

[30, 109]. While S_{TI} is different from S_0, one can show that the integrand in S_θ is a perfect differential, so only terms on the boundary of the spacetime manifold contribute to the integral. Furthermore, on a manifold with periodic boundary conditions in both space and time, S_θ is quantized to be an integer multiple of θ and is immune to small variations in the electromagnetic fields. Since physical responses are proportional to the change in the action due to the field fluctuations, they do not pick up the effect of $\theta \neq 0$ in a periodic system.

However, at the interface between a topological and a trivial insulator, θ changes from 0 to π as one goes from the trivial to the topological insulator. This *change* in θ is measurable and from the form of S_θ, it is obvious that the behavior to look for is a polarization proportional to the magnetic field or a magnetization proportional to the electric field. This *magnetoelectric effect* can be exploited to obtain unusual phenomena such as image magnetic monopoles [110], which are discussed below along with other exotic phenomena involving topological insulator surface states.

2.3 Exotic phenomena

2.3.1 Majorana modes in surface superconductors

One way to gap out the metallic surface states of a topological insulator is by depositing an ordinary s-wave superconductor on top of it. The proximity to a superconductor induces

[1] θ can only take values 0 and π for time-reversal invariant insulators. This is because under time-reversal, $\boldsymbol{E} \to \boldsymbol{E}$ and $\boldsymbol{B} \to -\boldsymbol{B}$, so $\theta \to -\theta$, which permits $\theta = 0$. Additionally, θ is only defined modulo 2π for a periodic system because a change in θ by 2π can always be undone by a gauge transformation. Thus, $\theta = \pm\pi$ represents the same system and thus, $\theta = \pi$ is allowed for time-reversal symmetric insulators.

pairing in the surface states and gaps them out. Fu and Kane [36] showed that a vortex in this surface superconductor traps a topologically protected Majorana zero mode, similar to the Majorana modes mentioned in Sec. 1.1.3. This can be seen as follows.

Consider a topological insulator surface represented by H_{surf} as in (2.1.2) in the presence of s-wave pairing $\Delta(\boldsymbol{r})$. The appropriate BdG Hamiltonian in real space is

$$H_{BdG} = \int \mathrm{d}^2 r \Psi^\dagger(\boldsymbol{r}) \begin{pmatrix} -iv_F \boldsymbol{\sigma}\cdot\boldsymbol{\nabla} & \Delta(\boldsymbol{r}) \\ \Delta(\boldsymbol{r}) & iv_F\boldsymbol{\sigma}\cdot\boldsymbol{\nabla} \end{pmatrix} \Psi(\boldsymbol{r}) \tag{2.3.1}$$

where $\Psi^\dagger(\boldsymbol{r}) = \left(\psi^\dagger(\boldsymbol{r}), \sigma_y\psi(\boldsymbol{r})\right)$ and $\psi(\boldsymbol{r})$ is a two-component spinor in spin space. Suppose $\Delta(\boldsymbol{r})$ forms a vortex around $\boldsymbol{r}=0$, that is, $\Delta(\boldsymbol{r}) = \Delta(r)e^{i\theta}$, $\Delta(0)=0$ and $\Delta(r\to\infty)=\Delta_0$. Then, it is straightforward to show that H_{BdG} has exactly one zero energy solution and it is given by

$$\Psi(\boldsymbol{r}) = (i,0,0,1)^T\, e^{-\int_0^r \mathrm{d}r\Delta(r)/v_F} \tag{2.3.2}$$

The corresponding field operator is $\gamma_0(\boldsymbol{r}) = \left(ic_\uparrow - ic_\uparrow^\dagger\right) e^{-\int_0^r \mathrm{d}r\Delta(r)/v_F}$. Clearly, $\gamma_0^\dagger = \gamma_0$, so γ_0 is a Majorana mode.

Similarly, they showed that if $\Delta(\boldsymbol{r})$ was constrained to be real, domain walls separating regions of opposite signs of $\Delta(\boldsymbol{r})$ trapped a pair of Majorana modes counter-propagating along the walls. These *Majorana wires* can potentially be used to build circuits for transporting Majorana fermions.

2.3.2 Half-integer quantum hall effect

The surface of a topological insulator shows a form of the integer quantum Hall effect in which the surface Hall conductivity σ_{xy} is quantized to be a half-integer (in units of e^2/h), in contrast to the conventional integer quantum Hall effect where σ_{xy} is quantized to be an integer. This can be seen in two ways.

The simplest way is by directly diagonalizing the surface Hamiltonian in the presence of a time-reversal symmetry breaking perturbation such as a perpendicular magnetic field $B\hat{\boldsymbol{z}}$. Thus,

$$H_{\text{surf}}(B) = -v_F\left(i\boldsymbol{\nabla} + e\boldsymbol{A}(\boldsymbol{r})\right)\cdot\boldsymbol{\sigma} \tag{2.3.3}$$

where $\boldsymbol{A}(\boldsymbol{r}) = \frac{1}{2}B(x\hat{\boldsymbol{y}} - y\hat{\boldsymbol{x}})$ is the vector potential in the symmetric gauge, can be shown to have the spectrum

$$E_n = \mathrm{sgn}(n)\sqrt{2|n|B}\,,\ n = 0, \pm1, \pm2\ldots \tag{2.3.4}$$

with each energy level having a degeneracy equal to the number of flux quanta penetrating the surface. Due to the $E\to -E$ symmetry of the spectrum, the system at half-filling is particle-hole symmetric, with the $n<0$ ($n>0$) Landau levels being filled (empty) and the $n=0$ Landau level being half-filled, thus making the system metallic. However, it becomes insulating if the filling fraction ν is a half-integer. In particular, at $\nu = n+1/2$, all the Landau levels up to the n^{th} one are fully filled and the ones above are empty. Since σ_{xy} changes by e^2/h every time the Fermi level crosses a Landau level and vanishes at the particle-hole symmetric point $\nu=0$ since electrons and hole contribute oppositely to it, $\sigma_{xy} = \nu e^2/h = (n+1/2)e^2/h$. This is similar to the quantum Hall effect in graphene, except that the Dirac nodes in graphene are four-fold degenerate.

The second way is by explicitly breaking time-reversal symmetry on the surface and gapping out the surface spectrum. This can be done by adding a term $m\sigma_z$, which corresponds to a surface magnetization, to H_{surf} in (2.1.2). Similarly to the conventional integer quantum Hall effect, a Hall conductivity appears as long as the system is insulating, and it is straightforward to show that $\sigma_{xy} = \frac{1}{2}\text{sgn}(m)e^2/h$ by explicitly computing the Chern number of the valence band. Furthermore, the same result can be obtained directly from the effective field theory, in which a surface parallel to the xy-plane can be simulated by assuming θ to vary slowly from 0 to π along z, thus breaking time-reversal symmetry. Then, $S_\theta = (e^2/2\pi hc)\int \mathrm{d}^3x\mathrm{d}t\theta(\boldsymbol{r})\boldsymbol{E}\cdot\boldsymbol{B}$ and evaluating the functional derivative $j_\alpha = \delta\mathcal{L}/\delta\mathcal{A}_\alpha$ immediately gives the desired result. Clearly, the half-integer quantum Hall effect is intimately tied to the magnetoelectric effect because of the $\boldsymbol{E}\cdot\boldsymbol{B}$ term in the action for topological insulators.

A caveat, however, is that a non-integer Hall conductivity does not imply the presence of any kind of fractionally charged excitations. This is because the Hall conductivity of a real sample receives contributions from both the top as well as the bottom surfaces, and is actually an integer times e^2/h.

2.3.3 Image magnetic monopole

A remarkable consequence of the magnetoelectric effect in topological insulators is the appearance of an image magnetic monopole when a point charge is brought near the surface of a topological insulator [110]. The image magnetic charge appears in addition to the usual image electric charge that appears for conventional electromagnetic media. Thus, for the configuration show in Figure 2.3.1 where a point charge q is placed at a distance d from the surface of a topological insulator, the total electromagnetic fields in the upper half plane are due to the point charge q, the image electric charge q_2 and the image magnetic monopole g_2.

The appearance of the magnetic monopole can be understood as follows. The point charge q placed a distance d near the surface produces an electric field which in turn generates circulating currents on the surface because of the magnetoelectric effect, as shown in the inset of a Figure 2.3.1. These circulating currents produce a magnetic field which can be shown to be the same as that produced by an image monopole placed a distance d below the surface. For the configuration of Figure 2.3.1, the strengths of the various electric and magnetic charges are

$$q_1 = q_2 = \frac{(\varepsilon_1-\varepsilon_2)(1/\mu_1+1/\mu_2)-\alpha^2}{\varepsilon_1(\varepsilon_1+\varepsilon_2)(1/\mu_1+1/\mu_2)+\alpha^2}q \tag{2.3.5}$$

$$g_1 = -g_2 = -\frac{2\alpha}{(\varepsilon_1+\varepsilon_2)(1/\mu_1+1/\mu_2)+\alpha^2}q \tag{2.3.6}$$

where $\alpha = e^2/\hbar c$ is the fine structure constant.

2.4 Real materials

A crucial reason why topological insulators have gained so much popularity is that a number of existing systems have been confirmed and many more have been predicted to be in this

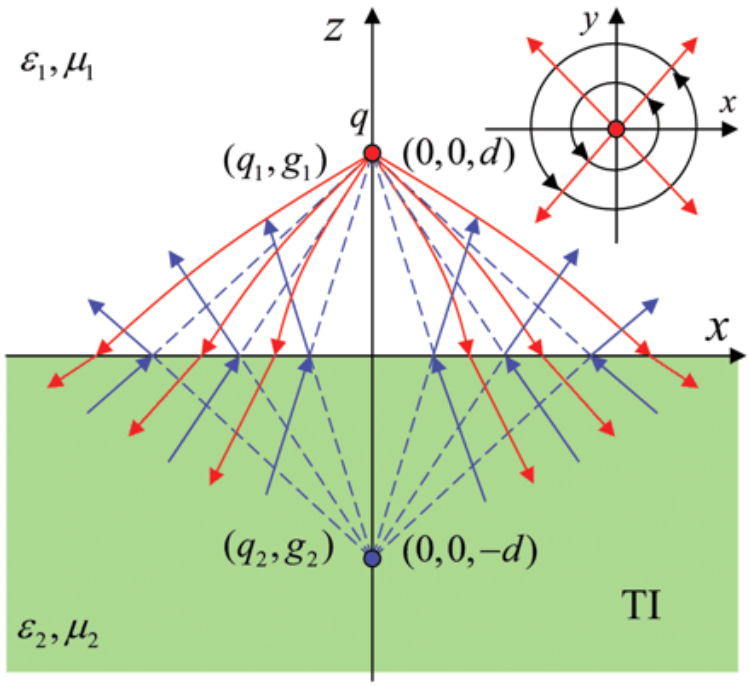

Figure 2.3.1: Illustration of the image charge and monopole of a point-like electric charge. The lower-half space is occupied by a topological insulator (TI) with dielectric constant ε_2 and magnetic permeability μ_2. The upper-half space is occupied by a topologically trivial insulator (or vacuum) with dielectric constant ε_1 and magnetic permeability μ_1. A point electric charge q is located at $(0, 0, d)$. When seen from the lower-half space, the image electric charge q_1 and magnetic monopole g_1 are at $(0, 0, d)$; when seen from the upper-half space, the image electric charge q_2 and magnetic monopole g_2 are at $(0, 0, -d)$. The red solid lines represent the electric field lines, and blue solid lines represent magnetic field lines. (Inset) Top-down view showing the in-plane component of the electric field at the surface (red arrows) and the circulating surface current (black circles). (From Qi *et. al.*, Science, 323(5918):1184–1187, 2009. Reprinted with permission from AAAS)

phase. All the predictions so far have been made using the parity criterion (2.1.1) for inversion symmetric systems (e.g. [152, 148, 147], and the experimental confirmations have mostly been made by directly observing an odd number of surface Dirac cones in angle-resolved photoemission spectroscopy (ARPES) experiments (e.g. [144, 86, 69, 70]).

The early topological insulators were all bismuth based. Owing to its fairly high atomic number, electrons in Bi have strong spin-orbit coupling, which is a necessary ingredient for topological insulators. The first confirmed candidate was Bi_xSb_{1-x} with $x \sim 0.9$, which was found to have five surface Dirac nodes [68]. Soon after, Bi_2Se_3 [144] and Bi_2Te_3 [22] were found to have single surface Dirac nodes. Currently, there are over a dozen families of candidate topological insulators, some of which have been confirmed. All of them have the common feature that they contain at least one element with strong spin-orbit coupling such as Tl [118, 23, 85, 147], Te [22, 135] and in some cases, rare-earth elements [20, 87].

Chapter 3

Chiral topological insulators, superconductors and other competing orders in three dimensions

3.1 Introduction

Having reviewed the main ideas in band structure topology and the basics of topological insulators, we now investigate other possible gapped phases of band Hamiltonians in three dimensions. A convenient starting point is a three Dirac dispersion, since it is proximate to a variety of orders, which when established, lead to an energy gap. In the context of graphene, charge density wave [76, 82] and valence bond solid (VBS) (or Kekule) order [21, 67, 71] as well as antiferromagnetism [124, 93, 107] are known to induce a gap, and lead to an insulating state. Several years back Haldane pointed out that the integer quantum Hall state could be realized starting from the graphene semimetal, in the absence of external magnetic fields [50]. A valuable outcome of this Dirac proximity approach, was the discovery of an entirely new phase of matter, the $\mathbb{Z}_2$ Quantum Spin Hall insulator [14, 81, 74], obtained in theory by perturbing the graphene Dirac dispersion. By analogy, here we study three dimensional Dirac fermions, and their proximate gapped phases, on a cubic lattice.

In three dimensions, Dirac points naturally occur in some heavy materials like bismuth and antimony, with strong spin orbit interactions. A three dimensional version of the quantum spin Hall state - the $\mathbb{Z}_2$ topological insulator [38, 96, 117, 35], can be realized by appropriately perturbing such a state, as demonstrated in [38], in a toy model on the diamond lattice. According to recent experiments, this phase is believed to be realized by several Bi-based materials including $Bi_{0.9}Sb_{0.1}$ [68], Bi_2Se_3 [144] and Bi_2Te_3 [22]. Both the $\mathbb{Z}_2$ quantum spin Hall and the $\mathbb{Z}_2$ topological insulator phases require time-reversal symmetry (TRS) to be preserved. The $\mathbb{Z}_2$ index represents the fact that only an odd number of edge or surface Dirac nodes are stable in these phases.

In contrast, in this chapter we study a toy model on the cubic lattice, with π flux through the faces, which realizes three dimensional Dirac fermions, and identify the proximate states. To begin with, we consider insulating phases of spin polarized electrons. In addition to conventional insulators, e.g., with charge or bond order, we also find an additional novel

topological insulator phase within this model, the chiral Topological Insulator (cTI). This provides a concrete realization of this phase, which was recently predicted on the basis of a general topological classification of three dimensional insulators in different symmetry classes [119, 77]. This phase is distinct from the spin-orbit Z_2 topological insulators in two main respects. First, it is realized in the *absence* of time-reversal symmetry. Instead, it relies on another discrete symmetry called the chiral symmetry. Second, these insulators also host protected Dirac nodes at their surface, but *any integer* number of Dirac nodes is stable on its surface. Thus, it has a $\mathbb{Z}$ rather than $\mathbb{Z}_2$ character. In an insulator, chiral symmetry restricts us to Hamiltonians with only hopping terms between opposite sublattices. Clearly, this is not a physical symmetry, and hence such insulators are less robust than topological insulators protected by time reversal symmetry. However our results will be relevant if such symmetry breaking terms are weak, or in engineered band structures in lattice cold atom systems [125]. With spin, an interesting gapped state that can be reached from the Dirac limit is the singlet topological superconductor (sTS), also first discussed in [119]. This state also possesses protected Dirac surface states. The stability of these states is guaranteed, as long as time reversal symmetry and SU(2) spin symmetry, both physical symmetries, are preserved.

The Dirac limit allows for an easy calculation of the charge (spin) response of the cTI (sTS), and provides an intuitive picture of these phases. For example, the cTI can be understood as arising from a quasi 2D limit of layered Dirac semi-metals, with a particular pattern of node pairings, leading to a bulk gap, but protected surface states. It is hoped that this intuition will help in the search for realistic examples of these phases. Additionally, this picture helps in understanding $\mathbb{Z}_2$ topological insulators protected by TRS whose bulk Dirac nodes are at time-reversal-invariant momenta (TRIM), such as Bi_2Se_3, Bi_2Te_3 and Sb_2Se_3 [152].

Finally, we utilize the Dirac starting point to derive relations between different gapped phases. We show that there is a duality between Neel and VBS phases: point defects of the Neel order (hedgehogs) are found to carry quantum numbers of the VBS state and vice versa. This is done by studying the midgap states induced by these defects, and the results agree with spin model calculations [98] that are appropriate deep in the insulating limit. Thus, the Dirac approach is a convenient way to capture universal properties of the gapped phases in its vicinity. These results are also derived following a technique applied to the one and two dimensional cases [4, 2, 127, 121], by integrating out the Dirac fermions and deriving an effective action for a set of orders. In particular we focus on the Berry's phase (or Wess-Zumino-Witten) term which, when present, implies non-trivial quantum interference between them. Such sets of 'quantum competing' orders can be readily identified within this formalism. We show that in addition to Neel and VBS orders, interestingly, Neel order and the singlet topological superconductor also share such a relation. The consequence of such a relation in 3D is discussed.

The organization of this chapter is as follows. We introduce the cubic lattice Dirac model and a transformation on the low energy Dirac fermions to bring it into a 'normal' form in Sec. 3.2.2, from which one can easily read off the orders that lead to an energy gap. The chiral topological insulator is identified, and a microscopic model with hopping along the body diagonals of the cube, is shown to lead to this phase. An intuitive picture in terms of a quasi 2D starting point is developed in Sec. 3.3.2, which directly demonstrates the existence

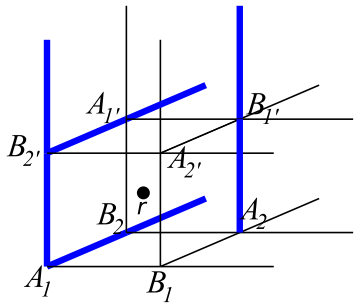

Figure 3.2.1: The cubic lattice with π-flux for each plaquette. Blue (bold) lines represent negative hopping integrals. $\mathbf{r}$ is at the center of cube drawn above.

of surface Dirac states. Here, we also show how a $\mathbb{Z}_2$ topological insulator protected by TRS with bulk Dirac nodes at TRIM can be understood within this picture. In Sec. 3.4 the magnetoelectric coefficient 'θ' of such an insulator is argued to be quantized , and is calculated to be $\theta = \pi$ for the spinless fermion model we discuss. Introducing spin, and studying gapped superconducting states, we show in Sec. 3.6 that only a pair of singlet superconductors is allowed, which, in addition to the regular onsite s-wave paired state, includes a singlet topological superconductor, with pairing along the body diagonals. Sec. 3.7 describes an attempt to move towards a more physical realization of the cTI phase, utilizing a layered honeycomb lattice structure. Finally, in Sec. 3.8, we explore some topological properties of the 3D Dirac fermion system by studying its physics in the presence of point topological defects in its order parameters, and deriving the Berry's phase terms that determine quantum interference of different orders.

A word on our notation is warranted before taking the plunge into the main content. Throughout the chapter, we use '$\mathbb{H}$' to denote the full Hamiltonian for a system. An ordinary 'H' shall represent the Hamiltonian as a function of certain indices, the expression being valid over the entire energy range, and a calligraphic '$\mathcal{H}$' shall represent the Hamiltonian at low energies. For example, $\mathbb{H} = \sum_{\mathbf{k}} \psi^\dagger_{\mathbf{k}} H_{\mathbf{k}} \psi^\dagger_{\mathbf{k}}$ when momentum is conserved and $H_{\mathbf{Q}+\mathbf{k}} \simeq \mathcal{H}_{\mathbf{k}}$ for small $\mathbf{k}$, if $H_{\mathbf{Q}} = 0$.

3.2 Cubic lattice Dirac model

Consider a 3D tight-binding model of *spinless* fermions on the cubic lattice shown in Figure 3.2.1:

$$\mathbb{H}_0 = -\sum_{\langle R,R'\rangle} t_{RR'} c^\dagger_R c_{R'} \tag{3.2.1}$$

where c_R is the fermion annihilation operator at site R on the cubic lattice and the nearest neighbor hoppings are chosen so that each square plaquette encloses π-flux ($\prod_\square \frac{t_{RR'}}{|t_{RR'}|} = -1$). A particular gauge choice is shown in the Figure , where the blue (bold) lines represent hopping with $-|t|$ and the others with $+|t|$. We choose an enlarged eight site unit cell, that turns out to be convenient for what follows, and label the sites A_1, A_2, B_1, B_2 in a layer and $A_{1'}$, $A_{2'}$, $B_{1'}$, $B_{2'}$ in the following layer. The A and B labels represent the two sublattices of the cubic lattice, and will be denoted by the eigenvalues of the τ_z operator, a Pauli matrix.

Similarly, the $1,2$ index will correspond to the ν_z operator, and the bilayer index, to the μ_z operator.

With the Fourier transformation $A_{\mathbf{r}-\frac{\mathbf{x}}{2}-\frac{\mathbf{y}}{2}-\frac{\mathbf{z}}{2}} = V_A^{-1/2}\sum_{\mathbf{k}} e^{i\mathbf{k}\cdot(\mathbf{r}-\frac{\mathbf{x}}{2}-\frac{\mathbf{y}}{2}-\frac{\mathbf{z}}{2})}A_{\mathbf{k}}$ etc., with V_A being the total number of A sites, $\mathbf{r}$ denoting the locations of the 8-site unit cells and $\mathbf{k}$ being in the (reduced) Brillouin zone (Bz), $\mathbf{k} \in (-\pi/2, \pi/2]^3$, the Hamiltonian is written in momentum space as

$$\mathbb{H}_0 \;=\; \sum_{\mathbf{k}} f_{\mathbf{k}}^\dagger H_{\mathbf{k}}^0 f_{\mathbf{k}} \tag{3.2.2}$$

where the eight component fermion operator at momentum $\mathbf{k}$ is defined by

$$f_{\mathbf{k}}^\dagger \;=\; \left(A_{1\mathbf{k}}^\dagger, A_{2\mathbf{k}}^\dagger, A_{1'\mathbf{k}}^\dagger, A_{2'\mathbf{k}}^\dagger, B_{1\mathbf{k}}^\dagger, B_{2\mathbf{k}}^\dagger, B_{1'\mathbf{k}}^\dagger, B_{2'\mathbf{k}}^\dagger\right) \tag{3.2.3}$$

and

$$H_{\mathbf{k}}^0 \;=\; -2|t|\left(\cos k_x \Gamma_x + \cos k_y \Gamma_y + \cos k_z \Gamma_z\right) \tag{3.2.4}$$

where

$$\Gamma_x = \tau_x\,,\; \Gamma_y = \tau_y\nu_y\,,\; \Gamma_z = \tau_y\mu_y\nu_x, \tag{3.2.5}$$

Clearly, $H_{\mathbf{k}}^0$ anticommutes with τ_z.

$$H_{\mathbf{k}}^0\tau_z = -\tau_z H_{\mathbf{k}}^0 \tag{3.2.6}$$

Hamiltonians for which such an anticommuting operator is present, will be called **chiral Hamiltonians**. A consequence is that positive and negative energy eigenvalues will come in pairs. Note that this operation amounts to changing the sign of the wavefunction on all B sublattice sites. Applying this to the eigenstate with energy E, of a hopping Hamiltonian that only connects opposite sublattices, maps it to an eigenstate with energy $-E$.

$H_{\mathbf{k}}^0$ also preserves time-reversal symmetry (TRS):

$$H_{-\mathbf{k}}^{0*} = H_{\mathbf{k}}^0 \tag{3.2.7}$$

3.2.1 Continuum limit

The energy spectrum of $H_{\mathbf{k}}^0$ is given by

$$E_{\mathbf{k}} = \pm 2|t|\sqrt{\cos^2 k_x + \cos^2 k_y + \cos^2 k_z} \tag{3.2.8}$$

and each band is four-fold degenerate for each $\mathbf{k}$. The conduction and valence bands touch at zero energy at the BZ corner

$$\mathbf{Q} = (\pi/2, \pi/2, \pi/2). \tag{3.2.9}$$

Hence, at half-filling, it is a Dirac semi-metal, with a three dimensional Dirac point. Near this point, the Hamiltonian is Dirac like:

$$H_{\mathbf{Q}+\mathbf{k}}^0 \simeq \mathcal{H}_{\mathbf{k}} = v_F \sum_{i=x,y,z}^{3} k_i \Gamma_i, \tag{3.2.10}$$

where we have introduced the Fermi velocity $v_F = 2|t|$. From now on, we will assume $v_F \equiv 1$.

This dispersion of the Dirac semimetal can acquire a gap, leading to an insulating state, in a variety of ways. All of these require symmetry breaking of one kind or the other, leading to different orders. Some obvious insulating state that can lead to such a gap (ignoring for a moment the electron spin) are:

1. Charge Density Wave (CDW) order with wave-vector (π, π, π). This will lead to a Staggered Potential (SP) on the two sublattices, $\Delta H_{CDW} = (-1)^r \mu$. This generates a mass term for the Dirac equation, since $\Delta H \propto \tau_z$, which anticommutes with the velocity matrices Γ_i, leading to a gap.

2. Valence Bond Solid (VBS) order. Staggering the hopping matrix elements also opens up a gap. For example, we pick hopping along the x direction and modulate their amplitude as $t_{RR+\hat{X}} = t^0 + (-1)^{R_x} \delta t$. The relevant order is called valence bond solid, since in the extreme limit where only the stronger bonds are present, the resulting insulating state may be thought of as a 'molecule' composed of pairs of sites connected by these strong bonds. Similarly, one can construct VBS orders along the y and z directions, leading to three different mass terms. Note, these preserve the *chiral* property of the Hamiltonian, in that it still consists only of nearest neighbor hoppings.

3. Layered Quantum Hall Effect (QHE) in the xy, yz and zx layers. In three dimensional lattices, a stacked version of the integer quantum Hall effect occurs [80], which, however, breaks the cubic symmetry of the lattice. These orders can be realized by selecting a plane, say, the xy-plane, and introducing imaginary hoppings between second neighbor sites in this plane in such a way that the reflection symmetry m_{xy} is broken, but m_{yz} and m_{zx} are unbroken. Note, time reversal symmetry is necessarily broken here.

It is possible to systematically list all the perturbations that describe distinct insulating phases by looking at matrices that anticommute with the velocity-matrices, Γ_is. Each anticommuting term introduces a mass gap and converts the system into a true insulator, while leaving the fourfold degeneracy of each band intact. Such an insulating phase with completely degenerate conduction and valence bands is representative of a given insulating phase. We will list all such matrices in the next section, after a convenient canonical transformation that makes the counting trivial and yields a total of eight matrices (for spinless electrons). Thus, the seven orders listed above (the VBS and QHE have degeneracies of three each) do not exhaust all possible insulating states. The remaining insulator will be found to maintain the chiral condition, but will display unusual band topology. Hence we call it the chiral Topological Insulator (cTI), and discuss its properties in the following section.

The Dirac mass matrices corresponding to these orders before the canonical transformation and their symmetry properties are summarized in Table 3.1.

3.2.2 Transformation to normal form

It will be useful to write the kinetic part of the Dirac Hamiltonian $H^0_{\mathbf{k}+\mathbf{Q}}$ in a form where the Dirac and flavor indices are separated out. Since the Dirac matrices in three dimensions are represented by 4×4 matrices, for the eight dimensional representation we have here this will

Mass matrix ($\mathcal{M}$)	Physical interpretation	TRS (spinless)	Chiral symmetry	Inversion
$\tau_y\nu_z$	VBS_x	◯	◯	◯
$-\tau_y\mu_z\nu_x$	VBS_y	◯	◯	◯
$-\tau_y\mu_x\nu_x$	VBS_z	◯	◯	◯
τ_z	CDW	◯	×	×
$\tau_y\mu_y\nu_z$	cTI	×	◯	◯
$\tau_z\mu_y$	QH_{yz}	×	×	×
$-\tau_z\mu_x\nu_y$	QH_{zx}	×	×	×
$-\tau_z\mu_z\nu_y$	QH_{xy}	×	×	×

Table 3.1: Mass terms and their symmetries for spinless fermions in a geometrically friendly representation, i.e., one in which the eight components of the spinor are simply the eight sites of the unit cell. The kinetic matrices are $\Gamma_x = \tau_x$, $\Gamma_y = \tau_y\nu_y$, $\Gamma_z = \tau_y\mu_y\nu_x$ ◯ and × denote preserved and broken symmetry, respectively.

result in two flavors of Dirac fermions. We seek a representation where the velocity matrices are independent of the flavor index. There are several distinct transformations that achieve this, and we choose to use the following unitary transformation that selects μ as the flavor index.

$$\mathcal{H}^{\text{Dirac}}_{\mathbf{k}} = UH^0_{\mathbf{k}+\mathbf{Q}}U^\dagger \ , \ U = e^{i\frac{\pi}{4}\nu_z}e^{-i\frac{\pi}{4}\tau_x}e^{i\frac{\pi}{4}\mu_y\nu_y} \tag{3.2.11}$$

hence, giving us a new set of velocity matrices α_i

$$\begin{aligned}\mathcal{H}^{\text{Dirac}}_{\mathbf{k}} &= (k_x\alpha_x + k_y\alpha_y + k_z\alpha_z)\\ \alpha_x = \tau_x \ , \ \alpha_y &= \tau_z\nu_x \ , \ \alpha_z = \tau_z\nu_z\end{aligned} \tag{3.2.12}$$

Note, they do not involve the μ_a Pauli matrices. Now, any mass term must anticommute with these three matrices. There are two Dirac matrices that have this property, which we call β_0, β_5:

$$\beta_0 = \tau_y,\ \beta_5 = \tau_z\nu_y \tag{3.2.13}$$

Note also, that these anticommute with one another $\{\beta_0, \beta_5\} = 0$. Any hermitian 2×2 flavor matrix multiplying one of the matrices, will also lead to a mass term. Since there are four such flavor matrices $\{\mathbb{I}_{2\times 2}, \mu_x, \mu_y, \mu_z\}$, we have eight mass terms in all, representing eight insulators that can be accessed from the Dirac theory. The seven orders identified earlier can now be identified with their mass matrices as in Table 3.2. In addition we identify the eighth mass term $\beta_5\otimes\mathbb{I}_{2\times 2}$ as that of a type of topological insulator, which satisfies the chiral condition. The chiral condition (3.2.6) is now implemented by

$$\{H_{\mathbf{k}}, \beta_0\} = 0 \tag{3.2.14}$$

and TRS for a Hamiltonian $\mathbb{H} = \sum_{\mathbf{k}} f^\dagger_{\mathbf{k}} H_{\mathbf{k}} f_{\mathbf{k}}$ is preserved if

$$\beta_0\beta_5\mu_y H^*_{-\mathbf{k}}\mu_y\beta_5\beta_0 = H_{\mathbf{k}} \tag{3.2.15}$$

While evaluating the TRS properties of the perturbations listed in Table 3.2, note that under $\mathbf{k} \to -\mathbf{k}$, the perturbations in the second set change sign.

β_0	τ_y
Order	$\mathcal{M}$
CDW	β_0
QHE_{xy}	$\beta_0\mu_x$
QHE_{yz}	$\beta_0\mu_y$
QHE_{zx}	$\beta_0\mu_z$

β_5	$\tau_z\nu_y$
Order	$\mathcal{M}$
cTI	β_5
VBS_z	$\beta_5\mu_x$
VBS_x	$\beta_5\mu_y$
VBS_y	$\beta_5\mu_z$

Table 3.2: Mass matrices ($\mathcal{M}$) in canonical representation. The β matrices are antisymmetric and anticommute with the symmetric α-matrices in (3.2.12) and also with each other. The "flavor" index, μ, is absent from the α-matrices.

One advantage of writing the Hamiltonian in this form is that the commutation relationships between the various mass matrices can be determined trivially. Perturbations described by commuting mass matrices are separated by a quantum critical point. For example, a quantum phase transition is required to go from the VBS phase to the cTI phase, but not to the CDW phase. The other advantage will be seen in Sec. 3.6.

3.3 Chiral topological insulator: Protected surface states

There is only one mass term which preserves the chiral symmetry (3.2.14) and breaks TRS (3.2.15), and we propose that this is a 3D topological insulator discussed in [119]. We call this a **chiral Topological Insulator (cTI)**. On the cubic lattice, this mass term corresponds to the purely imaginary third neighbor hopping, along the body diagonal of the cube. The corresponding microscopic Hamiltonian is given by

$$H^{b.d.} = i|t''| \sum_{\mathbf{R}} \sum_{\Delta\mathbf{R}=1}^{8} c^\dagger_{\mathbf{R}} \Phi^{site}_{\mathbf{R}} \Phi^{dir}_{\Delta\mathbf{R}} c_{\mathbf{R}+\Delta\mathbf{R}} \tag{3.3.1}$$

where $\mathbf{R} = (X, Y, Z)$ labels sites on a cubic lattice with a one-site unit cell and $\Delta\mathbf{R} = (\Delta X, \Delta Y, \Delta Z) = (\pm 1, \pm 1 \pm 1)$ connects the site at $\mathbf{R}$ to its eight third-neighbors. $\Phi^{site}_{\mathbf{R}}$ and $\Phi^{dir}_{\Delta\mathbf{R}}$ are phase factors depending on the site$\mathbf{R}$ and the direction of $\Delta\mathbf{R}$, respectively, as

$$\Phi^{site}_{\mathbf{R}} = (-1)^{X+Z} \ , \ \Phi^{dir}_{\Delta\mathbf{R}} = \Delta X \Delta Y \Delta Z \tag{3.3.2}$$

The result is shown for a particular $\mathbf{R}$ in Figure 3.3.1. Note that the third neighbor hopping texture that gives a cTI depends on the gauge choice. The texture shown is appropriate for our chosen gauge, in which there are negative hoppings along Y and Z.

This renders the total Hamiltonian $\mathbb{H} = \int d^3k \, f^\dagger_{\mathbf{k}} (H^0_{\mathbf{k}} + H^{b.d.}_{\mathbf{k}}) f_{\mathbf{k}}$ a member of symmetry class AIII of the Altland-Zirnbauer classification [155, 60, 7]. A class AIII topological insulator is characterized by a non-zero topological invariant ν introduced in [119], which, in this case, is given by $\nu = \pm 1$ where the sign depends on the sign of the third neighbor hopping.

3.3.1 Protected surface states

A physical consequence of the presence of the cTI mass term with non-zero winding number $\nu = \pm 1$ is the presence of a single (2+1)-dimensional Dirac cone at the surface. The node

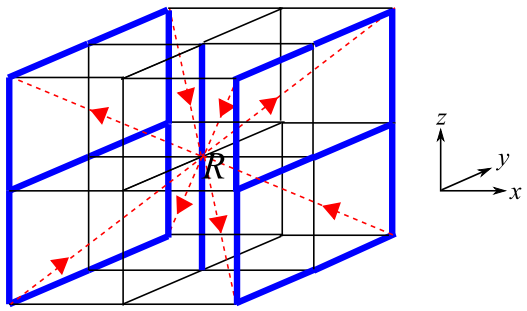

Figure 3.3.1: Imaginary third neighbor hopping pattern that results in a topological insulator. The arrows denote the directions in which the hopping is $+i$. The Figure shows how a particular site bonds to its eight third-neighbors. This pattern must be replicated around each site, after taking into account the appropriate phase factor $\Phi_{\mathbf{R}}^{site} = (-1)^{X+Z}$ for that site. In other words, all the arrows must be reversed every time the pattern is translated by a unit distance along X or Z.

is centered at zero energy. Figure 3.3.2 shows the results of a numerical calculation of the surface band structure for the (001) surface. Clearly, there is a single Dirac cone at $(\pi/2, \pi/2)$.

This is analogous to the odd number of Dirac nodes found on the surface of the spin-orbit topological insulators. However, there are several important differences. Firstly, the surface nodes of the spin-orbit TIs are protected by TRS. In our model, however, TRS is explicitly broken, given the imaginary third neighbor hoppings and spin polarized (spinless) fermions. Instead, another discrete symmetry - the chiral symmetry - protects the node. However, a much more striking difference is the fact that the cTI can host *any integer* number of Dirac nodes on its surface, making it markedly different from the spin-orbit TIs which become trivial insulators if there are even numbers of Dirac nodes on their surfaces. We will explicitly prove these features of the cTI in the ensuing sections. Also, in the cTI, the surface Dirac nodes are centered at the chemical potential, because of sublattice symmetry.

The fact that a single Dirac cone is stable should be contrasted with the corresponding phenomenon on two-dimensional systems on a lattice, where the no-go theorem prohibits a single Dirac cone, although that requires TRS. If TRS is broken, one *can* have a single Dirac node in 2D, but it is not protected against disorder. In our model, one can never localize this surface mode [91] for arbitrary strength of disorder, as far as the disorder respects the chiral symmetry (3.2.6); the dc conductivity σ_{xx} is not affected by disorder, and is always given by the dc conductivity of a clean (2+1)D Dirac fermion, $\sigma_{xx} = 1/\pi$ (in unit of e^2/h), for arbitrary strength of disorder. The (surface) density of states exhibits power-law $\rho(E) \sim |E|^\alpha$ with continuously varying exponent [91].

Figure 3.3.3 shows the exponential decay of the surface states into the bulk for various values of the third-neighbor hopping strength $|t''|$. The fermion "mass" in the low-energy theory is $8|t''|$. Note, when $8|t''| = 1$ the wavefunction is exactly localized within one unit cell of the surface. This should not come as a complete surprise. Other systems are known in condensed matter physics that have edge states bound to a single cell on the surface at a certain point in the parameter space of the coupling constants, and which decay into the

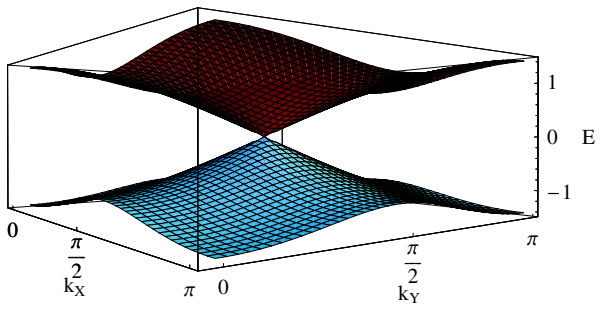

Figure 3.3.2: The surface spectrum in the presence of the proposed cTI term for the (001) surface for 100 bilayers in the $z-$direction. k_x and k_y were incremented in steps of $\pi/40$. Only the lowest conduction and highest valence band states are shown. Higher conduction and lower valence band levels that gradually merge into the bulk spectrum have not been displayed for clarity.

bulk as we move away from this point. A famous example is the spin-1 Heisenberg chain with a biquadratic coupling which carries a free spin-$1/2$ state at each end. Precisely at the 'AKLT point', each of these states lives exactly on the lattice site at its end, and seeps-in along the chain as we move away from that point [5].

3.3.2 Physical picture

At the microscopic level, this feature of the surface spectrum can be understood by starting from a quasi-2D limit and then increasing the strength of the interaction between adjacent sheets. In the decoupled limit, each layer has a pair of Dirac nodes. In the presence of interactions, the degeneracy between the states in adjacent sheets gets destroyed. However, we will show that, on any given layer, the combination of direct and body-diagonal hopping will cause one of the nodes to interact only with the layer above and the other, only with the layer below. This way, the bulk will get gapped out but a single Dirac node will be left on the surface. For calculational convenience and in order to interpret our results most transparently, we work in a different gauge in this section.

We start by considering a system of decoupled square lattices with π-flux plaquettes.

For a two-site unit cell, this has two Dirac nodes at $\mathbf{Q}_{R(L)} = \left[\frac{\pi}{2}\left(-\frac{\pi}{2}\right), 0\right]$ on each layer. Then, we weakly couple these layers through regular nearest-neighbor hopping in the z direction and imaginary third-neighbor interactions with textures like in Figs. 3.2.1 and 3.3.1, respectively, but modified for the current gauge choice. This is expected to mix the nodes in different layers and open a gap. Once again, for ease of calculation and interpretation of the results, we double the unit cell along z, i.e., imagine a stack of bilayers coupled weakly both internally and externally. Now, the Pauli matrices $\nu_{x,y,z}$ act on the space of Dirac nodes. $\tau_{x,y,z}$ act on the A/B sublattice index and $\mu_{x,y,z}$ act on the bilayer index along z (primed vs unprimed fields), as before.

In the basis

$$\Psi = \left(A_R\, A'_R\, B_R\, B'_R\, A_L\, A'_L\, B_L\, B'_L\right)^T \tag{3.3.3}$$

where the primed and the unprimed wavefunctions represent different layers and $A_{1R} \equiv$

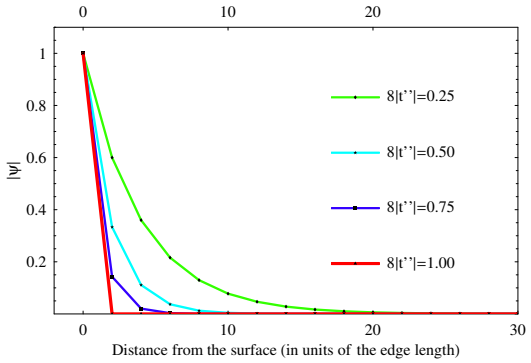

Figure 3.3.3: Decay of the zero-energy surface states on the $z = 0$ surface into the bulk for various values of the third-neighbor hopping strength $|t''|$ (in units of the bulk Fermi velocity). The effective Dirac fermion mass is $8|t''|$. The total thickness of the lattice for this calculation is the same as that in Figure 3.3.2, viz., 200 layers or 100 bilayers. At $8|t''| = 1$, there is no penetration of the surface states into the bulk. In each case, the wavefunction is normalized such that it is unity on the surface.

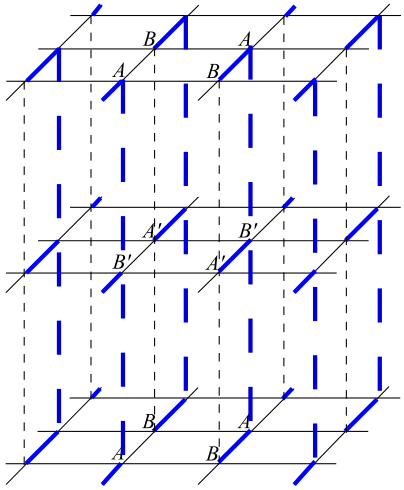

Figure 3.3.4: A quasi-2D approach to creating the π-flux cubic lattice. The blue (bold) lines denote negative bonds. The in-plane hoppings have strength $|t|$ and the interlayer hoppings that are shown have strength $|t_z|$. The imaginary third neighbor hoppings (strength $|t''|$, see text) have not been shown for clarity. Alternate layers are labeled by primed variables, effectively doubling the unit cell in the vertical direction.

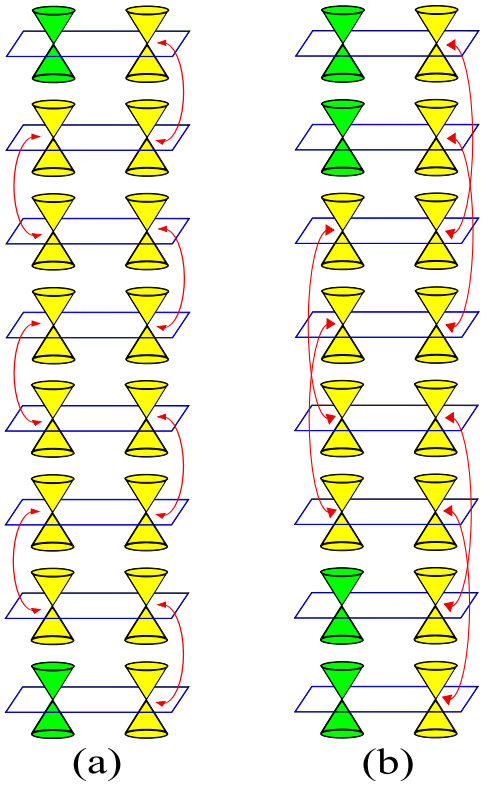

Figure 3.3.5: Schematic representation of the staggered interlayer mixing pattern of Dirac nodes. The degenerate Dirac points at the ends of the red arrows mix and split, opening up a gap. A surface Dirac node (colored green) is left behind in (a). A pair of surface Dirac nodes arises when we mix nodes separated by two layers as in (b).

$A_1(\mathbf{Q}_R)$ etc., the intra-bilayer hopping Hamiltonian takes the form

$$\mathcal{H}_{in} = -\left(|t_z| + 4|t''|\nu_z\right)\tau_y\mu_y \tag{3.3.4}$$

whereas hopping from $z-1$ to z is described by

$$\mathcal{H}^+ = \left(|t_z| - 4|t''|\nu_z\right) i\tau_y \left(\frac{\mu_x + i\mu_y}{2}\right) \tag{3.3.5}$$

Here $|t_z|$ and $|t''|$ are the strengths of the regular and the third neighbor hoppings, respectively.

In the limit $|t_z| = 4|t''|$, $\mathcal{H}_{in}$ and $\mathcal{H}^+$ become proportional to the orthogonal projection operators $\frac{1+\nu_z}{2}$ and $\frac{1-\nu_z}{2}$, respectively. This means that the R Dirac points mix and split only *within* the bilayer, and the L Dirac points, only *between* bilayers, resulting in a staggered mixing pattern as shown in Figure 3.3.5-(a). Clearly, if we terminate the lattice at a surface, a single node is left unpaired. This model is in concurrence with the numerical results presented in the previous section, because, when $|t_z|$ equals the in-plane hopping, the above limit is equivalent to the condition $8|t''| = 1$.

When $|t_z| \neq 4|t''|$, the Hamiltonian can be split into two parts: one consisting of projection operators as described above which leave the surface gapless, and the other, of the residual

t_z which does not open a gap anywhere (although it causes the surface states to penetrate into the bulk). Thus, the surface remains gapless for arbitrary $|t_z|$ and $|t''|$ as well. Note that since the right and the left nodes behave differently, TRS is explicitly broken as expected.

For the purists, a more rigorous calculation for the full theory shows the same.

In the basis $\Psi^z_{\mathbf{k}} = (A^z_{\mathbf{k}}\, A'^z_{\mathbf{k}}\, B^z_{\mathbf{k}}\, B'^z_{\mathbf{k}})^T$, the intra- and inter-bilayer Hamiltonians take the form

$$\begin{aligned} H^{in}_{\mathbf{k}} &= -2|t|(\tau_x \cos k_x - \tau_y \sin k_y) \\ &\quad - \{|t_z| + 2t'' [\sin(k_x + k_y) + \sin(k_x - k_y)]\}\, \tau_y \mu_y \\ H^{\pm}_{\mathbf{k}} &= \pm i \{|t_z| - 2t'' [\sin(k_x + k_y) + \sin(k_x - k_y)]\}\, \tau_y \mu_{\pm} \end{aligned} \tag{3.3.6}$$

where $\mu_{\pm} = \frac{1}{2}(\mu_x \pm i\mu_y)$. By the cone-pairing picture described above, terminating the crystal from below at an unprimed layer should result in a pair of zero-energy states at the L node. Indeed, solving Schrödinger's equation at $E = 0$ and $\mathbf{k} = \mathbf{Q}_L$ with the boundary condition $\Psi^0_{\mathbf{Q}_L} = 0$ gives two solutions

$$\begin{aligned} \Psi^z_{\mathbf{Q}_L} &= \left(\frac{1-\alpha}{1+\alpha}\right)^{z-1} \begin{pmatrix} 1 \\ 0 \\ 0 \\ 0 \end{pmatrix} \\ \text{and} \quad & \left(\frac{1-\alpha}{1+\alpha}\right)^{z-1} \begin{pmatrix} 0 \\ 0 \\ 1 \\ 0 \end{pmatrix} \end{aligned} \tag{3.3.7}$$

where $\alpha = |t_z|/|4t''|$. These are both wavefunctions localized at the surface. At $\mathbf{k} = \mathbf{Q}_R$, effectively $\alpha \to -\alpha$, resulting in exponentially growing solutions. When $\alpha \to 1$, $\Psi^z_{\mathbf{Q}_L} \to 0$ for $z > 1$. This is consistent with our model that when $|t_z| = 4|t''|$, there is no penetration of the surface states into the bulk.

3.3.3 Stability of nodes and the $\mathbb{Z}$-cTI

The single Dirac node is stable against static perturbations as long as the chiral condition is preserved. This has been discussed in [119]. Here, we repeat the proof in brief.

In the absence of any perturbations, the low-energy surface Hamiltonian can be written as

$$\begin{aligned} \mathcal{H}_S &= -i\partial_x \eta_x - i\partial_y \eta_y \\ &= \begin{pmatrix} & -i\partial \\ -i\bar{\partial} & \end{pmatrix} \end{aligned} \tag{3.3.8}$$

where η_i are Pauli matrices corresponding to the two branches of the Dirac spectrum and $\partial = \partial_x - i\partial_y$, $\bar{\partial} = \partial_x + i\partial_y$. Now, since the bulk chiral operator, which is simply the CDW mass matrix, is local (i.e., purely on-site), it must have a well-defined realization on the surface too. The only matrix that anti-commutes with $\mathcal{H}_S$ is η_z. Thus, this must be

the chiral operator for the surface. In other words, the chiral condition on the surface is implemented by

$$\{\mathcal{H}_S, \eta_z\} = 0 \tag{3.3.9}$$

All the other perturbations which open a bulk gap are non-local, and thus, will couple the two Dirac cones on the two opposite surfaces of a finite slab system.

If the chiral symmetry is to be preserved, the only possible modifications to $\mathcal{H}_S$ in the presence of surface perturbations can be of the form

$$\mathcal{H}_S \to \begin{pmatrix} & -i\partial + A \\ -i\bar{\partial} + A^* & \end{pmatrix} \tag{3.3.10}$$

But this is simply a gauge transformation, and its only effect is to shift the location of the Dirac node. Thus, the chiral symmetry protects gapless surface states.

The consequence of the chiral symmetry, though, is even more profound. Unlike the 2D and 3D time-reversal symmetric topological insulators where only an odd number of gapless surface nodes are stable leading to a $\mathbb{Z}_2$-classification, *any integer* number of surface nodes is stable on the cTI and each belongs to a distinct university class. In the node-pairing picture, a way to generate an integer n number of nodes is by assuming pairing only between nodes that are n layers apart, as shown in Figure 3.3.5-(b) for $n = 2$. In other words, we assume n independent intercalated layers. Alternately, we can think of the n layers as n orbitals (or any n internal degrees of freedom) on the same layer. Since the surface modes are protected by the chiral symmetry (3.2.6), mixing of the orbitals will not change the topological characteristics of the surface. In other words, A in (3.3.10) becomes an $n \times n$ matrix corresponding to the orbital space and $A^* \to A^\dagger$. Diagonalizing A by an appropriate similarity transformation will give n copies of the single Dirac node, in general at different positions in the surface Brillouin zone. Thus, the cTI can alternately be called a "$\mathbb{Z}$-cTI" or simply, "$\mathbb{Z}$TI".

3.3.4 Application to spin-orbit $\mathbb{Z}_2$ topological insulators

Here we show how three dimensional topological insulators with time reversal symmetry [38, 96] can be realized using a node-pairing picture similar to the one shown above for a cTI. Since, in the above description, the left and the right Dirac nodes behave differently, TRS is explicitly broken. However, if the two nodes on the 2D sheets are both at TRIM, it is possible to realize a TRS-protected $\mathbb{Z}_2$ topological insulator (TI) through a similar mechanism. Here, we present a microscopic model for the same.

Consider a cubic lattice with each site carrying spin-orbit coupled s and p orbitals with total angular momentum $1/2$:

$$\begin{aligned} S_+ &= s\uparrow \quad , \quad P_+ = \frac{1}{\sqrt{3}} p_0 \uparrow - \sqrt{\frac{2}{3}} p_1 \downarrow \\ S_- &= s\downarrow \quad , \quad P_- = \frac{1}{\sqrt{3}} p_0 \downarrow + \sqrt{\frac{2}{3}} p_{-1} \uparrow \end{aligned} \tag{3.3.11}$$

where $\uparrow$ ($\downarrow$) refers to up (down) spins, s and p are atomic-like orbitals and the subscripts on the p's refer to the z-components of their angular momenta, i.e., $p_0 = p_z$ and $p_{\pm 1} =$

$\frac{1}{\sqrt{2}}(p_x \pm ip_y)$. $S_\pm(P_\pm)$ are even (odd) under inversion. Under time-reversal, they transform as

$$\begin{aligned} \mathcal{T}\, S_+ = S_- \quad &, \quad \mathcal{T}\, P_+ = P_- \\ \mathcal{T}\, S_- = -S_+ \quad &, \quad \mathcal{T}\, P_- = -P_+ \end{aligned} \tag{3.3.12}$$

where $\mathcal{T}$ is the time-reversal operator.

The tight-binding Hamiltonian for this system is particularly easy to write down, if we only consider on-site and nearest neighbor overlaps between the various orbitals. Many matrix elements vanish; for instance, the overlap integral between an s and a p_0 orbital on the same xy-plane vanishes since they opposite parities under $z \to -z$. Similarly, overlap of orbitals with opposite spin vanishes. On the other hand, s and p_x orbitals on nearest neighbor sites in the same xy-plane have non-zero overlap. A similar calculation was performed in 2D in [13]. The result is $\mathbb{H} = \sum_k \Psi_k^\dagger H_k \Psi_k$ where $\Psi^\dagger = \left(S_+^\dagger,\, S_-^\dagger,\, P_+^\dagger,\, P_-^\dagger\right)$ and

$$\begin{aligned} H_k \;=\; & v_f\left(\tau_x\sigma_y \sin k_x - \tau_x\sigma_x \sin k_y + \tau_y \sin k_z\right) \\ & + \left[M + m\left(\cos k_x + \cos k_y + \cos k_z\right)\right]\tau_z \\ & + n\left(\cos k_x + \cos k_y + \cos k_z\right). \end{aligned} \tag{3.3.13}$$

Here τ_i and σ_i are Pauli matrices and v_F is the Fermi velocity. τ_i act on the S-P space and σ_i act on the $\pm$ index. The first set of terms come from overlaps between orbitals of different types on neighboring sites (e.g., S_+ with P_-). These terms, being off-diagonal in the τ index are odd functions of momentum because of opposite parities of the S and P orbitals. The overlap between each orbital with another orbital of the same type on the same or neighboring site gives the remaining terms. Since the magnitude of the overlap integrals will in general be different for the S and the P orbitals, we get two kinds of terms - one, proportional to τ_z incorporates the difference in the magnitudes, and the other, proportional to identity, describes their sum. The above Hamiltonian clearly preserves TRS:

$$\sigma_y H_{-k}^* \sigma_y = H_k \tag{3.3.14}$$

and inversion:

$$\tau_z H_{-k} \tau_z = H_k. \tag{3.3.15}$$

All the cubic symmetries are also preserved, because the basis states form representations of the full three-dimensional rotation group and the Hamiltonian preserves inversion.

The term proportional to τ_z gaps out the spectrum. The only other term that can create a gap must be proportional to $\sigma_z\tau_z$, but that breaks TRS. Therefore, the τ_z term gives a strong topological insulator (STI) for appropriate values of m and M.

For simplicity, let us assume $n = 0$. This ensures that the Fermi surface is always in the gap, unless the gap closes, in which case the Fermi surface contains the Dirac point. If $n \neq 0$, and sufficiently large, then it is possible that the system no longer remains insulating. Using the prescription outlined in [35], according to which the topological character of the band structure of an inversion symmetric system is determined by the parities of the occupied bands at the TRIM, it is straightforward to obtain the phase diagram shown in Figure 3.3.6. In particular, in the region $1/3 < m/M < 1$, a strong topological insulator is obtained. We use

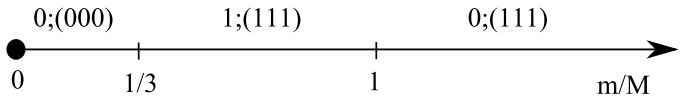

Figure 3.3.6: Phase diagram for the 3D TRS Hamiltonian with Dirac nodes at the TRIM points as a function of the parameter m/M in (3.3.13). We assume $n = 0$. The numbers $\nu_0;(\nu_1\nu_2\nu_3)$ are the $\mathbb{Z}_2$ invariants that characterize the phases [35]. ν_0 is the so-called "strong index" and ν_1, ν_2 and ν_3 are the three "weak" indices corresponding to the x, y and z directions respectively. $\nu_0 = 1$ for a strong topological insulator, as in the region $1/3 < m/M < 1$

the notation $\nu_0;(\nu_1\nu_2\nu_3)$ to specify the "strong" index ν_0 and the three "weak" indices ν_1, ν_2 and ν_3 corresponding to the x, y and z directions respectively. For an inversion symmetric system, $(-1)^{\nu_0} = \prod_{k\in TRIM} P_k$ where P_k is the product of the parity eigenvalues of the occupied states at momentum k, and a STI has $\nu_0 = 1$. For non-zero n, the system is in an insulating state if $|m|$, $|M| > |n|$.

To understand how the STIs are formed, define

$$\tilde{\Psi}^\dagger = \frac{1}{\sqrt{2}}\left(S_+^\dagger + P_+^\dagger, S_-^\dagger + P_-^\dagger, -S_+^\dagger + P_+^\dagger, -S_-^\dagger + P_-^\dagger\right) \tag{3.3.16}$$

If we turn off the interlayer coupling in the z-direction, we get decoupled 2D sheets with the Hamiltonian

$$\begin{aligned} \tilde{H}_k &= v_F\left(\tau_z\sigma_y \sin k_x - \tau_z\sigma_x \sin k_y\right) && (3.3.17)\\ &\quad -\left[M + m\left(\cos k_x + \cos k_y\right)\right]\tau_x && (3.3.18)\end{aligned}$$

in the new basis. If we now turn on the interlayer coupling, the total Hamiltonian can be written as

$$\mathbb{H} = \sum_{k_x,k_y,z}\left(\tilde{\Psi}_z^\dagger \tilde{H}\,\tilde{\Psi}_z + \tilde{\Psi}_z^\dagger H^+ \tilde{\Psi}_{z-1} + \tilde{\Psi}_z^\dagger H^- \tilde{\Psi}_{z+1}\right) \tag{3.3.19}$$

where $H^\pm = \pm i\frac{v_F}{2}\tau_y - \frac{m}{2}\tau_x$. At the special point $m = M/2 = v_F$, the 2D Hamiltonian is gapless at (π,π) and $H^\pm = -\frac{v_F}{2}\tau_\mp$. This means that as the interlayer coupling is introduced, the Dirac points are gapped out in the following way. The first pair of time-reversal partners in each layer, $S_+ + P_+$ and $S_- + P_-$, mix with the second pair, $-S_+ + P_+$ and $-S_- + P_-$ in the layer above. Therefore, the surface of a finite insulator has a single Dirac node on the surface. At the special point chosen here, the node is exactly on the surface. If we move away from that point, the surface states start penetrating into the bulk.

In the current model, the full cubic symmetry is preserved. We may break some symmetries by, for example, changing the numerical coefficients of the p-orbitals in (3.3.11). Then, there will be more parameters in the model and it is possible to get several more phases with different weak indices.

3.4 Chiral topological insulator: Electromagnetic response

We now discuss a field theory which describes the electromagnetic response of a chiral topological insulator which can be readily calculated from the Dirac limit. This can be done by considering the fermionic path integral

$$\int \mathcal{D}\left[c^\dagger, c\right] e^{iS[c^\dagger, c, A_\mu]} =: e^{iW_{\text{eff}}[A_\mu]}, \tag{3.4.1}$$

where the fermionic action $S[c^\dagger, c, A_\mu] = \int dt L[c^\dagger, c, A_\mu]$ is given by

$$L = \sum_{R,R'} c_R^\dagger \left\{(i\partial_t + A_0)\delta_{RR'} - \mathcal{H}_{RR'}[\boldsymbol{A}]\right\} c_{R'},$$

and $\mathcal{H}_{RR'}[\boldsymbol{A}]$ represents a (tight-binding) Hamiltonian of a chiral topological insulator, minimally coupled to the external electromagnetic U(1) gauge field A_μ. [109, 30] $W_{\text{eff}}[A_\mu]$ is the effective action for the electromagnetic field, which encodes all electromagnetic responses of the system. When the system of our interest is gapped in the bulk, $W_{\text{eff}}[A_\mu]$ includes the Maxwell term with modified permeability and dielectric constant. Besides the Maxwell term, $W_{\text{eff}}[A_\mu]$ can also include the so-called theta term [136],

$$\frac{\theta e^2}{4\pi^2\hbar}\boldsymbol{E}\cdot\boldsymbol{B} = \frac{\theta e^2}{32\pi^2\hbar}\epsilon^{\mu\nu\kappa\lambda}F_{\mu\nu}F_{\kappa\lambda}, \tag{3.4.2}$$

(Here we reinstated the Planck constant and the electric charge.) The effective field theory of the same type was discussed previously for three-dimensional $\mathbb{Z}_2$ topological insulators [109].

While in principle θ can take any value, in the presence of chiral symmetry, the theta angle is constrained to be $\theta = 0$ or π: When there is chiral symmetry, under the unitary transformation (particle-hole transformation)

$$\mathcal{C} c_R \mathcal{C}^{-1} = (-1)^R c_R^\dagger, \tag{3.4.3}$$

followed by time-reversal

$$\mathcal{T} c_R(t) \mathcal{T}^{-1} = c_R(-t), \quad \mathcal{T} i \mathcal{T}^{-1} = -i, \tag{3.4.4}$$

the fermion bilinear $\int dt \sum_{R,R'} c_R^\dagger \mathcal{H}_{RR'}[\boldsymbol{A}] c_{R'}$ is left unchanged while the sign of A_0 is flipped, i.e., $\mathcal{TC}$ sends

$$\boldsymbol{E} \to -\boldsymbol{E}, \quad \boldsymbol{B} \to \boldsymbol{B}. \tag{3.4.5}$$

Thus, θ can be mapped to $-\theta$ by $\mathcal{TC}$. On the other hand, under periodic boundary conditions, the theta term is invariant under $\theta \to \theta + 2\pi$. Thus, chiral symmetry is consistent with $\theta = \pi$ as well as $\theta = 0$. As we will show in Sec. 3.4.1, by integrating out fermions explicitly, a chiral topological insulator realizes $\theta = \pi$; $\theta = \pi$ is a hallmark of chiral topological insulators.

This is anticipated since the theta term is a surface term

$$\epsilon^{\mu\nu\kappa\lambda} F_{\mu\nu} F_{\kappa\lambda} = 2\epsilon^{\mu\nu\kappa\lambda} \partial_\mu \left(A_\nu F_{\kappa\lambda} \right) \tag{3.4.6}$$

and upon partial integration gives rise to the (2+1)-dimensional Chern-Simons action at the surface of chiral topological insulator. When $\theta = \pi$, the Hall conductivity σ_{xy} on the surface, which is the coefficient of the surface Chern-Simons action, is one half, $\sigma_{xy} = \pm 1/2$ (in unit of e^2/h),

$$S_{\rm CS} = \frac{\sigma_{xy}}{4\pi} \int d^3x \, \epsilon^{\mu\nu\rho} A_\mu \partial_\nu A_\rho, \quad \sigma_{xy} = \pm \frac{1}{2}, \tag{3.4.7}$$

which indeed reproduces our results from microscopic calculations.

Note that the effect of the theta term shows up only when θ is non-uniform [109, 145]. In particular, when we make an interface between a chiral topological insulator and a trivial insulator (or vacuum), the theta angle changes from $\theta = \pi$ (inside the topological insulator) to $\theta = 0$ (outside the topological insulator). Then, in the presence of the chiral symmetry, there exist gapless surface states. If the chiral symmetry is broken on the surface, for example, by breaking the A/B sublattice symmetry, the surface states will be gapped and lead to a quantized hall response. This also defines a smooth path for θ to evolve from 0 to π near the surface.

3.4.1 Derivation of the theta term

Dirac model

In this section, we demonstrate $\theta = \pi$ in the chiral topological insulator we introduced by carrying out the fermionic path integral. Below, we will use the Euclidean formalism (imaginary-time path integral), in which case the theta term appears as the imaginary part of the effective action while the Maxwell term appears as the real part. To compute the theta angle of the effective action within the continuum Dirac Hamiltonian, it will prove useful to compare the effective action for two different states, VBS and chiral topological insulator,

$$W_{\rm eff,VBS}, \quad W_{\rm eff,cTI}. \tag{3.4.8}$$

The two states can be connected to each other by continuous (adiabatic) deformation of the Hamiltonian, if we break the chiral symmetry during the deformation. Namely, we can interpolate, by one parameter, say, $\alpha \in [0, \pi]$, the two mass terms representing the TI ($M_{\rm cTI}$), and VBS ($M_{\rm VBS}$), respectively, without closing the bulk band gap,

$$M(\alpha = 0) = M_{\rm cTI}, \quad M(\alpha = \pi) = M_{\rm VBS}. \tag{3.4.9}$$

The variation of the theta angle with respect to α, $\delta\theta/\delta\alpha$, can then be computed along the deformation path. We know that the imaginary part of $W_{\rm eff}$ should be zero for VBS, $\mathrm{Im}\, W_{\rm eff,VBS} = 0$, since the VBS state can continuously be connected, without breaking chiral symmetry, to the trivial insulator, $\theta(\alpha) = 0$. The theta angle for chiral topological insulator can then be obtained by integrating the variation $\delta\theta/\delta\alpha$ with the boundary condition $\theta(\alpha = \pi) = 0$.

We now compute the variation $\delta\theta/\delta\alpha$. To connect $M_{\rm CTI}$ and $M_{\rm VBS}$, we can flip the sign of the mass term for a 4×4 subsector of the 8×8 Dirac Hamiltonian, while keeping the other half intact: when we smoothly connect the Hamiltonians with the masses $M_{\rm CTI}$ and $M_{\rm VBS}$, $\mathcal{H}^0_{\mathbf{k}}+(1-t)M_{\rm CTI}+tM_{\rm VBS}$ $(0\le t\le 1)$, keeping chiral symmetry during the interpolation, four out of eight eigenvalues (for each $\mathbf{k}$) cross while the remaining four are not affected by the interpolation. We thus consider the following single 4×4 continuum Dirac model,

$$\mathcal{H} \;=\; \boldsymbol{k}\cdot\boldsymbol{\alpha}+m\beta. \tag{3.4.10}$$

The corresponding partition function and the imaginary-time action are:

$$\begin{aligned} Z \;&=\; \int \mathcal{D}\left[\psi^\dagger,\psi\right] e^{-S},\\ S \;&=\; \int d\tau d^3r\, \psi^\dagger\left(\partial_\tau - i\boldsymbol{\partial}\cdot\boldsymbol{\alpha}+m\beta\right)\psi, \end{aligned} \tag{3.4.11}$$

With $\bar\psi = \psi^\dagger\beta$, and with the inclusion of the background gauge field, the action can be written as

$$S \;=\; \int d^4x\,\bar\psi\left[\left(\partial_\mu+iA_\mu\right)\gamma_\mu+m\right]\psi, \tag{3.4.12}$$

where $\mu=1,\ldots,4$, and we have introduced Euclidean gamma matrices, $\gamma_{i=1,2,3}=-i\beta\alpha_i$, $\gamma_4=\beta$, which satisfy

$$\{\gamma_\mu,\gamma_\nu\}=2\delta_{\mu\nu},\quad \gamma_\mu^\dagger=\gamma_\mu,\quad \mu=1,2,3,4. \tag{3.4.13}$$

We also introduce

$$\gamma_5=-\gamma_1\gamma_2\gamma_3\gamma_4. \tag{3.4.14}$$

As advertised, we can flip the sign of mass, in a continuous fashion, by the following chiral rotation

$$\psi\to\psi=e^{i\alpha\gamma_5/2}\psi',\quad \bar\psi\to\bar\psi=\bar\psi' e^{i\alpha\gamma_5/2}, \tag{3.4.15}$$

under which

$$\begin{aligned} \bar\psi\left(\nabla_\mu\gamma_\mu+m\right)\psi \;&=\; \bar\psi'\left(\nabla_\mu\gamma_\mu+m'(\alpha)\right)\psi',\\ m'(\alpha) \;&=\; me^{i\alpha\gamma_5}=m\left[\cos\alpha+i\gamma_5\sin\alpha\right], \end{aligned} \tag{3.4.16}$$

so that $m'(\alpha=0)=m$ and $m'(\alpha=\pi)=-m$.

Calculation of the effective action by gradient expansion

The fermionic path integral defined by (3.4.11) and (3.4.12) can be evaluated for slowly varying external gauge field A_μ by derivative expansion. Given the fact that the space-time

variation of the theta angle couples to the electromagnetic field, it is convenient to consider the case where the mass term also changes slowly in spacetime according to

$$\begin{aligned} m &\to m\left[\cos\left(\alpha(\tau,x)\right)+i\gamma_5\sin\left(\alpha(\tau,x)\right)\right] \\ &\simeq m+i\gamma_5\delta m(\tau,x), \\ \delta m(\tau,x) &= m\delta\alpha(\tau,x). \end{aligned} \tag{3.4.17}$$

Below, we compute the derivation of the theta angle with respect to small change in the mass term, $\delta\theta/\delta\alpha$, by gradient expansion.

We integrate out the fermions and derive the effective action for the gauge fields A_μ and δm,

$$\int \mathcal{D}\left[\bar{\psi},\psi\right] e^{-S} = e^{-W_{\text{eff}}[A_\mu,\delta m]}, \tag{3.4.18}$$

by a derivative expansion

$$\begin{aligned} W_{\text{eff}} &= -\text{Tr}\,\ln\left(G_0^{-1}-V\right) \\ &= -\text{Tr}\,\ln G_0^{-1}+\sum_{n=1}^{\infty}\frac{1}{n}\text{Tr}\,\left(G_0V\right)^n, \end{aligned} \tag{3.4.19}$$

where G_0 denotes the propagator of free (3+1)D massive Dirac fermions, which is given in momentum space by

$$G_0(k) = -\frac{i\not{k}+m}{k^2+m^2}, \tag{3.4.20}$$

whilst

$$V(q) = +i\not{A}(q)+i\gamma_5\delta m(q). \tag{3.4.21}$$

The resultant effective action, to leading order in the derivative expansion, takes the following form

$$i\delta\text{Im}W_{\text{eff}} = \frac{i}{8\pi}\int d^4x\,\frac{\delta m}{m}\epsilon^{\mu\nu\rho\sigma}\partial_\rho A_\mu\partial_\sigma A_\nu. \tag{3.4.22}$$

Integrating the variation,

$$i\text{Im}W_{\text{eff}} = \frac{i}{8\pi}\int d^4x\,\epsilon^{\mu\nu\rho\sigma}\partial_\rho A_\mu\partial_\sigma A_\nu. \tag{3.4.23}$$

Calculation of the effective action by Fujikawa method

We now give an alternative derivation based on the Fujikawa method [39]. Since M_{CTI} can continuously be rotated into M_{VBS}, one would think, naively, $W_{\text{eff,VBS}} = W_{\text{eff,CTI}}$. This is not true, however, as we have demonstrated: $W_{\text{eff,VBS}}$ and $W_{\text{eff,CTI}}$ should differ by the theta term. The reason why this naive expectation breaks down is the chiral anomaly. The chiral

transformation which rotates $M_{\rm CTI}$ continuously into $M_{\rm VBS}$ costs the Jacobian $\mathcal{J}$ of the path integral measure,

$$\int \mathcal{D}\left[\bar{\psi},\psi\right] e^{-S[m]} = \int \mathcal{D}\left[\bar{\psi}',\psi'\right] \mathcal{J} e^{-S[m']}. \tag{3.4.24}$$

The chiral anomaly (the chiral Jacobian $\mathcal{J}$) is responsible for the theta term.

We now compute the Jacobian $\mathcal{J}$ explicitly, by breaking up the chiral transformation into an infinitesimal chiral rotation

$$\begin{aligned} &\psi \to \psi = U(t)\psi_t \quad \bar{\psi} \to \bar{\psi} = \bar{\psi}_t U(t) \\ &U(t) = e^{t\Theta}, \quad t \in [0,1], \quad \Theta = i\gamma_5 \frac{\pi}{2} \end{aligned} \tag{3.4.25}$$

For each step t

$$\begin{aligned} \bar{\psi}\left(\nabla_\mu \gamma_\mu + m\right)\psi &= \bar{\psi}_t \left(\nabla_\mu \gamma_\mu + m e^{2i(\pi/2)t\gamma_5}\right)\psi_t \\ &\equiv \bar{\psi}_t D_t \psi_t. \end{aligned} \tag{3.4.26}$$

Observe that when t becomes unity, we completely flip the sign of the mass term. The Jacobian is given by

$$\begin{aligned} \mathcal{J}(t) &= \exp\left[-\int_0^t du \mathcal{W}(u)\right], \\ \mathcal{W}(u) &= \frac{d}{du}\left(\ln \mathrm{Det}\, D_u\right). \end{aligned} \tag{3.4.27}$$

This can be computed as

$$\begin{aligned} \mathcal{W}(u) &= \lim_{\Delta u \to 0} \frac{1}{\Delta u} \mathrm{Tr}\, \left[D_u^{-1} \Delta u \left(\Theta D_u + D_u \Theta\right)\right] \\ &= 2\mathrm{Tr}\, \left[\Theta\right]. \end{aligned} \tag{3.4.28}$$

This expression, if naively interpreted, is divergent and should be regularized by the heat-kernel method,

$$\mathcal{W}(u) = \lim_{M^2 \to \infty} 2\mathrm{Tr}\, \left[\Theta e^{-D_u^2/M^2}\right], \tag{3.4.29}$$

where M^2 is the regulator mass which is sent to be infinity at the end of calculations. The trace can explicitly evaluated by inserting the set of eigenstates of D_u and then using the momentum basis as

$$\mathcal{W}(u) = 2 \lim_{M^2 \to \infty} \int d^4x \int \frac{d^4k}{(2\pi)^4} \mathrm{tr}\, \left[\Theta e^{-\langle k|D_u^2|k\rangle/M^2}\right]$$

where $\langle k|D_u^2|k\rangle$ is the matrix elements of D_u^2 in the momentum basis. Noting that

$$\left(\not{\nabla}\right)^2 = \nabla_\mu \nabla_\mu + \frac{i}{4}\left[\gamma_\mu, \gamma_\nu\right] F_{\mu\nu}, \tag{3.4.30}$$

and keeping pieces which survive the limit $M^2 \to \infty$,

$$\begin{aligned}\mathcal{W}(u) &= 2 \lim_{M^2\to\infty} \int d^4x \int \frac{d^4k}{(2\pi)^4} \\ &\quad \times \mathrm{tr}\left[\Theta e^{-ikx} e^{-\left(\nabla_\mu\nabla_\mu + \frac{i}{4}[\gamma_\mu,\gamma_\nu]F_{\mu\nu}\right)/M^2} e^{+ikx}\right] \\ &= 2\int d^4x\, \mathrm{tr}\left[\Theta \frac{1}{2!}\left(-\frac{i}{4}\left[\gamma_\mu,\gamma_\nu\right]F_{\mu\nu}\right)^2\right] \\ &\quad \times \int \frac{d^4k}{(2\pi)^4} e^{-k_\mu k_\mu} \end{aligned} \tag{3.4.31}$$

Finally, noting $\mathrm{tr}\left[\gamma_5\left[\gamma_\mu,\gamma_\nu\right]\left[\gamma_\kappa,\gamma_\lambda\right]\right] = -16\epsilon_{\mu\nu\kappa\lambda}$ and $\int d^4k/(2\pi)^4 e^{-k_\mu k_\mu} = 1/(16\pi^2)$,

$$\mathcal{W}(u) = 2i\frac{\pi}{2}\frac{-1}{32\pi^2}\epsilon_{\mu\nu\kappa\lambda}F_{\mu\nu}F_{\kappa\lambda}. \tag{3.4.32}$$

By integrating over $u \in [0,1]$, we reproduce the previous result.

3.5 Chiral topological insulator with spin

In order to explore all possible insulating and superconducting phases, it is necessary to introduce spin using the spin Pauli matrices σ_i:

$$\vec{\mathcal{M}}_{spinful} = \mathcal{M}_{spinless} \otimes \vec{\sigma} \tag{3.5.1}$$

For example, the tensor product of the CDW mass matrix with the spin Pauli matrices gives a mass matrix describing (π,π,π) Neel order. Similarly, we can get a **spin-chiral Topological Insulator** (s-cTI) by starting from the cTI mass (β_5 in Table 3.2) and considering its tensor product with $\sigma_{x,y,z}$, forming a spin-dependent and TRS mass term. The resulting Hamiltonian is $\mathbb{H}_{s-cTI} = \sum_{\mathbf{k}}(f^\dagger_{\mathbf{k}\uparrow}, f^\dagger_{\mathbf{k}\downarrow})\sigma_y \otimes H^{cti}_{\mathbf{k}}(f_{\mathbf{k}\uparrow}, f_{\mathbf{k}\downarrow})^T$ where

$$\begin{aligned} H^{cti}_{\mathbf{k}} &= 2|t''|[\sin(k_x+k_y-k_z) - \sin(k_x+k_y-k_z) \\ &\quad + \sin(k_x-k_y+k_z) - \sin(k_x-k_y-k_z)]\tau_y\mu_y\nu_z \end{aligned} \tag{3.5.2}$$

and $f_{\mathbf{k}\uparrow(\downarrow)}$ is as defined in (3.2.3) with obvious extension to include spin. According to Sec. 3.3, there are now two surface massless Dirac fermion states, one for each spin. The gapless nature of these surface modes turns out to be stable, and the gapped Hamiltonian H_{s-cTI} is indeed a topological insulator. In the terminology of [119], they can be also called class CII topological insulator. In general, when arbitrary spin-orbit interactions are permitted, spin chiral topological insulators are characterized by a $\mathbb{Z}_2$ quantity rather than the integer winding number, which is the even-odd parity of the winding number ν for either one of the two spin sectors. Spin chiral topological insulators are in many ways analogous to the more familiar quantum spin Hall effect (QSHE) in two spatial dimensions, but require the chiral symmetry in addition to TRS. To have an intuitive understanding of the QSHE, one can first start from two decoupled and independent QHE states with opposite chirality for each spin and glue them together. More general QSH states can then be obtained by rotating the S_z conserving QSHE by $SU(2)$ rotation, which is quite analogous to the construction of the spin chiral topological insulators above.

3.6 Singlet topological superconductors

The π-flux cubic lattice can also host various kinds of superconducting orders which can be obtained by performing particle-hole transformations on the spin-versions of the insulators.

In order to enumerate the various classes of proximate superconductors, it is sufficient to look at the low-energy physics in the vicinity of the Dirac nodes. Assuming pairing between opposite crystal momenta, and looking for fully gapped superconductors, we may write a general low-energy Hamiltonian as:

$$H(\mathbf{Q}+\mathbf{k}) \simeq \mathcal{H}_{SC}(\mathbf{k}) = \frac{1}{2}\sum_{\mathbf{k}} \left(F^\dagger_{\mathbf{k}},\, F_{-\mathbf{k}}\right) \begin{pmatrix} (\mathbf{k}.\boldsymbol{\alpha}\otimes \mathbb{I}_{4\times 4}) & \Delta \\ \Delta^\dagger & (\mathbf{k}.\boldsymbol{\alpha}\otimes \mathbb{I}_{4\times 4}) \end{pmatrix} \begin{pmatrix} F_{\mathbf{k}} \\ F^\dagger_{-\mathbf{k}} \end{pmatrix} \quad (3.6.1)$$

where $F_{\mathbf{k}}$ is a fermion operator with 16 components, including the 8 sublattice indices and spin. It is related to the microscopic fermion operators f via $F_n = (U\otimes\sigma_0)_{nm} f_m$, with U as defined in (3.2.11) to bring the Dirac theory into canonical form, and σ_0 the identity matrix in the spin basis. Δ is a 16×16 matrix describing the pair potential in the vicinity of the Dirac node. From fermion anticommutation, it must be antisymmetric $\Delta = -\Delta^{\mathrm{T}}$. Also, in order to anticommute with the kinetic energy and open up a full gap, it must be proportional to one of the two Dirac mass terms β_0, β_5. Thus, in general $\Delta = \beta_{0,5}\mu_i\sigma_j$, $i,j = 0,1,2,3$ where μ is the node index. Since in the the normal form described in Sec.3.2.2, β_0 and β_5 are antisymmetric, the product $\mu_i\sigma_j$ must be symmetric. Of the 10 symmetric possibilities for this product, 9 are also symmetric in spin ($\mu_{0,x,z}\sigma_{0,x,z}$) and thus describe triplet superconductors, whereas the lone spin antisymmetric matrix $\mu_y\sigma_y$ describes spin singlets. Therefore, our model contains two spin singlet superconductors - $\beta_0\mu_y\sigma_y$ and $\beta_5\mu_y\sigma_y$. The former is readily shown to be onsite s-wave pairing. The latter however is interesting and corresponds to a **singlet Topological Superconductor**(sTS), and that is what we shall focus on now.

At the microscopic level, the singlet topological superconductor superconductor arises when pairing is added along the body diagonals of the cube, in a specified form. It can be conveniently obtained from the spin chiral topological insulator H_{s-cTI}, by performing a spin-dependent particle-hole transformation

$$f_\uparrow \to f_\uparrow\,,\; f_\downarrow \to \tau_z f^\dagger_\downarrow \quad (3.6.2)$$

on the spin-cTI Hamiltonian. As a result of the hopping being imaginary, the sTS is a spin singlet:

$$\begin{aligned} & i|t''|A^\dagger B + \text{h.c.} \quad \text{(spinless insulator)} \\ \longrightarrow \quad & i|t''|(A^\dagger_\uparrow\, A^\dagger_\downarrow)\sigma_y \begin{pmatrix} B_\uparrow \\ B_\downarrow \end{pmatrix} + \text{h.c.} \quad \text{(spin-insulator)} \quad (3.6.3) \\ \longrightarrow \quad & -|t''|(A^\dagger_\uparrow B^\dagger_\downarrow - A^\dagger_\downarrow B^\dagger_\uparrow) + \text{h.c.} \quad \text{(singlet SC)} \quad (3.6.4) \end{aligned}$$

In momentum space, (3.6.2) corresponds to

$$f_{\mathbf{k}\uparrow} \to f_{\mathbf{k}\uparrow}\;,\;\; f_{\mathbf{k}\downarrow} \to \tau_z f^\dagger_{-\mathbf{k}\downarrow} \quad (3.6.5)$$

This converts H_{s-cTI} into a pairing Hamiltonian:

$$\begin{aligned}\mathbb{H}_{sTS} &= \sum (f^\dagger_{\mathbf{k}\uparrow}\tau_z f_{-\mathbf{k}\downarrow})\sigma_y \otimes H^{cti}_{\mathbf{k}} \begin{pmatrix} f_{\mathbf{k}\uparrow} \\ \tau_z f^\dagger_{-\mathbf{k}\downarrow} \end{pmatrix} \\ &= -i\sum_{\mathbf{k}} f^\dagger_{\mathbf{k}\uparrow} H^{cti}_{\mathbf{k}} \tau_z f^\dagger_{-\mathbf{k}\downarrow} + \text{h.c.} \end{aligned} \tag{3.6.6}$$

which is clearly a superconducting singlet.

$\mathbb{H}_{sTS}$ can be written as $\frac{1}{2}\sum_{\mathbf{k}} \Psi^\dagger_{\mathbf{k}} H^{sTS}_{\mathbf{k}} \Psi_{\mathbf{k}}$ where $\Psi^\dagger_{\mathbf{k}} = (f^\dagger_{\mathbf{k}\uparrow} f^\dagger_{\mathbf{k}\downarrow} f_{-\mathbf{k}\uparrow} f_{-\mathbf{k}\downarrow})$ and $H^{sTS}_{\mathbf{k}} = i\pi_y\sigma_y H^{cti}_{\mathbf{k}}\tau_z$ where π_y is a Pauli matrix in the particle-hole basis. It is $SU(2)_{spin}$-symmetric:

$$\pi_x H^{sTS*}_{-\mathbf{k}} \pi_x = -H^{sTS}_{\mathbf{k}} \tag{3.6.7}$$

it also preserves TRS:

$$\sigma_y H^{sTS*}_{-\mathbf{k}} \sigma_y = H^{sTS}_{\mathbf{k}} \tag{3.6.8}$$

Thus, it belongs to class CI of BdG Hamiltonians according to the Altland-Zirnbauer classification.

Having been obtained from the cTI by particle-hole rotation allows us to conclude that there are protected 2D Dirac nodes on the surface of the topological superconductor. In this minimal case, a pair of Dirac nodes is present. The intuitive node pairing picture presented for cTIs, should also hold here, which suggests a route to a topological superconductor by stacking nodal two dimensional superconductors. Since the latter are commonly encountered, we hope this might help in the search for these exotic paired states.

However, as shown in [119], the combination of TRS and $SU(2)_{spin}$-symmetry results in a *second* chiral condition (i.e., chiral symmetry which is not related to sublattice symmetry), which, in our representation is

$$\pi_x\sigma_y H^{sTS}\sigma_y\pi_x = -H^{sTS} \tag{3.6.9}$$

As a consequence, the surface states of the sTS are protected by the physical symmetries of time-reversal and spin-rotation, and are therefore robust against the destruction of the chiral symmetry (3.2.6) which stabilizes the cTI.

The surface states can be detected, for example, by a tunneling experiment. In the absence of disorder, the surface density of states $\rho(E)$ is linear in energy, $\rho(E) \sim |E|$, characteristic to the 2D Dirac dispersion. On the other hand, randomness is a relevant perturbation to the surface modes, and flows to a strong coupling renormalization group fixed point. The random SU(2) gauge potential, known not to be able to localize the Dirac fermions, renormalizes to an exactly solved strong coupling renormalization group (RG) fixed point at long distances. Likewise to the surface Dirac fermion mode of a chiral topological insulator (see Sec. 3.3.1), disorder is not able to localize the surface Dirac fermions in a singlet topological superconductor. However, under the influence of disorder, the (tunneling) density of states $\rho(E)$ changes from a linear dependence to $\rho(E) \sim |E|^{1/7}$ [131, 83, 15, 90].

3.7 Toward physical realization

The π-flux cubic lattice, although very convenient for computational purposes, is somewhat unnatural. Here, we discuss an alternate system which has the same salient features and

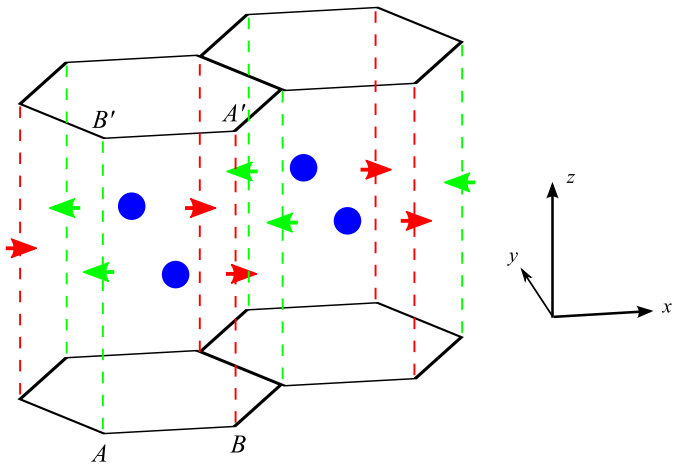

Figure 3.7.1: Honeycomb sheets coupled via spin-orbit interactions as a result of the electric fields (small arrows) generated by additional atoms (blue dots) at the centers of the vertical faces normal to $\hat{y}$. An electron "going up" along a green (AB' bond) or red ($A'B$ bond) dotted line effectively feels a hopping of $-i\lambda_{SO}$ or $i\lambda_{SO}$, respectively. Thus, the path $AB'A'BA$ encloses a flux of π.

hence gives rise to the same physics for the ordered state as the π-flux cubic lattice, but is somewhat more physical.

A stack of honeycomb sheets coupled in such a way that every vertical face encloses a flux of π has three dimensional Dirac nodes in its band structure. However, unlike the cubic lattice, the π-flux can be generated very naturally through spin-orbit (SO) interactions by placing an atom with strong SO interactions at the center of every alternate vertical face, as shown in Figure 3.7.1.

For a single honeycomb layer, the Hamiltonian takes the form

$$H_{\mathbf{k}}^{honey} = -t\left[A_{\mathbf{k}}^{\dagger}B_{\mathbf{k}}(e^{ik_x}+e^{i\frac{-k_x+\sqrt{3}k_y}{2}}+e^{i\frac{-k_x-\sqrt{3}k_y}{2}})\right]+\text{h.c.}\ , \tag{3.7.1}$$

t being the hopping strength. For the layered system shown in Figure 3.7.1, we must add a term

$$\mathbb{H}_{SO}=\sum_z(v_z\hat{z}\times E\hat{x}).\vec{\sigma}\equiv i|\lambda_{SO}|\sigma_y \tag{3.7.2}$$

at each (k_x,k_y) to the sum of single layer Hamiltonians of the form (3.7.1) for each layer. Here, the velocity operator for the z-th layer is given by

$$v_z=-i\,A_z^{\dagger}(B'_{z+1}-B'_{z-1})-B_z^{\dagger}(A'_{z+1}-A'_{z-1})+\text{h.c.}, \tag{3.7.3}$$

the electric field $E=-|E|$ for the $A-B'$ bonds and $+|E|$ for the $A'-B$ bonds, and σ_i are Pauli matrices in the spin space. The planar momentum has been suppressed in (3.7.3) to enhance its readability. The band structure of this system has three-dimensional Dirac nodes at $\mathbf{Q}_{R(L)}=\left(0,\pm\frac{4\pi}{3\sqrt{3}},0\right)$ and the low-energy Hamiltonian now takes the form

$$\mathcal{H}_{\mathbf{p}}=\tau_y\mu_z p_x+\tau_x\nu_z p_y-2|\lambda_{SO}|\tau_y\mu_y\sigma_y p_z \tag{3.7.4}$$

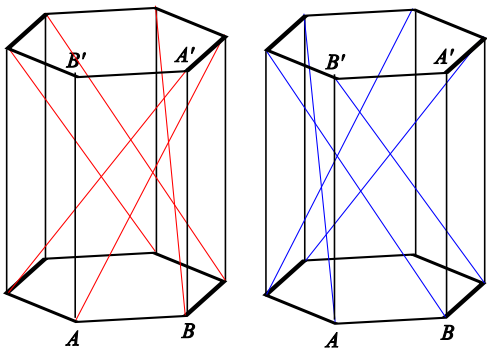

Figure 3.7.2: Hopping texture that results in a chiral topological insulator. The red (left Figure) and blue lines (right Figure) represent bonds of opposite signs when the vertical hopping is purely due to spin-orbit coupling, respectively. When ordinary real hopping in the z-direction is also present, the two colors can be interpreted as bonds of different strengths for some values of the parameters. Two separate Figure s have been drawn for clarity.

where τ, ν and μ are Pauli matrices on the sublattice, node and layer space, respectively. This Hamiltonian preserves the chiral symmetry

$$\tau_z \mathcal{H}_{\mathbf{p}} \tau_z = -\mathcal{H}_{\mathbf{p}} \tag{3.7.5}$$

and TRS

$$\sigma_y \nu_x \mathcal{H}^*_{-\mathbf{p}} \nu_x \sigma_y = \mathcal{H}_{\mathbf{p}}. \tag{3.7.6}$$

The cTI is now realized through a texture of *real* third-neighbor hoppings as shown in Figure 3.7.2. In the low-energy theory, it corresponds to the mass term

$$\mathcal{M}_{cTI} = \tau_y \nu_z \mu_x. \tag{3.7.7}$$

This preserves TRS for spinful electrons and thus, results in the spin-cTI discussed in Sec. 3.5. For spin-polarized electrons, the Hamiltonian for each spin individually breaks TRS, but time-reversal connects the two components of the spin. Therefore, we get two time-reversal related copies of the spinless cTI.

A calculation like that in Sec. 3.3.2 gives surface states that decay into the bulk as $\left(\frac{|\lambda_{SO}|-3\sqrt{3}|t_{cTI}|}{|\lambda_{SO}|+3\sqrt{3}|t_{cTI}|}\right)^{|z|}$, where $|t_{cTI}|$ is the strength of the third-neighbor hopping and $|z|$ is the distance from the surface ($|z| = 0$ represents the surface bilayer).

This is still not very realistic, though. In a real system, we expect ordinary hopping in the z-direction. Also, it is more natural for a system to have alternately strong and weak third-neighbor bonds rather than bonds of opposite signs. Thus, we must include two more terms into the Hamiltonian, vertical hopping of strength $|t_z|$ and a mean third-neighbor hopping $|t_{avg}|$. $|t_{cTI}|$ now becomes the deviation from this mean. It is straightforward to check that both these terms are proportional to $\tau_x \mu_x$, and hence, destroy the pure Dirac dispersion.

The system is a topological insulator if it has zero energy surface states while the bulk is fully gapped. The latter condition can be easily checked to be true as long as $3\sqrt{3}|t_{cTI}| > |t_z - 3t_{avg}|$, while an explicit calculation shows that the zero energy surface states exist and

decay into the bulk as $\left[\frac{|t_z-3t_{avg}|+\tau_z\left(|\lambda_{SO}|-3\sqrt{3}|t_{cTI}|\right)i}{|t_z-3t_{avg}|-\tau_z\left(|\lambda_{SO}|+3\sqrt{3}|t_{cTI}|\right)i}\right]^{|z|}$, where τ_z represents the eigenvalues of τ_z Pauli matrix, for all values of $|t_{avg}|$ and $|t_{cTI}|$. If $|t_{avg}| > |t_{CTI}|$, the bonds of opposite signs now become bonds of different strengths. Thus, even in the presence of $|t_{avg}|$ and $|t_{cTI}|$, there is a region in parameter space where the system is still a cTI.

3.8 Topological defects and dualities

Finally, we make a slight digression and discuss duality relationships between the various order parameters. Because of the plethora of phases possible for the 3D Dirac fermion system, the physics of such a system in the presence of topological defects in one or more of these phases is extremely rich. When a set of six order parameters is chosen so as to form an $O(6)$ vector in the space of mass matrices (see below for details), then the core of a point topological defect in the 3D vector field defined by three components of such a vector carries quantum numbers corresponding to the other three components. Such an intimate connection among seemingly different order parameters, which are not related by symmetry or symmetry breaking, is the heart of the non-Landau-Ginzburg transition that has been discussed in two dimensions [122, 120, 127, 121]. In this section, we will explore the duality relationships among order parameters we have discussed so far, for the simplest physically interesting case.

3.8.1 VBS and Neel

We start by describing the duality between the VBS and Neel order parameters [127, 121]. Suppose the Hamiltonian contains VBS order:

$$\mathcal{H}(\boldsymbol{r}) = -i\partial_i\alpha_i + \beta_5 \boldsymbol{V}.\boldsymbol{\mu} \tag{3.8.1}$$

where $\beta_5\boldsymbol{\mu}$ the mass terms representing three VBS orders (Table 3.2), and $\boldsymbol{V} = (V_x, V_y, V_z)$ is the corresponding VBS order parameter and could in general, be slowly varying on the scale of the lattice spacing.

Let us study the physics of this system when $\boldsymbol{V}(\boldsymbol{r})$ contains a point topological defect at the origin. For simplicity, let us assume an isotropic "hedgehog" configuration, $\boldsymbol{V}(\boldsymbol{r}) = V(r)\hat{\mathbf{r}}$ where $V(0) = 0$ to ensure analyticity. Then it is possible to analytically solve $\mathcal{H}(\boldsymbol{r})\psi(\boldsymbol{r}) = 0$ for the zero-energy modes $\psi(\boldsymbol{r})$. Note that in general these are mid gap states, but for the simple model we discuss here they appear precisely at zero energy. Since, $\boldsymbol{V}(\boldsymbol{r})$ has been assumed to be isotropic, we seek solutions that depend only on the magnitude of $\boldsymbol{r}$, i.e., $\psi(\boldsymbol{r}) \equiv \psi(r)$. Thus, we would like to solve

$$\begin{aligned}
\sin\theta\cos\phi\left(-i\alpha_x\psi'(r) + V(r)\beta_5\mu_x\psi(r)\right) &+ \\
\sin\theta\sin\phi\left(-i\alpha_y\psi'(r) + V(r)\beta_5\mu_y\psi(r)\right) &+ \\
\cos\theta\left(-i\alpha_z\psi'(r) + V(r)\beta_5\mu_z\psi(r)\right) &= 0
\end{aligned} \tag{3.8.2}$$

where θ and ϕ are the usual spherical polar co-ordinates in real space.

The only angular dependence in this equation is through the trigonometric factors outside the parentheses. Therefore, the solution must satisfy

$$-i\alpha_j\psi'(r) + V(r)\beta_5\mu_j\psi(r) = 0 \tag{3.8.3}$$

for $j = x, y, z$. Clearly, it must be of the form

$$\psi(r) = e^{-\int_0^r V(r)dr}\chi \tag{3.8.4}$$

where χ satisfies $i\alpha_x\beta_5\mu_x\chi = i\alpha_y\beta_5\mu_y\chi = i\alpha_z\beta_5\mu_z\chi = \chi$. (The eigenvectors χ of $i\alpha_j\beta_5\mu_j$ corresponding to eigenvalues -1 lead to unnormalizable exponentially growing solutions, $\psi(r) = e^{+\int_0^r V(r)dr}\chi$). Using the explicit forms of the matrices, it turns out that the only non-zero component of χ is the one corresponding to the $B_{1'}$ sites. Since our chosen texture for $\boldsymbol{V}(\boldsymbol{r})$ has unit topological charge, we expect, and will show more rigorously in the next subsection, that the solution just found is the only solution. Moreover, it ensures that any topologically equivalent configuration must carry a single zero mode at its core. Analogous calculations in D=2 were discussed in Refs. [67, 61].

We have not included the spin degree of freedom so far. For spinful electrons, there are two degenerate zero-modes, and the texture carries spin $\frac{1}{2}$ if one of these levels is filled.

Similarly, we expect that a hedgehog in Neel order carry a "VBS-spin-1/2" [127, 121]. This is subtler, because the meaning of a "VBS-spin-1/2" must be defined first. This is easiest to do for a cubic lattice. Along any given cubic direction, there are clearly two degenerate ways of Kekule ordering of the bonds. These two degenerate patterns of alternating low (strong bond) and high (weak bond) energy densities are defined as the "up" and "down" components of a VBS-spin-1/2 along that direction.

We obtain the zero modes by repeating the above calculation after replacing the μ_i's above by σ_i's and β_5 by β_0 to get the Neel order mass matrix [See Table 3.2 and (3.5.1)]. The (two) zero modes we get have the following structure: within each zero mode wavefunction, the real spins on neighboring sites are ferromagnetically ordered along one space direction and Neel ordered in the perpendicular plane. However, all the spins are flipped as one goes from one zero mode to the other [See Figure 3.8.1 (b) and (c)].

For $\vec{N} = N(r)\hat{r}$, the wavefunctions are

$$\begin{aligned}
\psi_1(r) &= e^{-\int_0^r N(r)dr} \\
&\quad \times(0,1,0,i,i,0,1,0,i,0,-1,0,0,-1,0,i)^T, \\
\psi_2(r) &= e^{-\int_0^r N(r)dr} \\
&\quad \times(1,0,-i,0,0,i,0,-1,0,i,0,1,-1,0,-i,0)^T,
\end{aligned} \tag{3.8.5}$$

in the basis defined in Sec. 3.2 with the innermost gradation referring to spin, which is quantized along z. Clearly, this is related to the two VBS patterns oriented along the vertical direction of the cubic lattice. Also, under a unit translation in that direction followed by a spin flip, to maintain the mean field Neel configuration, they exchange roles as one would except from VBS orders. VBS-spins along along x and y can be obtained by performing appropriate $SU(2)$ rotations on the spinor $(\psi_1, \psi_2)^T$. Thus, the core of a Neel hedgehog contains states defined by VBS-spin quantum numbers.

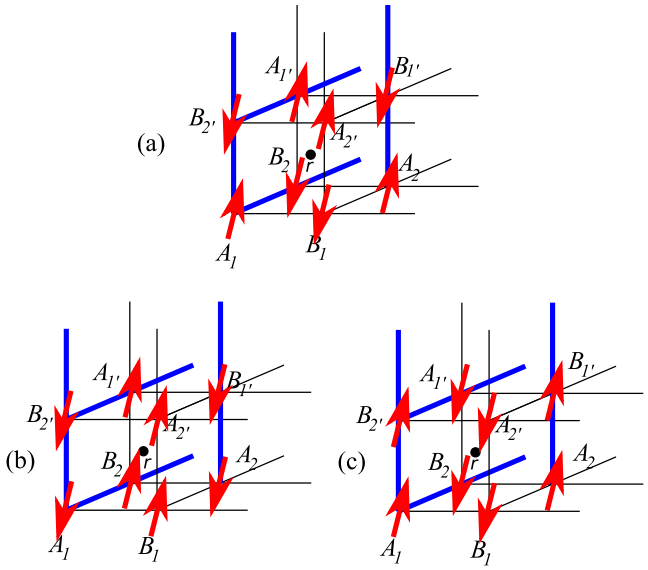

Figure 3.8.1: The mean field spin configuration at site r (a) and the spin configurations of the two zero modes ψ_1 (b) and ψ_2 (c) at the core of a point topological defect in Neel order (See text). $\psi_1(\psi_2)$ has spins parallel (anti-parallel) to the mean field spins on the $A_{1'}B_{1'}A_{2'}B_{2'}$plane and anti-parallel (parallel) to them on the $A_1B_1A_2B_2$ plane.

3.8.2 $O(6)$ vectors of order parameters and the WZW term

We now discuss the relation between the VBS and Neel order parameters in terms of the effective field theory behind them. Subsequently, we will show that such relations exists for a much wider class of order parameters.

The dual nature of the order parameters can be understood by observing that all the six matrices in the sets $\beta_5\vec{\mu}$ (the VBS mass terms) and $\beta_0\vec{\sigma}$ (the Neel mass terms) anticommute with each other. As a result, with the mass term $H_M = \boldsymbol{V}\cdot\beta_5\vec{\mu} + \boldsymbol{N}\cdot\beta_5\vec{\sigma}$ the energy eigenvalues depend only on the length of the six component vector $(\boldsymbol{V},\boldsymbol{N})$, but not on their direction. Thus, we can separate the modulus and direction of the six components of order parameters, the latter of which forms six component vector with fixed length.

$$\hat{n} = \frac{1}{\sqrt{\boldsymbol{V}^2+\boldsymbol{N}^2}}(\boldsymbol{V},\boldsymbol{N}) \tag{3.8.6}$$

The existence of the midgap states, and the quantum numbers thereof can then be computed following the spirit of the Goldstone-Wilczek formula [47]: we integrate over gapped fermions in the presence of the slowly varying background of the $\hat{n}$ vector. The resulting effective action has a Wess-Zumino-Witten (WZW) topological term. (See Refs. [127, 121, 2] and Sec. 3.8.3). This is most conveniently written by introducing an additional fictitious coordinate $u \in [0,\,1]$ such that one evolves from a reference configuration at $u = 0$ to the desired space-time configuration of $\hat{n}$ at $u = 1$. Then,

$$S_{WZW} = i\frac{2\epsilon_{a_0a_1a_2a_3a_4a_5}}{\pi^2}\int n^{a_0}\partial_x n^{a_1}\partial_y n^{a_2}\partial_z n^{a_3}\partial_t n^{a_4}\partial_u n^{a_5} \tag{3.8.7}$$

where ϵ is the antisymmetric symbol, the integral is over space-time and u, and a sum on the $a_i = 0 \dots 5$ is assumed.

The existence of the WZW topological term signals the fact that a solitonic configuration of the order parameter is dressed by an appropriate quantum number; if the defect is created in $\boldsymbol{V}(\boldsymbol{r})$ ($\boldsymbol{N}(\boldsymbol{r})$) it carries a quantum number related to $\boldsymbol{N}(\boldsymbol{r})$ ($\boldsymbol{V}(\boldsymbol{r})$), respectively. In turn, this is ascribed, at the microscopic level, to the existence of the midgap states in the Dirac Hamiltonian. This can be explicitly seen by assuming a static background texture for the VBS order and deriving the consequences of (3.8.7). Assuming a hedgehog defect of the VBS order, and integrating over space, one obtains an effective action for the Neel order parameter $\hat{\boldsymbol{s}} = \boldsymbol{N}/ \parallel \boldsymbol{N} \parallel$ near the core of the defect.

$$S_{WZW}^{\text{defect}} = \frac{i}{2} \int dudt\, \hat{\boldsymbol{s}} \cdot \partial_t \hat{\boldsymbol{s}} \times \partial_u \hat{\boldsymbol{s}} \tag{3.8.8}$$

which is simply the action of a spin 1/2 object. Thus a hedgehog defect of the VBS order is shown to carry spin 1/2. This also means that the hedgehog core hosts a single zero mode as claimed in the previous subsection, because then the two degenerate states of a spinor-$^1/_2$ would correspond to the zero mode being occupied or unoccupied.

Such duality relation can be found for other sets of order parameters. Among order parameters (fermion bilinears) we have discussed so far, we now look for a set of six mass matrices $M_{a=1,\dots,6}$ which anticommutes with each other,

$$\{M_a, M_b\} = \delta_{ab}, \quad a, b = 1, \dots, 6, \tag{3.8.9}$$

and with the Dirac kinetic term $-i\partial_i \alpha_i$, and satisfies

$$\text{tr}\,[\alpha_1\alpha_2\alpha_3 M_1 M_2 M_3 M_4 M_5 M_6] = 16. \tag{3.8.10}$$

(See Sec. 3.8.3 for details.) Such order parameters are intricately correlated with each other, in the same way as the VBS and Neel order parameters are related to each other. Indeed, in Sec. 3.8.3, we show for any such set of six anticommuting order parameters, the same WZW term (3.8.7) exists when the gapped fermions are integrated out.

We list below some of such 6-tuplets of order parameters for the 3D π-flux lattice model. We first note that the triplet of VBS order parameters ($\text{VBS}_{x,y,z}$) can form a pair with CDW and s-wave superconductivity (the real and imaginary components)(sSC). Similarly, replacing the three VBS orders with a triplet of spin chiral topological insulators (s-$\text{cTI}_{x,y,z}$) (class CII) from Sec. 3.5 also leads to a WZW term in the action:

$$\{\text{VBS}_{x,y,z}, \text{CDW}, \text{sSC}\} \tag{3.8.11}$$

$$\{\text{s-cTI}_{x,y,z}, \text{CDW}, \text{sSC}\} \tag{3.8.12}$$

These are generalizations of known relations in two spatial dimensions discussed in [45, 120] and [49] respectively.

Finally the singlet topological superconductor (sTS) discussed in Sec. 3.6 can be paired with the triplet of Neel orders, and the chiral topological insulator (cTI) with spin degeneracy,

$$\{\text{Neel}_{x,y,z}, \text{cTI}, \text{sTS}\}. \tag{3.8.13}$$

The last set is unique in a sense that it relates a singlet superconducting order to the triplet of Neel orders. Indeed, there is no analog of this in 2D, either on the π-flux square lattice or the honeycomb lattice, where singlet SC orders can be paired only with easy-plane SDW order ($\text{SDW}_{x,y}$), but not the full SU(2) set of Neel orders[112]. If we consider a situation where only the Neel and superconducting orders are relevant, and the sixth component above can be neglected, then one can derive a topological term for this five component set. This is the higher dimensional analog of the Haldane O(3) topological term for the spin 1/2 chain. Thus, if $\hat{n}$ is the five component unit vector comprising of three Neel and the two (real and imaginary parts) of the singlet Topological Superconductor, we have the following theta term in the action:

$$\begin{aligned} S_{\text{Top}} &= i\theta Q \\ Q &= \frac{3}{8\pi^2}\int d^3x dt \epsilon_{a_1a_2a_3a_4a_5} n^{a_1}\partial_x n^{a_2}\partial_y n^{a_3}\partial_z n^{a_4}\partial_t n^{a_5} \end{aligned} \tag{3.8.14}$$

where $\theta = \pi$, and the quantity Q is an integer characterizing the topology $\Pi_4[S_4]$ of smooth four dimensional space-time configurations of this five component vector. Thus the quantum interference between Neel order and superconductivity in D=3 is described by an SO(5) model with a topological term. What is the physical consequence of such a term? In D=2, these are associated with unconventional (deconfined) quantum critical points between the pair of ordered states [122, 127, 121]. However, in D=3, a stable insulating spin liquid phase, with a spin gap, can separate the Neel and superconducting state. Such a spin liquid is expected to have electric and magnetic charges which are associated with the spin and superconducting orders. Condensing one or the other will lead to the two ordered phases. Further study of such competing orders in D=3 is left to future work.

3.8.3 Non-linear sigma model with WZW term

The purpose of this section is to show the duality relation for any 6-tuplets of order parameters satisfying the anticommutation relation (3.8.9), in particular for the 6-tuplets discussed in Sec. 3.8. We do so by showing that when gapped fermions are integrated out in the presence of the slowly varying background of the $O(6)$ vector, there is the WZW term.

Non-unitary transformation

Let us start from the Hamiltonian contains both VBS and Neel order parameters: [see (3.8.1)]

$$\mathcal{H}(\boldsymbol{r}) = -i\partial_i\alpha_i + \beta_5 \boldsymbol{V}.\boldsymbol{\mu} + \beta_0 \boldsymbol{N}.\boldsymbol{\sigma} \tag{3.8.15}$$

where $\boldsymbol{V}$ represents the VBS order parameter, and $\boldsymbol{N}$ the Neel vector. The imaginary-time path integral corresponding to this Hamiltonian is given by the partition function $Z = \int \mathcal{D}\left[\chi^\dagger, \chi\right] \exp\left(-\int d\tau d^3x\, \mathcal{L}\right)$ with the Lagrangian $\mathcal{L} = \chi^\dagger\left(\partial_\tau + \mathcal{H}(\boldsymbol{r})\right)\chi$ where $\chi^\dagger$ and χ are a fermionic path integral variable. We will integrate fermions out to derive the effective action for the $O(6)$ vector $(\boldsymbol{N}, \boldsymbol{V})$, from which we will try to read off the duality relation of the order parameters. The same procedure can be repeated for any other 6-tuplets of order parameters discussed in Sec. 3.8. But before doing this, we will make a change of variables to transform the action into a canonical form.

To discuss all duality relations discussed in Sec. 3.8 in a unified fashion, let us start from a set of nine $2^4 \times 2^4$ anticommuting hermitian matrices,

$$\xi_i \xi_j + \xi_j \xi_i = 2\delta_{ij}, \quad i,j = 1,\ldots,9, \tag{3.8.16}$$

with

$$\xi_9 = -\xi_1 \xi_2 \cdots \xi_8. \tag{3.8.17}$$

These matrices form a spinor representation of SO(9). Three out of these matrices $\xi_{1,2,3}$ can be used to form a Dirac kinetic energy, whereas the remaining six matrices can be used as a mass matrix representing an order parameter,

$$\mathcal{H}_{\mathbf{k}} \;=\; \sum\nolimits_{i=1}^{3} k_i \xi_i + \sum\nolimits_{a=4}^{9} m_a \xi_a, \tag{3.8.18}$$

where $m_{a=4,\ldots,9} \in \mathbb{R}$ represents a six-component order parameter. For example, for (3.8.15),

$$\xi_{1,2,3} = \alpha_{1,2,3},\;\; \xi_{3,4,5} = \beta_5 \mu_{1,2,3},\;\; \xi_{5,6,7} = \beta_0 \sigma_{1,2,3}, \tag{3.8.19}$$

and

$$m_{4,5,6} = (V_x, V_y, V_z), \quad m_{7,8,9} = (N_x, N_y, N_z). \tag{3.8.20}$$

The imaginary-time path Lagrangian is given by

$$\mathcal{L} \;=\; \chi^\dagger \left(\partial_\tau + \sum\nolimits_{i=1}^{3} k_i \xi_i + \sum\nolimits_{a=4}^{9} m_a \xi_a \right) \chi. \tag{3.8.21}$$

For other 6-tuplets discussed in Sec. 3.8, we can choose similarly an appropriate set of 9 matrices ξ_i, where the three matrices are for the Dirac kinetic term, and the remaining three for the any $O(6)$ order parameters in Sec. 3.8. To this end, observe that once we consider superconducting orders we are lead to consider $2^5 \times 2^5$ mass matrices acting on sublattice indices (τ), the 1 and 2 indices (ν) introduced in Figure 3.2.1, the bilayer indices (μ), spin indices (σ), and particle-hole spaces (π). However, when we limit ourselves to singlet superconductivity, by making use of spin rotation symmetry, we can always reduce the dimensionality of mass matrices down to $2^4 \times 2^4$.

We now make a change of the fermionic path integral variables to transform the Lagrangian into the canonical form [see (3.8.23) below]. To this end, we introduce

$$\begin{aligned}
&\bar\psi := \chi^\dagger \xi_9, \quad \psi := \chi, \\
&\gamma_0 := \xi_9, \quad \gamma_i := -i \xi_9 \xi_i \quad (i = 1,\ldots,3), \\
&\gamma_5 = -\gamma_0 \gamma_1 \gamma_2 \gamma_3, \\
&\Sigma_a = (\xi_4 \xi_5 \xi_6 \xi_7 \xi_8)\, \xi_a \quad (a = 4,\ldots,8),
\end{aligned} \tag{3.8.22}$$

wherein the Lagrangian in terms of the new variables is given by

$$\mathcal{L} \;=\; \bar\psi \left(\partial_\mu \gamma_\mu + m_9 + \sum\nolimits_{a=4}^{8} m_a i \gamma_5 \Sigma_a \right) \psi. \tag{3.8.23}$$

The merit of this change of variables is that it untangles rotations in the order parameter space and in the real space: the mass matrices ($\Sigma_{a=4,\ldots,8}$) and the matrices entering in the Dirac kinetic term ($\gamma_{\mu=0,\ldots,3}$) are made mutually commuting,

$$[\gamma_\mu, \Sigma_a] = 0, \quad \forall \mu, a, \tag{3.8.24}$$

where γs and Σs form SO(4) and SO(5), respectively,

$$\begin{aligned} &\gamma_\mu\gamma_\nu + \gamma_\nu\gamma_\mu = 2\delta_{\mu\nu}, \quad \mu, \nu = 0, 1, 2, 3, \\ &\Sigma_a\Sigma_b + \Sigma_b\Sigma_a = 2\delta_{ab}, \quad a, b = 4, \ldots, 8. \end{aligned} \tag{3.8.25}$$

Below, we will use the following notation for the order parameters and mass matrices,

$$M := m_9 + m_a i\gamma_5\Sigma^a = |M| \sum_{l=1}^{6} n_l \Upsilon^l, \tag{3.8.26}$$

where the set of matrices Υ^l, the modulus $|M|$, and the six-component unit vector n_l are introduced by

$$\begin{aligned} \Upsilon^l &:= \{I, i\gamma_5\Sigma_4, \cdots, i\gamma_5\Sigma_8\}, \\ |M|^2 &:= m_9^2 + \sum_{a=4}^{8} m_a^2, \\ n_l &:= |M|^{-1}(m_9, m_4, \cdots, m_8). \end{aligned} \tag{3.8.27}$$

For later use, we also introduce

$$\tilde{M} := m_9 - m_a i\gamma_5\Sigma_a, \tag{3.8.28}$$

which satisfies $M\tilde{M} = |M|^2 I$.

Gradient expansion

So far the order parameter $m_{4,\ldots,9}$ has been assumed to be static. We now consider a situation where $m_{4,\ldots,9}$ changes slowly (smoothly) in space-time, $m_{4,\ldots,9} \to m_{4,\ldots,9}(\tau, x)$ [$M \to M(\tau, x)$]. We consider the case where length of the vector is constant, $\sum_{a=4}^{9} |m_a(\tau, x)|^2 = $ const., whereas its direction varies. I.e., the modulus $|M|$ is constant whereas the six-component unit vector n_l in (3.8.27) changes in space-time.

We now proceed to derive the effective action for the bosonic field [the set of order parameters $m_{4,\ldots,9}(\tau, x)$], the O(6) non-linear sigma model with the WZW term, following [2]. The effective action S_{eff} is derived by integrating over fermions,

$$\begin{aligned} e^{-S_{\text{eff}}} &:= \int \mathcal{D}\left[\bar{\psi}, \psi\right] e^{-S} = e^{\ln \text{Det}\,(\gamma_\mu\partial_\mu + M)}, \\ S_{\text{eff}} &= -\text{Tr}\,\ln(\gamma_\mu\partial_\mu + M) =: -\text{Tr}\,\ln\mathcal{D}. \end{aligned} \tag{3.8.29}$$

We compute the effective action by first computing the variation $\delta S_{\rm eff}[M]$ under a small change in the bosonic field $M(\tau, x)$, and then by recovering the full functional $S_{\rm eff}[M]$. Taking a small variation in $M(\tau, x)$,

$$\mathcal{D} \to \mathcal{D} + \delta\mathcal{D}, \quad \delta\mathcal{D} = \delta M, \tag{3.8.30}$$

the change in the effective action to the leading order in δM is given by

$$\delta S_{\rm eff} \;=\; -{\rm Tr}\Big[\big(p^2 + |M|^2 + \gamma_\mu \partial_\mu M\big)^{-1}\big(-\gamma_\mu\partial_\mu + \tilde{M}\big)\delta M\Big] \tag{3.8.31}$$

Assuming the order parameter field M changes smoothly in space-time, we expand

$$\big(p^2 + |M|^2 + \gamma_\mu\partial_\mu M\big)^{-1} = \big[1 + (p^2+|M|^2)^{-1}\gamma_\mu\partial_\mu M\big]^{-1}(p^2+|M|^2)^{-1} \tag{3.8.32}$$

in terms of the derivative $\partial_\mu M$, which leads to

$$\begin{aligned}\delta S_{\rm eff} \;&=\; -\sum_n (-1)^n {\rm Tr}\Big\{\big[(p^2+|M|^2)^{-1}\gamma_\mu\partial_\mu M\big]^n \\ &\qquad \times (p^2+|M|^2)^{-1}\big(-\gamma_\mu\partial_\mu + \tilde{M}\big)\delta M\Big\} \\ &=\; \sum_{n=0}\delta S_{\rm eff}^{(n)}.\end{aligned} \tag{3.8.33}$$

The term which can potentially give rise to the WZW term is the following piece in $\delta S_{\rm eff}^{(4)}$:

$$\delta\Gamma \;:=\; -{\rm Tr}\Big\{\big[(p^2+|M|^2)^{-1}\gamma_\mu\partial_\mu M\big]^4 (p^2+|M|^2)^{-1}\tilde{M}\delta M \tag{3.8.34}$$

This can be written as

$$\begin{aligned}\delta\Gamma \;&=\; -|M|^6 {\rm tr}_{16}\Big[\gamma_{\mu_1}\Upsilon^{a_1}\gamma_{\mu_2}\Upsilon^{a_2}\gamma_{\mu_3}\Upsilon^{a_3}\gamma_{\mu_4}\Upsilon^{a_4}\tilde{\Upsilon}^b\Upsilon^c\Big] \\ &\qquad \times {\rm tr}_k\left\{\left[\prod_{i=1}^4 (p^2+|M|^2)^{-1}(\partial_{\mu_i} n_{a_i})\right] n_b(\delta n_c)\right\},\end{aligned}$$

where ${\rm tr}_{16}$ represents the 16-dimensional trace, whereas ${\rm tr}_k$ represents the trace over the momenta/spatial coordinates. By noting

$$\begin{aligned}&{\rm tr}_{16}\Big[\gamma_{\mu_1}\Upsilon^{a_1}\gamma_{\mu_2}\Upsilon^{a_2}\gamma_{\mu_3}\Upsilon^{a_3}\gamma_{\mu_4}\Upsilon^{a_4}\tilde{\Upsilon}^b\Upsilon^c\Big] \\ &=16i\epsilon_{\mu_1\mu_2\mu_3\mu_4}\epsilon_{a_1a_2a_3a_4bc},\end{aligned} \tag{3.8.35}$$

$\delta\Gamma$ is computed as

$$\begin{aligned}\delta\Gamma \;&=\; -16i\epsilon_{\mu_1\mu_2\mu_3\mu_4}\epsilon_{a_1a_2a_3a_4bc}J\int d^4x \\ &\qquad \times(\partial_{\mu_1}n_{a_1})(\partial_{\mu_2}n_{a_2})(\partial_{\mu_3}n_{a_3})(\partial_{\mu_4}n_{a_4})n_b(\delta n_c),\end{aligned} \tag{3.8.36}$$

where the integral J is given by

$$J = \int \frac{d^4p}{(2\pi)^4} \frac{|M|^6}{(p^2+|M|^2)^5} = \frac{\pi}{2^3} \frac{1}{\text{Area}\,(S^5)} \frac{1}{4!}, \tag{3.8.37}$$

and Area $\left(S^d\right) := 2\pi^{(d+1)/2}/\Gamma\left[(d+1)/2\right]$ represents the area of the d-dimensional unit super-sphere.

(3.8.36) can be rewritten, by introducing an artificial coordinate $u \in [0,1]$, as a surface integral,

$$\begin{aligned} \delta\Gamma \;=\; & \frac{2\pi i \epsilon_{\mu_1\mu_2\mu_3\mu_4}\epsilon_{a_1a_2a_3a_4bc}}{\text{Area}\,(S^5)\,4!} \int d^4x \int_0^1 du \\ & \times \partial_u \left[(\partial_{\mu_1} n_{a_1})(\partial_{\mu_2} n_{a_2})(\partial_{\mu_3} n_{a_3})(\partial_{\mu_4} n_{a_4}) n_b (\delta n_c)\right], \end{aligned} \tag{3.8.38}$$

where we extend the integrand properly in such a way that (integrand) $= 0$ at $u = 1$, whereas at $u = 0$ the integrand gives the original expression (3.8.36). (3.8.38) is nothing but the functional derivative of the WZW functional,

$$\begin{aligned} \Gamma \;=\; & \frac{2\pi i}{\text{Area}\,(S^5)\,5!} \int_{D^5} d^5x\, \epsilon_{\mu_1\cdots\mu_5}\epsilon_{a_1\cdots a_6} \\ & \times (\partial_{\mu_1} n_{a_1})(\partial_{\mu_2} n_{a_2})(\partial_{\mu_3} n_{a_3})(\partial_{\mu_4} n_{a_4})\,(\partial_{\mu_5} n_{a_5})\, n_{a_6}, \end{aligned} \tag{3.8.39}$$

where $dx^5 = dud^4x = dud\tau d^3x$, and the integration domain B is topologically equivalent to a five-dimensional disk (i.e., $\partial D^5 = S^4$) with a boundary at $u = 0$. We thus conclude the effective action S_{eff} includes the WZW term Γ, together with the kinetic term of the SO(6) non-linear sigma model.

We now discuss why this implies the presence of midgap modes when a defect is created in the ordered state. For concreteness, consider the six components of $\hat{n}$ above as being composed of VBS and Neel order parameters. Introduce a static hedgehog defect in the VBS order, and derive the effective action for the remaining Neel components. If we use the ansatz $\hat{n} = [\rho(r)\hat{\boldsymbol{v}}, \sqrt{1-\rho^2}\hat{\boldsymbol{s}}(t,u)]$, where $\rho(r=0) = 0$ and $\rho(r\to\infty) = 1$, and $\hat{\boldsymbol{v}}$ encodes the hedgehog defect, one obtains after integration:

$$S_{WZW}^{\text{defect}} = \frac{i}{2} \int dudt\, \hat{\boldsymbol{s}} \cdot \partial_t \hat{\boldsymbol{s}} \times \partial_u \hat{\boldsymbol{s}} \tag{3.8.40}$$

which, for the Neel variables, is the action of a spin 1/2 object.

3.9 Conclusions

In this chapter, we have discussed *chiral* topological insulators and *singlet* topological superconductors in three spatial dimensions, proposed in [119].

We constructed two concrete lattice models that realize a chiral topological insulator in symmetry class AIII: The first model is constructed by starting from the 3D π-flux cubic lattice model. The second model consists of stacked honeycomb layers with string SO interactions generating non-trivial π-flux for hopping in the direction perpendicular to the layers.

While the stacked honeycomb lattice model is quasi-realistic, the 3D π-flux lattice is not particularly realistic. Nevertheless, it is a convenient canonical model to uncover interesting properties shared by general chiral topological insulators.

In many ways, a chiral topological insulator can be viewed as a close cousin of the known topological states in 3D, such as a $\mathbb{Z}_2$ topological insulator: A hallmark of both of these states is an appearance of non-trivial surface modes when topological bulk states are terminated by a boundary. However, for a chiral topological insulator, an *arbitrary* number of flavors of Dirac fermions can appear at the surface and be stable. We discussed a physically transparent picture of the chiral topological insulator, which explains the appearance of surface Dirac fermion states, and their stability in the presence of chiral symmetry. A similar picture also explains the stability of TRS $\mathbb{Z}_2$ topological insulators whose bulk Dirac nodes are centred at TRIM. It is shown that the $\theta = \pi$ axion electrodynamics can also be realized in chiral topological insulators, in addition to the known realization in $\mathbb{Z}_2$ topological insulators. We should also stress that chiral symmetry, which is realized in the models discussed here as sublattice symmetry, is likely broken in any realistic systems. Nevertheless, as far as breaking of chiral symmetry is sufficiently weak, θ is expected to be close to π, and can

It is also worth while mentioning that chiral symmetry need not to be realized only as sublattice symmetry: class AIII symmetry can be realized in the BdG Hamiltonians for S_z-conserving superconductors. Thus, chiral symmetry when realized in this way is much more robust than sublattice symmetry.

Furthermore, in the 3D π-flux lattice model with inclusion of spin degree of freedom, we found a spin-chiral topological insulator (topological insulator in class CII), and also a singlet topological superconductor (topological superconductor in class CI). The latter is stable as long as the physical symmetries of SU(2) spin rotation and time reversal are present.

Finally, utilizing the proximity to a Dirac state, we derived an interesting correlation, or "duality", between the singlet topological superconductor and Neel order. These order parameters are dual in the sense that a topological defect in either one of these phases carry complementary quantum numbers: e.g.. a defect in the Neel vector ("hedgehog") can carry electric charge. We also find many such 6-tuplets of order parameters, including a six component vector consists of three Neel order and three VBS order parameters. These dualities are a natural extension of those discussed in 1D and 2D quantum spin models, the latter in the context of deconfined criticality. While in this chapter we have studied the properties of these topological defects at single particle level, and hence the topological defects are static objects, we cannot resist contemplating more interesting situation where they are dynamical entities. In particular, it is interesting to ask if there is a counterpart of the non Landau-Ginzburg transition, realized in two dimensions, can exist, possibly in the presence of strong electron correlations in three dimensions. This is left for future study.

P.H. would like to thank Shinsei Ryu and Ashvin Vishwanath for the collaboration in this work. We wish to thank Ying Ran and Tarun Grover for insightful discussions, and the Center for Condensed Matter Theory at University of California, Berkeley (SR) and NSF-DMR-0645691 (AV) for support. This work is published in *Physical Review B*, **81**, 045120 (2010).

Chapter 4

Fermionic Hopf solitons and Berry phase in topological surface superconductors

In the last chapter, we saw interesting physics emerge when appropriate sets of phases were combined together to form three component order parameters, and topological defects were created in them. A natural question to ask is whether there are other topologically non-trivial ways of combining the phases which give rise to unconventional phenomena. The strong topological insulator (TI) is a good candidate for being involved in some novel physics, since rich phenomena have already been predicted to arise when this phase is combined with conventional orders such as magnetism [30, 151], crystalline order [113] and superconductivity. The last is particularly interesting. Superconductivity induced on the surface of a TI was predicted to have vortices harboring Majorana zero modes [36]. These are of interest to quantum information processing, since they are intrinsically robust against errors. Recently, superconductivity was discovered in a doped TI [65], which could be used to induce surface superconductivity. Below we discuss a new theoretical approach to studying this remarkable superconducting phase, which provides different insights and directions for experiments.

We focus on smooth configurations where the energy gap never vanishes. In this case, the low energy description of the system is entirely in terms of bosonic coordinates (order parameter), much as the Landau Ginzburg order parameter theory describes superconductors at energies below the gap. Can fermions ever emerge is such a theory? While it is easy to imagine obtaining bosons from a fermionic theory, the reverse is harder to imagine. However, it has been shown in principle that bosonic theories that contain additional Berry's phase (or Wess-Zumino-Witten) terms, can accomplish this transmutation of statistics. We show that this indeed occurs in the superconductor-TI (Sc-TI)system; the order parameter theory contains a Berry phase term which implies that a particular configuration of fields - the Hopf soliton (or *Hopfion*) - carries fermionic statistics. While such statistics transmutation is common in one dimension [46], it is a rare phenomenon in higher dimensions. In the condensed matter context, an physically realizable example exists in two dimensions: solitons of quantum Hall ferromagnets (skyrmions) are fermionic and charged, and have been observed [123, 84, 12]. However, the superconductor-TI system is, to our knowledge, the first explicit condensed matter realization of this phenomenon in three dimensions.

The organization of this chapter is as follows. First, we introduce our simplified model of a topological insulator with surface superconductivity, and review properties of the Hopf

texture. We then discuss evidence from numerical calculations on a lattice model, that demonstrate the Hopfions are fermions. We also discuss the connection between fermionic Hopfions and 3D non-abelian statistics of [128]. A simplified two dimensional example, where skyrmions are fermionic, is also discussed. Next, we provide a field theoretical derivation of the same result in the continuum, and introduce the necessary theoretical tools to compute a topological term, that leads to the fermionic statistics. Finally, we mention physical consequences, for tunneling experiments as well as for Josephson junctions.

4.1 Model and Hopf Texture

The essential properties of a topological insulator are captured by a simplified low energy theory with a three dimensional Dirac dispersion (a microscopic realization is described later):

$$H_D = \psi^\dagger [v_F \alpha \cdot \mathbf{p} + m\beta_0]\psi \tag{4.1.1}$$

where (α_1, α_2, α_3, β_0) are 4×4 anti-commuting matrices which square to the identity and involve both spin and sublattice degrees of freedom. The dispersion then is $\epsilon(p) = \pm\sqrt{v_F^2 p^2 + m^2}$. An insulator is obtained for $m \neq 0$. Changing the sign of m results in going from a trivial to a topological insulator. Which sign of 'm' is topological is set by the band structure away from the node - we assume $m < 0$ is topological. Consider now adding (on-site) superconducting pairing, which may be proximity induced by an s-wave superconductor. Then

$$H_{\text{pair}} = \Delta \psi^\dagger \beta_5 \psi^\dagger + \text{h.c.} \tag{4.1.2}$$

where $\beta_5 = \alpha_1\alpha_2\alpha_3\beta_0$. The matrices α_i can be taken to be symmetric, while β_0, β_5 are antisymmetric. We can write the total Hamiltonian $H_f = H_D + H_{\text{pair}}$ then as:

$$\begin{aligned} H_f &= \begin{bmatrix} \psi^\dagger & \psi \end{bmatrix} \mathcal{H}_f \begin{bmatrix} \psi \\ \psi^\dagger \end{bmatrix} \\ \mathcal{H}_f &= \begin{bmatrix} -iv_F\alpha\cdot\partial + m\beta_0 & \Delta\beta_5 \\ \Delta^*\beta_5 & -iv_F\alpha\cdot\partial + m\beta_0 \end{bmatrix} \end{aligned} \tag{4.1.3}$$

The spectrum now is $\epsilon(p) = \pm\sqrt{v_F^2 p^2 + M^2}$ where $M^2 = m^2 + |\Delta|^2$. The single particle Hamiltonian can be written as: $\mathcal{H}_f = [-iv_F\alpha\cdot\partial + m\beta_0]\mathbf{1} + \beta_5(\Delta\nu^+ + \Delta^*\nu^-)$ where the ν^a are Pauli matrices acting on the particle-hole space. It is readily verified that this Hamiltonian enjoys particle-hole symmetry: $C\mathcal{H}_f^* C = -\mathcal{H}_f$, where $C = \nu^x$, and we have used that fact that α_i are symmetric and $\beta_{0,5}$ are antisymmetric.

It is convenient to define a three vector $\vec{n} = (\mathcal{R}e\Delta, \mathcal{I}m\Delta, m)$, such that $|\vec{n}| = M$. A singular configuration is one where all three components of this vector go to zero. Since the vacuum can be taken to be a trivial insulator, m changes sign at the topological insulator surface. The components of the pairing Δ vanish in the vortex core. This can also be viewed as a hedgehog [128] configuration in $\vec{n}$. It has been pointed out that a TI-surface vortex with odd winding number will give rise to an unpaired Majorana zero mode [36]. Note, at the core of these singular configurations the gap closes, allowing for the possibility of localized bound states at zero energy. In this work we will only consider *smooth* textures of

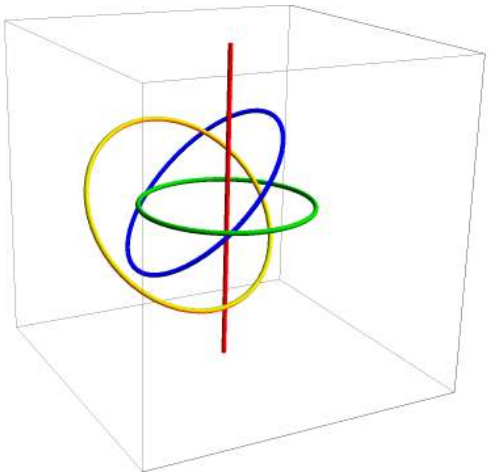

Figure 4.1.1: The Hopf map: $f_H : \vec{r} \to \hat{n}$ is shown by displaying contours of equal $\hat{n}$. Points at infinity are all mapped to the same point on the sphere $f_H(\infty) = \hat{z}$. In red is $f_H^{-1}[\hat{n} = \hat{z}]$, in green $f_H^{-1}[-\hat{z}]$, in blue $f_H^{-1}[\hat{x}]$, and in yellow $f_H^{-1}[\hat{y}]$. Note the unit linking of any pair of curves, which can be used to define the Hopf texture.

the $\vec{n}$ field, where the single particle gap is nonzero everywhere. An effective theory of slow fluctuations of the 'order parameter' field $\vec{n}(r,t)$, occurring over spatial (time) scales much larger than $\xi = \hbar v_F/M$ ($\tau = \xi/v_F$), can be obtained by integrating out the gapped fermions. An analogous procedure is well know in the context of the BCS theory of superconductivity, where it leads to the Landau-Ginzburg action. Here we will find that an extra topological term arises, that transmutes statistics and leads to fermionic solitons.

Consider a smooth configuration of $\vec{n}(r)$, which can be normalized to give a unit vector $\hat{n}(r)$ at each point. This defines a mapping from each point of three dimensional space, to a unit three vector, which describes the surface of a sphere S^2. We require that the mapping approaches a constant at infinity: $\hat{n}(|r| \to \infty) = \text{const}$ (e.g the vacuum). Can all such mappings be smoothly distorted into one another? A surprising result due to Hopf [63] 1931, is that there are topologically distinct mappings, which can be labeled by distinct integers h (the Hopf index). No smooth deformation can connect configurations with different Hopf indices. Mathematically, Hopf showed that the homotopy group: $\Pi_3[S^2] = Z$. A straightforward way to establish the index is to consider the set of points in space that map to a particular orientation of $\hat{n}$. In general this is a curve. If we consider two such orientations $(\hat{n}_1, \hat{n}_2)$, we get a pair of curves. The linking number of the curves is the Hopf index. A configuration with unit Hopf index can be constructed by picking a reference vector $\hat{n} = \hat{z}$, say, and rotating it: $\hat{n}(\vec{r}) \cdot \vec{\sigma} = U(\vec{r})\sigma_z U^\dagger(\vec{r})$ by the spatially varying rotation $U(\vec{r}) = e^{i\frac{\theta(r)}{2}\hat{r}\cdot\sigma}$. Here the angle of rotation varies as we move in the radial direction, from $\theta = 0$ at the origin, to $\theta = 2\pi$ at radial infinity, and the axis of rotation is the radial direction $\hat{r}$. By studying which spatial points map to e.g.. $\hat{n} = \pm\hat{z}$, as in Figure 4.1, one can conclude this texture has unit Hopf index. What is the physical interpretation of this Hopf texture in the context of TIs? A torus of TI (Figure 4.2) has superconductivity induced on its surface. There is vacuum far away and through the hole of the torus, which counts as a trivial insulator, $\hat{n} = \hat{z}$. The center of the strong topological insulator corresponds to $\hat{n} = -\hat{z}$. On the topological

insulator surface $n_z = 0$, and the superconducting phase varies such that there is a unit vortex trapped in each cycle of the torus. We now argue that such a texture is a fermion.

4.2 Hopf Solitons are Fermions

The mean field Hamiltonian (4.1.3) for a general texture, has no physical symmetry (charge conservation is broken by the superconducting pairing and time reversal is broken by the nontrivial phases associated with the texture). However, a fermion Hamiltonian always has a the symmetry of changing the sign of the fermion field (since a term with odd number of fermions does not appear in a local Hamiltonian). The conserved quantity associated with this symmetry is fermion parity. So the only quantum number that can be assigned to the ground state is the parity of the total number of fermions $(-1)^F$. Superconducting pairing only changes the number of fermions by an even number, hence one can assign this fermion parity quantum number to any eigenstate. We now argue that the fermion parity of a smooth texture is simply the parity of its Hopf index h.

$$(-1)^F = (-1)^h \tag{4.2.1}$$

First, we argue that the ground state with a topologically trivial texture has an *even* number of fermions. As a representative, consider a configuration where the superconductor pairing amplitude is real. This is a time reversal invariant Hamiltonian. If the ground state had an odd number of fermions, it must be at least doubly degenerate, by Kramers theorem. However, the ground state of any smooth texture is fully gapped and hence unique. Thus, this configuration must have an even fermion parity. Now, any other texture in the same topological class can be reached by a continuous deformation, during which the gap stays open. The fermion parity stays fixed during this process. Note, this argument cannot be applied to configurations with nonzero Hopf index, since these necessarily break time reversal symmetry. For example, the configuration shown in Figure 4.1, contains phase windings.

To find the fermion parity of the nontrivial Hopf configurations, we consider evolving the Hamiltonian between the trivial and $h = 1$ configuration. In this process we must have $\vec{n} = 0$ at some point, which will allow for the gap to close, and a transfer of fermion parity to potentially occur. Indeed, as shown below in separate calculations, a change in fermion parity is induced when the Hopf index changes by one.

Numerical Calculation: We study numerically the microscopic topological insulator model defined in reference [66], with a pair of orbitals ($\tau_z = \pm 1$) on each site of a cubic lattice. The tight binding Hamiltonian

$$H = \sum_k [\psi_k^\dagger \mathcal{H}_k \psi_k + H_{\text{pair}}(k)] \tag{4.2.2}$$

is written in momentum space using a four component fermion operator ψ_k with two orbital and two spin components. Then,

$$\mathcal{H}_k = -2t \sum_{a=1}^{3} \alpha_a \sin k_a - m\beta_0 [\lambda + \sum_{a=1}^{3} (\cos k_a - 1)] \tag{4.2.3}$$

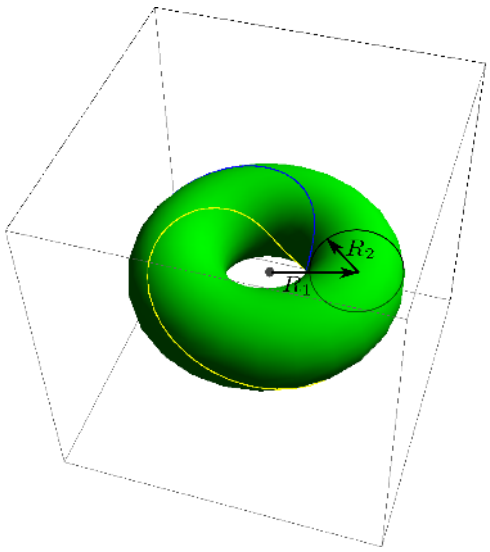

Figure 4.2.1: This Figure shows a torus of strong topological insulator (green) in vacuum, whose surface is superconducting . There is unit superconductor phase winding about each cycle of the torus. We plot the equal phase contours on the surface whose pairing phase is 0(blue) and π(yellow). The unit linking of these curves indicates this is the Hopf mapping.

where $(\vec{\alpha},\, \beta_0) = (\tau_x\sigma_x,\, \tau_x\sigma_y,\, -\tau_y, \tau_z)$. For $t,\, m > 0$ a strong topological insulator is obtained when $\lambda \in (0, 2)$. In addition we introduce onsite singlet pairing

$$H_{\text{pair}}(k) = \Delta[\psi_k^\dagger]^{\mathrm{T}}\sigma_y\psi_{-k}^\dagger + \text{ h.c.} \tag{4.2.4}$$

Note, when $\lambda \approx 0$, $\vec{k} \approx (0,\, 0,\, 0)$, (4.1.3) is recovered as the low energy theory.

The energy spectrum is studied as we interpolate between a topologically trivial texture ($h = 0$) and the Hopf texture ($h = 1$). We choose to define a torus shaped strong topological insulator with trivial insulator (vacuum) on the outside, as in Figure 4.2. The surface is gapped by superconducting pairing Δ, which in the trivial texture is taken to be real Δ_0. (Note, the energy gap in the bulk arises from the insulating gap, while on the surface the gap arises from pairing. There is a smooth evolution between these limits over a scale associated with the surface states). In the Hopf texture, the superconducting pairing Δ_1 has a phase that winds around the surface, with a unit winding about both cycles of the torus. This can be interpreted as 'vortices' inside the holes of the torus. Note, the vortex cores are deep inside the insulators, so there is a finite gap in the Hopf texture. We interpolate between these two fully gapped phases be defining $\Delta(\lambda) = \lambda\Delta_1 + (1 - \lambda)\Delta_0$ and changing $\lambda = 0 \to 1$. On the way, the gap must close since the two textures differ in topology. We study the evolution of eigenvalues as shown in Figure 4.2. We find that exactly one pair of $\pm E$ eigenvalues are pumped through zero energy. As argued below, this signals a change in the fermion parity of the ground state on the two sides. Since the trivial texture has even fermion parity from time reversal symmetry, the Hopf texture must carry odd fermion number.

To see why the crossing of a $\pm E$ conjugate pair of levels corresponds to a change in fermion number, consider a single site model $H = E_0(c^\dagger c - cc^\dagger)$. This has a pair of single particle levels at $\pm E_0$, which will cross if we tune E_0 from say positive to negative values.

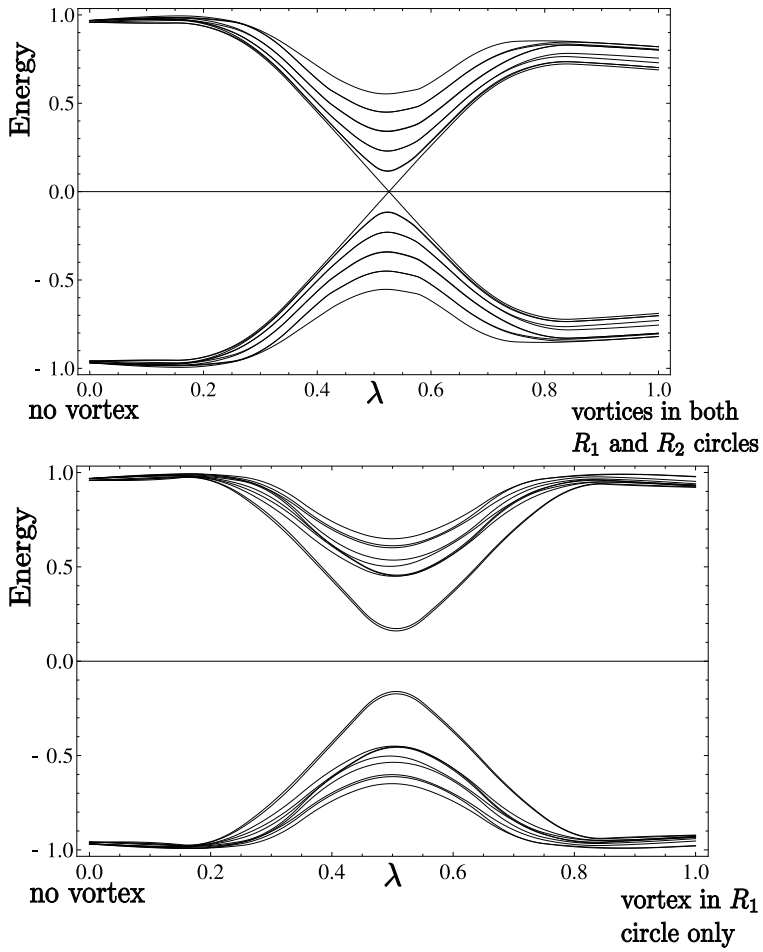

Figure 4.2.2: The spectral flow of the lowest 20 eigenvalues when the pairing on the surface of the topological insulator in Figure 4.2 is linearly interpolated between two limits: $\Delta(x,\lambda) = (1-\lambda)\Delta_0(x) + \lambda\Delta_1(x)$. $\Delta_0(x)$ is constant over the whole surface. TOP: $\Delta_1(x)$ has a unit phase winding (vortex) in both the R_1 and R_2 cycles of the torus, i.e. the Hopf texture. BOTTOM: $\Delta_1(x)$ has a unit phase winding in only the R_1 cycle. It is clear that there is a single level crossing in the TOP case, meaning the ground state fermion parity is changed in the process. The initial state has even fermion parity, so the final state, the Hopf texture,must have odd fermion parity. The calculation is on the cubic lattice model defined in the text, with $R_1 = 13$ and $R_2 = 5$ lattice units, and only points within the torus are retained. Parameters used: $t = M = \lambda = 1$, and pairing $|\Delta| = 1$.

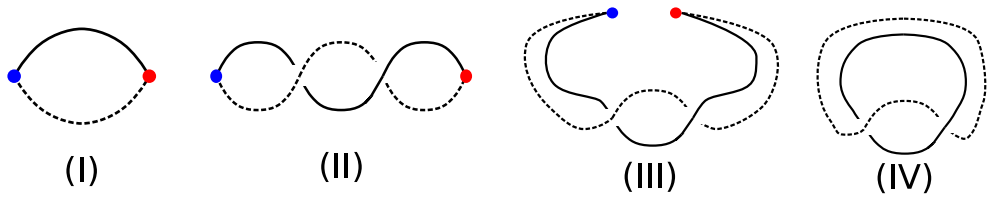

Figure 4.2.3: Creating a Hopf soliton by a hedgehog-antihedgehog pair. The blue(red) dot is the hedgehog(antihedgehog). The solid and dotted lines are preimages of two different points on the 2-sphere. (I) creating a pair of hedge and antihedgehog (II) rotating the hedgehog by 2π while leaving the antihedgehog invariant (III)(IV) annihilating the hedgehog-antihedgehog pair. The final state in (IV) clearly shows linking number 1 of the two preimage loops, which indicates the non-trivial Hopf index.

However, writing this Hamiltonian in terms of the number operators $H = E_0(2\hat{n} - 1)$, shows that the ground state fermion number changes from $n = 0$ to $n = 1$ in this process. Thus the ground state fermion parity is changed whenever a pair of conjugate levels cross zero energy. We mention that it is possible to confirm the numerical results analytically, by solving for the low energy modes in the vicinity of the vortex core, where the insulating mass term is set to be near zero. The linking of vortices in the Hopf texture plays a crucial role in deriving this result.

A. The Pfaffian: Previously, the ground state fermion parity was found by interpolating between two topological sectors. Can one directly calculate the fermion parity for a given Hamiltonian's ground state? We show this is achieved by calculating the Pfaffian of the Hamiltonian in the Majorana basis. The Pfaffian of an antisymmetric matrix is the square root of the determinant - but with a fixed sign. It is convenient to recast the Hamiltonian in terms of Majorana or real fermions defined via $\psi_a = (\chi_{1a} + i\chi_{2a})/2$. Since a pair of Majorana fermions anticommute $\{\chi_i, \chi_j\} = \delta_{ij}$, the Hamiltonian written in these variables will take the form:

$$H = -i \sum_{ij} \mathbf{h}_{ij} \chi_i \chi_j \tag{4.2.5}$$

where $\mathbf{h}_{ij}$ is an even dimensional antisymmetric matrix, with real entries and the Majorana fields appear as a vector $\chi = (\ldots, \chi_{1a}, \chi_{2a}, \ldots)$, where a refers to site, orbital and spin indices. The $\pm E$ symmetry of the spectrum is an obvious consequence of h being an antisymmetric matrix. The ground state fermion parity in this basis is determined via:

$$(-1)^F = sign\left[\text{Pfaffian}(\mathbf{h})\right] \tag{4.2.6}$$

We numerically calculated the Pfaffian of a Hamiltonian with a single Hopf texture for small systems and confirmed it has a negative sign. In contrast, the trivial Hopf texture Hamiltonian has positive Pfaffian in the same basis.

4.2.1 Connections to 3D non-Abelian statistics

It is well known that vortices piercing a superconductor on the topological insulator surface carry Majorana zero modes in their cores [36, 128]. In the $\vec{n}$ vector representation of (4.1.3),

this corresponds to a hedgehog defect [128], a singular configuration where the vector points radially outwards from the center. Although in this chapter we only work with smooth textures, we discuss below an indirect connection with those works. Note, we can go from a trivial texture to the Hopf texture by creating a hedgehog-antihedgehog pair, rotating one of them by an angle of 2π, and annihilating them to recover a smooth texture. This is just the Hopf texture, as can be seen in the Figure 4.2.1. However, as pointed out in [128], in the process of rotation, the Majorana mode changes sign. This signals a change in fermion parity, consistent with our results.

4.3 A Two Dimensional Analog

We briefly mention a two dimensional analog of the physics described earlier, since it provides a simpler setting to discuss the relevant ideas. We Readers interested in the 3D results alone can skip this section.

Note, (4.1.3) with the third component of momentum absent $p_z = 0$, describes a quantum spin Hall insulator (trivial insulator) when $m > 0$ ($m < 0$), in the presence of singlet pairing Δ. Again, as before a three vector characterizes a fully gapped state, and the nontrivial textures are called skyrmions ($\Pi_2(S_2) = Z$). A unit skyrmion can be realized with a disc of quantum spin Hall insulator with superconductivity on the edge, whose phase winds by 2π on circling the disc. Again, one can show that the skyrmion charge Q determines the fermion parity $(-1)^Q = (-1)^F$. An important distinction from the three dimensional case is that the low energy theory here has a conserved charge. If instead of superconductivity, one gapped out the edge states with a time reversal symmetry breaking perturbation which had a winding, then this charge is the electrical charge. It is readily shown that the charge is locked to the skyrmion charge Q. Hence odd strength skyrmions are fermions. The effective field theory for the $\vec{n}$ vector in this case includes a Hopf term [137, 1], which ensures fermionic skyrmions. This is closely analogous to the Quantum Hall ferromagnet, where charged skyrmions also occur [84, 123]. Returning to the case with pairing, since that occurs on a one dimensional edge, it is difficult to draw a clear-cut separation between fermions and collective bosonic coordinates, in contrast to the higher dimensional version. Hence we focused on the 3DTIs.

Topological Term for D=2+1 Quantum Spin Hall Case: As a warmup, consider the simpler case of D=2+1, briefly discussed above. Here, we start with the Hamiltonian in (4.1.3), but drop the term $p_z\alpha_z$ since we are in D=2+1. This describes a quantum Spin Hall insulator with singlet superconductivity induced near the edge. The order parameter is still a three vector, whose smooth textures in this case are skyrmions ($\Pi_2(S_2) = Z$), and the skyrmion density is given by: $\frac{1}{4\pi}\hat{n} \cdot \partial_x\hat{n} \times \partial_y\hat{n}$. On integrating out the fermions one obtains a topological term. Assuming $\hat{n}(\infty) = const$, the topological term depends on $\Pi_3(S_2) = Z$, which is nothing but H, the Hopf index of the space-time configuration of $\hat{n}$. We will show below that $S_{\text{top}} = i\pi H[\hat{n}(x, y, t)]$. Although there is no simple way to express the Hopf invariant directly in terms of the vector field, its physical effect is well known [137] - it modifies the statistics of the skyrmions so that they are now fermionic.

Calculating S_{topo} in $D = 2 + 1$ Although charge is not conserved in this mean field Hamiltonian, the minimal Dirac model has a U(1) conservation - which can be seen from

the fact that the operator $i\psi^\dagger\alpha_z\beta_0\psi$ commutes with (4.1.3). This introduces a simplicity not present on going to D=3+1. In particular, the D=2+1 problem can be mapped onto the one studied in [1]. It is convenient to introduce the CP^1 representation of the unit vector $\hat{n}$. Introduce a pair of complex fields $z^T = (z_1\, z_2)$ that satisfy $z^\dagger z = 1$. Then $\hat{n}\cdot\vec{\sigma} = (2zz^\dagger - 1)$, where σ are the Pauli matrices. In order to calculate the topological term, we would like to expand the order parameter space, so as to smoothly go between the different topological configurations. In this way we can calculate the topological term perturbatively. A suitable expansion of the order parameter space from CP^1 to CP^M, $M > 1$ was suggested in [1]. Here the complex fields $z = (z_1\, z_2\, \ldots z_{M+1})$. Since $\Pi_3(CP^M) = 0$ for $M > 1$, different topological sectors can be connected. Following this procedure the topological term can be expressed in terms of the vector potential: $a_\mu = \frac{i}{2}z^\dagger\partial_\mu z$

$$S_{\rm top} = i\pi H[\hat{n}(x,y,t)] \tag{4.3.1}$$

$$H = \frac{1}{4\pi^2}\int d^2x dt\, \epsilon^{\mu\nu\sigma} a_\mu \partial_\nu a_\sigma \tag{4.3.2}$$

as also noted in [137].

4.4 Effective Theory and Topological Term

We now present a field theoretical calculation of the results of the previous section. The gap to the ψ fermions never vanishes since $|\vec{n}| > 0$, so one can integrate them out to obtain a low energy theory written solely in terms of the bosonic order parameter $\vec{n}$. How can this field theory describe a fermionic texture? As described below, this is accomplished by a topological Berry phase term which appears in the effective action for the $\hat{n}$ field.

In computing the topological term, it is sufficient to consider a gap whose magnitude is constant $\vec{n}(r,t) = M\hat{n}(r,t)$. Integrating out the fermion fields with action $S_f = \int d^4\, x[\psi^\dagger\partial_t\psi - H_f]$, (the integral is over space and (Euclidean) time), one obtains the effective action for the bosonic fields:

$$e^{-S_B(\hat{n}(r,t)} = \int \mathcal{D}\psi\mathcal{D}\psi^\dagger e^{-S_f[\hat{n},\psi,\psi^\dagger]} \tag{4.4.1}$$

This computation may be performed using a gradient expansion, i.e. assuming slow variation of the $\hat{n}$ field over a scale set by the gap. Two terms are obtained: $S_b = S_0 + S_{\rm top}$. The first [1] is a regular term that penalizes spatial variation: $S_0 = \frac{1}{2g}\int(\partial_\mu\hat{n})^2$. The second is a topological term which assigns a different amplitude to topologically distinct space-time configurations of $\hat{n}$. We first discuss the structure of this topological term and its physical consequences, before describing a calculation to compute it in D=3+1 dimensions.

Topological Term in D=3+1 Dimensions: Assuming $\hat{n}(\infty) = const$, it is known that the spacetime configurations of the unit vector $\hat{n}$ are characterized by a Z_2 distinction since $\Pi_4(S_2) = Z_2$ [101]. That is, there are two classes of maps - the trivial map, which

[1] While the Dirac theory in (4.1.3) has an O(3) symmetry, physically the symmetry is lower, corresponding to O(2) charge rotations. Hence other terms consistent with this lower symmetry are allowed in the effective action, however, the topological term, which is the main focus, does not depend on this detail.

essentially corresponds to the uniform configuration, and a non-trivial class of maps, which can all be smoothly related to a single representative configuration $\hat{n}_1(r,t)$. If the function $\Gamma[\{\hat{n}(r,t)\}] = 0, 1$ measures the topological class of a spacetime configuration, then the general form of the topological term is $S_{\rm top} = i\theta\Gamma[\{\hat{n}(r,t)\}]$. The topological angle θ can be argued to take on only two possible values 0, π, since composing a pair of nontrivial maps, leads to the trivial map. Via an explicit calculation, outlined below, we find $\theta = \pi$. Let us first examine the consequences of such a term. The nontrivial texture $\hat{n}_1(r,t)$ can be described as a Hopfion-antiHopfion pair being created at time t_1, the Hopfion being rotated slowly by 2π, and then being combined back with the anitHopfion at a later time t_2 [137]. The topological term assigns a phase of $e^{i\pi}$ to this configuration. This is equivalent to saying the Hopfion is a fermion, since it changes sign on 2π rotation. An intuitive way to understand this is that exchange can be accomplished by a π rotation about the midpoint connecting a pair of identical particles, which is equivalent to a 2π rotation of a single particle, or by invoking the spin statistics connection. A more pictorial proof for the D=2+1 analog, which can be readily generalized to D=3+1 is in [137].

Calculating the topological term requires connecting the pair of topologically distinct configurations. To do this in a smooth way keeping the gap open at all times requires enlarging the order parameter space for this purpose. If $\mathbf{m}(r,t,\lambda)$ is an element of this enlarged state that smoothly interpolates between the trivial configuration $\mathbf{m}(r,t,0) = \text{const.}$ and the nontrivial one $\mathbf{m}(r,t,1) = \hat{n}_1(r,t)$, as we vary λ, then one can analytically calculate the change in the topological term $\partial S_{\rm top}/\partial\lambda$, and integrate it to get the required result [28, 79, 1, 2]. The key technical point is finding a suitable enlargement of our order parameter space S_2. Remembering that this can be considered as $S_2 = SU(2)/SO(2)$, we can make a natural generalization $M_3 = SU(3)/SO(3)$. The latter has all the desirable properties of an expanded space, e.g.. there are no nontrivial spacetime configurations, so everything can be smoothly connected ($\Pi_4(M_3) = 0$). This extension allows us to calculate the topological term, (as explained in detail in the section below), which yields $\theta = \pi$.

4.5 Calculation of Topological Term

In this section we discuss how the topological term is calculated. This is the most technical part of the present chapter - and the results have already been stated. Therefore readers interested mainly in physical consequences can skip to the next section.

The calculation of the topological term in D=2+1 is relatively straightforward, and we can utilize existing results in the literature [1]. However, the same procedure unfortunately does not work in D=3+1, which is technically harder and requires some innovation. We previously discussed the D=2+1 dimensional case, and utilize some of the general lessons learnt there to attack the D=3+1 problem. More details can be found in Sec. 4.5.2.

Note, although there is no simple way to express the Hopf invariant H directly in terms of the vector field, it may be expressed in terms of the vector potential a as above. Thus, in D=2+1, the Hopf index is directly connected to the topological term. However, in D=3+1, the Hopf index characterizes the soliton, and we will need to look at a higher dimensional homotopy group to pin down the topological term. In that case the topological term does not have a simple expression even in terms of the vector potentials a. Also, due to the different

form of the Dirac theory, we will not be able to utilize the extension to CP^M to calculate the topological term, and a new construction will be needed.

4.5.1 Calculating S_{topo} in $D = 3 + 1$:

We begin by rewriting (4.1.3) in terms of an eight component Majorana fermion field $\mathbf{\Psi}$:

$$H_f = \mathbf{\Psi}^\dagger v_F(-i\partial_i\alpha_i)\mathbf{\Psi} + M\mathbf{\Psi}^\dagger(n_1\beta_0 + n_2\beta_5\eta_x + n_3\beta_5\eta_z)\mathbf{\Psi}, \tag{4.5.1}$$

where the αs are symmetric and βs are antisymmetric matrices, and $\Psi^\dagger = \Psi^T$. For example, we can build them out of three Pauli matrices as below (and as shown in (4.1.3)):

$$\alpha_1 = \sigma_z,\ \alpha_2 = \tau_x\sigma_x,\ \alpha_3 = -\tau_z\sigma_x,\ \beta_0 = \tau_y\sigma_x,\ \beta_5 = \sigma_y. \tag{4.5.2}$$

Note, if we think of σ_a as referring to spin indices, then indeed α_i are odd under time reversal (making the Dirac kinetic energy even under time reversal). The β_0 mass term is also time reversal even, as required for a topological insulator. Finally the pairing term $\Psi^\dagger\beta_5\Psi^\dagger$ is clearly spin singlet with the choice above. We further assume the order parameters n_i are restricted to unit 2-sphere: $\sum_i n_i^2 = 1$ so that $\hat{n} = (n_1, n_2, n_3)$ is a unit vector living on S^2.

We need to show that starting from this fermionic model (4.5.1) and integrating out the fermions, the obtained S^2-NLSM has an imaginary term (topological Berry's phase) $i\theta H_{\pi_4(S^2)}(\hat{n}(x, y, z, t))$ with $\theta = \pi$ in the action (from now on we use $H_{\pi_n(M)}$ to denote the homotopy index of a mapping.). Because this term is non-perturbative, in order to compute it, we need to embed the manifold S^2 into a larger manifold M with $\pi_4(M) = 0$, which allows us to smoothly deform a $H_{\pi_4(S^2)}(\hat{n}(x, y, z, t)) = 1$ mapping to a constant mapping. This means that a $H_{\pi_4(S^2)}(\hat{n}(x, y, z, t)) = 1$ mapping can be smoothly extended over the 5-dimension disk: $V(x, y, z, t, \rho) : D^5 \to M$ ($\rho \in [0, 1]$) such that on the boundary: $V(x, y, z, t, \rho = 1) = \hat{n}(x, y, z, t)$ and $V(x, y, z, t, \rho = 0) = V_0$ is constant. With an extension V, we can perturbatively keep track of the total change of Berry's phase when going from a constant mapping to a non-trivial mapping.

How can we find a suitable M? We note the global symmetry of model (4.5.1) in the massless limit is $U(1)_{chiral} \times SU(2)_{isospin}$, whose generators are:

$$U(1)_{chiral} : \gamma_5 = -i\beta_0\beta_5 \qquad\qquad SU(2)_{isospin} : \eta_y, \gamma_5\{\eta_x, \eta_z\}. \tag{4.5.3}$$

In our convention, $\beta_0, \beta_5, \gamma_5$ are all anti-symmetric matrices. Starting from a given mass, for instance, $\mathbf{\Psi}^\dagger\beta_0\mathbf{\Psi}$, one can generate the full order parameter manifold by action of $SU(2)_{isospin}$: $\mathbf{\Psi}^\dagger W\beta_0 W^\dagger\mathbf{\Psi}$ - where $W \in SU(2)_{isospin}$. $SU(2)_{isospin}$ is broken down to $U(1)$, the invariant group generated by η_y. Thus the order parameter space is $SU(2)/U(1) = SU(2)/SO(2) = S^2$.

Now we generalize the 8-component fermion $\mathbf{\Psi}$ to 12-component $\tilde{\mathbf{\Psi}}$. The 2-dimensional $\eta_{x,y,z}$-space is enlarged to a 3-dimensional space, and we let the eight λ_i-matrices ($i = 1, 2...8$) of the standard $SU(3)$ generators(see, e.g., page 61 in [44]) act within this 3-dimensional space, among which $\lambda_2, \lambda_5, \lambda_7$ are antisymmetric while others are symmetric. And $\lambda_{1,2,3}$ are just the old $\eta_{x,y,z}$ matrices. The symmetry of the generalized massless theory of $\tilde{\mathbf{\Psi}}$: $H = \tilde{\mathbf{\Psi}}^\dagger(-i\partial_i\alpha_i)\tilde{\mathbf{\Psi}}$ is $U(1)_{chiral} \times SU(3)_{isospin}$, where the generators of the $SU(3)_{isospin}$ are $\lambda_2, \lambda_5, \lambda_7, \gamma_5\{\lambda_1, \lambda_3, \lambda_4, \lambda_6, \lambda_8\}$.

Starting from a given mass $\tilde{\mathbf{\Psi}}^\dagger\beta_0\tilde{\mathbf{\Psi}}$, we use $SU(3)_{isospin}$ to generate the order parameter manifold: $\tilde{\mathbf{\Psi}}^\dagger U\beta_0 U^\dagger\tilde{\mathbf{\Psi}} \equiv \tilde{\mathbf{\Psi}}^\dagger V\tilde{\mathbf{\Psi}}$, $U \in SU(3)_{isospin}$. It is clear that the $SO(3)$ subgroup generated by $\lambda_2, \lambda_5, \lambda_7$ is the invariant group and the order parameter manifold is $M_3 \equiv SU(3)/SO(3)$. We thus embed the original order parameter manifold S^2 into M_3, and it is known that $\pi_4(M_3) = 0$ [11].

The idea is to smoothly extend a $H_{\pi_4(S^2))} = 1$ mapping over D^5 (denote by $V(x, y, z, t, \rho)$) by embedding S^2 into M_3. In fact if we can extend a $H_{\pi_4(SU(2))} = 1$ mapping over D^5 (denote by $U(x, y, z, t, \rho)$) by embedding $SU(2)_{isospin}$ into $SU(3)_{isospin}$, it will generate the extension V by $V = U\beta_0 U^\dagger$. This is because a $H_{\pi_4(S^2))} = 1$ mapping can be thought as a combination of a $H_{\pi_4(SU(2))} = 1$ mapping and a Hopf $H_{\pi_3(S^2)} = 1$ mapping. Such an extension $U : D^5 \to SU(3)_{isospin}$ has already been explicitly given by Witten (see (9-13) in [141]), which we will term Witten's map. Witten's map was introduced to compute a $i\theta H_{\pi_4(SU(2))}$ topological Berry's phase. Basically, on the boundary $\partial D^5 = S^4$ ($\rho = 1$), Witten's map is a $H_{\pi_4(SU(2))} = 1$ mapping defined as a rotating $H_{\pi_3(SU(2))} = 1$ soliton (by 2π) along the time direction. This $H_{\pi_4(SU(2))} = 1$ mapping at $\rho = 1$ is smoothly deformed into a trivial mapping at $\rho = 0$ by embedding $SU(2)$ into $SU(3)$.

We use Witten's map to generate V, with which we compute the Berry's phase perturbatively by a large mass expansion [2, 66] of Lagrangian:

$$L = \tilde{\mathbf{\Psi}}^\dagger[\partial_\tau + i\partial_i\alpha_i]\tilde{\mathbf{\Psi}} + M\tilde{\mathbf{\Psi}}^\dagger V\tilde{\mathbf{\Psi}} \equiv \tilde{\mathbf{\Psi}}^\dagger[D]\tilde{\mathbf{\Psi}}, \tag{4.5.4}$$

where $D = [\partial_\tau + i\partial_i\alpha_i + MV]$ and partition function is $Z = \int \mathcal{D}\tilde{\mathbf{\Psi}}^\dagger\mathcal{D}\tilde{\mathbf{\Psi}}\mathcal{D}V e^{-\int d^4xL}$. After integrating out fermion, we obtain a NLSM of V: $\tilde{L} = -\frac{1}{2}\mathrm{Tr}\ln[\partial_\tau + i\partial_i\alpha_i + MV]$. Here the factor $1/2$ is because we are integrating out majorana fields. If there is a variation δV, the variation of the imaginary part $\Gamma \equiv \mathrm{Im}(\tilde{L})$ is:

$$\delta\Gamma = \frac{-K}{2}\int dx^4\epsilon^{\alpha\beta\gamma\mu}\mathrm{Tr}\{\gamma_5 V\partial_\alpha V\partial_\beta V\partial_\gamma V\partial_\mu V\delta V\} \tag{4.5.5}$$

where $K = \int \frac{d^4p}{(2\pi)^4}\frac{M^6}{(p^2+M^2)^5} = \frac{1}{192\pi^2}$. Denoting $\partial_\rho = \partial_4$, after some algebra, the Berry's phase can be written in the fully antisymmetric way:

$$\Gamma = \frac{-K}{10}\int dx^5\epsilon^{\alpha\beta\gamma\mu\nu}\mathrm{Tr}\{\gamma_5 V\partial_\alpha V\partial_\beta V\partial_\gamma V\partial_\mu V\partial_\nu V\} \tag{4.5.6}$$

In fact Γ is not fully well defined because the ambiguity of the extension of $\hat{n}(x, y, z, t)$ to the 5-disk: two different extensions $V(x, y, z, t, \rho)$ can differ by a mapping $S^5 \to M_3$. We will soon show that this ambiguity means that Γ is well defined up to mod 2π.

As V is generated by U, plugging $V = U\beta_0 U^\dagger, U \in SU(3)_{isospin}$ in (4.5.6), one can further simplify it by trace out the $\beta_{0,5}$ space. Firstly note that $\partial_\mu V = U[U^\dagger\partial_\mu U, \beta_0]U^\dagger$, and because $U^\dagger\partial_\mu U$ is an element of the $SU(3)_{isospin}$ Lie algebra spanned by $\lambda_2, \lambda_5, \lambda_7, \gamma_5\{\lambda_1, \lambda_3, \lambda_4, \lambda_6, \lambda_8\}$, $[U^\dagger\partial_\mu U, \beta_0]$ simply picks out the latter five generators. After some algebra [2], one finds

$$\Gamma = \frac{1}{15\pi^2}\int dx^5\epsilon^{\alpha\beta\gamma\mu\nu}\mathrm{Tr}(g^{-1}\partial_\alpha g)_\perp(g^{-1}\partial_\beta g)_\perp(g^{-1}\partial_\gamma g)_\perp(g^{-1}\partial_\mu g)_\perp(g^{-1}\partial_\nu g)_\perp\}, \tag{4.5.7}$$

where g is defined as the corresponding 3 by 3 $SU(3)$ matrix of U: if U is the exponential of $a_1\lambda_2 + a_2\lambda_5 + a_3\lambda_7 + a_4\gamma_5\lambda_1 + a_5\gamma_5\lambda_3 + a_6\gamma_5\lambda_4 + a_7\gamma_5\lambda_6 + a_8\gamma_5\lambda_8$, then g is the exponential

of $a_1\lambda_2 + a_2\lambda_5 + a_3\lambda_7 + a_4\lambda_1 + a_5\lambda_3 + a_6\lambda_4 + a_7\lambda_6 + a_8\lambda_8$. g is nothing but the Witten's map. And $(g^{-1}\partial_\mu g)_\perp$ denotes the symmetric part: $(g^{-1}\partial_\mu g)_\perp = \left[(g^{-1}\partial_\mu g) + (g^{-1}\partial_\mu g)^T\right]/2$.

We simply need to compute Γ by integration. Because it is clear that Γ can only be 0 or π (mod 2π), a numerical integration is enough to determine it unambiguously. We performed integration (4.5.7) with Witten's map g by standard Monte Carlo approach, and find:

$$\Gamma = (1.000 \pm 0.005)\pi \tag{4.5.8}$$

This proves that Hopf-skyrmion is a fermion. In addition it confirms that Γ is well-defined only up to mod 2π: different extensions of g can differ by a doubled Witten's map is known to have $H_{\pi_5(SU(3))} = 1$, and the above calculation indicate that this ambiguity only add an integer times 2π in Γ.

4.5.2 Long Exact Sequence in Homotopy Theory

A very powerful theorem in algebraic topology is the long exact sequence: given a manifolds E and its submanifold $F \subset E$, the following sequence is exact:

$$...\pi_{n+1}(E,F) \to \pi_n(F) \xrightarrow{f} \pi_n(E) \xrightarrow{g} \pi_n(E,F) \xrightarrow{h} \pi_{n-1}(F)... \tag{4.5.9}$$

By "exact" it means that the kernel of one mapping is the same as the image of the previous mapping in the sequence. For example $\ker(g) = \text{image}(f)$. $\pi_n(F), \pi_n(E)$ are the n-dimensional homotopy group of F and E respectively. $\pi_n(E,F)$ is called relative homotopy group, which is defined to be all different classes of mappings from a n-dimensional disk D^n to E which map the boundary of $\partial D^n = S^{n-1}$ into F. In particular, when the quotient manifold E/F can be defined, the relative homotopy group $\pi_n(E,F)$ is isomorphic to the homotopy group of the quotient manifold $\pi_n(E/F)$. In this case, the order of the manifolds showing up in each dimension is always: the smaller manifold, the larger manifold, their quotient manifold.

Now we specify the definition of the mappings in the long exact sequence. Mapping f is the natural mapping between two homotopy groups induced by inclusion $x \in F \to x \in E$. Mapping g is also natural. For any mapping from S^n to E, one can choose an arbitrary point $P \in S^n$ and smoothly enlarge that point into a small n-disk U. Then $S^n - U$ is also a n-disk, and the mapping from $S^n - U$ is an element of $\pi_n(E,F)$. When the quotient manifold E/F can be defined, it is easy to see that a mapping in $\pi_n(E,F)$, after modding out the F, will induce a mapping from S^n to E/F. This naturally mapping between $\pi_n(E,F)$ and $\pi_n(E/F)$ turns out to be isomorphism. Finally the mapping h is induced by restricting an element in $\pi_n(E,F)$ to its boundary S^{n-1}.

As a demonstration, we now use the long exact sequence to study Witten's extension

[141]:

$$\begin{array}{ccccccccc}
\pi_5(SU(2)) & \longrightarrow & \pi_5(SU(3)) & \longrightarrow & \pi_5\left(\frac{SU(3)}{SU(2)} = S^5\right) & \longrightarrow & \pi_4(SU(2)) & \longrightarrow & \pi_4(SU(3)) \\
\| & & \| & & \| & & \| & & \| \\
Z_2 & \longrightarrow & Z & \longrightarrow & Z & \longrightarrow & Z_2 & \longrightarrow & 0
\end{array} \tag{4.5.10}$$

$$\begin{array}{ccccccc}
 & & & & 2k+1 & \longrightarrow & 1 \\
 & & & & & \searrow & \\
k & \longrightarrow & 2k & \longrightarrow & 0 & \longrightarrow & 0
\end{array}$$

This means that if we extend a $S^4 \to SU(2)$ mapping over 5-disk by embedding $SU(2)$ into $SU(3)$, then the extended mapping $D^5 \to SU(3)(\partial D^5 \to SU(2))$ has odd index. In fact this index can be computed by the standard winding number of $\pi_5(S^5)$. Thus if we glue different mappings $D^5 \to SU(3)(\partial D^5 \to SU(2))$ together this index simply adds up. If we glue two identical extensions to form a mapping $S^5 \to SU(3)$, it must have a odd $\pi_5(SU(3))$ index $H_{\pi_5(SU(3))} = 2(2k+1)/2 = 2k+1$. Witten's explicit form of extension (see (9-13) in [141]) is the element 1 in $\pi_5(SU(3)/SU(2))$, and doubled Witten's extension is element $1 \in \pi_5(SU(3))$.

Finally we apply the long exact sequence to study the property of $\pi_5(SU(3)/SO(3))$, relevant to the calculation of Hopfion statistics. It is known that $\pi_5(SU(3)/SO(3)) = Z \oplus Z_2$[].

$$\begin{array}{ccccccccc}
\pi_5(SO(3)) & \longrightarrow & \pi_5(SU(3)) & \longrightarrow & \pi_5\left(\frac{SU(3)}{SO(3)}\right) & \longrightarrow & \pi_4(SO(3)) & \longrightarrow & \pi_4(SU(3)) \\
\| & & \| & & \| & & \| & & \| \\
Z_2 & \longrightarrow & Z & \longrightarrow & Z \oplus Z_2 & \longrightarrow & Z_2 & \longrightarrow & 0
\end{array} \tag{4.5.11}$$

$$\begin{array}{ccccccc}
 & & & & (k,1) & \longrightarrow & 1 \\
 & & & & & \searrow & \\
k & \longrightarrow & (k,0) & \longrightarrow & 0 & \longrightarrow & 0
\end{array}$$

This means that the Z part of $\pi_5(SU(3)/SO(3))$ is completely given by the Z index of $\pi_5(SU(3))$. For example, if we take a fundamental element of $\pi_5(SU(3))$ ($H_{\pi_5(SU(3))} = 1$), for example, doubled Witten's extension, after modding out the $SO(3)$ subgroup, it will be a fundamental element of the Z part of $\pi_5(SU(3)/SO(3))$ ($H_{\pi_5(SU(3)/SO(3))} = (1,0)$). Because the Berry's Γ for a single Witten's extension is found to be π by numerical integration of (4.5.7), we prove that the integration for doubled Witten's extension is 2π. Thus we prove that (4.5.7), when integrated over S^5, is exactly 2π times the Z index of $\pi_5(SU(3)/SO(3)) = Z \oplus Z_2$.

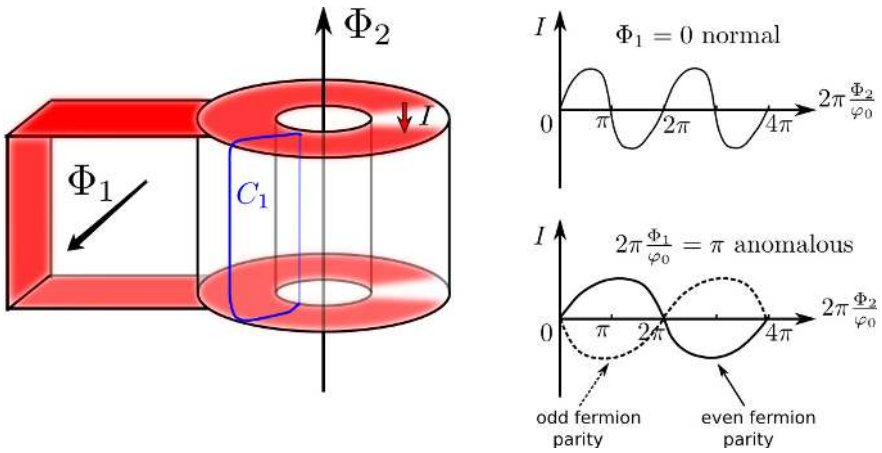

Figure 4.6.1: Anomalous Josephson Response connected to fermionic Hopfions: An annular cylinder of TI with pairing induced on the top and bottom surfaces via proximity to a superconductor (present in the red regions) is shown. Tuning the flux to $\Phi_1 \approx \varphi_0/2$, induces a vortex in the C_1 cycle. Now, the Josephson effect on tuning Φ_2 will be anomalous, with a part that is not periodic in the flux φ_0. This is directly related to the change in ground state fermion parity at $\Phi_2 = 2\pi(\varphi_0/2\pi)$, where the Hopf texture is realized. Adding a fermion inverts this current, indicating that the ground state in this sector is at $\Phi_2 = 2\pi(\varphi_0/2\pi)$. If however $\Phi_1 \approx 0$, there is no vorticity in the C_1 cycle, and the Josephson effect is the usual one, periodic in the flux quantum $\varphi_0 = h/2e$.

4.6 Physical Consequences

We now discuss two kinds of physical consequences arising from fermionic Hopfions. The first relies on the dynamical nature of the superconducting order parameter, while the second utilizes the Josephson effect to isolate an anomalous response. The first class conceptually parallels experiments used to identify skyrmions in quantum hall ferromagnets. There, when skyrmions are the cheapest charge excitations, they are detected on adding electrons to the system [12].

Consider surface superconductivity on a mesoscopic torus shaped topological insulator as in Figure 4.2. The Hopf texture corresponds to unit phase winding in each cycle of the torus. The energy cost, $E_H = (\rho_s/2)\int(\nabla\phi)^2 d^2x$ is simply proportional to the superfluid density $E_H = A\rho_s$, where A is in general an $O(1)$ constant. If we have $E_H < \Delta$ the superconducting gap, then the Hopfion is the lowest energy fermionic excitation. Tunneling a single electron onto the surface should then spontaneously generate these phase windings in equilibrium. Measuring the corresponding currents (ρ_s = 1Kelvin corresponds to a few nano-amps of current) can be used to establish the presence of the Hopf texture. A daunting aspect of this scheme is to obtain a fully gapped superconductor with $\rho_s < \Delta$.

A different approach which does not depend on the above inequality, relies on the Josephson effect as illustrated in Figure 4.6. A hollow cylinder of topological insulators is partially coated with superconductor on the top and bottom surfaces, forming a pair of Josephson junctions. The superconducting proximity effect induced through the surface states will ultimately gap out the entire surface. A unit vortex along the C_1 cycle can be induced

by enforcing a phase difference of π between the top and bottom surfaces, using the flux $\Phi_1 = \varphi_0/2$ (where $\varphi_0 = h/2e$ is the superconductor flux quantum). This phase difference makes the order parameter to wind by π on going from the bottom to the top surface. The lowest energy phase configuration that accomplishes this is just the unit winding on going around the circumference, so that the phase is π at the half way stage.

Now, the vorticity enclosed by the annulus determines the Hopf number, and hence the ground state fermion parity. This vorticity can be traded for magnetic flux Φ_2 (parameterized via $f_2 = 2\pi(\Phi_2/\varphi_0)$) threading the cylinder, since only $\nabla\phi - eA$ is gauge invariant. Consider beginning in the ground state with $f_2 = 0$ and then tuning to $f_2 = 2\pi$. One is now in an excited state since the ground state at this point has odd fermion parity. This must be reflected in the Josephson current I. We argue this implies doubling the flux period of the Josephson current. Since $I = \partial E(\Phi_2)/\partial\Phi_2$, the area under the $(I,\ \Phi_2)$ curve : $\int_0^{\varphi_0} d\Phi_2\, I[\Phi_2] = E[\varphi_0] - E[0] > 0$ is the excitation energy which does not vanish. Hence, the Josephson current is not periodic in flux φ_0, as in usual Josephson junctions. If we started with an odd fermion number to begin with, then the state of affairs would be reversed - the ground state would be achieved at multiples of $f_2 = 2\pi$. The ground state with a particular fermion parity can be located by studying the slope of the current vs phase curve. Since the energy of the ground state increases on making a phase twist $\partial I/\partial\Phi_2 = \partial^2 E/\partial\Phi_2^2 > 0$, it is associated with a positive I vs Φ_2 slope. This positive slope will be at even (odd) multiples of $f_2 = 2\pi$ for even (odd) fermion parity. If on the other hand unit vorticity was not induced in the cycle C_1, (e.g.. if $\Phi_1 \sim 0$) there is no Hopf texture, and the Josephson relation would be the usual one - i.e. one that is periodic in $f_2 = 2\pi$. This is summarized in Figure 4.6.

Note, a similar anomalous 4π Josephson periodicity was pointed out in the context of the 2D QSH case with proximate superconductivity in [37]. We interpret this result in terms of the fermionic nature of the solitons there - which lends a unified perspective. In the 3D case, the Hopf texture allows one to tune between the normal and anomalous Josephson effect by tuning the C_1 vorticity via Φ_1.

4.7 Conclusions

The low energy field theory of the superconductor-TI system was derived and shown to possess a topological Berry phase term, which leads to fermionic Hopf solitons. We note that topological terms are particularly important in the presence of strong quantum fluctuations. In one dimension where fluctuations dominate, the Berry phase term of the spin 1/2 Heisenberg chain [51] leads to an algebraic phase. It would be very interesting to study the destruction of superconductivity on a TI surface driven by quantum fluctuations. The Berry phase, or relatedly, the fact that a conventional insulator must break time reversal on the TI surface, will provide an interesting twist to the well know superconductor-insulator transition studied on conventional substrates [56].

P.H. would like to thank Ying Ran and Ashvin Vishwanath for this collaboration. We acknowledge helpful discussions with C. Kane, A. Turner and S. Ryu. A.V. and P.H. were supported by NSF DMR- 0645691. This work is published in *Physical Review B*, **84**, 184501 (2011).

Chapter 5

Majorana modes at the ends of superconductor vortices in doped topological insulators

5.1 Introduction

Majorana fermions, defined as fermions that are their own anti-particles unlike conventional Dirac fermions such as electrons, have long been sought by high energy physicists, but so far in vain. Of late, the search for Majorana fermions has remarkably shifted to condensed matter systems [78, 25, 114], especially, to superconductors (SCs), where states appear in conjugate pairs with equal and opposite energies. Then, a single state at zero energy is its own conjugate and hence, a Majorana state or a *Majorana zero mode* (**MZM**). These states are immune to local noise and hence, considered strong candidates for storing quantum information and performing fault tolerant quantum computation [102]. Moreover, they show non-Abelian rather than Bose or Fermi statistics which leads to a number of extraordinary phenomenon [95].

Despite many proposals direct experimental evidence for a MZM is still lacking. While initial proposals involved the $\nu = 5/2$ quantum Hall state and SCs with unconventional pairing such as p_x+ip_y [114], a recent breakthrough occurred with the discovery of topological insulators (TIs) [53, 111, 54], which feature metallic surface bands. When a conventional s-wave SC is brought near this metallic surface, a single MZM is trapped in the vortex core [36]. As pointed out in the previous chapter, MZMs also appear on the surface of a topological insulator when it has bulk s-wave pairing with unit winding around an axis perpendicular to the surface. Since then, several TIs were found to exhibit *bulk* superconductivity on doping [64] or under pressure [27, 154]. The normal phase of these SCs is now metallic, which raises the question: can a SC vortex host a surface MZM even when the bulk is *not* insulating?

In this Letter, we answer this question in the affirmative and in the process, discover a convenient way to obtain a MZM, which allows us to conclude that some existing experimental systems should possess these states. Our proposal involves simply passing a magnetic field through a TI-based SC, such as superconducting Bi_2Te_3, in which the doping is below

a certain threshold value. We also find general criteria for SCs to host vortex MZMs and show that some non-TI-based SCs satisfy them too.

A heuristic rule often applied to answer the above question is to examine whether the normal state bulk Fermi surface (FS) is well separated from surface states in the Brillouin zone. If it is, MZMs are assumed to persist in the bulk SC. While this may indicate the presence of low energy states, it is not a topological criterion since it depends on non-universal details of surface band structure, and cannot signal the presence of true MZMs. For MZMs to disappear, a gapless channel must open that allows pairs to approach each other and annihilate. We therefore search for and offer a bulk rather than surface criterion. In this process, we have uncovered the following interesting facts. We assume inversion ($\mathcal{I}$) and time reversal ($\mathcal{T}$) symmetric band structures, and weak pairing, since these lead to a technical simplification and capture many real systems. *(i)* The appearance of surface MZMs is tied to the topological state of the vortex, viewed as a 1D topological SC. The critical point at which they disappear is linked to a vortex phase transition **(VPT)** where this topology changes. If verified, this may be the first instance of a phase transition inside a topological defect. *(ii)* The topological state of a vortex depends in general on its orientation. *(iii)* Symmetry dictates that the normal state FS is doubly degenerate, leading to an $SU(2)$ non-Abelian Berry phase [138] for closed curves, which determines the condition for quantum criticality of the vortex. This is a rare example of a *non-Abelian* Berry phase directly influencing measurable physical properties of an electronic system. Spin-orbit coupling is essential to obtaining the SU(2) Berry Phase. *(iv)* Using this criterion and available band structures we find that MZMs occur in p-doped superconducting Bi_2Te_3 [154] and in Cu-doped Bi_2Se_3 [64] if the vortex is sufficiently tilted off the c-axis. C-axis vortices in Cu-doped Bi_2Se_3 are predicted to be near the topological transition.

5.1.1 The Problem

Consider a 3D insulating band structure H, which we dope by changing the chemical potential μ away from the middle of the band gap. Now, add conventional 's-wave' even parity pairing Δ (in contrast to the p-wave pairing of [33]) and introduce a single vortex line into the pairing function $\Delta(\boldsymbol{r})$, stretching between the top and bottom surfaces. We neglect the effect of the magnetic field used to generate the vortices, assuming extreme type II limit. When H is a strong TI, and μ is in the band gap, the pair potential primarily induces superconductivity on the surface states. In this limit it is known [36] that MZMs appear on the surface, in the vortex core. [1] Now consider tuning μ deep into the bulk bands. By modifying states well below μ, one could tune the band structure to one with uninverted bands. One now expects 'normal' behavior, and the absence of MZMs. Therefore, a quantum phase transition must occur between these limits and $\mu = \mu_c$.

To understand the nature of the transition, we recall some basic facts of vortex electronic structure, which are also derived below. Once μ enters the bulk bands, low energy Caroli-de Gennes-Matricon excitations appear, bound to the vortex line [19]. These excitations are still typically gapped, although by a small energy scale, the 'mini-gap': $\delta \sim \Delta/(k_F\xi)$,

[1] It is convenient to discuss pairing over the entire range of μ, using the mean field Hamiltonian (5.1.1), although in reality superconductivity only appears once bulk carriers are induced.

(where k_F is the Fermi wave-vector and ξ is the coherence length. In the weak pairing limit $k_F\xi \gg 1$). This small energy scale arises because the gap vanishes in the vortex core leading to a droplet of normal fluid, which is eventually gapped by the finite vortex size. However, the presence of the minigap is important, since it blocks the tunneling of the surface MZMs into the vortex line, and confines them near the surface. The closing of the mini-gap allows the surface MZMs to tunnel along the vortex line annihilate.

5.1.2 Vortex as a 1D topological SC

The VPT may be viewed as a change in the topology of the electronic structure of the vortex line. The relevant energy scale is of the order of the mini-gap $\delta \ll \Delta$, with excitations localized within the 1D vortex core. The vortex admits particle-hole symmetry ($\mathcal{C}$) but breaks $\mathcal{T}$-symmetry and hence, belongs to class D of the Altland-Zirnbauer classification [7]. Thus, the problem reduces to classifying gapped phases in 1D within the symmetry class D, which are known to be distinguished by a $\mathbb{Z}_2$ topological invariant [78]. The two kinds of phases differ in whether they support MZMs at their ends. The topologically nontrivial phase does and hence, corresponds to the $\mu < \mu_c$ phase of the vortex line. On raising μ, the vortex line transitions into the trivial phase, via a quantum critical point at which it is gapless along its length. This is reminiscent of recent proposals to generate MZMs at the ends of superconducting quantum wires [92, 106, 108, 139]. Note, since there is no 'local' gap in the vortex core, the powerful defect topology classification of [129] cannot be applied.

The Hamiltonian is $\mathbf{H} = \frac{1}{2}\sum_{\boldsymbol{k}} \Psi^\dagger_{\boldsymbol{k}} \mathcal{H}^{\mathrm{BdG}}_{\boldsymbol{k}} \Psi_{\boldsymbol{k}}$ where $\Psi^\dagger_{\boldsymbol{k}} = (\mathbf{c}^\dagger_{\boldsymbol{k}\uparrow}, \mathbf{c}^\dagger_{\boldsymbol{k}\downarrow}, \mathbf{c}_{-\boldsymbol{k}\downarrow}, -\mathbf{c}_{-\boldsymbol{k}\uparrow})$ and $\mathbf{c}^\dagger_{\boldsymbol{k}\sigma}$ is assumed to have $a = 1 \ldots N$ orbital components $\mathrm{c}^\dagger_{\boldsymbol{k}\sigma a}$ and

$$\mathcal{H}^{\mathrm{BdG}}_{\boldsymbol{k}} = \begin{bmatrix} H_{\boldsymbol{k}} - \mu & \Delta \\ \Delta^* & \mu - H_{\boldsymbol{k}} \end{bmatrix}. \tag{5.1.1}$$

where scalars like μ and Δ multiply the identity matrix $\mathbf{1}_{2N\times 2N}$. The band Hamiltonian, $H_{\boldsymbol{k}}$, is a $2N \times 2N$ matrix with $\mathcal{T}$ symmetry: $\sigma_y H^*_{-\boldsymbol{k}} \sigma_y = H_{\boldsymbol{k}}$, where σ_y acts on the spin, which yields the Hamiltonian structure above. When $\mathcal{I}$-symmetry is also present, $H_{\boldsymbol{k}}$ will be doubly degenerate, since the combined operation $\mathcal{T}\mathcal{I}$ leads to a Kramers pair at every momentum. $\mathcal{H}^{\mathrm{BdG}}_{\boldsymbol{k}}$ has particle hole symmetry implemented by the transformation $\mathcal{C} = \Pi_y \sigma_y \mathcal{K}$, where Π matrices act on Nambu particle-hole indices, and $\mathcal{K}$ is complex conjugation. A vortex given by $\Delta(\boldsymbol{r}) = |\Delta(r)|e^{-i\theta}$, breaks $\mathcal{T}$ but preserves $\mathcal{C}$.

Role of vortex orientation

Consider a straight vortex along $\hat{z}$. The dispersion $\mathcal{E}(k_z)$ in general, has a minigap δ as in Figure 5.1.1. A topological phase transition requires closing of the minigap and reopening with inverted sign. Since the $\mathbb{Z}_2$ topological index is only changed by an odd number of such band crossings, the only relevant momenta are $k_z = 0, \pi$. Band touchings at other k_z points occur in pairs at $\pm k_z$ which do not alter the $\mathbb{Z}_2$ index [78]. In the weak pairing limit, one expects the critical point μ_c to be determined by a FS property, which will be outlined in detail below. Here we simply observe that the relevant FSs to consider lie in the $k_z = 0, \pi$ planes, the planes determined by the vortex orientation. This implies that the topological phase of the vortex, and hence μ_c depend on its orientation.

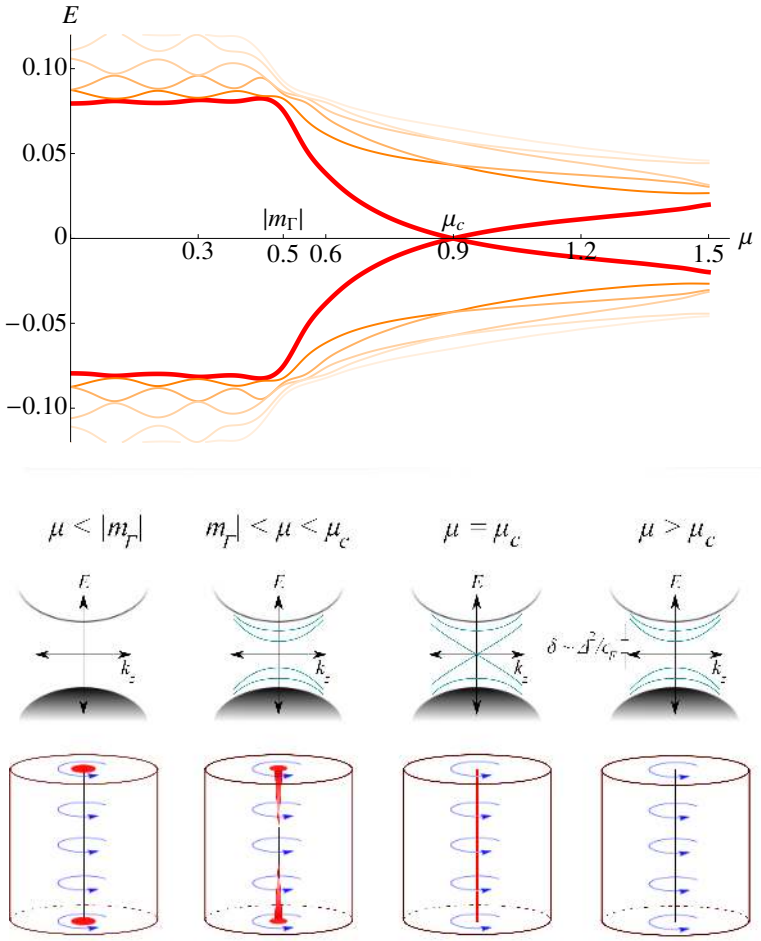

Figure 5.1.1: Evolution of the lowest eigenstates at $k_z = 0$ (top row), of the dispersion within the vortex (middle row) and of the surface MZMs (bottom row) as μ is varied when the normal phase has a band inversion at Γ. At $\mu = 0$, the normal phase is a strong TI and a superconducting vortex traps a MZM at its ends. As μ is increased, it first enters the conduction band at $\mu = |m_\Gamma|$ and mid-gap states appear inside the vortex. For $\mu < \mu_c$, the vortex stays gapped, but with a minigap δ smaller than the bulk gap. The MZMs remain trapped near the surface. At $\mu_c = 0.9$, the gap vanishes signaling a phase transition. Beyond μ_c, the vortex is gapped again, but there are no surface MZMs. We used the lattice Hamiltonian with the parameters $t = 0.5$, $M = 2.5$ and $m_0 = -1.0$. The pairing strength is $\Delta_0 = 0.1$ far from the vortex and drops sharply to zero at the core. Other profiles give similar results.

5.1.3 VPT in a lattice model

Before discussing the general criterion for a VPT, we present numerical and analytical evidence in a specific lattice model from [66]. While the numerics explicitly demonstrate the phase transition, the analytical treatment of the continuum limit allows us to conjecture a Berry phase condition for the transition, which is later proved. The model is on a simple cubic lattice with two orbitals per site: $H^{\text{latt}}_{\boldsymbol{k}} = \tau_x \boldsymbol{d}_{\boldsymbol{k}} \cdot \boldsymbol{\sigma} + m_{\boldsymbol{k}} \tau_z - \mu$ where τ_i (σ_i) are Pauli

matrices in the orbital (spin) basis, $d^i_{\boldsymbol{k}} = 2t \sin k_i$, $m_{\boldsymbol{k}} = (M + m_0 \sum_i \cos k_i)$, $i = x, y, z$, and t, m_0 and M are parameters of the model and μ is the chemical potential. The model is in the strong TI phase if $-3 < \frac{M}{m_0} < -1$. We add mean field s-wave pairing to H^{latt}, insert a unit winding into the pairing function and diagonalize the Hamiltonian numerically. We focus on $k_z = 0$.

Figure 5.1.1 illustrates the evolution of the bulk vortex bound states, the dispersion within the vortex and the surface MZMs as a function of μ, when the normal state has a band inversion only at the $\Gamma = (0, 0, 0)$-point, *i.e.*, $m_\Gamma < 0$. At $\mu = 0$, the bulk is gapped and must have a pair of MZMs on opposite surfaces in a slab geometry. As μ is raised, these MZMs leak deeper into the bulk, but survive even after μ crosses $|m_\Gamma|$ despite the bulk now having a FS in the normal phase, gapped by superconductivity. A VPT eventually occurs at $\mu_c = 0.9$, at which the vortex is gapless and the surface MZMs merge into vortex line. Beyond μ_c, there are no longer any protected MZMs on the surface.

5.2 Continuum model: Analytical solution

In the continuum limit of the lattice model, we can analytically calculate μ_c. For $k_z = 0$ and small $k_{x,y}$ around Γ, $H^{\text{latt}}_{\boldsymbol{k}}$ reduces to the isotropic form $\mathcal{H}_{\boldsymbol{k}} = v_D \tau_x \boldsymbol{\sigma} \cdot \boldsymbol{k} + (m - \epsilon k^2)\tau_z - \mu$. In this form, a band inversion exists if $m\epsilon > 0$. Thus, $m\epsilon < 0$ (> 0) defines a trivial insulator (strong TI). At $k = \sqrt{m/\epsilon}$, $m_{\boldsymbol{k}} = m - \epsilon k^2$ vanishes and $\mathcal{H}_{\boldsymbol{k}}$ resembles two copies of a TI surface. In particular, the Berry phase around each $\tau_x = \pm 1$ FS is π. We show later that this leads to a pair of vortex zero modes, signaling the VPT at $\mu_c = v_D\sqrt{m/\epsilon}$.

We solve analytically for the two bulk zero modes at μ to first order in Δ_0 assuming $|\Delta(\boldsymbol{r})| = \Delta_0 \Theta(r - R)$, where Θ is the step-function and $\mu R/v_D \gg 1$. Calculating the zero modes separately for $r \leq R$ and $r \geq R$ and matching the solutions at $r = R$ gives a pair of zero modes, only when $\mu = v_D\sqrt{m/\epsilon}$, for all vortex orientations. This is precisely where the momentum dependent 'mass' term changes sign as shown in Sec. 5.2. Using the model parameters and the linearized approximation gives an estimate of $\mu_c \approx 1$, in agreement with the lattice numerics.

In the continuum limit of the lattice model with cubic symmetry, we can analytically calculate μ_c. For $k_z = 0$ and small $k_{x,y}$ around Γ, the lattice model reduces to the isotropic form $\mathcal{H}_{\boldsymbol{k}} = v_D \tau_x \boldsymbol{\sigma} \cdot \boldsymbol{k} + (m - \epsilon k^2)\tau_z - \mu$. In this form, a band inversion exists if $m\epsilon > 0$. Thus, $m\epsilon > 0 (< 0)$ characterizes a strong TI (trivial insulator). At $k = \sqrt{m/\epsilon}$, $m_{\boldsymbol{k}} = m - \epsilon k^2$ vanishes. Below we show that $\mu_c = v_D\sqrt{m/\epsilon}$ is the critical chemical potential at which the VPT occurs.

We solve for the two bulk zero modes at μ_c analytically to first order in Δ_0 by assuming $|\Delta(\boldsymbol{r})| = \Delta_0 \Theta(r - R)$, where Θ is the step-function R is a large radius such that $R(\Delta_0/v_D\hbar) \gg 1$. In the basis $\big(\psi(\boldsymbol{r}), i\sigma_y\psi^\dagger(\boldsymbol{r})\big)$ where $\psi(\boldsymbol{r})$ is a four-component spinor of electron annihilation operators indexed by spin and orbital indices, the Bogoliubov-de Gennes Hamiltonian in real space for a unit vortex is

$$\mathcal{H}^{\text{BdG}} = \begin{pmatrix} \mathcal{H}_{\boldsymbol{r}} & \Delta_0 \Theta(r - R) e^{i\theta} \\ \Delta_0 \Theta(r - R) e^{-i\theta} & -\mathcal{H}_{\boldsymbol{r}} \end{pmatrix} \tag{5.2.1}$$

where $\mathcal{H}_{\boldsymbol{r}} = -iv_D \tau_x \boldsymbol{\sigma} \cdot \boldsymbol{\nabla} + \tau_z(m + \epsilon\nabla^2) - \mu$. The θ-dependence of $\mathcal{H}^{\text{BdG}}$ can be removed

by observing that it commutes with the generalized angular momentum operator $L_z = -i\partial_\theta + \frac{\sigma_z+\Pi_z}{2}$. Since $\{L_z, \mathcal{C}\} = 0$, a single MZM, such as the one on the surface, must have an eigenvalue n of L_z, equal to zero. Now, the bulk zero modes can be thought of as the avenues through which the surface MZMs penetrate the bulk. Thus, they must have $n = 0$ as well. The vortex preserves a mirror symmetry about the xy-plane described by $\mathcal{M} = \tau_z\sigma_z$. Thus, $\mathcal{H}^{\text{BdG}}$ can be block-diagonalized into sectors with opposite $\mathcal{M}$ eigenvalues. The two blocks are particle-hole conjugates since $\{\mathcal{M}, \mathcal{C}\} = 0$ and each must contribute a single bulk MZM at μ_c. The radial Hamiltonian for the $\mathcal{M} = +1$ sector is

$$\begin{aligned}\mathcal{H}_{\text{rad}} &= -i\Pi_z\nu_y\left(\partial_r + \frac{1}{2r}\right) + \frac{\nu_x}{2r} + \\ &\quad \Pi_z\nu_z\left[m + \epsilon\left(\partial_r^2 + \frac{1}{r}\partial_r - \frac{1}{2r^2}\right)\right] - \frac{\epsilon}{2r^2} - \Pi_z\mu + \Pi_x\Delta_0\Theta(r-R)\end{aligned} \tag{5.2.2}$$

where ν_i are Pauli matrices in a combined orbital (τ_i) and spin (σ_i) space. For $r < R$, $\mathcal{H}_{\text{rad}}$ has four zero modes

$$\begin{pmatrix} -k_\pm J_1(k_\pm r) \\ (\mu - m_{\boldsymbol{k}_\pm})J_0(k_\pm r) \\ 0 \\ 0 \end{pmatrix}, \begin{pmatrix} 0 \\ 0 \\ -k_\pm J_0(k_\pm r) \\ (\mu - m_{\boldsymbol{k}_\pm})J_1(k_\pm r) \end{pmatrix}, \tag{5.2.3}$$

where $k_\pm$ are roots of $g(k) = \epsilon^2 k^4 + (1-2m\epsilon)k^2 + (m^2 - \mu^2)$ and $J_i(x)$ are Bessel functions of the first kind of order i. For $r > R$, we drop all terms that contain r in the denominator. The zero modes of the remaining Hamiltonian are of the form $e^{i\lambda_\pm r}\chi_\pm$, where $\lambda_\pm$ is a root of $\epsilon^2\lambda^4 + (1-2m\epsilon)\lambda^2 + (m^2 - (\mu \pm i\Delta_0)^2) = 0$ with positive imaginary part and

$$\chi_\pm = \begin{pmatrix} -i\lambda_\pm \\ \mu \mp i\Delta_0 - m + \epsilon\lambda_\pm^2 \\ \pm\lambda_\pm \\ \pm i(\mu \mp i\Delta_0 - m + \epsilon\lambda_\pm^2) \end{pmatrix}. \tag{5.2.4}$$

Matching the solutions and their derivatives at $r = R$ to first order in Δ_0, using the asymptotic forms of the Bessel functions, is only possible at $\mu = v_D\sqrt{m/\epsilon}$. This gives an analytic solution to the critical chemical potential μ_c.

5.3 General Fermi surface Berry phase condition

For weak pairing, the VPT is expected to be governed by properties of the bulk FS. For concreteness, we begin by assuming we have a *single* FS in the $k_z = 0$ plane, which will be doubly degenerate due to the combined symmetry $\mathcal{TI}$. We now argue that the VPT occurs when an appropriately defined Berry phase for each of the two degenerate bulk FSs is π.

A convenient model for the vortex is $\Delta(\boldsymbol{r}) = \frac{\Delta_0}{\xi}(x - iy)$. The linear profile here simplifies calculations, but does not affect location of the zero mode. The choice of ξ as the length scale gives the right minigap scale for the low energy excitations. Working in momentum

space, we substitute $\boldsymbol{r}$ by $i\partial_{\boldsymbol{k}}$, which gives

$$\mathcal{H}_{\boldsymbol{k}}^{\mathrm{BdG}} = \begin{bmatrix} H_{\boldsymbol{k}} - \mu & i\frac{\Delta_0}{\xi}(\partial_{k_x} - i\partial_{k_y}) \\ i\frac{\Delta_0}{\xi}(\partial_{k_x} + i\partial_{k_y}) & \mu - H_{\boldsymbol{k}} \end{bmatrix}, \tag{5.3.1}$$

transforming now to the band basis $|\varphi_{\boldsymbol{k}}^{\nu}\rangle$, which are eigenstates of the band Hamiltonian $H_{\boldsymbol{k}}|\varphi_{\boldsymbol{k}}\rangle = E|\varphi_{\boldsymbol{k}}\rangle$. Since we are only interested in very low energy phenomena, we project onto the two degenerate bands near the Fermi energy $\nu = 1, 2$. The projected Hamiltonian then is:

$$\tilde{\mathcal{H}}_{\boldsymbol{k}}^{\mathrm{BdG}} = \begin{bmatrix} E_{\boldsymbol{k}} - \mu & i\frac{\Delta_0}{\xi}(D_{k_x} - iD_{k_y}) \\ i\frac{\Delta_0}{\xi}(D_{k_x} + iD_{k_y}) & -E_{\boldsymbol{k}} + \mu \end{bmatrix}. \tag{5.3.2}$$

where $D_{k_\alpha} = \partial_{k_\alpha} - i\mathbf{A}_\alpha(\boldsymbol{k})$ and $\mathbf{A}_\alpha(\boldsymbol{k})$, the $SU(2)$ connections, are 2×2 matrices: $[\mathbf{A}]_\alpha^{\mu\nu}(\boldsymbol{k}) = i\langle\varphi_{\boldsymbol{k}}^{\mu}|\partial_{k_\alpha}|\varphi_{\boldsymbol{k}}^{\nu}\rangle$.

(i) Abelian case: Let us first consider the case when an additional quantum number (such as spin) can be used to label the degenerate FSs. Then, $[\mathbf{A}]_\alpha^{\mu\nu}$ must be diagonal, and reduces to a pair of $U(1)$ connections for the two FSs. In this situation, (5.3.2) is identical to the effective Hamiltonian for a $p_x + ip_y$ SC, if we interpret momenta as position and ignore the gauge potential. The diagonal terms represent a transition from weak to strong pairing phase on crossing the FS when $E_{\boldsymbol{k}} = \mu$ [114]. Thus mid-gap are expected, composed of states near the Fermi energy. Due to the finite size of the FS, these states have an energy spacing of $\mathcal{O}\big(\frac{\Delta_0}{k_F\xi}\big)$, the minigap energy scale. However, a zero energy state appears if the FS encloses a π-flux [114]. This can be implemented via the gauge potential if $\oint_{\mathrm{FS}} \mathbf{A}\cdot\mathrm{d}\mathbf{l} = \pi$ leading to a pair of zero modes, since the other FS has the same Berry phase by $\mathcal{T}$.

(ii) General case, $SU(2)$ connection: In the absence of any quantum number distinguishing the bands, one integrates the vector potential $\mathbf{A}(\boldsymbol{k})$ around the FS in the $k_z = 0$ plane, to give the non-Abelian Berry phase: $U_B = \mathcal{P}\exp\big[i\oint_{\mathrm{FS}}\mathbf{A}\cdot\mathrm{d}\mathbf{l}\big] \in SU(2)$, where $\mathcal{P}$ denotes path ordering. (There is no $U(1)$ phase by $\mathcal{T}$ symmetry.) Although U_B itself depends on the choice of basis, its eigenvalues $e^{\pm i\phi_B}$ are gauge invariant. A semiclassical analysis described below in Sec. 5.3.1 gives the Bohr-Sommerfield type quantization condition for the low energy levels:

$$E_n = \frac{\Delta_0}{l_F\xi}(2\pi n + \pi \pm \phi_B) \tag{5.3.3}$$

where n is an integer and l_F is the FS perimeter. A pair of zero modes appears when $\phi_B = \pi$, *i.e.* when $U_B = -\mathbf{1}$.

We have considered a single closed FS in the $k_z = 0$ plane. Such a FS necessarily encloses a $\mathcal{T}$ invariant momentum (TRIM), (*e.g.* Γ), given the symmetries. When there are multiple FSs, the condition above is applied individually to each FS, since tunneling between them is neglected in the semiclassical approximation. Closed FSs that do not enclose a TRIM, or pairs of open FSs, cannot change the vortex topology.

5.3.1 Vortex modes and the Berry phase of the Fermi surface

We consider a 3D system with s-wave pairing, where the bulk is pierced by a quantum flux $h/2e$. Assuming that the metallic Hamiltonian $H_{\boldsymbol{k}}$ (the system without superconductiv-

ity/quantum flux) has time-reversal symmetry, we will derive the condition which governs the existence of zero vortex modes to the properties of the FS, namely the Berry phase.

The mean field Bogoliubov-de Gennes (BdG) Hamiltonian with s-wave pairing is of the form:

$$\mathcal{H} = \frac{1}{2}\sum_{\boldsymbol{k}\boldsymbol{k}'} \Psi^\dagger_{\boldsymbol{k}} \mathcal{H}^{\mathrm{BdG}}(\boldsymbol{k},\boldsymbol{k}')\Psi_{\boldsymbol{k}'}, \tag{5.3.4}$$

where $\Psi^\dagger_{\boldsymbol{k}} = \left(\mathbf{c}^\dagger_{\boldsymbol{k}}, \mathbf{c}^T_{-\boldsymbol{k}}(i\sigma_y)\right)$ is written in the Nambu basis, capturing all orbital and spin degrees of freedom. The single particle Hamiltonian is

$$\mathcal{H}^{\mathrm{BdG}}(\boldsymbol{k},\boldsymbol{k}') = \begin{bmatrix} (H_{\boldsymbol{k}} - \mu)\delta_{\boldsymbol{k}\boldsymbol{k}'} & \Delta(\boldsymbol{r}) \\ \Delta^*(\boldsymbol{r}) & (\mu - \sigma_y H^*_{-\boldsymbol{k}}\sigma_y)\delta_{\boldsymbol{k}\boldsymbol{k}'} \end{bmatrix}, \tag{5.3.5}$$

where the pairing potential, given by $\Delta^*(\boldsymbol{r}) = \left\langle \Psi^\dagger_\uparrow(\boldsymbol{r})\Psi^\dagger_\downarrow(\boldsymbol{r})\right\rangle$, is position dependent due to the vortex.

The quasi-particle operators $\Psi^\dagger, \Psi$ are defined in such as a way that leads to spin singlet pairing. Since the metallic Hamiltonian $H_{\boldsymbol{k}}$ has time-reversal symmetry, $\sigma_y H^*_{-\boldsymbol{k}}\sigma_y = H_{\boldsymbol{k}}$ and the BdG Hamiltonian may be written as

$$\mathcal{H}^{\mathrm{BdG}} = \begin{bmatrix} H_{\boldsymbol{k}} - \mu & \Delta(\boldsymbol{r}) \\ \Delta^*(\boldsymbol{r}) & \mu - H_{\boldsymbol{k}} \end{bmatrix}. \tag{5.3.6}$$

(We drop the $\boldsymbol{k}, \boldsymbol{k}'$ dependence, treating $\mathcal{H}^{\mathrm{BdG}}$ as an operator.)

We take the vortex to lie in the $\hat{z}$ direction, hence the pairing term takes the form $\Delta^*(\boldsymbol{r}) = \Delta(r_\perp)e^{i\theta}$, independent of z, where $r_\perp e^{i\theta} = x + iy$. The pairing amplitude becomes constant for large $r_\perp$: $\Delta(r_\perp) \to \Delta_0$. Although the vortex breaks translational symmetry in the xy-plane, it is preserved in the z direction and hence, k_z remains a good quantum number. The 3D system thus decouples into many 2D Hamiltonians enumerated by k_z. Henceforth, we refer to $r_\perp$ as simply r, and $\boldsymbol{k}$ as the 2D momentum coordinate (k_x, k_y).

The time-reversal operator is $-i\sigma_y\mathcal{K}$, taking $k_z \to -k_z$, $\boldsymbol{k} \to -\boldsymbol{k}$, which is broken by the imaginary part of Δ. In addition, the system must have particle-hole (charge conjugation) symmetry given by the operator $\mathcal{C} = \Pi_y\sigma_y\mathcal{K}$, where Π_i are the Pauli matrices acting on particle-hole space. Note that $\mathcal{C}$ also takes $k_z \to -k_z$, $\boldsymbol{k} \to -\boldsymbol{k}$, hence particle-hole is a symmetry of the 2D system only when $k_z \sim -k_z$ (*i.e.* at 0 or π).

In the remainder of this section, we do not assume anything about the value of k_z, nor the symmetries of the 2D Hamiltonian $H_{\boldsymbol{k}}|_{k_z}$ at a fixed k_z. Our results remain valid applied to any 2D slice (with a smooth FS) of the 3D Brillouin zone, as long as the 3D Hamiltonian has time-reversal symmetry.

Pairing potential

In this section, we compute the pairing potential of a vortex in k-space via a Fourier transform. We confine our system to be on a disk with radius ξ, the superconducting correlation

length. The matrix element $\Delta_{\boldsymbol{k}'\boldsymbol{k}}$ is

$$\begin{aligned}\Delta_{\boldsymbol{k}'\boldsymbol{k}} &= \langle \boldsymbol{k}'|\Delta(\boldsymbol{r})|\boldsymbol{k}\rangle \\ &= \frac{1}{\pi\xi^2}\int d^2r\, e^{i(\boldsymbol{k}-\boldsymbol{k}')\cdot\boldsymbol{r}}\Delta(\boldsymbol{r}) \\ &= \frac{1}{\pi\xi^2}\int_0^{\xi} rdr\,\Delta(r)\int_0^{2\pi} d\theta\, e^{iqr\cos(\theta-\theta_q)}e^{-i\theta},\end{aligned}$$

where $\mathbf{q} = \boldsymbol{k}-\boldsymbol{k}' = q(\cos\theta_q\hat{x}+\sin\theta_q\hat{y})$. The θ integral evaluates to a Bessel function (of the first kind): $2\pi i e^{-i\theta_q}J_1(qr)$. The matrix element becomes

$$\Delta_{\boldsymbol{k}'\boldsymbol{k}} = \frac{2\pi i e^{-i\theta_q}}{\pi\xi^2}\int_0^{\xi} rdr\,\Delta(r)J_1(qr). \tag{5.3.7}$$

- At large q ($q\xi \gg 1$), $J_1(qr) \approx \sin qr/\sqrt{qr}$, and $\Delta(r) \to \Delta_0$ becomes constant. The integral scales as $\frac{\Delta_0}{q^2}(q\xi)^{1/2}\cos q\xi$ and the matrix element $\Delta_{\boldsymbol{k}'\boldsymbol{k}} \approx i\Delta_0 e^{-i\theta_q}(q\xi)^{-3/2}\cos q\xi \to 0$.

- At small q ($q\xi < 1$), $J_1(qr) \approx qr/2$ and the integral evaluates to $q\Delta_0\xi^3/6$. The matrix element scales as $\frac{i}{3}\Delta_0 e^{-i\theta_q}q\xi$ and is linear in q.

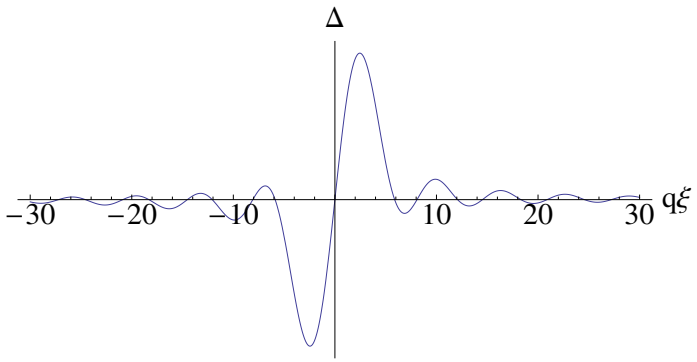

Figure 5.3.1: The pairing potential. $\Delta_{\boldsymbol{k}'\boldsymbol{k}}$ as a function of $q\xi$ where $q = |\boldsymbol{k}-\boldsymbol{k}'|$ and ξ is the system radius. The wavefunction $\psi(\boldsymbol{k})$ is smooth on the scale of ξ^{-1}, and hence the pairing potential may be modeled as $-\delta'(q)$.

We can model the pairing matrix element as a derivative of the delta function: $\Delta_{\boldsymbol{k}'\boldsymbol{k}} \propto ie^{-i\theta_q}(-\delta'(q))$, this approximation is valid in the regime where the wavefunction $\psi(\boldsymbol{k})$ is smooth on the length scale of ξ^{-1}. In Cartesian coordinates, the pairing term becomes $i\Delta_e(\partial_{k_x} - i\partial_{k_y})$, where Δ_e is the effective $p+ip$ pairing strength, with units energy $\times$ length^{-1}. From a simple analysis, we expect that $\Delta_e \approx \Delta_0/\xi$.

The Hamiltonian in k-space is of the form:

$$\mathcal{H}^{\mathrm{BdG}} = \begin{bmatrix} H_{\boldsymbol{k}} - \mu & i\Delta_e(\partial_{k_x} - i\partial_{k_y}) \\ i\Delta_e(\partial_{k_x} + i\partial_{k_y}) & \mu - H_{\boldsymbol{k}} \end{bmatrix}. \tag{5.3.8}$$

The eigenstates are of the form

$$|\psi\rangle = \sum_{\boldsymbol{k},\nu} \psi_\nu(\boldsymbol{k})|\varphi^\nu_{\boldsymbol{k}}\rangle, \tag{5.3.9}$$

where $|\varphi^\nu_{\boldsymbol{k}}\rangle$ is an eigenstate of $H_{\boldsymbol{k}}$ and ν labels the band index.

Projecting to the low energy states

Solutions to the Hamiltonian (5.3.8) will consists of mostly states near the FS, where $E_{\boldsymbol{k}} \sim \mu$. Hence we can simplify the system by projecting to the band eigenstates $|\varphi^\mu_{\boldsymbol{k}}\rangle$ with energy near the chemical potential, where μ, ν is the band index:

$$\tilde{\mathcal{H}} = \langle\varphi^\mu_{\boldsymbol{k}}|\mathcal{H}|\varphi^\nu_{\boldsymbol{k}}\rangle. \tag{5.3.10}$$

If inversion symmetry is present, each band will be doubly degenerate.

The projection of the metallic Hamiltonian $H_{\boldsymbol{k}}$ gives a diagonal matrix $E^{\mu\nu}_{\boldsymbol{k}} = \langle\varphi^\mu_{\boldsymbol{k}}|H_{\boldsymbol{k}}|\varphi^\nu_{\boldsymbol{k}}\rangle$ with its entries being the energies. The projection of the derivative operator gives the Berry connection: $\langle\varphi^\mu_{\boldsymbol{k}}|i\boldsymbol{\nabla}_{\boldsymbol{k}}|\varphi^\nu_{\boldsymbol{k}}\rangle = i\boldsymbol{\nabla}_{\boldsymbol{k}} + \mathbf{A}^{\mu\nu}$, where the non-Abelian Berry connection is defined as: $\mathbf{A}^{\mu\nu} = i\langle\varphi^\mu_{\boldsymbol{k}}|\boldsymbol{\nabla}_{\boldsymbol{k}}|\varphi^\nu_{\boldsymbol{k}}\rangle$. Explicitly:

$$\tilde{\mathcal{H}} = \begin{bmatrix} E^{\mu\nu}_{\boldsymbol{k}} - \mu & \Delta_e \begin{pmatrix} i(\partial_{p_x} - i\partial_{p_y}) \\ +A^{\mu\nu}_x - iA^{\mu\nu}_y \end{pmatrix} \\ \Delta_e \begin{pmatrix} i(\partial_{p_x} + i\partial_{p_y}) \\ A^{\mu\nu}_x + iA^{\mu\nu}_y \end{pmatrix} & -E^{\mu\nu}_{\boldsymbol{k}} + \mu \end{bmatrix}. \tag{5.3.11}$$

The connections A_x, A_y are hermitian matrices which depends on the choice of Bloch states $|\varphi^\nu_{\boldsymbol{k}}\rangle$.

Dropping the band indices and writing $E_{\boldsymbol{k}}$ as $E(\boldsymbol{k})$, the Hamiltonian is:

$$\tilde{\mathcal{H}} = \begin{bmatrix} E(\boldsymbol{k}) - \mu & \Delta_e \begin{pmatrix} i(\partial_{p_x} - i\partial_{p_y}) \\ +A_x - iA_y \end{pmatrix} \\ \Delta_e \begin{pmatrix} i(\partial_{p_x} + i\partial_{p_y}) \\ +A_x + iA_y \end{pmatrix} & -E(\boldsymbol{k}) + \mu \end{bmatrix}, \tag{5.3.12}$$

If we interpret momenta $(\boldsymbol{k})$ as position, then we can treat $A_{x,y}$ as a gauge potential and the Berry curvature $F = \partial_{k_x} A_y - \partial_{k_y} A_x - i[A_x, A_y]$ as an effective magnetic field in the model. This system was studied by Read, Green, Ludwig, Bocquet and Zirnbauer in context of a Dirac Hamiltonian with random mass as well as $p+ip$ superconducting systems [114, 115, 16].

While superficially similar to a $p + ip$ superconductor, there is an important distinction – our system may not have particle-hole symmetry (unless $k_z = 0$ or π), and hence does not belong to the D class. To illustrate how $\mathcal{C}$ is broken, suppose that there is only one FS and hence A_i are simply 1×1 (Abelian) matrices. The system resembles a superconductor with $p + ip$ pairing, but with an effective magnetic field $\boldsymbol{\nabla} \times \mathbf{A}$. Unlike a superconductor, the effective field does not have to be localized nor quantized within the FS.

Consequently, the spectrum of vortex states in our 2D system does not have any symmetry, and the zero modes are not topologically protected. We can only show that these

modes are stable within the weak pairing limit under perturbation theory. We can restore particle-hole symmetry by combining the 2D systems at k_z with that at $-k_z$, at the cost of doubling the number of zero energy states.

In the remainder of the section, we will explicitly show the following: when (an eigenvalue of) the Berry phase of the FS ϕ_F is π, there is an effective half quantum flux $\frac{h}{2e}$ in the system which supports a Majorana mode [114, 115, 16].

Explicit solution with rotational symmetry

This section is not necessary to the solution, but is instructive and aids in the understanding of what the terms in the more general solutions mean. For simplicity, we only consider a single FS at wavevector k_F. We also assume an Abelian Berry connection, so A_x, A_y are simply real numbers.

With rotational symmetry, we can simplify the expressions in polar coordinates: $k_x+ik_y = ke^{i\theta}$: $E(\boldsymbol{k}) = E(k)$, $\partial_{k_x} - i\partial_{k_y} = e^{-i\theta}(\partial_k - \frac{i}{k}\partial_\theta)$, $A_x - iA_y = e^{-i\theta}(A_k - \frac{i}{k}A_\theta)$. In addition, it is possible to find a gauge for which $A_k = 0$, and A_θ is a function of k, but independent of θ. Explicitly, the Berry connection is

$$2\pi A_\theta(k) = 2\pi \int_0^k k'dk'\, F(k'), \tag{5.3.13}$$

where $F(\boldsymbol{k}) = \boldsymbol{\nabla}_{\boldsymbol{k}} \times \mathbf{A}$ is the Berry curvature. The left side of (5.3.13) is the Berry phase along a circle of radius k, while the right side is the integrated Berry curvature.

Our Hamiltonian simplifies to

$$\tilde{\mathcal{H}} = \begin{bmatrix} E(k) - \mu & i\Delta_e e^{-i\theta}\left(\partial_k - \frac{i\partial_\theta + A_\theta}{k}\right) \\ i\Delta_e e^{i\theta}\left(\partial_k + \frac{i\partial_\theta + A_\theta}{k}\right) & -E(k) + \mu \end{bmatrix}. \tag{5.3.14}$$

The Hamiltonian commutes with $J_z = -i\partial_\theta + \Pi_z$, that is to say that the solutions are of the form

$$\psi(k,\theta) = \frac{1}{\sqrt{k}} \begin{pmatrix} u(k)e^{i(n-1)\theta} \\ -iv(k)e^{in\theta} \end{pmatrix}, \tag{5.3.15}$$

for integers n (required by the wavefunction being single-valued). Via the transformation

$$W_{ph} = k^{\frac{1}{2}} \begin{bmatrix} e^{-i(n-1)\theta} & \\ & i\, e^{-in\theta} \end{bmatrix}, \tag{5.3.16}$$

the effective Hamiltonian for (u, v) is

$$\begin{aligned} \tilde{\mathcal{H}}_n &= W_{ph}\, \tilde{\mathcal{H}}\, W_{ph}^{-1} \\ &= \begin{bmatrix} E(k) - \mu & \Delta_e\left(\partial_k + \frac{n-\frac{1}{2}-A_\theta}{k}\right) \\ \Delta_e\left(\frac{n-\frac{1}{2}-A_\theta}{k} - \partial_k\right) & -E(k) + \mu \end{bmatrix}. \end{aligned} \tag{5.3.17}$$

Notice that the Hamiltonian is symmetric except for the terms proportional to ∂_k, due to our choice of W_{ph}.

Our assumption is to replace k by the Fermi wavevector k_F, A_θ by $A_\theta^F = A_\theta(k_F)$ and $\frac{1}{k}$ by $\frac{1}{k_F}$. This is justified as the amplitude of the wavefunction $|u(k)|, |v(k)|$ is largest at the FS $k = k_F$ and exponentially decays away from the FS. The resulting Hamiltonian is equivalent to the Jackiw-Rebbi model [72]:

$$\tilde{\mathcal{H}}_n = \frac{\Delta_e}{k_F}\left(n - A_\theta^F - \tfrac{1}{2}\right)\Pi_x + i\Delta_e\partial_k\Pi_y + (E(k) - \mu)\Pi_z \tag{5.3.18}$$

A midgap state exists whenever $E(k) - \mu$ changes sign, with energy

$$\mathcal{E}_n = \frac{\Delta_e}{k_F}\left(n - \frac{\phi_F}{2\pi} - \frac{1}{2}\right), \tag{5.3.19}$$

where $\phi_F = 2\pi A_\theta^F$ is the Berry phase of the FS. Hence, a zero energy solution exists when ϕ_F is an odd multiple of π.

Explicitly, the eigenstates are of the form [72, 114]

$$u(k) = \exp\int^k \beta(k')\,dk', \tag{5.3.20}$$

where $\beta(k)$ must a be a decreasing function of k for $u(k)$ to be normalizable. Assuming that $E(k)$ is an increasing function of k, then

$$\beta(k) = \frac{\mu - E(k)}{\Delta_e} \tag{5.3.21a}$$

$$v(k) = u(k) \tag{5.3.21b}$$

By inspection, this satisfies the Schrödinger equation for the Hamiltonian (5.3.18):

$$\tilde{\mathcal{H}}_n\begin{pmatrix}u\\v\end{pmatrix} = \begin{bmatrix}-\Delta_e\beta & \mathcal{E}_n + \Delta_e\beta\\ \mathcal{E}_n - \Delta_e\beta & \Delta_e\beta\end{bmatrix}\begin{pmatrix}1\\1\end{pmatrix} = \begin{pmatrix}\mathcal{E}_n\\\mathcal{E}_n\end{pmatrix} \tag{5.3.22}$$

For a Fermi velocity v_F, $E(k) - \mu \approx \hbar v_F(k - k_F)$. We can see that $u(k)$ is a Gaussian with width $\sqrt{\Delta_e/\hbar v_F} \approx \sqrt{\Delta_0/\hbar v_F\xi}$, which justifies the substitution $k \to k_F$ earlier.

We would like to point the reader to one last detail before moving on to the general solution. Putting our solution back in to the wavefunction (5.3.15) gives

$$\psi(k,\theta) = \frac{u(k)e^{in\theta}}{\sqrt{k}}\begin{pmatrix}e^{-i\theta}\\-i\end{pmatrix}. \tag{5.3.23}$$

The pseudo-spinor (in the Nambu basis) is an eigenstate of $\mathbf{t}\cdot\mathbf{\Pi}$, where $\mathbf{t}$ is a vector tangent to the FS at (k_F, θ). The pseudo-spin locking to the the momentum gives rise to the π phase around the FS in the Hamiltonian (5.3.17) and (5.3.19).

General solution without rotational symmetry

The solution is similar in spirit to the case with circular symmetry. Now, we label the momentum by energy contours (E, η) instead of (r, θ) and demand constant E contours to be orthogonal to constant η contours. Similar to θ, η is periodic with periodicity of 2π.

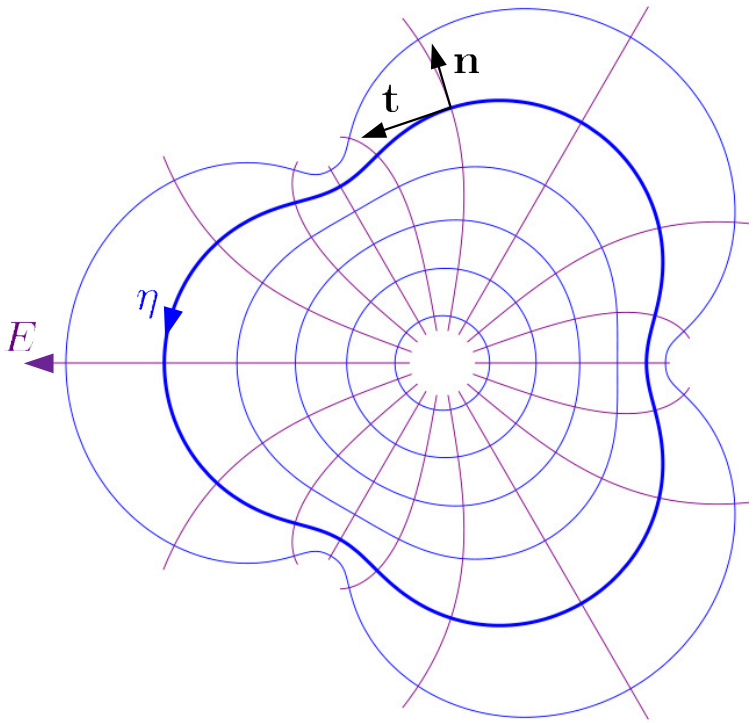

Figure 5.3.2: Parameterization of the reciprocal space with orthogonal coordinates (E, η). The (blue) closed contours are plotted for constant energies E, with the bold contour being the FS at the chemical potential μ. The (purple) open contours are at constant η, running from 0 to 2π. At each point, $\mathbf{t}(E,\eta) = \frac{\partial \boldsymbol{k}}{\partial \eta}$ and $\mathbf{n}(E,\eta) = \frac{\partial \boldsymbol{k}}{\partial E}$ are vectors tangent and normal, respectively, to the energy contours. Notice that, for a closed FS, the direction of the vectors $\mathbf{t}, \mathbf{n}$ rotate once counterclockwise as η is varied around the surface.

The idea of the derivation is as follows. We rewrite the Hamiltonian in a Jackiw-Rebbi form as a function E, perpendicular to the FS. Let $\Gamma^1, \Gamma^2, \Gamma^3$ be matrices which anticommute with each other, and square to the identity matrix. Then the differential equation

$$\Gamma^1(i\Delta_e \partial_E) + i\Gamma^2(E-\mu) + \Gamma^3 f(\eta) \tag{5.3.24}$$

has a bound state when $E-\mu$ changes sign, the bound state is an eigenvector of Γ^3 and has energy $f(\eta)$ [72]. The remaining η degree of freedom governs the existence of zero energy states, by requiring the wavefunction $\psi(E,\eta)$ to be single valued.

Define the vectors tangent and normal to the energy contours $\mathbf{t} = \frac{\partial \boldsymbol{k}}{\partial \eta}$, $\mathbf{n} = \frac{\partial \boldsymbol{k}}{\partial E}$. Clearly, $\mathbf{t} \perp \mathbf{n}$. (Figure 5.3.1). The derivatives and connections in (E, η) coordinates are related to those in the Cartesian coordinates:

$$\begin{pmatrix} \partial_E \\ \partial_\eta \end{pmatrix} = \begin{bmatrix} n^x & n^y \\ t^x & t^y \end{bmatrix} \begin{pmatrix} \partial_{k_x} \\ \partial_{k_y} \end{pmatrix}, \tag{5.3.25}$$

and we define the 2×2 matrix to be J^{-1}.

$$\begin{pmatrix} \partial_{k_x} \\ \partial_{k_y} \end{pmatrix} = J \begin{pmatrix} \partial_E \\ \partial_\eta \end{pmatrix}, \quad \begin{pmatrix} A_x \\ A_y \end{pmatrix} = J \begin{pmatrix} A_E \\ A_\eta \end{pmatrix},$$

where J is the Jacobian matrix:

$$J = \frac{\partial(E,\eta)}{\partial(k_x,k_y)} = \begin{bmatrix} J_x^E & J_x^\eta \\ J_y^E & J_y^\eta \end{bmatrix}. \tag{5.3.26}$$

From $J^{-1}J = 1$, we can see that $\mathbf{J}^E \cdot \mathbf{t} = 0$, $\mathbf{J}^\eta \cdot \mathbf{n} = 0$, hence $\mathbf{J}^E \parallel \mathbf{n}$, $\mathbf{J}^\eta \parallel \mathbf{t}$.

First we rewrite the pairing term in terms of E and η. $i(\partial_{k_x} - i\partial_{k_y}) + A_x - iA_y = d_E + d_\eta$, where

$$d_E = i(J_x^E - iJ_y^E)(\partial_E - iA_E), \tag{5.3.27a}$$
$$d_\eta = i(J_x^\eta - iJ_y^\eta)(\partial_\eta - iA_\eta). \tag{5.3.27b}$$

It is always possible to find a gauge transformation which eliminates A_E near the FS. The transformation is of the form $U_A^\dagger = \mathcal{P}\exp\left[i\int_0^E A_E(E')dE'\right]$, where $\mathcal{P}$ is the path-ordering operator. Since $\partial_E U_A^\dagger = iA_E U_A^\dagger$,

$$U_A(\partial_E - iA_E)U_A^\dagger = \partial_E \tag{5.3.28}$$

This transformation will alter A_η, since the derivative ∂_η acts on $U_A^\dagger$. In general, it impossible to make both A_E and A_η disappear.

We make the substitution $J_x^E - iJ_y^E = |\mathbf{J}^E|e^{-i\theta_\mathbf{n}}$, where $\theta_\mathbf{n}$ gives the direction of the normal vector $\mathbf{n}$. As $\mathbf{t}$ is perpendicular to $\mathbf{n}$, $J_x^\eta - iJ_y^\eta = -i|\mathbf{J}^\eta|e^{-i\theta_\mathbf{n}}$, (5.3.27) becomes

$$d_E = ie^{-i\theta_\mathbf{n}}|\mathbf{J}^E|\partial_E, \tag{5.3.29a}$$
$$d_\eta = e^{-i\theta_\mathbf{n}}|\mathbf{J}^\eta|(\partial_\eta - iA_\eta). \tag{5.3.29b}$$

At the moment, our Hamiltonian (5.3.12) is of the form:

$$\tilde{\mathcal{H}} = \begin{bmatrix} E-\mu & \Delta_e e^{-i\theta_\mathbf{n}}\left(i|\mathbf{J}^E|\partial_E + |\mathbf{J}^\eta|(\partial_\eta - iA_\eta)\right) \\ \Delta_e e^{i\theta_\mathbf{n}}\left(i|\mathbf{J}^E|\partial_E - |\mathbf{J}^\eta|(\partial_\eta - iA_\eta)\right) & -E+\mu \end{bmatrix}. \tag{5.3.30}$$

The angle $\theta_\mathbf{n}$ rotates by $+2\pi$ around a closed FS as η varies from 0 to 2π. The $e^{i\theta_\mathbf{n}}$ phase in the off diagonal terms of the Hamiltonian give rise to a π phase in the eigenstates. We transform this phase away via the unitary transformation:

$$U_{ph} = \begin{bmatrix} e^{i\theta_\mathbf{n}} & \\ & 1 \end{bmatrix}, \tag{5.3.31}$$

such that

$$U_{ph}\,\tilde{\mathcal{H}}\,U_{ph}^\dagger = \begin{bmatrix} E-\mu & \Delta_e D^- \\ \Delta_e D^+ & \mu - E \end{bmatrix}. \tag{5.3.32}$$

where

$$D^- = i|\mathbf{J}^E|\partial_E - i|\mathbf{J}^\eta|(i\partial_\eta + A_\eta) \tag{5.3.33a}$$
$$D^+ = i|\mathbf{J}^E|\partial_E + i|\mathbf{J}^\eta|(i\partial_\eta + A_\eta) + i|\mathbf{J}^\eta|\frac{\partial\theta_\mathbf{n}}{\partial\eta} \tag{5.3.33b}$$

We have ignored the term $\partial_E \theta_{\mathbf{n}}$ from the assumption that the FS is smooth (no cusps). The term $\partial_\eta \theta_{\mathbf{n}}$ is extremely important as it will give us the π Berry phase shift.

At any fixed value of η, we write the Hamiltonian in the form of (5.3.24):

$$U_{ph}\tilde{\mathcal{H}}U_{ph}^\dagger = (E-\mu)\tau_z + \Delta_e D^x \tau_x + \Delta_e D^y \tau_y, \tag{5.3.34}$$

where D^x and D^y are the symmetric and the antisymmetric parts of off the diagonal elements $D^\pm$.

$$D^x = \frac{D^+ + D^-}{2} = i|\mathbf{J}^E|\partial_E + i\frac{|\mathbf{J}^\eta|}{2}\frac{\partial\theta_{\mathbf{n}}}{\partial\eta}, \tag{5.3.35a}$$

$$D^y = \frac{D^+ - D^-}{2i} = |\mathbf{J}^\eta|\left(i\partial_\eta + A_\eta + \frac{1}{2}\frac{\partial\theta_{\mathbf{n}}}{\partial\eta}\right). \tag{5.3.35b}$$

In the first expression (5.3.35a), there is an extra term $\frac{i|\mathbf{J}^\eta|}{2}\frac{\partial\theta_{\mathbf{n}}}{\partial\eta}$, which we can absorb in to the energy derivative via the transformation

$$\exp\left[\int g_\eta\, dE\right]\,\partial_E\,\exp\left[-\int g_\eta\, dE\right] = \partial_E - g_\eta \tag{5.3.36}$$

where $g_\eta(E) = \frac{|\mathbf{J}^\eta|}{2|\mathbf{J}^E|}\frac{\partial\theta_{\mathbf{n}}}{\partial\eta}$. This introduces a term $\partial_\eta g_\eta$ in D^y, but is irrelevant as g_η is single-valued. (In the case with rotational symmetry, the term $\exp\int g_\eta$ is $k^{1/2}$ in (5.3.16).)

The (E dependent portion of the) solution to Jackiw-Rebbi Hamiltonian (5.3.34) is:

$$\psi(E,\eta) \sim u(\eta)\exp\left[-\int\frac{E-\mu}{\Delta_e|\mathbf{J}^E|}dE\right]\begin{pmatrix}1\\-i\end{pmatrix}, \tag{5.3.37}$$

by treating D^y as a constant (independent of E) on the energy scale of $\sqrt{\Delta_e|\mathbf{J}^E|}$. The effective Hamiltonian is $\mathcal{H}_\eta = -\Delta_e D^y$.

Finally, we solve for $D^y(\eta)u(\eta) = 0$ for a Majorana vortex bound state, subject to the constraint that $u(\eta)$ is single-valued. We can solve for $u(\eta)$ explicitly:

$$u(\eta) = \mathcal{P}\exp\left[i\int_0^\eta d\eta'\left(A_\eta(\eta') + \frac{1}{2}\frac{\partial\theta_{\mathbf{n}}}{\partial\eta}\right)\right]u(0). \tag{5.3.38}$$

Since $\theta_{\mathbf{n}}$ winds by 2π around a *closed* FS, $\oint\frac{1}{2}\partial_\eta\theta_{\mathbf{n}} = \pi$ gives an overall phase of-1. We have $u(2\pi) = -U_B u(0)$, where the Berry phase of the FS is

$$U_B = \mathcal{P}\exp\left[i\oint_0^{2\pi} A_\eta d\eta\right]. \tag{5.3.39}$$

Hence a solution exists for every -1 eigenvalue of U_B.

Vortex bound states

We can solve for the spectrum Caroli-de Gennes-Matricon bound states [19]. For an arbitrary energy $\mathcal{E}$, the 'angular' portion of the wavefunction satisfies $-\Delta_e D^y u(\eta) = \mathcal{E}u(\eta)$, equivalent to:

$$-i\partial_\eta u(\eta) = \left(\frac{\mathcal{E}}{\Delta_e|\mathbf{J}^\eta|} + A_\eta + \frac{1}{2}\frac{\partial\theta_{\mathbf{n}}}{\partial\eta}\right)_{E=\mu} u(\eta). \tag{5.3.40}$$

Note that $|\mathbf{J}^\eta|^{-1} = |\mathbf{t}|$. The solution for $u(\eta)$ is a the path-ordered exponential

$$u(\eta) = \mathcal{P} \exp\left[i \int_0^\eta \left(\frac{\mathcal{E}|\mathbf{t}|}{\Delta_e} + A_\eta + \frac{1}{2}\frac{\partial \theta_\mathbf{n}}{\partial \eta} \right)_{E=\mu} d\eta' \right] u(0). \tag{5.3.41}$$

The full solution to the Hamiltonian (5.3.30) is:

$$\psi(E,\eta) \;\propto\; u(\eta) \exp\left[- \int^E \left(\frac{E'-\mu}{\Delta_e |\mathbf{J}^E(E')|} + g_\eta(E') \right) dE' \right] \begin{pmatrix} e^{-i\theta_\mathbf{n}} \\ -i \end{pmatrix}. \tag{5.3.42}$$

While A_η is a hermitian matrix, $\mathcal{E}|\mathbf{t}|/\Delta_e$ and $\partial_\eta \theta_\mathbf{n}$ are simply numbers, hence the integral may be evaluated separately for each term. The integral $\oint_0^{2\pi} |\mathbf{t}| d\eta$ is simply the perimeter of the FS l_F. The integral $\frac{1}{2}\oint_0^{2\pi} \partial_\eta \theta_\mathbf{n} d\eta$ is π for a closed FS, and 0 for an open FS (modulo 2π). The single-valued requirement $u(2\pi) = u(0)$ (for a closed FS) becomes:

$$u(0) = -\exp\left(i \frac{l_F}{\Delta_e} \mathcal{E} \right) U_B u(0). \tag{5.3.43}$$

From this, we can calculate the allowed energies for an arbitrary Berry phase:

$$\mathcal{E}_n = \frac{\Delta_e}{l_F}(2\pi n + \pi - \phi), \tag{5.3.44}$$

for integers n, where $e^{i\phi}$ are the eigenvalues of U_B. Note that the eigenvalues always come in pairs $\pm\phi$ due to the particle-hole symmetry of the system (considering both k_z and $-k_z$ slices of the BZ).

5.4 Candidate materials

We now apply the Berry phase criterion to some candidate materials to see which of them can have protected MZMs at the ends of vortices.

5.4.1 $Cu_xBi_2Se_3$

The insulating phase of Bi_2Se_3 is a strong TI with a single band inversion occurring at the Γ point. On Cu doping, Bi_2Se_3 becomes n-type with an electron pocket at Γ and is reported to superconduct below $T_c = 3.8\,\mathrm{K}$ [65, 64]. Photoemission measurements show $\mu \approx 0.25\,\mathrm{eV}$ above the conduction band minimum at optimal doping [143]. We calculate the Berry phase eigenvalues for a FS around the Γ point numerically as a function of μ, which evaluates to $\pm\pi$ at $\mu_c \approx 0.24\,\mathrm{eV}$ above the conduction band minimum for a vortex along the c-axis of the crystal (see below). Hence $\mu \gtrsim \mu_c$ indicates c-axis vortices are near the topological transition. However, tilting the vortex away from the c-axis is found to raise μ_c to upto $\mu_c = 0.30eV$, for a vortex perpendicular to the c-axis. Therefore, sufficiently tilted vortices should host MZMs at the experimental doping level.

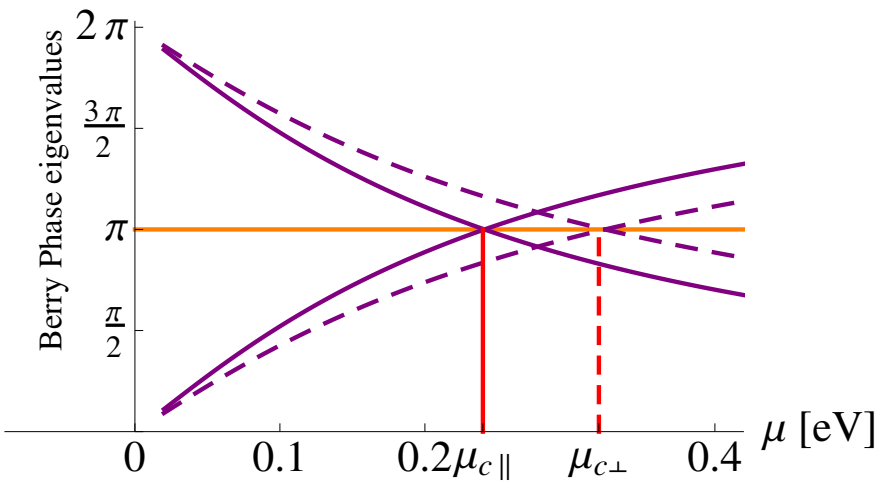

Figure 5.4.1: Berry phase eigenvalues ϕ_B for Bi_2Se_3 as a function of μ relative to the bottom of the conduction band for a Fermi surface relevant to a vortex along the c-axis (solid curves) and perpendicular to the c-axis at an angle of $\pi/6$ to the binary axis (dashed curves) of Bi_2Se_3. The eigenvalues appear in $\pm$ pairs and are only defined modulo 2π. The phases ϕ_B are zero (modulo 2π) at both the conduction band minimum and at energies far above the conduction band. Clearly, the $\phi_B = \pi$ at $\mu_{c||} = 0.24\,\text{eV}$ and $\mu_{c\perp} = 0.24\,\text{eV}$, signaling a VPT. Photoemission measurements show $\mu \approx 0.25\,\text{eV} \sim \mu_c$ above the conduction band minimum at optimal doping [143], and hence Cu doped Bi_2Se_3 is predicted to be near the vortex phase transition for a c-axis vortex, and to have end MZMs for vortices sufficiently tilted off the c-axis

Numerical calculation of the Berry phase for Bi_2Se_3

The insulating phase of Bi_2Se_3 is a strong TI, with a band inversion occurring at the Γ point in its rhombohedral Brillouin zone. $Cu_xBi_2Se_3$ is reported to superconduct below $T_c = 3.8\,\text{K}$ [65, 64]. Before the superconducting transition, the carrier (electron) density is approximately $2 \times 10^{20}\,\text{cm}^{-3}$ from Hall measurements [64]. Using the effective eight-band model from [88], we estimate μ theoretically in this material from the carrier density to be $\approx 0.4\,\text{eV}$ relative to the conduction band bottom. However, photoemission measurements show $\mu \approx 0.25\,\text{eV}$ above the bottom of the conduction band at the optimal doping ($x = 0.12$) [143].

The conduction band minimum is at the Γ-point. For small carrier densities, we expect the FS to be centered around Γ. Using the same model from [88], we determine μ_c for this material by calculating the Berry phase eigenvalues for a FS around the Γ point numerically as a function of μ for various vortex orientations. In Figure 5.4.1, we show the results for a vortex parallel to the c-axis (solid line) and for a vortex perpendicular it making an angle of $\pi/6$ with the binary axis (dashed line).

This calculation is done by discretizing the FS contour and making the pair of Bloch functions continuous and the Berry connection vanish at all but one points on this contour. More precisely, we parameterize the FS via $\eta \in [0, 2\pi]$ and compute the eigenstates $|\varphi^\nu(\eta)\rangle$ for $\nu = 1, 2$. The phase is chosen such that $A_\eta^{\mu\nu} = i\langle\varphi^\mu(\eta)|\partial_\eta|\varphi^\nu(\eta)\rangle = 0$ for $0 < \eta < 2\pi$ along the FS.

In general, the Bloch functions will not be single-valued, *i.e.* $|\varphi^\nu(2\pi)\rangle \neq |\varphi^\nu(0)\rangle$. The unitary transformation required to rectify the discontinuity at this one point is precisely the non-Abelian phase: $|\varphi^\mu(0)\rangle = [U_B]^{\mu\nu}|\varphi^\nu(2\pi)\rangle$. Because of time-reversal symmetry in the normal phase of Bi_2Se_3, the Berry phase $U_B \in SU(2)$ has eigenvalues $e^{\pm i\phi}$ which come in complex conjugate pairs. Figure 5.4.1 shows the variation of the Berry phase eigenvalues ϕ as a function of μ for two different FSs of Bi_2Se_3 in the $k_z = 0$ plane, where the z-axis is along the vortex. Here, μ is measured relative to the bottom of the conduction band at the Γ point, which is where the band inversion occurs. When $\hat{z}$ is along the c-axis, $\mu_c \approx 0.24\,\text{eV}$, which happens to be close to the chemical potential for these doped materials according to ARPES [143]. Thus, we expect these vortices to be close to the phase transition. Note that the model does not taken into account the renormalization of the Bi_2 Se_3 bands due Cu doping. On the other hand, $\mu_c \approx 0.30\,\text{eV}$ for a vortex perpendicular to the c-axis. Such a vortex should have end MZMs.

5.4.2 $TlBiTe_2$, Bi_2Te_3 under pressure and $Pd_xBi_2Te_3$

The bands of $TlBiTe_2$ and Bi_2Te_3 are topologically non-trivial because of a band inversion at the Γ point [147, 85, 29, 23, 22, 153]. The topological character of Bi_2Te_3 is believed to be preserved under a pressure of up to 6.3 GPa, at which it undergoes a structural phase transition. On p-doping to a density of $6 \times 10^{20}\,\text{cm}^{-3}$ (3-6 $\times 10^{18}\,\text{cm}^{-3}$), $TlBiTe_2$ (Bi_2Te_3 under 3.1 GPa) becomes a SC below $T_c = 0.14\,\text{K}$ ($\sim 3\,\text{K}$) [59, 154], making it a natural system to search for the possibility of MZMs. Similarly, n-doping Bi_2Te_3 to a concentration of $9 \times 10^{18}\,\text{cm}^{-3}$ by adding Pd reportedly results in $T_c = 5.5\,\text{K}$ [64] in a small sample fraction. The superconductivity in Bi_2Te_3 under pressure, and in $TlBiTe_2$ ($Pd_xBi_2Te_3$) is believed to arise from six symmetry related hole (electron) pockets around the Γ-T line. This is an even number so vortex lines in superconducting $TlBiTe_2$ and both p- and n-type Bi_2Te_3 should have MZMs at their ends in all orientations.

5.4.3 MZMs from trivial insulators

The bulk criterion derived does not require a 'parent' topological band structure. As a thought example, say we have four TRIMs with Hamiltonians like the continuum Hamiltonian $\mathcal{H}_{\boldsymbol{k}}$ in their vicinity. Such band inversions at four TRIMs in a plane leads to a trivial insulator [35]. However, if their critical chemical potentials μ_c differ, then there could be a range of μ where there are an *odd* number of VPTs below and above μ, leading to topologically non-trivial vortices. Interestingly PbTe and SnTe are both trivial insulators with band inversions relative to each other at the four equivalent L points. They both exhibit superconductivity on doping below $T_c = 1.5\,\text{K}$ [94] and 0.2 K [57] respectively. A combination of strain (to break the equivalence of the four L points) and doping could potentially create the scenario described above in one of these systems. GeTe is similar to SnTe with $T_c \sim 0.3\,\text{K}$ [58] but undergoes a spontaneous rhombohedral distortion resulting in the desired symmetry. Thus, $\mathcal{I}$- and $\mathcal{T}$-symmetric systems with strong spin orbit can lead to SCs with vortex end MZMs, even in the absence of a proximate topological phase. Investigating the Fermi surface SU(2) Berry phases, and thus the vortex electronic structure, in this wide class of systems is a promising future direction in the hunt for Majorana fermions.

In closing, we note that the VPT could potentially be probed via thermal transport along the vortex line. A hurdle is the small minigap scale ($\Delta/k_F\xi \sim \Delta^2/E_F$), and the long confinement length of the MZMs to the surface, which may be ameliorated by considering strong coupling SCs or materials such as heavy fermions where E_F is reduced.

P.H. would like to thank Pouyan Ghaemi, Roger Mong and Ashvin Vishwanath for this collaboration. We thank A. M. Turner, J. H. Bardarson, A. Wray and C. L. Kane for insightful discussions, and NSF-DMR 0645691 for funding. In parallel work, L. Fu, J. C. Y. Teo and C. L. Kane have arrived at similar conclusions. This work in published in *Physical Review Letters*, **107**, 097001 (2011).

Chapter 6

Circular photogalvanic effect on topological insulator surface states: Berry curvature dependent response

6.1 Introduction

In the previous chapters, the focus has largely been on bulk topological phases and especially on the bulk of the topological insulator. Although the Majorana zero mode discussed in the previous chapter was localized on the surface, its existence was governed by the bulk topological phase. In contrast, in this chapter we focus only on the surface states (SSs) of the strong topological insulator (TI). In their simplest incarnation, the SSs of TIs correspond to the dispersion of a single Dirac particle, which cannot be realized in a purely two dimensional band structure with time reversal invariance. This dispersion is endowed with the property of spin-momentum locking, i.e., for each momentum there is a unique spin direction of the electron. Since several materials were theoretically predicted to be in this phase, most of the experimental focus on TIs so far has been towards trying to directly observe these exotic SSs in real or momentum space, in tunneling [116] and photoemission [22, 68, 144, 87, 118] experiments, respectively, and establish their special topological nature. However, there has so far been a dearth of experiments which study the response of these materials to external perturbations, such as an external electromagnetic field.

In order to fill this gap, we calculate here the response of TI surfaces to circularly polarized (CP) light. Since photons in CP light have a well-defined angular momentum, CP light can couple to the spin of the surface electrons. Then, because of the spin-momentum-locking feature of the SSs, this coupling can result in dc transport which is sensitive to the helicity (right- vs left-circular polarization) of the incident light. This phenomenon is known as the circular photogalvanic effect (CPGE). In this work, we derive general expressions for the direct current on a TI surface as a result of the CPGE at normal incidence within a two-band model and estimate its size for the (111) surface of Bi_2Se_3, an established TI, and find it to be well within measurable limits. Since bulk Bi_2Se_3 has inversion symmetry and the CPGE, which is a second-order non-linear effect, is forbidden for inversion symmetric systems, this current can only come from the surface.

We find, remarkably, that the dominant contribution to the current is controlled by the *Berry curvature* of the electron bands and *grows linearly with time*. In practice this growth is cut-off by a scattering event which resets the current to zero. At the microscopic level, this part of the current involves the absorption of a photon to promote an electron from the valence to the conduction band. The total current contains two other terms - both time-independent - one again involving an interband transition and the other resulting from intraband dynamics of electrons. However, for clean samples at low temperatures, the scattering or relaxation time is expected to be large, and these contributions will be eclipsed by the linear-in-time one. Hence, this experiment can also be used to measure the relaxation time for TI SSs.

Historically, the Berry curvature has been associated with fascinating phenomena such as the anomalous Hall effect [52] and the integer quantum Hall effect [130] and therefore, it is exciting that it appears in the response here. Its main implication here is that is gives us a simple rule, in addition to the requirement of the right symmetries, for identifying the perturbations that can give a linear-in-time CPGE at normal incidence: we look for perturbations that result in a non-zero Berry curvature. Put another way, we can identify perturbations that have the right symmetries but still do not give this current because the Berry curvature vanishes for these perturbations. Importantly, for TI SSs, the requirement of a non-zero Berry curvature amounts to the simple physical condition that the spin-direction of the electrons have all three components non-zero. In other words, if the electron spin in the SSs is completely in-plane, the Berry curvature is zero and no linear-in-time CPGE is expected. The spins must somehow be tipped slightly out of the plane, as shown in Figure 6.1.1a, in order to get such a response. Thus, a pure Dirac (linear) dispersion, for which the spins are planar, cannot give this response; deviations from linearity, such as the hexagonal warping on the (111) surface of Bi_2Te_3 [32], are essential for tilting the spins out of the plane.

CPGE has been observed in the past in GaAs [40], SiGe [41] and HgTe/CdHgTe [142] quantum wells - all systems with strong spin-orbit coupling. The effect in these systems can be understood within a four-band model consisting of two spin-orbit split valence bands and two spin-degenerate conduction bands. In contrast, TI SSs can be faithfully treated within a two-band model. The simplicity of the latter system makes it more convenient for studying theoretically compared to semiconductor quantum wells, and hence, enables us to determine a connection between the CPGE and the Berry curvature. In general, if a surface has no rotational symmetry about the surface normal, such a photocurrent is allowed.

Finally, we estimate the current on the (111) surface of Bi_2Se_3 using an effective model for the SSs [32, 88]. This model captures the deviations from linearity of the SS dispersion due to the threefold rotational symmetry of the (111) surface of Bi_2Se_3. These deviations have been observed in photoemission experiments on Bi_2Te_3 [22]. Similar deviations are expected for Bi_2Se_3 [88], though they cannot be seen in the slightly smaller momentum range compared to Bi_2Te_3 over which data is currently available [69]. In order to get a direct current with CP light at normal incidence, rotational symmetry about the surface normal needs to be broken. Based on the requirement of non-zero Berry curvature, we propose to do this in two ways:

1. by applying an in-plane magnetic field and including deviations from linearity of the dispersion

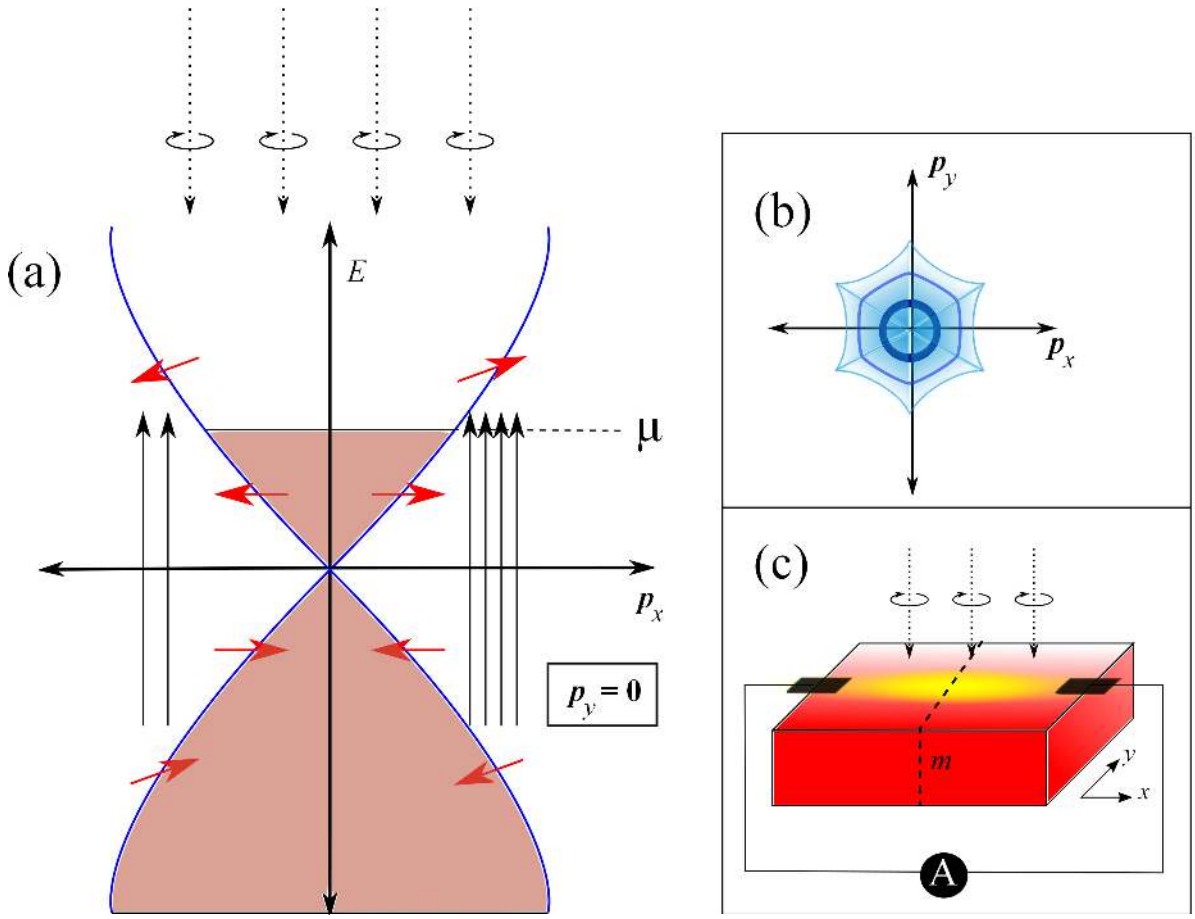

Figure 6.1.1: (a) Schematic illustration of preferential absorption at one out of two points related by the reflection symmetry about the yz-plane. The short arrows denote the spin direction of electrons in various states. At low energies, the spins are completely in-plane. They acquire a small out-of-plane component at higher energies. The dotted lines represent incoming photons of helicity -1 (left-CP photons). These photons can only *raise* the $\langle S_z \rangle$ of an electron, and thus are preferentially absorbed by electrons whose $\langle S_z \rangle < 0$ in the valence band. The chemical potential μ must be between the initial and final states for any absorption to occur. (b) Constant energy contours for the surface conduction band of Bi_2Se_3. Dark lines denote lower energy. (a) is drawn at $p_y = 0$. (c) Geometry of the experiment. Light is incident normally on (111) surface of Bi_2Se_3. The dotted lines represent the mirror plane m about which the lattice has a reflection symmetry. The current $j_{a2}(t)$ (see text) is along $\hat{x}$.

2. by applying a strain.

With a magnetic field of $10T$ (With a 1% strain) and assuming a scattering time of $10ps$, (the scattering time in GaAs is $\sim 1ns$ over a wide range of temperatures [100]; we use a conservative estimate for Bi_2Se_3 here) we find that a current density of $\sim 100nA/mm$ ($\sim 10nA/mm$) can be obtained due to the CPGE with a 1 Watt laser. This value can be easily measured by current experimental techniques. Conversely, the scattering time, crucial for transport processes, for Bi_2Se_3 SSs can be determined by measuring the current. In comparison, circular photogalvanic currents of a few nanoamperes per Watt of laser power have been measured in quantum wells of the semiconductors GaAs [40], SiGe [41] and HgTe/CdHgTe [142].

A connection between the optical response of a system and the Berry curvature of its bands has been previously noted at the low frequencies, where a semiclassical mechanism involving the anomalous velocity of electrons in a single band explains it [26, 89]. Here, we show it for inter band transitions where no quasiclassical approximation is applicable. Instead, we calculate the quadratic response function directly. A connection is still present which points to a deeper relation between the response functions and the Berry curvature.

This chapter is organized as follows. In Sec. 6.2, we state the symmetry conditions under which a CPGE may occur. We present our results, both general as well as for Bi_2Se_3 in particular, in Sec. 6.3.1 and describe the microscopic mechanism in Sec. 6.3.2. The calculation is described briefly in Sec. 6.3.3 and in detail in Sec. 6.3.4. In Sec. 6.4, we give our results for the optical injection of dc spin and in Sec. 6.5 we briefly discuss the situation where the rotational symmetry of the surface is broken by shining the light off-normally.

6.2 Symmetry considerations for the CPGE

In this section, we specify the symmetry conditions under which one can get a CPGE on the surface of a TI. But first, let us briefly review the concept of the CPGE in general.

The dominant dc response of matter to an oscillating electric field is, in general, quadratic in the electric field. When the response of interest is a current, the effect is known as the photogalvanic effect. This current can be written as

$$j_\alpha = \eta_{\alpha\beta\gamma}\mathcal{E}_\beta(\omega)\mathcal{E}_\gamma(-\omega) \tag{6.2.1}$$

where $\mathcal{E}_\alpha(t) = \mathcal{E}_\alpha(\omega)e^{i\omega t} + \mathcal{E}^*_\alpha(\omega)e^{-i\omega t}$ is the incident electric field, $\mathcal{E}^*_\alpha(\omega) = \mathcal{E}_\alpha(-\omega)$ and $\eta_{\alpha\beta\gamma}$ is a third rank tensor, which has non-zero components only for systems that break inversion symmetry, such as the surface of a crystal.

For j_α to be real, one has $\eta_{\alpha\beta\gamma} = \eta^*_{\alpha\gamma\beta}$. Thus, the real (imaginary) part of $\eta_{\alpha\beta\gamma}$ is symmetric (anti-symmetric) under interchange of β and γ, and therefore describes a current that is even (odd) under the transformation $\omega \to -\omega$. Consequently, j_α can be conveniently separated according to

$$j_\alpha = \mathtt{S}_{\alpha\beta\gamma}\left(\frac{\mathcal{E}_\beta(\omega)\mathcal{E}^*_\gamma(\omega) + \mathcal{E}^*_\beta(\omega)\mathcal{E}_\gamma(\omega)}{2}\right) + i\mathtt{A}_{\alpha\mu}(\boldsymbol{\mathcal{E}} \times \boldsymbol{\mathcal{E}}^*)_\mu \tag{6.2.2}$$

where $\mathtt{S}_{\alpha\beta\gamma}$ is the symmetric part of $\eta_{\alpha\beta\gamma}$ and $\mathtt{A}_{\alpha\mu}$ is a second-rank pseudo-tensor composed of the anti-symmetric part of $\eta_{\alpha\beta\gamma}$. For CP light, $\boldsymbol{\mathcal{E}} \propto \hat{x} \pm i\hat{y}$ if $\hat{z}$ is the propagation direction

and only the second term in (6.2.2) survives, and hence represents the CPGE. This effect is odd in ω. On the other hand, the first term, which is even in ω, represents the linear photogalvanic effect as it is the only contribution for linearly polarized light. Since the transformation $\omega \to -\omega$, or equivalently, $\boldsymbol{\mathcal{E}} \to \boldsymbol{\mathcal{E}}^*$ reverses the helicity of CP light, i.e., changes right-CP light to left-CP light and vice versa, the CPGE is the helicity-dependent part of the photogalvanic effect.

The helicity of CP light is odd (i.e., right- and left-CP light get interchanged) under mirror reflection about a plane that contains the incident beam, but invariant under arbitrary rotation about the direction of propagation. Let us consider normal incidence of CP light on a TI surface normal to the z axis. Let us further assume that there is a mirror plane which is the y-z plane (See Figure 6.1.1c). Then, the only component of direct current that reverses direction on switching the helicity is a current along the x axis. If there is also rotation symmetry R_z about the z-axis (such as the threefold rotation symmetry on the (111) surface of Bi_2Se_3), then no surface helicity-dependent direct photocurrent is permitted. One needs to break this rotation symmetry completely by applying, for example, and in-plane magnetic field, strain etc., to obtain a nonvanishing current.

6.3 Helicity-dependent direct photocurrent

We now present our main results for the photocurrent and estimate it for Bi_2Se_3. After painting a simple microscopic picture for the mechanism, we give a brief outline of the full quantum mechanical treatment of the phenomenon.

6.3.1 Results

A general two-band Hamiltonian (in the absence of the incident light) can be written as

$$\mathbb{H} = \sum_{\mathbf{p}} c^\dagger_{\mathbf{p}} H_{\mathbf{p}} c_{\mathbf{p}} = \sum_{\mathbf{p}} |E_{\mathbf{p}}| c^\dagger_{\mathbf{p}} \hat{\mathbf{n}}(\mathbf{p}).\boldsymbol{\sigma} c_{\mathbf{p}} \tag{6.3.1}$$

upto a term proportional to the identity matrix, which is not important for our main result which involves only inter-band transitions. Here $\hat{\mathbf{n}}(\mathbf{p})$ is a unit vector, $\boldsymbol{\sigma}$ are the spin-Pauli matrices and $c_{\mathbf{p}} = (c_{\mathbf{p}\uparrow}, c_{\mathbf{p}\downarrow})^T$ is the electron annihilation operator spinor at momentum $\mathbf{p}$. Clearly, this can capture a Dirac dispersion, e.g.. with $E(\mathbf{p}) = \pm v_F p$ and $\hat{n}(\mathbf{p}) = v_F \hat{\mathbf{z}} \times \mathbf{p}$. It can also capture the SSs of Bi_2Se_3 in the vicinity of the Dirac point, which includes deviations beyond the Dirac limit. We also assume the Hamiltonian has a reflection symmetry m about y-axis, where $\hat{\mathbf{z}}$ is the surface normal. Using the zero temperature quadratic response theory described in Sec 6.3.3, we calculate the current due to the CPGE and find that

$$\vec{j}_{CPGE}(t) = (j_{na} + j_{a1} + j_{a2}(t))\, \hat{\mathbf{x}} \tag{6.3.2}$$

where the subscripts a (na) stand for "absorptive" and "non-absorptive", respectively. The absorptive part of the response involves a zero momentum interband transition between a pair of levels separated by energy $\hbar\omega$. These terms are only non zero when there is one occupied and one empty level. In this part of the response, we find a term that is time-dependent, $j_{a2}(t)$. In particular, this term grows linearly with the time over which the electromagnetic

perturbation is present, which is allowed for a dc response. In reality, this linear growth is cut off by a decay process which equilibrates populations, and is characterized by a time constant τ. In clean samples at sufficiently low temperatures, characterized by large τ, this contribution is expected to dominate the response, and hence, is the focus of our work. The other contributions are discussed in Sec. 6.3.4. Conversely, because of the linear growth with time, one can determine the lifetime of the excited states by measuring the photocurrent. This term is

$$j_{a2}(t) = -\frac{\pi e^3 \hbar \mathcal{E}_0^2 t \mathrm{sgn}(\omega)}{4} \sum_{\mathbf{p}} \delta(\hbar|\omega| - 2|E_{\mathbf{p}}|) v_x(\mathbf{p}) \mathcal{F}(\mathbf{p}) \tag{6.3.3}$$

where we have assumed that the chemical potential is in between the two energy levels $\pm|E_{\mathbf{p}}|$ connected by the optical frequency $\hbar\omega$, and that temperature can be neglected compared to this energy scale. Here, $v_x(\mathbf{p}) = \frac{\partial|E_{\mathbf{p}}|}{\partial p_x}$ is the conventional velocity and $\mathcal{F}(\mathbf{p}) = i\sum_{\mathbf{p}}\langle\partial_{p_x}u(\mathbf{p})|\partial_{p_y}u(\mathbf{p})\rangle + c.c.$, where $|u(\mathbf{p})\rangle$ is the conduction band Bloch state at momentum $\mathbf{p}$, is the *Berry curvature* of the conduction band at momentum $\mathbf{p}$. For the class of Hamiltonians (6.3.1) that we are concerned with, the Berry curvature (as shown at the end of this subsection) is given by:

$$\mathcal{F}(\mathbf{p}) = \hat{\mathbf{n}}.\left(\frac{\partial\hat{\mathbf{n}}}{\partial p_x} \times \frac{\partial\hat{\mathbf{n}}}{\partial p_y}\right) \tag{6.3.4}$$

which is the skyrmion density of the unit vector $\hat{\mathbf{n}}$ in momentum space. Since $\partial_{p_i}\hat{\mathbf{n}} \perp \hat{\mathbf{n}}$ for $i = x, y$, $\mathcal{F}(\mathbf{p}) \neq 0$ only if all three components of $\hat{\mathbf{n}}$ are nonvanishing. For linearly dispersing bands, $\hat{\mathbf{n}}$ has only two non-zero components (e.g.. $H_{\mathbf{p}} = p_y\sigma_x - p_x\sigma_y$, $\hat{\mathbf{n}} \propto (p_y, -p_x, 0)$). Hence, corrections beyond the pure Dirac dispersion are essential. Also, due to m, the Berry curvature satisfies $\mathcal{F}(p_x, p_y) = -\mathcal{F}(-p_x, p_y)$. Since in (6.3.3) we have the x-velocity multiplying the Berry curvature, which also transforms the same way, a finite contribution is obtained on doing the momentum sum.

We now calculate $j_{a2}(t)$ for the threefold-symmetric (111) surface of Bi_2Se_3 starting from the effective Hamiltonian [32, 88]

$$H = v_F(p_x\sigma_y - p_y\sigma_x) + \frac{\lambda}{2}\left(p_+^3 + p_-^3\right)\sigma_z \tag{6.3.5}$$

where $v_F \sim 5 \times 10^5 m/s$ [152] and $\lambda = 50.1 eV{\cdot}\text{Å}^3$ [88]. A spin independent quadratic term has been dropped since it does not modify the answers for interband transitions, which only involve the energy difference between the bands.

To get a non-zero j_{CPGE}, the threefold rotational symmetry must be broken. We propose to do this in two separate ways:

1. **by applying a magnetic field B in the x-direction**
   This field has no orbital effect, and can be treated by adding a Zeeman term

   $$H'_{Zeeman} = -g_x\mu_B B\sigma_x \tag{6.3.6}$$

   , where g_x is the appropriate g-factor and μ_B is the Bohr magneton, to the Hamiltonian (6.3.5). To lowest order in λ and B, we get

   $$j_{a2}(t) = \frac{3e^3 v_F \mathcal{E}_0^2 \lambda (g_x\mu_B B)^2 t}{16\hbar^2\omega}\mathcal{A} \tag{6.3.7}$$

, where $\mathcal{A}$ is the laser spot-size. For $g_x = 0.5$ [88], and assuming the experiment is done in a $10T$ field with a continuous wave laser with $\hbar\omega = 0.1eV$ which is less than the bulk band gap of $0.35eV$ [144], $\mathcal{A} \sim 1mm^2$, a laser power of $1W$, and the spin relaxation time $t \sim 10ps$, we get a current density of $\sim 100nA/mm$, which is easily measurable by current experimental techniques. Note that the expression (6.3.7) for $j_{a2}(t)$ contains the parameter λ which measures the coupling to σ_z in (6.3.5). Since $\vec{B} = B\hat{\mathbf{x}}$ breaks the rotation symmetry of the surface completely, a naive symmetry analysis suggests, wrongly, that deviations from linearity, measured by λ, are not needed to get $j_{a2}(t)$.

2. **by applying a strain along** x
   This can be modeled by adding a term

$$H'_{strain} = \delta\lambda p_x^3 \sigma_z \tag{6.3.8}$$

   to H in (6.3.5). This gives

$$j_{a2}(t) = \frac{3e^3 v_F (\delta\lambda)\mathcal{E}_0^2 \omega t}{2^7}\mathcal{A} \tag{6.3.9}$$

   to lowest order in λ and $\delta\lambda$. For a 1% strain, $\delta\lambda/\lambda = 0.01$, and the same values for the other parameters as in (6.3.7), we get a current density of $\sim 10nA/mm$. (6.3.9) does not contain λ; this is because $\delta\lambda$ alone both breaks the rotation symmetry and tips the spins out of the xy-plane.

Proof of Berry curvature expression

Here we show that the Berry curvature defined for Bloch electrons as

$$\mathcal{F}(\mathbf{p}) = i\left(\langle\partial_{p_x}u|\partial_{p_y}u\rangle - \langle\partial_{p_y}u|\partial_{p_x}u\rangle\right) \tag{6.3.10}$$

can be written as

$$\mathcal{F}(\mathbf{p}) = \hat{\mathbf{n}}.\left(\partial_{p_x}\hat{\mathbf{n}} \times \partial_{p_y}\hat{\mathbf{n}}\right) \tag{6.3.11}$$

for the band with energy $|E_{\mathbf{p}}|$ for Hamiltonians of the form $H_{\mathbf{p}} = |E_{\mathbf{p}}|\hat{\mathbf{n}}(\mathbf{p}).\boldsymbol{\sigma}$.

At momentum $\mathbf{p}$, the Bloch state $|u_{\mathbf{p}}\rangle$ with energy $|E_{\mathbf{p}}|$ is defined as the state whose spin is along $\hat{\mathbf{n}}(\mathbf{p})$. Defining $|\uparrow\rangle$ as the state whose spin is along $+\hat{\mathbf{z}}$, $|u_{\mathbf{p}}\rangle$ is obtained by performing the appropriate rotations,

$$|u_{\mathbf{p}}\rangle = e^{-i\frac{\sigma_z}{2}\phi(\mathbf{p})}e^{i\frac{\sigma_y}{2}\theta(\mathbf{p})}|\uparrow\rangle \tag{6.3.12}$$

where $\theta(\mathbf{p})$ and $\phi(\mathbf{p})$ are the polar angles that define $\hat{\mathbf{n}}(\mathbf{p})$:

$$\hat{\mathbf{n}}(\mathbf{p}) = \sin\theta(\mathbf{p})\cos\phi(\mathbf{p})\hat{x} + \sin\theta(\mathbf{p})\sin\phi(\mathbf{p})\hat{y} + \cos\theta(\mathbf{p})\hat{z} \tag{6.3.13}$$

Substituting (6.3.12) in (6.3.10), one gets

$$\mathcal{F}(\mathbf{p}) = \sin\theta(\mathbf{p})\left(\partial_{p_x}\theta(\mathbf{p})\partial_{p_y}\phi(\mathbf{p}) - \partial_{p_x}\phi(\mathbf{p})\partial_{p_y}\theta(\mathbf{p})\right) \tag{6.3.14}$$

which, on using (6.3.13) and some algebra, reduces to the required expression (6.3.11).

6.3.2 Physical process

The appearance of the Berry curvature suggests a role of the anomalous velocity in generating the current. Such mechanisms have been discussed in the literature in the context of the CPGE [26, 97]. However, those mechanisms only work when the electric field changes slowly compared to the typical scattering time. The SSs of Bi_2Se_3 probably have lifetimes of tens of picoseconds, and thus, we are in the opposite limit when $\hbar\omega = 0.1eV$, which corresponds to a time scale 10^3 times shorter.

In this limit, the dc responses are a result of a preferential absorption of the photon at one of the two momentum points for each pair of points $(\pm p_x, p_y)$ related by m, as shown in Figure 6.1.1a for $p_y = 0$. According to the surface Hamiltonian (6.3.5), the spin vector $\mathbf{S} = \frac{\boldsymbol{\sigma}}{2}\hbar$ gets tipped out of the xy-plane for states that lie beyond the linear dispersion regime, but the direction of the tipping is opposite for (p_x, p_y) and $(-p_x, p_y)$. Thus, photons of helicity -1, which can only *raise* $\langle S_z\rangle$ of an electron, are preferentially absorbed by the electrons that have $\langle S_z\rangle < 0$ in the ground state. The response, then, is determined by the properties of these electrons. Clearly, the process is helicity-dependent as reversing the helicity would cause electrons with $\langle S_z\rangle > 0$ to absorb the light preferentially.

This is consistent with the requirement of a non-zero Berry curvature, which essentially amounts to the spin direction $\hat{\mathbf{n}}$ having to be a three-dimensional vector. In the linear limit, where $H = v_F(p_x\sigma_y - p_y\sigma_x)$, the spin is entirely in-plane, and all the electrons absorb the incident light equally.

6.3.3 Calculation in brief

We now briefly outline the calculation of the helicity-dependent photocurrent. The detailed calculation can be found in Sec. 6.3.4. Readers only interested in our results may wish to skip this section.

The Model: The Hamiltonian and relevant electric field (vector potential) perturbations for getting a direct current to second order in the electric field of the incident photon are

$$\begin{aligned} H &= |E_{\mathbf{p}}|\hat{\mathbf{n}}(p).\boldsymbol{\sigma} && (6.3.15)\\ H' &= j_x A_x(t) + j_y A_y(t) && (6.3.16)\\ j_\alpha &= \frac{\partial H}{\partial p_\alpha} && (6.3.17)\\ A_x(t) + iA_y(t) &= A_0 e^{i(\omega - i\epsilon)t} && (6.3.18)\end{aligned}$$

where $\mathbf{A}$ is the vector potential, $\hat{z}$ is assumed to be the surface normal, and ϵ is a small positive number which ensures slow switch-on of the light.

Quadratic response theory: In general, the current along x to all orders in the perturbation H' is

$$\langle j_x\rangle(t) = \left\langle T^*\left(e^{i\int_{-\infty}^{t} dt' H'(t')}\right) j_x(t) T\left(e^{-i\int_{-\infty}^{t} dt' H'(t')}\right)\right\rangle \qquad (6.3.19)$$

where T (T^*) denotes time-ordering (anti-time-ordering) and $O(t) = e^{iHt}Oe^{-iHt}$. Terms first order in H' cannot give a direct current. The contribution to the current from the second

order terms can be written as

$$\begin{aligned}\langle j_x\rangle(t) &= \int_{-\infty}^{t} dt' \int_{-\infty}^{t_1} dt'' \left\langle \left[\left[j_x(t), H'(t') \right], H'(t'') \right] \right\rangle \\ &= \int_{-\infty}^{t} dt' \int_{-\infty}^{t_1} dt'' \chi_{x\alpha\beta}(t,t',t'') A_\alpha(t') A_\beta(t'') \end{aligned} \tag{6.3.20}$$

where $\alpha, \beta \in \{x, y\}$, $\chi_{x\alpha\beta}(t,t',t'') = \chi_{x\alpha\beta}(0,t'-t,t''-t) = \left\langle \left[\left[j_x, j_\alpha(t'-t) \right], j_\beta(t''-t) \right] \right\rangle \equiv \chi_{x\alpha\beta}(t'-t,t''-t)$ due to time translational invariance, and the expectation value is over the ground state which has all states with $E_{\mathbf{p}} < (>) 0$ filled (empty). For Hamiltonians of the form of (6.3.15), the expectation value of any traceless operator O in the Fermi sea ground state can be written as a trace:

$$\langle O \rangle = \sum_{\mathbf{p}} \frac{1}{2} \mathrm{Tr} \left\{ \left(1 - \frac{H}{|E_{\mathbf{p}}|} \right) O \right\} = - \sum_{\mathbf{p}} \frac{\mathrm{Tr}\left(HO\right)}{2|E_{\mathbf{p}}|} \tag{6.3.21}$$

This gives,

$$\chi_{x\alpha\beta}(t_1,t_2) = - \sum_{p} \frac{\mathrm{Tr}\left(H \left[\left[j_x, j_\alpha(t_1) \right], j_\beta(t_2) \right] \right)}{2|E_{\mathbf{p}}|} \tag{6.3.22}$$

(6.3.22) is the zero temperature limit of the finite temperature expression for the quadratic susceptibility proven in [18].

Because of the mirror symmetry m, $\chi_{x\alpha\beta}(t_1,t_2)$ is non-vanishing only for $\alpha \neq \beta$. To get a direct current, we retain only the non-oscillating part of $A_x(t+t_i)A_y(t+t_j) = \frac{A_0^2}{2} e^{2\epsilon t} \left[\sin\left(2\omega t + \omega(t_i+t_j)\right) - \sin\left(\omega(t_i - t_j)\right) \right]$. Thus,

$$j_x^{dc}(t) = \frac{A_0^2 e^{2\epsilon t}}{4} \int_{-\infty}^{0} dt_1 \int_{-\infty}^{t_1} dt_2 \left(\chi_{xxy} - \chi_{xyx} \right)(t_1,t_2) e^{\epsilon(t_1+t_2)} \sin\left(\omega(t_2-t_1)\right) \tag{6.3.23}$$

The result: After carrying out the two time-integrals, we get the three currents mentioned in (6.3.2). For clean samples at low temperatures, $j_{a2}(t)$, which grows linearly with time, is expected to dominate. A general expression for this term is (in the units $e = \hbar = v_F = 1$ where v_F is the Fermi velocity)

$$j_{a2}(t) = \frac{i A_0^2 \pi t \mathrm{sgn}(\omega)}{2\omega^2} \sum_{\mathbf{p}} \delta(|\omega| - 2|E_{\mathbf{p}}|) \mathrm{Tr}(H j_x) \mathrm{Tr}(H [j_x, j_y]) \tag{6.3.24}$$

Using (6.3.15) and (6.3.17) and the Lie algebra of the Pauli matrices, $[\sigma_i, \sigma_j] = 2i\epsilon_{ijk}\sigma_k$ where ϵ_{ijk} is the anti-symmetric tensor, the above traces can be written as

$$\mathrm{Tr}(H j_x) = 2|E_{\mathbf{p}}| v_x(\mathbf{p}) \tag{6.3.25}$$

$$\begin{aligned}\mathrm{Tr}(H\left[j_x, j_y\right]) &= 4i|E_{\mathbf{p}}|^3 \hat{\mathbf{n}}. \left(\frac{\partial \hat{\mathbf{n}}}{\partial p_x} \times \frac{\partial \hat{\mathbf{n}}}{\partial p_y} \right) \\ &= 4i|E_{\mathbf{p}}|^3 \mathcal{F}(\mathbf{p}) \end{aligned} \tag{6.3.26}$$

(6.3.24), (6.3.25) and (6.3.26) give our main result (6.3.3).

6.3.4 Calculation in detail

Here we explain the current-calculation of Sec. 6.3.1 in more detail and also state results for the parts of the current that we chose not to focus on there.

As shown in Sec. 6.3.3, the relevant susceptibility is

$$\begin{aligned}\chi^{x\alpha\beta}(t,t',t'') &= -\frac{1}{2}\sum_{\mathbf{p}}\mathrm{Tr}\left(\frac{H}{|E_{\mathbf{p}}|}\left[[j^x(t),j^\alpha(t')],j^\beta(t'')\right]\right)\\ &= -\sum_{\mathbf{p}}\frac{1}{2|E_{\mathbf{p}}|}\mathrm{Tr}\left(H\left[[j^x,j^\alpha(t_1)],j^\beta(t_2)\right]\right)\\ &\equiv \chi^{x\alpha\beta}(t_1,t_2) \qquad (6.3.27)\end{aligned}$$

where $t_1 = t' - t$, $t_2 = t'' - t$, and the non-vanishing components of $\chi^{x\alpha\beta}$ are those for which $\alpha \neq \beta$. The non-oscillating part of the current, hence, is

$$\langle j_x^{dc}\rangle(t) = j_{CPGE}(t) = \frac{A_0^2 e^{2\epsilon t}}{4}\int_{-\infty}^{0}dt_1\int_{-\infty}^{t_1}dt_2 \left(\chi^{xxy}(t_1,t_2)-\chi^{xyx}(t_1,t_2)\right)e^{\epsilon(t_1+t_2)}\sin\left(\omega(t_2-t_1)\right) \qquad (6.3.28)$$

Since $j_{CPGE}(t)$ is an odd function of ω, it reverses on reversing the polarization, as expected.

The traces in the susceptibility expressions are calculated by introducing a complete set of states in place of the identity several times. Thus,

$$\begin{aligned}\chi^{xxy}(t_1,t_2) &= -\sum_{\mathbf{p}}\frac{1}{2|E_{\mathbf{p}}|}\mathrm{Tr}\left(H\left[[j^x,j^x(t_1)],j^y(t_2)\right]\right) \qquad (6.3.29)\\ &= -\frac{1}{2}\sum_{\mathbf{p}}\sum_{nml}\mathrm{sgn}(E_n)\Big\{e^{i(E_m-E_n)t_2}\times\\ &\quad\left(e^{i(E_l-E_m)t_1}-e^{-i(E_l-E_n)t_1}\right)X_{nl}X_{lm}Y_{mn}+\text{c.c.}\Big\}\end{aligned}$$

where $X_{nl} = \langle n\,|j_x|\,m\rangle$ etc. and the subscript $\mathbf{p}$ on $E_{\mathbf{p}}$ has been dropped to enhance the readability. Similarly,

$$\begin{aligned}\chi^{xyx}(t_1,t_2) &= -\sum_{\mathbf{p}}\frac{1}{2E_{\mathbf{p}}}\mathrm{Tr}\left(H\left[[j^x,j^y(t_1)],j^x(t_2)\right]\right) \qquad (6.3.30)\\ &= -\frac{1}{2}\sum_{\mathbf{p}}\sum_{nml}\mathrm{sgn}(E_n)\Big\{e^{i(E_m-E_n)t_2}X_{mn}\times\\ &\quad\left(e^{i(E_l-E_m)t_1}X_{nl}Y_{lm}-e^{-i(E_l-E_n)t_1}Y_{nl}X_{lm}\right)+\text{c.c.}\Big\}\end{aligned}$$

Substituting (6.3.29) and (6.3.30) in (6.3.23), we get

$$
\begin{aligned}
j_{CPGE}(t) &= \frac{A_0^2 e^{2\epsilon t}}{4}\mathfrak{Re}\int_{-\infty}^{0} dt_1 \int_{-\infty}^{t_1} dt_2 e^{\epsilon(t_1+t_2)} \times \\
&\sin\left(\omega(t_1-t_2)\right)\sum_{\mathbf{p},nml}\mathrm{sgn}(E_n)e^{i(E_m-E_n)t_2}\times \\
&\Big\{\left(e^{i(E_l-E_m)t_1}-e^{-i(E_l-E_n)t_1}\right)X_{nl}X_{lm}Y_{mn} - \\
&X_{mn}\left(e^{i(E_l-E_m)t_1}X_{nl}Y_{lm}-e^{-i(E_l-E_n)t_1}Y_{nl}X_{lm}\right)\Big\}
\end{aligned}
\tag{6.3.31}
$$

where $\mathfrak{Re}$ stands for 'the real part of'. Carrying out the the two time integrations gives

$$
\begin{aligned}
j_{CPGE}(t) &= \frac{A_0^2 e^{2\epsilon t}}{8}\mathfrak{Im}\sum_{\mathbf{p}}\sum_{nml}\mathrm{sgn}(E_n)\times \\
&\left[\frac{1}{E_m-E_n+\omega-i\epsilon}-\frac{1}{E_m-E_n-\omega-i\epsilon}\right]\times \\
&\left\{\frac{X_{nl}\left(X_{lm}Y_{mn}-Y_{lm}X_{mn}\right)}{E_l-E_n-2i\epsilon}+\frac{X_{lm}\left(Y_{mn}X_{nl}-X_{mn}Y_{nl}\right)}{E_l-E_m+2i\epsilon}\right\}
\end{aligned}
\tag{6.3.32}
$$

where $\mathfrak{Im}$ stands for 'the imaginary part of'. Using $\mathfrak{Im}\left(\frac{1}{\Omega-i\epsilon}\right)=\pi\delta(\Omega)$ and $\mathfrak{Re}\left(\frac{1}{\Omega-i\epsilon}\right)=\frac{1}{\Omega}$ in the limit $\epsilon\to 0$, we get after some algebra, $j_{CPGE}(t)=j_{na}+j_{a1}+j_{a2}(t)$, where (Tr denotes the trace)

$$
j_{na}=\frac{A_0^2}{16}\sum_{\mathbf{p}}\frac{\omega(\omega^2-12E_{\mathbf{p}}^2)}{i|E_{\mathbf{p}}|^3(\omega^2-4E_{\mathbf{p}}^2)^2}\mathrm{Tr}(Hj_x)\mathrm{Tr}(H\left[j_x,j_y\right]) \tag{6.3.33}
$$

comes from intraband processes and is constant in time,

$$
j_{a1}=-\frac{\pi A_0^2\mathrm{sgn}(\omega)}{32}\sum_{\mathbf{p}}\frac{\delta(|\omega|-2|E_{\mathbf{p}}|)}{E_{\mathbf{p}}^2}\mathrm{Tr}(H\left[j_x,\left[j_x,j_y\right]\right]) \tag{6.3.34}
$$

is a result of an interband transition absorption as indicated by the δ-function in energy and is also constant in time, and

$$
j_{a2}(t)=i\frac{A_0^2\pi t\,\mathrm{sgn}(\omega)}{8}\sum_{p}\delta(|\omega|-2|E_{\mathbf{p}}|)\frac{\mathrm{Tr}(Hj_x)\mathrm{Tr}(H\left[j_x,j_y\right])}{E_{\mathbf{p}}^2} \tag{6.3.35}
$$

which also results from interband absorption and increases linearly in time. The last term was the main focus of our work.

6.4 Optical spin injection

Having understood the microscopic mechanism underlying the generation of the photocurrent $j_{a2}(t)$, we wonder, next, whether such a population imbalance can lead to any other helicity-dependent macroscopic responses. Since each absorbed photon flips the z-component of the

spin of an electron, a net $\langle S_z \rangle$ is expected to be generated on the surface. Such a process of optical spin injection was discussed for thin films of topological insulators [89], without, however, recognizing the role of the Berry curvature in the interband transition.

The calculation of $\langle S_z \rangle$ is identical to that of j_{CPGE}. The total $\langle S_z \rangle$ generated consists of the same three parts as j_{CPGE}, and the dominant part is

$$S^z_{a2}(t) = -\frac{\pi e^2 \mathcal{E}_0^2 \hbar t \mathrm{sgn}(\omega)}{8} \sum_{\mathbf{p}} \delta(\hbar|\omega| - 2|E_p|) n_z(\mathbf{p}) \mathcal{F}(\mathbf{p}) \tag{6.4.1}$$

S_z does not break the rotational symmetry of the surface, so we calculate $S^z_{a2}(t)$ directly for the threefold symmetric Hamiltonian (6.3.5) and obtain

$$S^z_{a2}(t) = \frac{e^2 \mathcal{E}_0^2 (\hbar\omega)^3 \lambda^2 t}{2^{10}} \mathcal{A} \tag{6.4.2}$$

For the same values of all the parameters as for $j_{a2}(t)$, we get $S^z_{a2}(t) \sim 10\hbar$, which means only ten electron spins are flipped over an area of $\sim 1mm^2$. This is a very small number and cannot be measured by the current experimental techniques. However, the result that the dominant spin injected onto the surface is also controlled by the Berry curvature is still theoretically interesting, as it points towards a deeper connection between the Berry curvature of electron bands and the helicity-dependent dc responses of systems with strong spin-orbit coupled coupling.

6.5 CPGE at oblique incidence

Experimentally, a very attractive way of breaking the rotational symmetry of the surface is by performing the experiment with obliquely incident light. Indeed, such experiments have already been performed successfully on graphene at low frequencies [42]. At the microscopic level, the effect there has been attributed to photon-drag, where the current arises as a result of the in-plane component of the photon momentum $q_\parallel$ getting transferred to the electrons in graphene. In general, an analogous process is expected to contribute to the CPGE at high-frequencies as well. We can estimate the size of the photon-drag effect on TI surfaces in the Dirac limit by considering a mechanism is similar to the one described in Sec. 6.3.2, i.e., the electrons at $(\pm p_x, p_y)$ absorb the incident light unequally if the light is incident in the yz-plane. Now, no out-of-plane tipping of the spin is needed, because, if one thinks of the helical photon as simply a spin-raising or lowering operator for spins parallel to its propagation direction $\hat{\mathbf{z}}'$, the electrons at $(\pm p_x, p_y)$ already have opposite $\langle S_{z'} \rangle$ and hence, will absorb the light unequally. Thus, the general expression for the current may contain only those material parameters which appear in the pure Dirac dispersion. As before, it must be quadratic in the photon electric field, and must change sign when $q_\parallel$ and ω are both reversed, since that corresponds to switching the photon helicity. Thus, to lowest order in $q_\parallel$, the linear-in-time current, based simply on symmetry and dimensional analysis, must be of the form

$$\vec{\mathbf{j}}_{photon-drag}(t) \sim \frac{e^3 E_0^2 v_F^2 q_\parallel t}{\hbar^2 \omega^2} \mathcal{A} \hat{\mathbf{x}} \tag{6.5.1}$$

For $q_{\|} = c/\omega$, c being the speed of light in vacuum, and the same values for all the other parameters as in Sec. 6.3.1, we get a current density of $\sim 1\mu A/mm$. This will dominate the response at off-normal incidence, but can be suppressed by careful alignment of the experimental setup. However, since a response might appear even in the pure Dirac limit in which the Berry curvature vanishes, the role of the Berry curvature is not clear for this process.

In graphene, helicity-dependent direct photocurrents have also been predicted by applying a dc bias [105]. However, with a dc bias across a TI surface and ordinary continuous lasers, we find the current to be too low to be measurable.

6.6 Conclusions

In summary, we studied the CPGE on the surface of a TI at normal incidence, and applied the results to the (111) surface of Bi_2Se_3. If the rotational symmetry of the TI surface is broken by applying an in-plane magnetic field or a strain, we predict an experimentally measurable direct photocurrent. A striking feature of this current is that it depends on the Berry curvature of the electron bands. Such a dependence can be understood intuitively as a result of the incident photons getting absorbed unequally by electrons of different momenta and hence, different average spins. The current grows linearly with time until a decay process equilibrates populations, which provides a way of determining the excited states lifetime. We also calculated the amount of dc helicity-dependent out-of-plane component of the electron spin generated. This does not require any rotational symmetry breaking; however, the numerical value is rather small with typical values of the parameters. Finally, we estimated the size of the CPGE due to the photon-drag effect at oblique incidence assuming a differential absorption mechanism similar to the one discussed for normal incidence, and found a rather large value. However, the role of the Berry curvature in this process was unclear.

For future work, we wonder whether the Berry curvature dependence of the helicity-dependent response to CP light survives for three- and higher-band models. This is a practically relevant question, as semiconductor quantum wells such as those of GaAs, SiGe and HgTe/CdHgTe demand a four-band model for modeling the CPGE.

We would like to thank Ashvin Vishwanath for enlightening discussions, Joseph Orenstein for useful experimental inputs, and Ashvin Vishwanath and Yi Zhang for invaluable feedback on the draft.

This work was supported by the Office of Basic Energy Sciences, Materials Sciences Division of the U.S. Department of Energy under contract No. DE-AC02-05CH1123. This work is published in *Physical Review B*, **83**, 035309 (2011).

Chapter 7

Charge transport in Weyl semimetals

7.1 Introduction

There has been a surge of recent activity studying Dirac excitations in two dimensional media, most famously graphene [43] and the surface states of topological insulators, discussed in the previous chapter. A natural question is whether there are analogs in three dimensions, with a vanishing density of states at the chemical potential and linearly dispersing excitations. It has long been known that touchings between a pair of non-degenerate bands are stable in three dimensions, and typically have linear dispersion. Near these, electronic excitations are described by an analog of the Weyl equation of particle physics, which describes two-component chiral fermions [62, 3, 104]. Hence these states have been dubbed *Weyl semimetals* (WSMs) [134].

To remove a band touching (or Weyl node) one necessarily must connect to another node. This is in contrast with two dimensions: graphene's nodes can be gapped by different intranode perturbations that break inversion ($\mathcal{I}$) or time reversal ($\mathcal{T}$) symmetry. The enhanced protection in three dimensions is due to a topological property of the nodes - they are sources (monopoles) of Chern flux in the Brillouin zone (BZ). This momentum space topology is associated with several physical phenomena. In particular, it was recently realized [134] that unusual surface states will result as a consequence of the band topology. These take the form of Fermi arcs that connect the projections of the nodes onto the surface BZ. Such topological properties are sharply defined as long as one can distinguish band touching associated with opposite Chern flux. The presence of translation symmetry, and hence conserved crystal momenta, is sufficient to protect these defining properties since the nodes are separated in the BZ. In principle one needs perfect crystalline order to define these phases; in practice, smooth disorder that only weakly mixes nodes is expected to have little effect. Other manifestations of the band topology include an anomalous Hall effect [150, 17] that is tied to the momentum space displacement between nodes, and magneto-resistance arising from Adler-Bell-Jackiw anomaly of Weyl fermions [6, 104]. Note that the band topology of WSMs is very different from the band topology of gapped phases discussed in the previous chapters. The latter, unlike the former, does not require translational invariance and hence is robust against the appropriate symmetry-conserving disorder.

Physical realizations of WSMs require non-degenerate bands to touch; therefore spin

degeneracy must be lifted (by either spin-orbit interactions or magnetic order), and either $\mathcal{T}$ or $\mathcal{I}$ must be broken: otherwise, all bands would be doubly degenerate. We further require that the Fermi 'surface' consists exactly of the Weyl nodes. In $\mathcal{T}$-breaking realizations where $\mathcal{I}$ is unbroken, a simple 'parity criterion' applied to eight $\mathcal{T}$-invariant momenta in the BZ can be used to diagnose the existence of Weyl nodes [134]. In [134], certain pyrochlore iridates $A_2Ir_2O_7$ (A=Y or Eu), were proposed to be magnetically ordered WSMs, with $N = 24$ Weyl points, all at the Fermi energy; [140] reached similar conclusions but with $N = 8$. Alternate proposals include $HgCr_2Se_4$ in the ferromagnetic state [146] and topological insulator-ferromagnet heterostructures [17], with $N = 2$, the minimum allowed.

Motivated by the availability of transport data on the iridates [149, 126], we study the electrical conductivity of an idealized model of a WSM, with an even number N of isotropic Weyl nodes characterized by the same dispersion, with $N/2$ nodes of each chirality as required by topology [134, 104]. The leading behavior of the conductivity σ provides insight into the dominant scattering mechanism in the system, as in three dimensions, σ has dimensions of inverse length in units of e^2/h and the appropriate length scale is set by the quasiparticle mean free path. In the absence of impurities and interactions we expect the free fermion result, $\sigma_0^{(N)}(\omega) = N\frac{e^2}{12h}\frac{|\omega|}{v_F}$; we demonstrate how this is modified in two cases:
(i) in clean undoped systems with Coulomb interactions, current is carried equally by counter-propagating electrons and holes and can be relaxed via interactions alone. Solving a quantum Boltzmann equation (QBE) we find a finite conductivity proportional to the temperature T (upto logarithmic factors), as expected of a quantum critical system [31], where T is the sole energy scale,

$$\sigma_{\rm dc}^{(N)}(T) = \frac{e^2}{h}\frac{k_B T}{\hbar v_F(T)}\frac{1.8}{\alpha_T^2 \ln \alpha_T^{-1}} \tag{7.1.1}$$

Here $v_F(T) = v_F\,(\alpha_0/\alpha_T)^{\frac{2}{N+2}}$ and $\alpha_T = \alpha_0\left[1 + \frac{(N+2)\alpha_0}{3\pi}\ln\left(\frac{\hbar\Lambda}{k_B T}\right)\right]^{-1}$ are the Fermi velocity and fine structure constant renormalized to the scale of the temperature T, Λ is a momentum cut-off set by the separation between the Weyl nodes, and v_F and $\alpha_0 = e^2/\varepsilon\hbar v_F$ are the corresponding 'bare' values at the microscopic scale (See Sec. 7.2.1).
(ii) In the presence of impurities, power counting shows that white-noise disorder is an irrelevant perturbation, and a naive expectation is that the clean result $\sigma_0^{(N)}$ is reproduced. However, the result is more interesting: by evaluating a standard Kubo formula, we find that the finite-frequency conductivity exhibits different behaviors for $\omega \ll T$ and $\omega \gg T$: in the former regime we find in agreement with [17] a finite Drude-like response with a peak width vanishing as NT^2; in the latter, we recover $\sigma_0^{(N)}$ as the leading behavior, which is universal and independent of disorder. We also determine the manner in which the conductivity interpolates between these limits.

Previous studies of 3D Dirac points have assumed Lorentz invariance [10] or worked at a topological phase transition between insulators [48]. Although our work differs from both of these situations – instantaneous Coulomb interactions break Lorentz invariance, and we study a stable phase – there are sufficient parallels that a similar 'leading log' approximation suffices to solve the QBE. Coulomb interactions also lead to a finite dc conductivity in clean graphene – the 2D analog of a WSM – but the leading log approximation fails here and more analysis is needed [31, 75].

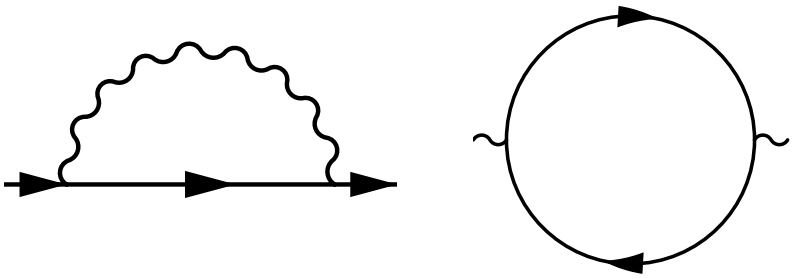

Figure 7.2.1: One-loop diagrams that govern the flow of the marginal couplings v_F and ϵ.

7.2 The Model

In a WSM, the electronic dispersion about a Weyl node is generically of the form $H_{\rm Weyl} = \boldsymbol{u}\cdot\boldsymbol{k}\,1 + \sum_{a=1}^{3} \boldsymbol{v}^a\cdot\boldsymbol{k}\,\sigma^a$, where σ^a are the Pauli matrices. The velocities satisfy $\boldsymbol{v}^1\cdot(\boldsymbol{v}^2\times\boldsymbol{v}^3) \neq 0$, and the Chern number ± 1 ('chirality') associated with the Weyl node is Sign $(\boldsymbol{v}^1\cdot(\boldsymbol{v}^2\times\boldsymbol{v}^3))$. For simplicity, we shall drop the term proportional to identity and assume isotropic dispersion; relaxing this assumption should only produce small corrections. The Hamiltonian for a system of N identically dispersing Weyl nodes ('flavors') with Coulomb interactions and disorder may then be written as $H = H_0 + H_I + H_D$, with (repeated indices summed)

$$\begin{aligned} H_0 &= \sum_a H_a = \sum_a \int_{\boldsymbol{k}} \psi^\dagger_{\boldsymbol{k},a}\left(\chi_a v_F \boldsymbol{k}\cdot\boldsymbol{\sigma}\right)\psi_{\boldsymbol{k},a} \\ H_I &= \frac{1}{2}\int_{\boldsymbol{k}_1\boldsymbol{k}_2\boldsymbol{q}} V(\boldsymbol{q})\psi^\dagger_{\boldsymbol{k}_2-\boldsymbol{q},a\sigma}\psi_{\boldsymbol{k}_2,a\sigma}\psi^\dagger_{\boldsymbol{k}_1+\boldsymbol{q},b\sigma'}\psi_{\boldsymbol{k}_1 b\sigma'} \\ H_D &= \int_{\boldsymbol{r}}\sum_{a,b}\psi^\dagger_a(\boldsymbol{r})U(\boldsymbol{r})\psi_b(\boldsymbol{r}) \end{aligned} \tag{7.2.1}$$

where $\psi_{\boldsymbol{k},a}$ is a two-component spinor in the (pseudo)spin indices σ, σ', $a, b = 1 \ldots N$ index the flavors, v_F is the Fermi velocity, which we set to unity, $\chi_a = \pm 1$ is the chirality of the a^{th} Weyl node, $V(\boldsymbol{q}) = \frac{4\pi e^2}{\varepsilon q^2}$ describes the Coulomb interaction in a material with dielectric constant ε, $U(\boldsymbol{r})$ is a random potential with white-noise correlations $\langle\langle U(\boldsymbol{r})U(\boldsymbol{r}')\rangle\rangle = n_{\rm i} v_0^2 \delta(\boldsymbol{r}-\boldsymbol{r}')$ where v_0 characterizes the strength of the individual impurities and $n_{\rm i}$ their concentration, $\int_{\boldsymbol{k}} \equiv \int \frac{d^3k}{(2\pi)^3}$, and we have written H_0 assuming that the Fermi level is at the Weyl nodes, which is the only case studied in this Letter. Here and below we set $\hbar = k_B = |e| = 1$, and define $\beta = 1/T$.

7.2.1 Renormalization of couplings

In order to make a meaningful comparison between the calculated conductivity and experimental data at temperature T, we need to use values of the various parameters renormalized to the characteristic energy scale $k_B T$. In order to determine these, we work with the Euclidean path integral $\mathcal{Z}[\boldsymbol{A}] = \int [DA_0 D\psi^\dagger D\psi] e^{-\mathcal{S}[\psi, A_0, \boldsymbol{A}]}$, written in terms of the gauge-fixed

action

$$\begin{aligned}\mathcal{S}[\psi, A_0, \boldsymbol{A}] &= \int d\boldsymbol{r}d\tau \Big[\psi_a^\dagger(\boldsymbol{r},\tau)[\partial_\tau - i|e|A_\tau(\boldsymbol{r},\tau) \\ &\quad + v_F \boldsymbol{\sigma}\cdot(i\boldsymbol{\nabla} + |e|\boldsymbol{A}/c)]\psi_a(\boldsymbol{r},\tau) \\ &\quad + \frac{1}{2}\int_{\boldsymbol{q}}\int d\tau \frac{\varepsilon q^2}{4\pi}|A_\tau(\boldsymbol{q},\tau)|^2\Big] \end{aligned} \tag{7.2.2}$$

which (as is easily verified) is equivalent to the Hamiltonian H described earlier. Here, $\boldsymbol{A}$ is a static external vector potential, while A_τ is a dynamical field that mediates the $e^2/(\varepsilon r)$ instantaneous Coulomb interaction between the electrons. We implement a momentum-space cutoff $k < \Lambda$, but leave the frequencies unrestricted so that the interaction always remains instantaneous; we then study the flow of $\mathcal{S}$ as we lower Λ. The action has three dimensionless parameters – the Fermi velocity v_F, the electric charge e and the dielectric constant ε – all of which are unrenormalized, and hence marginal, at tree level. Of these, e is further protected against renormalization to *all orders* in perturbation theory by gauge invariance. However, v_F and ε have no such protection and at one loop they acquire corrections of $\mathcal{O}(\alpha\frac{\delta\Lambda}{\Lambda})$ when Λ is lowered to $\Lambda - \delta\Lambda$. The diagrams governing the flow of v_F and ε at this order in α are the one-loop self-energy and the fermion (RPA) bubble (see Figure 7.2.1) diagrams respectively; performing the sum over flavors where appropriate, we find that the corrections are, respectively, independent of and proportional to N. Evaluation of the corresponding integrals leads to the flow equations

$$\frac{dv_F}{d\ell} = \frac{2}{3\pi}\alpha v_F,\ \frac{d\varepsilon}{d\ell} = \frac{N}{3\pi}\alpha\varepsilon \implies \frac{d\alpha}{d\ell} = -\frac{N+2}{3\pi}\alpha^2 \tag{7.2.3}$$

where $\ell = \log\Lambda$ is the usual RG scale parameter. Integrating (7.2.3) between an upper cutoff (which we leave unspecified for the time being, but will take to be much higher than any scale relevant to transport measurements, but lower than the energy at which band curvature corrections become significant) and the temperature scale, T gives the renormalized parameters used in the text. These renormalized values of v_F and α are to be used in the formula for $\sigma_{\rm dc}$ (7.1.1) to compute the conductivity at temperature T, while e retains its bare value due to gauge invariance. Representative results are shown in Figure 7.2.2.

We remark on an important distinction between the case of the Weyl semimetal in $d = 3$ and its two-dimensional analog, graphene. In the case of graphene, while the electrons are restricted to two dimensions, their interaction continues to be of the $1/r$ form since the electromagnetic field lines are not thus constrained; in momentum space, this leads to a non-analytic form for the instantaneous interaction, $V(\boldsymbol{q}) \sim 1/|\boldsymbol{q}|$. Since the RG procedure outlined above can only produce analytic corrections at any order, ε thus remains unrenormalized. In $d = 3$, we have an analytic $V(\boldsymbol{q}) \sim 1/q^2$, and so ε can and does receive corrections at one loop and beyond.

7.3 Conductivity with Interactions

Critical systems – such as graphene and the WSM at neutrality– are exceptions to the rule that disorder is essential for a finite conductivity, since they support current-carrying states

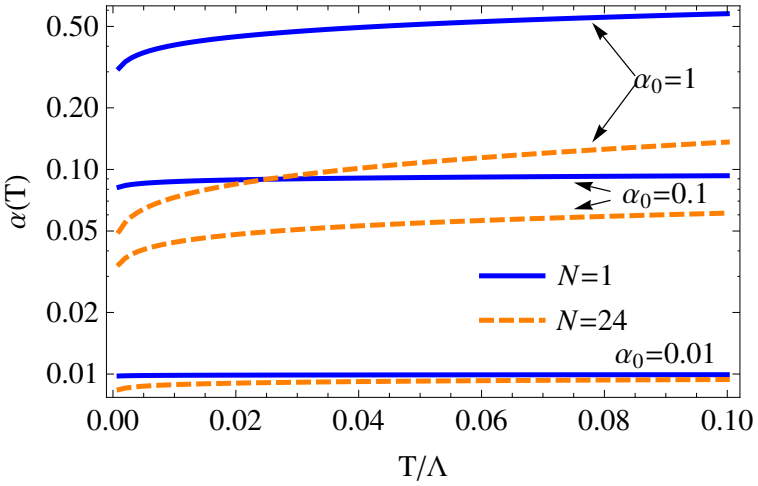

Figure 7.2.2: Renormalized fine-structure constant as a function of temperature for N-node Weyl semimetals with $N = 1$ and $N = 24$.

in which particles and holes transport charge with no net momentum by moving exactly opposite to each other. In contrast to conventional finite-momentum charge transport, such deviations from equilibrium can relax in the presence of interactions alone, leading to a finite conductivity.

We study transport in an interacting WSM by solving a QBE for the thermal distribution function of quasiparticle states. In doing so, it is convenient to first calculate the current from a single node (but interacting with all the nodes), before making the leap to the current carried by all N nodes. We focus on a node with flavor a, which we take to have $\chi_a = 1$. The single-quasiparticle states are obtained by diagonalizing H_a: $\psi_{\boldsymbol{k},a} \to W^\dagger \psi_{\boldsymbol{k},a} \equiv \gamma_{\boldsymbol{k},a}$, $H_a \to W H_a W^{-1} = \int_{\boldsymbol{k}} \lambda v_F k \gamma^\dagger_{\boldsymbol{k}\lambda a}\gamma_{\boldsymbol{k}\lambda a}$, and are labeled by their helicity λ (the eigenvalue of $\sigma \cdot \hat{\boldsymbol{p}}$.) From now on we will suppress the index a. In general, operators corresponding to various transport properties are *not* diagonal in the helicity; diagonal contributions correspond to motion of particles and holes in the applied field and may be characterized by appropriate distribution functions $f_\lambda(\boldsymbol{k}, t) = \langle \gamma^\dagger_{\boldsymbol{k}\lambda}\gamma_{\boldsymbol{k}\lambda}\rangle$, while the off-diagonal terms $(\gamma^\dagger_{\lambda\boldsymbol{k}}\gamma_{-\lambda\boldsymbol{k}})$ describe the motion of particle-hole pairs. For $\omega \ll T$, contributions of the latter to transport are expected to be suppressed, essentially by Pauli exclusion, as follows.

We focus on a single Weyl node and assume it has positive chirality; generalization to many nodes is straightforward. The Hamiltonian is

$$H_0 = \psi^\dagger_{\boldsymbol{k}} \boldsymbol{k} \cdot \boldsymbol{\sigma} \psi_{\boldsymbol{k}} = \Gamma^\dagger_{\boldsymbol{k}} k \tilde{\sigma}_z \Gamma_{\boldsymbol{k}} \equiv \Gamma^\dagger_{\boldsymbol{k}} \tilde{H}_0 \Gamma_{\boldsymbol{k}}, \tag{7.3.1}$$

and the perturbation

$$\begin{aligned} h'_S(t) &= e^{\eta t} \frac{E}{\omega} \cos\omega t \psi^\dagger_{\boldsymbol{k}} \sigma_x \psi_{\boldsymbol{k}} \\ &\to e^{\eta t} \frac{E}{\omega} \cos\omega t \Gamma^\dagger_{\boldsymbol{k}} \tilde{\sigma}_x \Gamma_{\boldsymbol{k}} \equiv \Gamma^\dagger_{\boldsymbol{k}} \tilde{h}'_S(t) \Gamma_{\boldsymbol{k}}, \end{aligned} \tag{7.3.2}$$

simulates an electric field $\boldsymbol{E} = E \sin\omega t \hat{\boldsymbol{x}}$. To determine the frequency-dependent conductivity, we look at the evolution of the single particle-density matrix with time. The subscript s

on h' and $\tilde{h}'$ denotes Schrodinger picture while $\eta > 0$ ensures slow switch-on of the electric field. We shall work in the interaction picture below and take the limit $\eta \to 0$ at the end of the calculation.

Before the field is switched on, the system is in a mixed state given by the density matrix at each $\boldsymbol{k}$, $\rho_{\boldsymbol{k}}(t = -\infty) = \frac{1}{f_-(k)+f_+(k)} \begin{pmatrix} f_-(k) & \\ & f_+(k) \end{pmatrix}$ where the $f_\pm = \left(1 + e^{\pm\beta k}\right)^{-1}$ are the Fermi distribution functions at particle-hole symmetry. The evolution of $\rho_{\boldsymbol{k}}(t)$ in the interaction picture is given by

$$\rho_{\boldsymbol{k}}(t) \approx \rho_{\boldsymbol{k}}(-\infty) - i \int_{-\infty}^{t} \mathrm{d}t' \left[h'(t'), \rho_{\boldsymbol{k}}(-\infty)\right] \tag{7.3.3}$$

to linear order in the electric field. Clearly, the change in $\rho_{\boldsymbol{k}}$ is

1. off-diagonal, since $\rho_{\boldsymbol{k}}(-\infty)$ is diagonal, which shows that the current is carried by particle-hole pairs;

2. only sensitive to the $\tilde{\sigma}_z$-part of $\rho_{\boldsymbol{k}}(-\infty)$, that is, to $\frac{f_-(k)-f_+(k)}{f_-(k)+f_+(k)} = \tanh(k/2T)$. We will see below that the current is mainly produced by momentum-conserving resonant absorption of photons from $\epsilon_{\boldsymbol{k}} = -|\omega|/2$ to $\epsilon_{\boldsymbol{k}} = |\omega|/2$; thus $k = |\omega|/2$ and the current is proportional to $\tanh(\omega/4T)$.

We now explicitly evaluate the current along $\boldsymbol{E}$, i.e., j_x

$$\langle j_x(\boldsymbol{k})\rangle\,(t) = \int_{\boldsymbol{k}} Tr\left(\rho_{\boldsymbol{k}}(t)\tilde{\sigma}_x(t)\right) \tag{7.3.4}$$

Evaluating the trace and doing the angular-part of the integral over $\boldsymbol{k}$, we get

$$\begin{aligned}
\langle j_x\rangle\,(t) &= \frac{2E}{3\pi^2\omega} \int_{-\infty}^{t} e^{\eta t'} \mathrm{d}t' \int_0^\infty k^2 \mathrm{d}k \tanh\left(\frac{k}{2T}\right) \sin 2k(t-t') \cos\omega t' \\
&= \frac{E}{3\pi^2\omega} \int_0^\infty k^2 \mathrm{d}k \tanh\left(\frac{k}{2T}\right) \left[\frac{(2k+\omega)\cos\omega t - \eta \sin\omega t}{\eta^2 + (2k+\omega)^2} + \right. \\
&\quad \left. \frac{(2k-\omega)\cos\omega t + \eta \sin\omega t}{\eta^2 + (2k-\omega)^2}\right] e^{\eta t}
\end{aligned} \tag{7.3.5}$$

The real part of the conductivity is given by the $\sin\omega t$ terms, which are the ones in phase with the electric field. Using the fact $\lim_{\eta\to 0} \frac{\eta}{\eta^2+x^2} = \pi\delta(x)$, we thus get

$$\mathrm{Re}\sigma_{xx}(\omega) = \frac{1}{3\pi|\omega|} \int k^2 \mathrm{d}k \tanh\left(\frac{k}{2T}\right) \delta(2k - |\omega|) \tag{7.3.6}$$

$$= \frac{e^2\omega}{12hv_F} \tanh\left(\frac{\omega}{4T}\right) \tag{7.3.7}$$

which vanishes as $\omega \to 0$. The δ-function in energy is the mathematical manifestation of the absorption process from $\epsilon_{\boldsymbol{k}} = -|\omega|/2$ to $\epsilon_{\boldsymbol{k}} = |\omega|/2$.

Thus, the contribution to the current by the motion of particle-hole pairs is negligible for $\omega \ll T$, and we drop it forthwith. In this approximation, it is therefore sufficient to solve the QBE for quasiparticle distribution functions $f_\lambda(\boldsymbol{k}, t)$, subject to an external force $\boldsymbol{F}$,

$$\left(\frac{\partial}{\partial t} + \boldsymbol{F} \cdot \nabla \boldsymbol{k}\right) f_\lambda(\boldsymbol{k}, t) = -w[f_\lambda(\boldsymbol{k}, t)] \tag{7.3.8}$$

where w is the rate at which quasiparticles scatter out of the state $(\lambda, \boldsymbol{k})$ at time t, and captures the effect of interactions. Our goal will be to determine the steady-state form of the non-equilibrium quasiparticle distribution function. We will restrict ourselves to linear response in $\boldsymbol{F}$, i.e. we assume that the deviation of f_λ from equilibrium is small. The result is a linear functional equation which may be recast as a variational problem. We solve the latter approximately by identifying 'leading log' contributions, which dominate the relaxation of the observable under consideration. As mentioned, we assume that the constants that enter the solution of (7.3.8) are renormalized to the energy scale of interest, namely T. Neglecting particle-hole pair contributions, the current is $\boldsymbol{J}(t) = -\int_{\boldsymbol{k}} \langle \psi^\dagger_{\boldsymbol{k}} \boldsymbol{\sigma} \psi_{\boldsymbol{k}} \rangle_t = -\sum_{\lambda=\pm} \int_{\boldsymbol{k}} \lambda \hat{\boldsymbol{k}} f_\lambda(\boldsymbol{k}, t)$. For a weak applied electric field $\boldsymbol{E}(t)$, the deviation of $f_\lambda(\boldsymbol{k}, \omega) = \int \mathrm{d}t f(\boldsymbol{k}, t) e^{i\omega t}$ from the equilibrium distribution function $f^0_\lambda(k) = \left(1 + e^{\lambda\beta k}\right)^{-1}$, and hence the conductivity $\sigma(\omega, T)$, can be parametrized [1] in terms of a dimensionless, isotropic function $g(k, \omega)$:

$$\begin{aligned} f_\lambda(\boldsymbol{k}, \omega) &= 2\pi\delta(\omega) f^0_\lambda(k) \\ &\quad + \lambda\beta^2 \hat{\boldsymbol{k}} \cdot \boldsymbol{E}(\omega) [f^0_\lambda(k) f^0_{-\lambda}(k)] g(k, \omega) \end{aligned} \tag{7.3.9}$$

$$\sigma(\omega, T) = 2\beta^2 \int_{\boldsymbol{k}} \left[\frac{k_x^2}{k^2} [f^0_+(k) f^0_-(k)] g(k, \omega)\right] \tag{7.3.10}$$

It therefore remains only to determine the function $g(k, \omega)$, to which we now turn. Inserting (7.3.9) into (7.3.8), and working to linear order in $\boldsymbol{E}$, we find $-\left(i\beta\omega g(k, \omega) + 1\right) f^0_+(k) f^0_-(k) \hat{\boldsymbol{k}} = \hat{\mathcal{C}}\left[g(k, \omega)\hat{\boldsymbol{k}}\right]$ where $\hat{\mathcal{C}}$ is the collision operator, a linear functional of $g(k, \omega)\hat{\boldsymbol{k}}$ given in Appendix 7.7.1. This is equivalent to the variational problem of extremizing the quadratic functional [48, 75, 31, 10]

$$\mathcal{Q}[g] \equiv \int_{\boldsymbol{k}} \left[\frac{1}{2} g(k, \omega) \hat{\boldsymbol{k}} \cdot \left(\hat{\mathcal{C}}\left[g(k, \omega)\hat{\boldsymbol{k}}\right]\right) + f^0_+(k) f^0_-(k) g(k, \omega) \left(i\omega g(k, \omega)/2 + 1\right)\right] \tag{7.3.11}$$

in which we have rescaled all momenta and frequencies by T. A key simplification, known as the 'leading log' approximation (LLA) stems from the power-law nature of the Coulomb interaction: as a result of this, logarithmically divergent small-momentum scattering dominates $\hat{\mathcal{C}}$. We may write $\hat{\mathcal{C}} = \hat{\mathcal{C}}_0 + \hat{\mathcal{C}}_1$, which when thought of as linear functionals of $g\hat{\boldsymbol{k}}$ have eigenvalues of $\mathcal{O}(\alpha^2 \log \alpha)$ and $\mathcal{O}(\alpha^2)$, respectively. In the LLA we approximately optimize $\mathcal{Q}$ by choosing $g\hat{\boldsymbol{k}}$ in the space spanned by eigenstates of $\hat{\mathcal{C}}_0$; as shown in Appendix 7.7.1 the choice $g = k\xi(\omega)$ yields

$$\mathcal{Q}[k, \xi(\omega)] \approx \frac{4}{\varepsilon^2}\left[i\omega\xi^2(\omega)\frac{7\pi^4}{30} + 9\xi(\omega)\zeta(3)\right] - \frac{4\pi^3}{9\varepsilon^2}\xi^2(\omega) N\alpha^2 \ln \alpha^{-1} \tag{7.3.12}$$

[1] We have used the fact that at particle-hole symmetry, the deviation from equilibrium is proportional to the sign of λ, and $f^0_\lambda(k) = 1 - f^0_{-\lambda}(k)$.

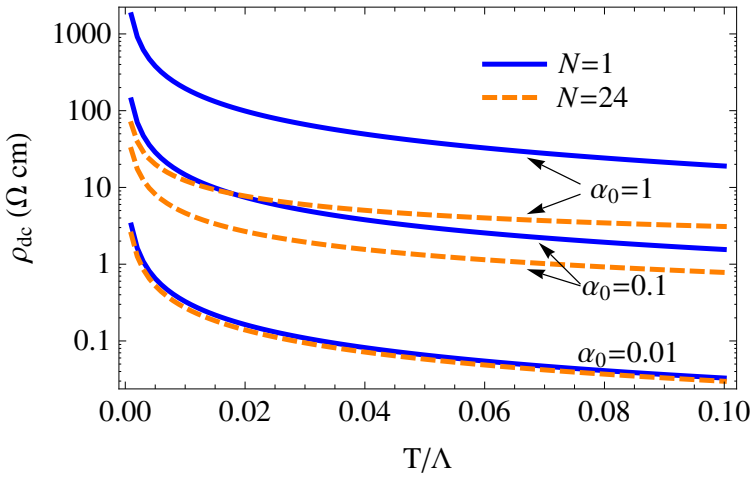

Figure 7.3.1: Resistivity as a function of temperature for N-node Weyl semimetals with $N = 1$ and $N = 24$ obtained using (7.3.13).

optimized by $\xi(\omega) = \frac{81\zeta(3)}{2\pi^3}\left(-i\omega\frac{21\pi}{10} + N\alpha^2 \ln\alpha^{-1}\right)^{-1}$. Finally, we observe that the flipped chirality of half the nodes is unimportant as they all give the same contribution to σ; thus using the result for $\xi(\omega)$ in (7.3.10) and multiplying by N we find the result for N nodes [2] ,

$$\sigma^{(N)}(\omega, T) = N\frac{e^2}{h}\frac{1.8}{-i6.6\frac{\hbar\omega}{k_B T} + N\alpha^2 \ln\alpha^{-1}}\left(\frac{k_B T}{\hbar v_F}\right) \tag{7.3.13}$$

The corresponding resistivity, $\rho = \sigma^{-1}$, is plotted in Figure 7.3.1.

Note that in the case of graphene, the LLA fails because the log divergence stems from a phase space effect due to enhanced scattering of collinear particles, which cannot relax a current. Thus, the eigenstates of $\hat{\mathcal{C}}_0$ do not contribute to the relaxation, which therefore occurs only via subleading, noncollinear scattering, i.e. $\hat{\mathcal{C}}_1$ [31, 75]. In 3D, $\hat{\mathcal{C}}_0$ includes noncollinear and thus current-relaxing processes, so that the LLA analysis is sufficient [10, 48].

In the dc limit, (7.3.13) reduces to (7.1.1), which we may rationalize using the Einstein relation, $\sigma_{dc} = e^2 D\frac{\partial n}{\partial \mu}$, where $D = v_F^2\tau$ is the diffusion constant, which depends on the scattering time τ and $\frac{\partial n}{\partial \mu} \sim NT^2/v_F^3$ is the density of states, at energy $\epsilon = T$, upto numerical factors. We may estimate τ from three observations: the scattering rate τ^{-1} is proportional to (i) N, the number of flavors contributing to the scattering; (ii) α^2, which is essentially the cross-section for scattering and (iii) T , which is the single energy scale in the dc limit. Thus, $\tau^{-1} \sim N\alpha^2 T$, which gives (1), modulo logarithms. This provides an estimate of the frequencies over which transport is collision-dominated and the preceding calculation is valid: in order for collisions to produce relaxation, we require $\omega \ll \tau^{-1}$, which occurs for $\hbar\omega/k_B T \ll N\alpha^2$.

[2] As mentioned in the introduction, α and v_F take on their renormalized values at temperature T

7.4 Conductivity with impurities

We turn now to the conductivity of the noninteracting, disordered system. We restrict to the case of scattering off random point impurities, characterized by $v_{\rm i}(\boldsymbol{r}) \sim v_0^2\delta(\boldsymbol{r})$ and the locations of which we shall assume are uncorrelated, $\langle\langle\rho_{\rm i}(\boldsymbol{r})\rho_{\rm i}(\boldsymbol{r'})\rangle\rangle \propto \delta(\boldsymbol{r}-\boldsymbol{r'})$. With these assumptions, we are led to H_D in (7.2.1) with $U(\mathbf{r}) \equiv \int d\mathbf{r}' v_{\rm i}(\mathbf{r}-\mathbf{r}')\rho_{\rm i}(\mathbf{r}')$. As before, we first compute the conductivity for a single node. Assuming that the impurities are sufficiently dilute that the Born approximation is valid, the quasiparticle lifetime due to impurity scattering from a single node is given by $\frac{1}{\tau(\omega)} = -2{\rm Im}\Sigma^{\rm ret}(\omega,\boldsymbol{k})$ where $\Sigma^{\rm ret}_\lambda(\omega,\boldsymbol{k}) = n_{\rm i}v_0^2\int\frac{d^3k'}{(2\pi)^3}\mathcal{F}_{\lambda\lambda'}(\boldsymbol{k},\boldsymbol{k}')G^{(0)}_{\lambda'}(\omega,\boldsymbol{k}')$ is the retarded self-energy, $G^{(0)}_\lambda(\omega,\boldsymbol{k}) = (\omega+i\delta-\lambda v_F k)^{-1}$ is the Green's function for a noninteracting Weyl fermion with helicity λ, and the form factor from the overlap of helicity eigenspinors, $\mathcal{F}_{\lambda\lambda'}(\boldsymbol{k},\boldsymbol{k}') = \frac{1}{2}(1+\lambda\lambda'\cos\theta_{\boldsymbol{k}\boldsymbol{k}'})$ to leading order. We find (see Appendix 7.7.2) $\frac{1}{\tau(\omega)} \equiv 2\pi\gamma g(\omega)$, where $g(\omega) = \frac{\omega^2}{2\pi^2v_F^3}$ is the density of states and $\gamma = \frac{1}{2}n_{\rm i}v_0^2$ characterizes the strength of the impurity potential.
To evaluate the conductivity we use the Kubo formula,

$$\sigma(\omega,T) = -\frac{1}{\omega}\lim_{q\to0}{\rm Im}\Pi^{\rm ret}_{xx}(\omega,|\boldsymbol{q}|) \tag{7.4.1}$$

where $\Pi^{\rm ret}_{\mu\nu}(\omega,\boldsymbol{q})$ is the retarded response function which for a system of linear dimension L is defined to be

$$\Pi^{\rm ret}_{\mu\nu}(\omega,\boldsymbol{q}) = -\frac{i}{L^3}\int_0^\infty {\rm d}t e^{i\omega t}\,\langle J_\mu(-\boldsymbol{q},t)J_\nu(\boldsymbol{q},t)\rangle \tag{7.4.2}$$

with $x_\mu = (t,\boldsymbol{r})$, $p_\mu = (\omega,\boldsymbol{p})$ and $J_\mu = (-\psi^\dagger\psi,\boldsymbol{J})$. From gauge invariance $\Pi^{\rm ret}_{\mu\nu}(\omega,\boldsymbol{q}) = \Pi^{\rm ret}(\omega,|\boldsymbol{q}|)\left(\delta_{\mu\nu}-\frac{q_\mu q_\nu}{q^2}\right)$, so that (suppressing $\boldsymbol{q}=0$), $\sigma(\omega,T) = -\frac{1}{\omega}{\rm Im}\,\Pi^{\rm ret}(\omega) = -\frac{1}{3\omega}{\rm Im}\Pi^{\rm ret}_{\mu\mu}(\omega)$. Some algebra yields (see Appendix 7.7.2)

$$\begin{aligned}\sigma(\omega,T) &= \frac{4}{3}e^2v_F^2\int\frac{d\epsilon}{2\pi}\frac{[f_T(\epsilon)-f_T(\epsilon+\omega)]}{\omega} \\ &\quad\times\sum_{\lambda,\lambda'}\int\frac{d^3k}{(2\pi)^3}{\rm Im}G^{\rm ret}_\lambda(\epsilon+\omega,k){\rm Im}G^{\rm ret}_{\lambda'}(\epsilon,k).\end{aligned} \tag{7.4.3}$$

where $f_T(\omega) = [e^{\omega/T}+1]^{-1}$ is the Fermi-Dirac function and we have used the retarded helicity-basis Green's function dressed with disorder lines, $G^{\rm ret}_\lambda(\omega,\boldsymbol{k}) = [\omega-\lambda v_F k+i/2\tau(\omega)]^{-1}$. After a tedious calculation, we may write $\sigma(\omega,T) = \frac{e^2v_F^2}{h\gamma}\mathcal{J}(\hat\omega,\hat T)$ where $\hat T = T/\omega_0$, $\hat\omega = \omega/\omega_0$, so that $f_T(\omega) = f_{\hat T}(\hat\omega)$, $\omega_0 = 2\pi v_F^3/\gamma$ is a characteristic scale set by the disorder strength, and $\mathcal{J}(\hat\omega,\hat T) = \frac{4}{3}\int\frac{d\hat\epsilon}{2\pi}\frac{[f_{\hat T}(\hat\epsilon)-f_{\hat T}(\hat\epsilon+\hat\omega)]}{\hat\omega}\mathcal{I}(\hat\epsilon+\hat\omega,\hat\epsilon)$ with $\mathcal{I}$ a complicated rational function (see Appendix 7.7.2).

In our model disorder can scatter between nodes, so $1/\tau(\omega)$ acquires a factor of N when $N>1$; in common with the interacting case, σ also has an overall prefactor of N. From these it is easy to show that for N nodes,

$$\sigma^{(N)}(\omega,T) = \frac{e^2v_F^2}{h\gamma}\mathcal{J}\left(N\frac{\omega}{\omega_0},N\frac{T}{\omega_0}\right) \tag{7.4.4}$$

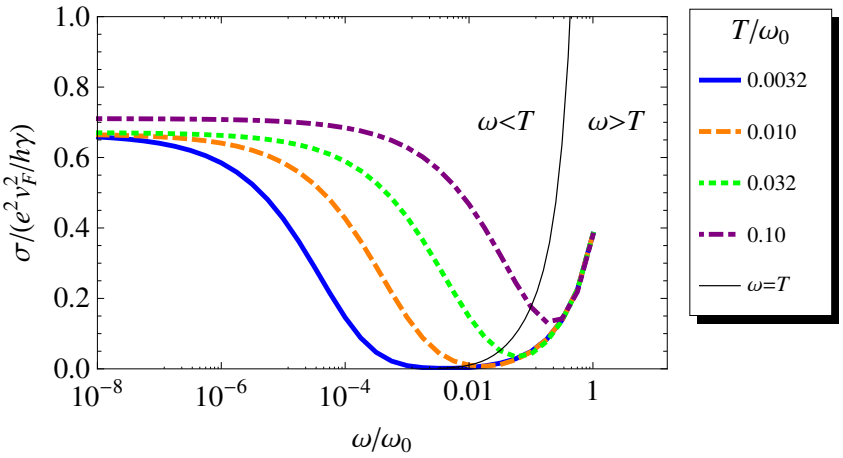

Figure 7.4.1: Frequency-dependent conductivity of a single Weyl node with disorder (constants defined in the text.)

which is identical to the $N = 1$ result (Figure 7.4.1) upon rescaling $\omega_0 \to \omega_0/N$.

While in general we integrate (7.4.4) numerically, in certain limits an analytic treatment is feasible. For $\omega \ll T$, $f_{\hat{T}}(\hat{\epsilon}) - f_{\hat{T}}(\hat{\epsilon} + \hat{\omega}) \approx -\hat{\omega} f'(\hat{\epsilon})$. Expanding $\mathcal{I}$ in powers of $\hat{\omega}$ and resumming only terms dominant as $\hat{\epsilon} \to 0$, we recover the result of Burkov and Balents ((15) of [17]): namely, a Drude-like response with a width vanishing as NT^2, and a finite dc limit of $\frac{2e^2v_F^2}{3h\gamma}$.

In the opposite limit, $T \to 0$ at finite ω we may replace the Fermi functions by step functions, which yields

$$\sigma^{(N)}(\omega) \approx N\frac{e^2}{12h}\frac{\omega}{v_F}\left[1 - \frac{16N\gamma\omega}{15\pi^2 v_F^3} + \mathcal{O}\left(\frac{N^2\omega^2}{\omega_0^2}\right)\right] \tag{7.4.5}$$

The leading term is universal and independent of disorder, and is simply $\sigma_0^{(N)}$. Both regimes are captured in Figure 7.4.1, which shows $\sigma(\omega, T)$ for $\omega \lesssim \omega_0$, beyond which the Born approximation is insufficient.

7.5 Experiments

In [149] the dc resistivity of polycrystalline $Y_2Ir_2O_7$ was found to vary with temperature as $\rho_{dc}T \approx 130\Omega \cdot \text{cm} \cdot \text{K}$ over $10\text{K} \lesssim T \lesssim 170\text{K}$, which is reminiscent of our result with interactions (7.1.1). Accordingly, we compare this data with a model of a clean WSM with $N = 24$ [134], as shown in Figure 7.4.2. We find rather good agreement with experimental data for physically reasonable parameter choices, shown inset. Very recently, transport in single crystals of another pyrochlore iridate, $Eu_2Ir_2O_7$, has been studied [126] under pressure for $2\text{K} \lesssim T \lesssim 300\text{K}$; at low pressures$\sim 2.06 - 6.06\,\text{GPa}$, $\rho_{\text{dc}}(T)$ resembles Figure 7.4.2, consistent with WSM behavior.

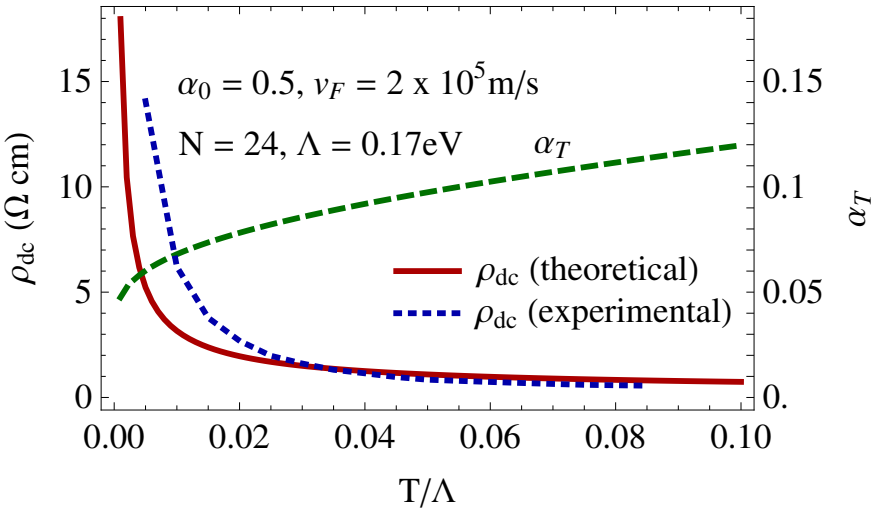

Figure 7.4.2: $\rho_{dc} = \sigma_{dc}^{-1}$ and α_T (defined in the text) for the inset parameter values compared to experimental data from [149].

7.6 Conclusions

The conductivity of WSMs thus exhibits a rich variety of behavior on varying frequency and temperature, in both the interacting clean and noninteracting disordered limits, as shown in Figs. 7.4.1 and 7.4.2. In particular, its nontrivial dependence on N is sensitive to the strength of the interactions; with just disorder, we find a striking difference between the $\omega \ll T$ and $\omega \gg T$ regimes, with the $T \to 0$ ac response dominated by a universal, disorder-independent contribution. While the limited existing dc conductivity data on the candidate iridates broadly agrees with our theory in the clean limit, we caution that more dc and ac conductivity measurements on single crystals with controlled disorder are required to make a rigorous comparison. Theoretically, the interplay of disorder and interactions, and corrections to the isotropic node approximation still need to be considered. In particular, it would be striking if the distinct behavior of the disordered system across the different frequency regimes survives the inclusion of interactions. A simultaneous treatment of disorder and interactions is, as always, challenging and is left open for future work.

P.H. would like to thank Siddharth Parameswaran and Ashvin Vishwanath for this collaboration. We thank P. Goswami, L. Fritz, S.L. Sondhi, S. Ryu and A. Turner for discussions, and acknowledge funding from the Simons Foundation (SAP) and the Laboratory Directed Research and Development Program of LBNL under US DOE Contract DE-AC02-05CH11231 (AV). This work is published in *Physics Review Letters*, **108**, 046602 (2012).

7.7 Appendix

7.7.1 The Collision Operator and the 'Leading Log' Approximation

In order to define the collision operator $\hat{\mathcal{C}}$, introduced in the main text, we need to determine the tree-level scattering amplitudes due to the interaction and how they couple the quasi-

particle distributions at different momenta. An additional complication stems from the fact that of the N Weyl nodes, $N/2$ have chirality -1. It is easily verified that the single-particle dispersion of the a^{th} Weyl node is given by $E_{\lambda,a}(\boldsymbol{k}) = \chi_a \lambda v_F k$, so that for $\chi_a = -1$ the eigenspinors of H_a with eigenvalues $\pm v_F k$ are interchanged relative to $\chi_a = +1$. For convenience, we define $\epsilon_a = \chi_a \lambda$, so that the energy is $E_a(\boldsymbol{k}) = \epsilon_a v_F k$ with $\epsilon_a = \pm 1$. As the Coulomb interaction is instantaneous, the collision operator is diagonal in frequency. H_I is then given by

$$\begin{aligned} H_I &= \frac{1}{2}\int_{\boldsymbol{k}_1\boldsymbol{k}_2\boldsymbol{q}} T^{\chi_a\chi_b}_{\epsilon_1\epsilon_2\epsilon_3\epsilon_4}(\boldsymbol{k}_1\boldsymbol{k}_2\boldsymbol{q}) \times \\ &\quad \gamma^\dagger_{\epsilon_4 b}(\boldsymbol{k}_1+\boldsymbol{q})\gamma^\dagger_{\epsilon_3 a}(\boldsymbol{k}_2-\boldsymbol{q})\gamma_{\epsilon_2 a}(\boldsymbol{k}_2)\gamma_{\epsilon_1 b}(\boldsymbol{k}_1) \end{aligned} \tag{7.7.1}$$

where

$$\begin{aligned} T^{\chi_a\chi_b}_{\epsilon_1\epsilon_2\epsilon_3\epsilon_4}(\boldsymbol{k}_1\boldsymbol{k}_2\boldsymbol{q}) &= \frac{V(\boldsymbol{q})}{2}\left[W^\dagger_{\chi_b}(\boldsymbol{k}_1+\boldsymbol{q})W_{\chi_b}(\boldsymbol{k}_1)\right]_{\epsilon_4\epsilon_1} \times \\ &\quad \left[W^\dagger_{\chi_a}(\boldsymbol{k}_2-\boldsymbol{q})W_{\chi_a}(\boldsymbol{k}_2)\right]_{\epsilon_3\epsilon_1} \end{aligned} \tag{7.7.2}$$

is the scattering amplitude for two-particle scattering from $\{(b,\epsilon_1,\boldsymbol{k}_1),(a,\epsilon_2,\boldsymbol{k}_2)\}$ to $\{(a,\epsilon_3,\boldsymbol{k}_2-\boldsymbol{q}),(b,\epsilon_4,\boldsymbol{k}_1+\boldsymbol{q})\}$ and in addition depends on the chiralities of the initial and final nodes. This dependence comes from the fact that the scattering amplitude depends explicitly on the overlap of the initial and final spinors, which in the ϵ-representation introduced above depends on their chiralities. We observe here that in the $q \to 0$ limit (which, as we will shortly see, dominates the current relaxation) $T^{++}_{\epsilon_1\epsilon_2\epsilon_3\epsilon_4} = T^{+-}_{\epsilon_1\epsilon_2\epsilon_3\epsilon_4}$, corresponding to the fact that $q \to 0$ scattering is indifferent to the chirality, so the fact that half the Weyl nodes have a chirality opposing the one under consideration is unimportant.

Using Fermi's golden rule, it is now straightforward to show that the collision operator is

$$\begin{aligned} &\hat{\mathcal{C}}\left[g(k,\omega)\hat{\boldsymbol{k}}\right] = \\ &-2\pi\int_{\boldsymbol{k}',\boldsymbol{q}}\Bigg\{\delta\left(k-k'-|\boldsymbol{k}+\boldsymbol{q}|+|\boldsymbol{k}'-\boldsymbol{q}|\right) f^0_-(k)f^0_+(k')f^0_+(|\boldsymbol{k}+\boldsymbol{q}|)f^0_-(|\boldsymbol{k}'-\boldsymbol{q}|)R_1\left(\boldsymbol{k},\boldsymbol{k}',\boldsymbol{q}\right)\times \\ &\left[\frac{\boldsymbol{k}}{k}g(k,\omega)-\frac{\boldsymbol{k}'}{k'}g(k',\omega)-\frac{\boldsymbol{k}+\boldsymbol{q}}{|\boldsymbol{k}+\boldsymbol{q}|}g(|\boldsymbol{k}+\boldsymbol{q}|,\omega)+\frac{\boldsymbol{k}'-\boldsymbol{q}}{|\boldsymbol{k}'-\boldsymbol{q}|}g(|\boldsymbol{k}'-\boldsymbol{q}|,\omega)\right]+ \\ &\delta\left(k+k'-|\boldsymbol{k}+\boldsymbol{q}|-|\boldsymbol{k}'-\boldsymbol{q}|\right) f^0_-(k)f^0_-(k')f^0_+(|\boldsymbol{k}+\boldsymbol{q}|)f^0_+(|\boldsymbol{k}'-\boldsymbol{q}|)R_2\left(\boldsymbol{k},\boldsymbol{k}',\boldsymbol{q}\right)\times \\ &\left[\frac{\boldsymbol{k}}{k}g(k,\omega)+\frac{\boldsymbol{k}'}{k'}g(k',\omega)-\frac{\boldsymbol{k}+\boldsymbol{q}}{|\boldsymbol{k}+\boldsymbol{q}|}g(|\boldsymbol{k}+\boldsymbol{q}|,\omega)-\frac{\boldsymbol{k}'-\boldsymbol{q}}{|\boldsymbol{k}'-\boldsymbol{q}|}g(|\boldsymbol{k}'-\boldsymbol{q}|,\omega)\right]\Bigg\} \end{aligned} \tag{7.7.3}$$

where

$$\begin{aligned} R_1\left(\boldsymbol{k},\boldsymbol{k}',\boldsymbol{q}\right) &= \left|T^{++}_{+--+}(\boldsymbol{k},\boldsymbol{k}',\boldsymbol{q})-T^{++}_{+-+-}(\boldsymbol{k},\boldsymbol{k}',\boldsymbol{k}'-\boldsymbol{k}-\boldsymbol{q})\right|^2 \\ &\quad +\left(\frac{N}{2}-1\right)\left[\left|T^{++}_{+--+}(\boldsymbol{k},\boldsymbol{k}',\boldsymbol{q})\right|^2+\left|T^{++}_{+-+-}(\boldsymbol{k},\boldsymbol{k}',\boldsymbol{k}'-\boldsymbol{k}-\boldsymbol{q})\right|^2\right] \\ &\quad +\left(\frac{N}{2}\right)\left[\left|T^{+-}_{+--+}(\boldsymbol{k},\boldsymbol{k}',\boldsymbol{q})\right|^2+\left|T^{+-}_{+-+-}(\boldsymbol{k},\boldsymbol{k}',\boldsymbol{k}'-\boldsymbol{k}-\boldsymbol{q})\right|^2\right] \end{aligned} \tag{7.7.4}$$

and

$$R_2\left(\boldsymbol{k},\boldsymbol{k}',\boldsymbol{q}\right) = \frac{1}{2}\left|T^{++}_{++++}(\boldsymbol{k},\boldsymbol{k}',\boldsymbol{q}) - T^{++}_{++++}(\boldsymbol{k},\boldsymbol{k}',\boldsymbol{k}'-\boldsymbol{k}-\boldsymbol{q})\right|^2 + \left(\frac{N}{2}-1\right)\left|T^{++}_{++++}(\boldsymbol{k},\boldsymbol{k}',\boldsymbol{q})\right|^2 + \left(\frac{N}{2}\right)\left|T^{+-}_{++++}(\boldsymbol{k},\boldsymbol{k}',\boldsymbol{q})\right|^2 \quad (7.7.5)$$

describe scattering between oppositely and identically charged particles, respectively. The diagrams corresponding to scattering processes are the same as in [31].

Turning now to the $\hat{\mathcal{C}}$-dependent portion of the expression for the functional $\mathcal{Q}$, we may use the symmetries of $\hat{\mathcal{C}}$ under combinatorial exchanges of momenta to write (in rescaled variables $k/T, \omega/T$) the first term in $\mathcal{Q}$ as

$$\int_{\boldsymbol{k}} g\hat{\mathcal{C}}g = -\frac{2\pi}{8}\times \quad (7.7.6)$$
$$\int_{\boldsymbol{k},\boldsymbol{k}',\boldsymbol{q}} \Bigg\{ \delta\left(k-k'-|\boldsymbol{k}+\boldsymbol{q}|+|\boldsymbol{k}'-\boldsymbol{q}|\right) f^0_-(k) f^0_+(k') f^0_+(|\boldsymbol{k}+\boldsymbol{q}|) f^0_-(|\boldsymbol{k}'-\boldsymbol{q}|) R_1\left(\boldsymbol{k},\boldsymbol{k}',\boldsymbol{q}\right) \times$$
$$\left[\frac{\boldsymbol{k}}{k}g(k,\omega) - \frac{\boldsymbol{k}'}{k'}g(k',\omega) - \frac{\boldsymbol{k}+\boldsymbol{q}}{|\boldsymbol{k}+\boldsymbol{q}|}g(|\boldsymbol{k}+\boldsymbol{q}|,\omega) + \frac{\boldsymbol{k}'-\boldsymbol{q}}{|\boldsymbol{k}'-\boldsymbol{q}|}g(|\boldsymbol{k}'-\boldsymbol{q}|,\omega)\right]^2 +$$
$$\delta\left(k+k'-|\boldsymbol{k}+\boldsymbol{q}|-|\boldsymbol{k}'-\boldsymbol{q}|\right) f^0_-(k) f^0_-(k') f^0_+(|\boldsymbol{k}+\boldsymbol{q}|) f^0_+(|\boldsymbol{k}'-\boldsymbol{q}|) R_2\left(\boldsymbol{k},\boldsymbol{k}',\boldsymbol{q}\right) \times$$
$$\left[\frac{\boldsymbol{k}}{k}g(k,\omega) + \frac{\boldsymbol{k}'}{k'}g(k',\omega) - \frac{\boldsymbol{k}+\boldsymbol{q}}{|\boldsymbol{k}+\boldsymbol{q}|}g(|\boldsymbol{k}+\boldsymbol{q}|,\omega) - \frac{\boldsymbol{k}'-\boldsymbol{q}}{|\boldsymbol{k}'-\boldsymbol{q}|}g(|\boldsymbol{k}'-\boldsymbol{q}|,\omega)\right]^2 \Bigg\}$$

We now specialize to a perturbation of the form $g(k,\omega) = k\xi(\omega)$, which is a zero mode of the R_2 processes. This leaves only the terms in (7.7.6) proportional to R_1. We may represent the energy-conserving δ-function as

$$\int_{-\infty}^{\infty} \delta\left(k-|\boldsymbol{k}+\boldsymbol{q}|+\Omega\right)\delta\left(k'-|\boldsymbol{k}'-\boldsymbol{q}|+\Omega\right) d\Omega$$

Next, we choose coordinates in which $\boldsymbol{q}$ is along $\hat{z}$ so that

$$\begin{aligned}\delta\left(k-|\boldsymbol{k}+\boldsymbol{q}|+\Omega\right) &= \delta\left(k-\sqrt{k^2+q^2+2kq\cos\theta}+\Omega\right)\\ &= \tfrac{k+\Omega}{kq}\delta\left(\cos\theta - \tfrac{\Omega^2+2k\Omega-q^2}{2kq}\right)\Theta(k+\Omega)\end{aligned}$$

and similarly for $\boldsymbol{k}'$. The angular integrals over θ and θ' can now be done trivially, at the cost of leaving a complicated dependence on Ω in k, k'. For $q < k, k'$, the θ and θ' integrals give one if $-q < \Omega < q$ and 0 otherwise; we will show that it suffices to consider small q, so the knowledge of this regime is sufficient. With these observations, we have

$$\int_{\boldsymbol{k}} g\hat{\mathcal{C}}g = -\frac{2\pi}{8}\int_{\boldsymbol{k},\boldsymbol{k}',\boldsymbol{q}}\int_{-q}^{q} d\Omega \frac{k'+\Omega}{k'q}\frac{k+\Omega}{kq} f^0_-(k) f^0_+(k') f^0_+(|\boldsymbol{k}+\boldsymbol{q}|) f^0_-(|\boldsymbol{k}'-\boldsymbol{q}|) R_1\left(\boldsymbol{k},\boldsymbol{k}',\boldsymbol{q}\right) \times$$
$$\left[\frac{\boldsymbol{k}}{k}g(k,\omega) - \frac{\boldsymbol{k}'}{k'}g(k',\omega) - \frac{\boldsymbol{k}+\boldsymbol{q}}{|\boldsymbol{k}+\boldsymbol{q}|}g(|\boldsymbol{k}+\boldsymbol{q}|,\omega) + \frac{\boldsymbol{k}'-\boldsymbol{q}}{|\boldsymbol{k}'-\boldsymbol{q}|}g(|\boldsymbol{k}'-\boldsymbol{q}|,\omega)\right]^2 \quad (7.7.7)$$

The cross-helicity scattering rate R_1 contains terms of the form $V(q)^2$, which diverge as $1/q^4$ at small q for direct scattering; the exchange contributions remain finite and do not contribute at leading order. The integral over the dummy Ω variable gives one power of q in the numerator and substitution of our ansatz shows that the term in braces gives two more powers of q, so that at small q, the integrand is proportional to $1/q$, which gives a logarithmic divergence. It is this logarithmically dominant contribution that is referred to in the text as $\hat{\mathcal{C}}_0$, whence we implicitly define $\hat{\mathcal{C}}_1 = \hat{\mathcal{C}} - \hat{\mathcal{C}}_0$.

Having identified the dominant contribution to the collision integral, we proceed as follows: first, we substitute our ansatz into the expression above, and perform the integral over q; as this integral is logarithmically divergent in both the UV and the IR, we will need to regulate it appropriately. The UV cutoff is the temperature T, as this is the largest physical energy scale in the problem; in the IR, the divergence is avoided due to thermal screening of the Coulomb interaction which occurs at an energy scale set by both the coupling constant and the temperature, which we take to be αT. With these choices, we may perform the integral over q, and then set $q = 0$ in the remainder, leaving integrals over Ω, k and k' which may then be performed straightforwardly; upon including the parts of the functional $\mathcal{Q}$ that are independent of the collision operator, we arrive at the results quoted in the text for the LLA.

7.7.2 Conductivity with Disorder

Scattering Time

The scattering time is given in terms of the imaginary part of the retarded self-energy by $\frac{1}{\tau(\omega)} = -2\mathrm{Im}\Sigma^{\mathrm{ret}}_{\lambda}(\omega, \boldsymbol{k})$, where

$$\mathrm{Im}\Sigma^{\mathrm{ret}}_{\lambda}(\omega, \boldsymbol{k}) = n_{\mathrm{i}} v_0^2 \mathrm{Im} \int \frac{d^3k'}{(2\pi)^3} \mathcal{F}_{\lambda\lambda'}(\boldsymbol{k}, \boldsymbol{k}') G^{(0)}_{\lambda'}(\omega, \boldsymbol{k}'). \tag{7.7.8}$$

with all quantities defined as in the text. Imposing a cutoff $|\boldsymbol{k}| < \Omega/v_F$, performing the angular integration, and rewriting the negative-helicity Green's function by changing variables we have

$$\begin{aligned} \mathrm{Im}\Sigma^{\mathrm{ret}}_{\lambda}(\omega, \boldsymbol{k}) &= \frac{n_{\mathrm{i}} v_0^2}{4\pi^2 v_F^3} \mathrm{Im} \int_{-\Omega}^{\Omega} dx \, \frac{x^2}{\omega + i\delta - x} \\ &= -\frac{n_{\mathrm{i}} v_0^2 \omega^2}{4\pi v_F^3}, \end{aligned} \tag{7.7.9}$$

independent of λ, whence $\frac{1}{\tau(\omega)} \equiv 2\pi\gamma g(\omega)$, where $g(\omega) = \frac{\omega^2}{2\pi^2 v_F^3}$ is the density of states and $\gamma = \frac{1}{2} n_{\mathrm{i}} v_0^2$. Note that $\mathrm{Re}\Sigma^{\mathrm{ret}}(\omega, \boldsymbol{k})$ is formally divergent with the cutoff regularization used here; however this can be absorbed into a renormalization of v_F and we shall not discuss it further.

Evaluation of the Kubo Response

In order to evaluate the conductivity we require the retarded response function $\Pi^{\mathrm{ret}}_{\mu\nu}(\omega)$ which is obtained most simply by working in the Matsubara formalism and analytically continuing

the results to real frequency. The leading contribution to the Matsubara response function $\Pi_{\mu\nu}$ corresponds to the particle-hole bubble with impurity-dressed propagators, and in terms of Matsubara Green's functions in the pseudospin basis takes the form

$$\Pi_{\mu\nu}(i\omega_n) = \frac{e^2 v_F^2}{\beta} \sum_m \int_{\boldsymbol{k}} \mathrm{Tr}\left[\mathcal{G}\left(i(\omega_n + \epsilon_m), \boldsymbol{k}\right) \sigma_\mu \mathcal{G}\left(i\epsilon_m, \boldsymbol{k}\right) \sigma_\nu\right] \tag{7.7.10}$$

where $\mathcal{G}(i\omega_n, \boldsymbol{k}) = (i\omega_n - \sigma \cdot \boldsymbol{k} + i/2\tau(\omega_n))^{-1}$ and the trace is over the pseudospin indices. Performing this trace and summing over the spatial index μ, we obtain

$$\Pi_{\mu\mu}(i\omega_n) = \frac{2e^2 v_F^2}{\beta} \sum_m \sum_{\lambda,\lambda'} \int_{\boldsymbol{k}} \mathcal{G}\left(i(\omega_n + \epsilon_m), \boldsymbol{k}\right) \mathcal{G}\left(i\epsilon_m, \boldsymbol{k}\right) \tag{7.7.11}$$

where $\mathcal{G}_\lambda(i\omega_n, \boldsymbol{k}) = (i\omega_n - \lambda v_F \boldsymbol{k} + i/2\tau(\omega_n))^{-1}$ is the Matsubara Green's function, now written in the helicity basis. Performing the sum over Matsubara frequencies by standard methods, analytically continuing the result to real frequencies via $\omega_n \to \omega + i\delta$ and using

$$\sigma(\omega, T) = -\frac{1}{\omega}\Pi^{\mathrm{ret}}_{xx}(\omega) = -\frac{1}{3\omega}\Pi^{\mathrm{ret}}_{\mu\mu}(\omega) \tag{7.7.12}$$

we arrive at the result,

$$\begin{aligned} \sigma(\omega, T) &= \frac{4}{3} e^2 v_F^2 \int \frac{d\epsilon}{2\pi} \frac{[f_T(\epsilon) - f_T(\epsilon + \omega)]}{\omega} \\ &\quad \times \sum_{\lambda,\lambda'} \int \frac{d^3k}{(2\pi)^3} \mathrm{Im} G^{\mathrm{ret}}_\lambda(\epsilon + \omega, k) \mathrm{Im} G^{\mathrm{ret}}_{\lambda'}(\epsilon, k) \end{aligned} \tag{7.7.13}$$

In order to perform the integrations in (7.4.3), it is convenient to write $\frac{1}{2\tau(\omega)} = \frac{\gamma}{2\pi v_F^3}\omega^2 \equiv \frac{\omega^2}{\omega_0}$. With this definition, we have

$$\begin{aligned} \mathrm{Im} G^{\mathrm{ret}}_\lambda(\omega, \boldsymbol{k}) &= \mathrm{Im} \frac{1}{\omega - \lambda v_F k + i\frac{\omega^2}{\omega_0}} \\ &= \frac{\omega^2}{\omega_0^3} \frac{1}{\left(\frac{v_F k}{\omega_0} - \lambda\frac{\omega}{\omega_0}\right)^2 + \left(\frac{\omega}{\omega_0}\right)^4} \end{aligned} \tag{7.7.14}$$

By a straightforward change of variable, followed by an angular integral we can write the sum over helicities and the dimensionless frequency parameter $\hat{\omega}_i = \omega_i/\omega_0$, for convenience replacing $\epsilon + \omega$ and ϵ by ω_i

$$\sum_{\lambda_1,\lambda_2} \int \frac{d^3k}{(2\pi)^3} \mathrm{Im} G^{\mathrm{ret}}_{\lambda_1}(\omega_1, \boldsymbol{k}) \mathrm{Im} G^{\mathrm{ret}}_{\lambda_2}(\omega_2, \boldsymbol{k}) = \frac{1}{2\pi\gamma} \mathcal{I}(\hat{\omega}_1, \hat{\omega}_2) \tag{7.7.15}$$

which serves to define the function $\mathcal{I}$, which contains a single integral over the dimensionless parameter $x = v_F|\boldsymbol{k}|/\omega_0$. Rewriting the Kubo formula and reinstating factors of $\hbar$ by

dimensional analysis we fin we can express the conductivity in terms of a single function of rescaled temperature and frequency,

$$\sigma(\omega, T) = \frac{e^2 v_F^2}{h\gamma} \mathcal{J}(\hat{\omega}, \hat{T}) \tag{7.7.16}$$

where $\hat{T} = T/\omega_0$, $\hat{\omega} = \omega/\omega_0$, so that $f_T(\omega) = f_{\hat{T}}(\hat{\omega})$, $\omega_0 = 2\pi v_F^3/\gamma$ is a characteristic scale set by the strength of the disorder, and

$$\mathcal{J}(\hat{\omega}, \hat{T}) = \frac{4}{3} \int \frac{d\hat{\epsilon}}{2\pi} \frac{[f_{\hat{T}}(\hat{\epsilon}) - f_{\hat{T}}(\hat{\epsilon} + \hat{\omega})]}{\hat{\omega}} \mathcal{I}(\hat{\epsilon} + \hat{\omega}, \hat{\epsilon}). \tag{7.7.17}$$

Numerical integration of this expression yields the conductivity for all T, ω, as shown in Figure 7.4.1 of the main text. and direct evaluation of the integrals yields an explicit form for $\mathcal{I}$,

$$\mathcal{I}(\hat{\epsilon} + \hat{\omega}, \hat{\epsilon}) = \tag{7.7.18}$$
$$\frac{4\pi\hat{\epsilon}^2(\hat{\epsilon} + \hat{\omega})^2(2\hat{\epsilon}^2 + 2\hat{\epsilon}\hat{\omega} + \hat{\omega}^2)(1 + 2\hat{\epsilon}^2 + 2\hat{\epsilon}\hat{\omega} + \hat{\omega}^2)(2 + 2\hat{\epsilon}^2 + 2\hat{\epsilon}\hat{\omega} + \hat{\omega}^2)}{(4\hat{\epsilon}^4 + 8\hat{\epsilon}^3\hat{\omega} + \hat{\omega}^2 + 8\hat{\epsilon}^2\hat{\omega}^2 + 4\hat{\epsilon}\hat{\omega}^3 + \hat{\omega}^4)(4\hat{\epsilon}^4 + 8\hat{\epsilon}^3\hat{\omega} + \hat{\omega}^2 + \hat{\omega}^4 + \hat{\epsilon}^2(4 + 8\hat{\omega}^2) + 4\hat{\epsilon}(\hat{\omega} + \hat{\omega}^3))}$$

Bibliography

[1] A. G. Abanov. Hopf term induced by fermions. *Physics Letters B*, 492(3–4):321–323, 2000.

[2] A. G. Abanov and P. B. Wiegmann. Theta-terms in nonlinear sigma-models. *Nuclear Physics B*, 570(3):685 – 698, 2000.

[3] A. A. Abrikosov and S. D. Beneslavskii. Some properties of gapless semiconductors of the second kind. *Journal of Low Temperature Physics*, 5:141–154, 1971.

[4] I. Affleck and F. D. M. Haldane. Critical theory of quantum spin chains. *Phys. Rev. B*, 36:5291–5300, Oct 1987.

[5] I. Affleck, T. Kennedy, E. H. Lieb, and H. Tasaki. Rigorous results on valence-bond ground states in antiferromagnets. *Phys. Rev. Lett.*, 59:799–802, Aug 1987.

[6] V. Aji. Adler-Bell-Jackiw anomaly in Weyl semi-metals: Application to Pyrochlore Iridates. *ArXiv e-prints*, August 2011.

[7] A. Altland and M. R. Zirnbauer. Nonstandard symmetry classes in mesoscopic normal-superconducting hybrid structures. *Phys. Rev. B*, 55(2):1142–1161, 1997.

[8] P. W. Anderson and W. F. Brinkman. Anisotropic superfluidity in ^{3}He: A possible interpretation of its stability as a spin-fluctuation effect. *Phys. Rev. Lett.*, 30:1108–1111, May 1973.

[9] P. W. Anderson and P. Morel. Generalized bardeen-cooper-schrieffer states and the proposed low-temperature phase of liquid he^3. *Phys. Rev.*, 123:1911–1934, Sep 1961.

[10] P. B. Arnold, G. D. Moore, and L. G. Yaffe. Effective kinetic theory for high temperature gauge theories. *Journal of High Energy Physics*, 1:30, January 2003.

[11] R. Auzzi and M. Shifman. Low-energy limit of yang–mills with massless adjoint quarks: chiral lagrangian and skyrmions. *Journal of Physics A: Mathematical and Theoretical*, 40(23):6221, 2007.

[12] S. E. Barrett, G. Dabbagh, L. N. Pfeiffer, K. W. West, and R. Tycko. Optically Pumped NMR Evidence for Finite-Size Skyrmions in GaAs Quantum Wells near Landau Level Filling $\nu = 1$. *Phys. Rev. Lett.*, 74:5112–5115, Jun 1995.

[13] B. A. Bernevig, T. L. Hughes, and S.-C. Zhang. Quantum Spin Hall Effect and Topological Phase Transition in HgTe Quantum Wells. *Science*, 314:1757–1761, 2006.

[14] B. A. Bernevig and S.-C. Zhang. Quantum spin hall effect. *Phys. Rev. Lett.*, 96:106802, Mar 2006.

[15] M. J. Bhaseen, J. S. Caux, I. I. Kogan, and A. M. Tsvelik. Disordered dirac fermions: the marriage of three different approaches. *Nuclear Physics B*, 618:465, 2001.

[16] M. Bocquet, D. Serban, and M. R. Zirnbauer. Disordered 2d quasiparticles in class D: Dirac fermions with random mass, and dirty superconductors. *Nuclear Physics B*, 578(3):628 – 680, 2000.

[17] A. A. Burkov and L. Balents. Weyl semimetal in a topological insulator multilayer. *Phys. Rev. Lett.*, 107:127205, Sep 2011.

[18] P. N. Butcher. *Non-linear Optical Phenomena*. Columbus, Engineering Experiment Station, Ohio state university, 1995.

[19] C. Caroli, P. G. De Gennes, and J. Matricon. Bound Fermion states on a vortex line in a type II superconductor. *Physics Letters*, 9(4):307 – 309, 1964.

[20] S. Chadov, X.-L. Qi, J. Kübler, G. H. Fecher, C. Felser, and S.-C. Zhang. Tunable Multifunctional Topological Insulators in Ternary Heusler Compounds. *Nature Materials*, 9(7):541–545, 2010.

[21] C. Chamon, Y. Hou, C.-Y., R. Jackiw, C. Mudry, S.-Y. Pi, and A. P. Schnyder. Irrational versus rational charge and statistics in two-dimensional quantum systems. *Phys. Rev. Lett.*, 100:110405, Mar 2008.

[22] Y. L. Chen, J. G. Analytis, J.-H. Chu, Z. K. Liu, S.-K. Mo, X. L. Qi, H. J. Zhang, D. H. Lu, X. Dai, Z. Fang, S. C. Zhang, I. R. Fisher, Z. Hussain, and Z.-X. Shen. Experimental Realization of a Three-Dimensional Topological Insulator, Bi_2Te_3. *Science*, 325(5937):178–181, 2009.

[23] Y. L. Chen, Z. K. Liu, J. G. Analytis, J.-H. Chu, H. J. Zhang, B. H. Yan, S.-K. Mo, R. G. Moore, D. H. Lu, I. R. Fisher, S. C. Zhang, Z. Hussain, and Z.-X. Shen. Single Dirac cone topological surface state and unusual thermoelectric property of compounds from a new topological insulator family. *Phys. Rev. Lett.*, 105:266401, Dec 2010.

[24] A. Cook and M. Franz. Majorana fermions in a topological-insulator nanowire proximity-coupled to an *s*-wave superconductor. *Phys. Rev. B*, 84:201105, Nov 2011.

[25] S. Das Sarma, C. Nayak, and S. Tewari. Proposal to stabilize and detect half-quantum vortices in strontium ruthenate thin films: Non-abelian braiding statistics of vortices in a $p_x + ip_y$ superconductor. *Phys. Rev. B*, 73(22):220502, 2006.

[26] E. Deyo, L. E. Golub, E. L. Ivchenko, and B. Spivak. Semiclassical theory of the photogalvanic effect in non-centrosymmetric systems. *ArXiv e-prints*, April 2009.

[27] M. Einaga, Y. Tanabe, A. Nakayama, A. Ohmura, F. Ishikawa, and Y. Yamada. New superconducting phase of Bi_2Te_3 under pressure above 11 GPa. *Journal of Physics: Conference Series*, 215(1):012036, 2010.

[28] S. Elitzur and V. P. Nair. Non perturbative anomalies in higher dimensions. *Nuclear Physics B*, 243(2):205–211, 9 1984.

[29] S.V. Eremeev, Y.M. Koroteev, and E.V. Chulkov. Ternary thallium-based semimetal chalcogenides Tl-V-VI2 as a new class of three-dimensional topological insulators. *JETP*, 91(11):594–598, 2010.

[30] A. M. Essin, J. E. Moore, and D. Vanderbilt. Magnetoelectric Polarizability and Axion Electrodynamics in Crystalline Insulators. *Phys. Rev. Lett.*, 102(14):146805, 2009.

[31] L. Fritz, J. Schmalian, M. Müller, and S. Sachdev. Quantum critical transport in clean graphene. *Phys. Rev. B*, 78:085416, Aug 2008.

[32] L. Fu. Hexagonal warping effects in the surface states of the topological insulator Bi_2Te_3. *Phys. Rev. Lett.*, 103:266801, Dec 2009.

[33] L. Fu and E. Berg. Odd-parity topological superconductors: Theory and application to $Cu_xBi_2Se_3$. *Phys. Rev. Lett.*, 105(9):097001, 2010.

[34] L. Fu and C. L. Kane. Time reversal polarization and a $\mathbb{Z}_2$ adiabatic spin pump. *Phys. Rev. B*, 74(19):195312, 2006.

[35] L. Fu and C. L. Kane. Topological insulators with inversion symmetry. *Phys. Rev. B*, 76(4):045302, 2007.

[36] L. Fu and C. L. Kane. Superconducting Proximity Effect and Majorana Fermions at the Surface of a Topological Insulator. *Phys. Rev. Lett.*, 100(9):096407, 2008.

[37] L. Fu and C. L. Kane. Josephson current and noise at a superconductor/quantum-spin-hall-insulator/superconductor junction. *Phys. Rev. B*, 79:161408, Apr 2009.

[38] L. Fu, C. L. Kane, and E. J. Mele. Topological Insulators in Three Dimensions. *Phys. Rev. Lett.*, 98(10):106803, 2007.

[39] K. Fujikawa and H. Suzuki. *Path Integrals and Quantum Anomalies*. Clarendon Press, 2004.

[40] S. D. Ganichev, E. L. Ivchenko, S. N. Danilov, J. Eroms, W. Wegscheider, D. Weiss, and W. Prettl. Conversion of spin into directed electric current in quantum wells. *Phys. Rev. Lett.*, 86:4358–4361, May 2001.

[41] S. D. Ganichev, F.-P. Kalz, U. Rössler, W. Prettl, E. L. Ivchenko, V. V. Bel'kov, R. Neumann, K. Brunner, and G. Abstreiter. Circular photogalvanic effect in SiGe semiconductor quantum wells. *MRS Online Proceedings Library*, 690:null–null, 2001.

[42] S. D. Ganichev, J. Karch, P. Olbrich, M. Schmalzbauer, C. Zoth, C. Brinsteiner, U. Wurstbauer, M.M. Glazov, S.A. Tarasenko, D. Weiss, J. Eroms, R. Yakimova, S. Lara-Avila, S. Kubatkin, and E.L. Ivchenko. Photon helicity driven currents in graphene. In *Infrared Millimeter and Terahertz Waves (IRMMW-THz), 2010 35th International Conference on*, page 1, sept. 2010.

[43] A. K. Geim and K. S. Novoselov. The rise of graphene. *Nat. Mater.*, 6(3):183–191, 03 2007.

[44] H. Georgi. *Lie Algebras in Particle Physics*. Perseus Books, Advanced Book Program, 1999.

[45] P. Ghaemi, S. Ryu, and D.-H. Lee. Quantum valley hall effect in proximity-induced superconducting graphene: An experimental window for deconfined quantum criticality. *Phys. Rev. B*, 81:081403, Feb 2010.

[46] T. Giamarchi. *Quantum physics in one dimension*. International series of monographs on physics. Clarendon, 2004.

[47] J. Goldstone and F. Wilczek. Fractional quantum numbers on solitons. *Phys. Rev. Lett.*, 47:986–989, Oct 1981.

[48] P. Goswami and S. Chakravarty. Quantum criticality between topological and band insulators in $3 + 1$ dimensions. *Phys. Rev. Lett.*, 107:196803, Nov 2011.

[49] T. Grover and T. Senthil. Topological spin hall states, charged skyrmions, and superconductivity in two dimensions. *Phys. Rev. Lett.*, 100:156804, Apr 2008.

[50] F. D. M. Haldane. Model for a quantum Hall effect without Landau levels: Condensed-matter realization of the "parity anomaly". *Phys. Rev. Lett.*, 61:2015–2018, 1988.

[51] F. D. M. Haldane. O(3) nonlinear σ model and the topological distinction between integer- and half-integer-spin antiferromagnets in two dimensions. *Phys. Rev. Lett.*, 61:1029–1032, Aug 1988.

[52] F. D. M. Haldane. Berry curvature on the fermi surface: Anomalous hall effect as a topological fermi-liquid property. *Phys. Rev. Lett.*, 93:206602, Nov 2004.

[53] M. Z. Hasan and C. L. Kane. Colloquium: Topological insulators. *Rev. Mod. Phys.*, 82(4):3045–3067, 2010.

[54] M. Z. Hasan and J. E. Moore. Three-dimensional topological insulators. *Annual Review of Condensed Matter Physics*, 2(1):55–78, 2012/05/01 2011.

[55] Y. Hatsugai. Chern number and edge states in the integer quantum hall effect. *Phys. Rev. Lett.*, 71(22):3697–3700, 1993.

[56] D. B. Haviland, Y. Liu, and A. M. Goldman. Onset of superconductivity in the two-dimensional limit. *Phys. Rev. Lett.*, 62:2180–2183, May 1989.

[57] R. A. Hein. Critical magnetic fields of superconducting snte. *Physics Letters*, 23(7):435 – 436, 1966.

[58] R. A. Hein, J. W. Gibson, R. Mazelsky, R. C. Miller, and J. K. Hulm. Superconductivity in germanium telluride. *Phys. Rev. Lett.*, 12:320–322, Mar 1964.

[59] R. A. Hein and E. M. Swiggard. Superconductivity in $Cu_xBi_2Se_3$ and its implications for pairing in the undoped topological insulator $TlBiTe_2$: A low carrier density (III-V)VI_2 compound. *Phys. Rev. Lett.*, 24(2):53–55, 1970.

[60] P. Heinzner, A. Huckleberry, and M. R. Zirnbauer. Symmetry classes of disordered fermions. *Communications in Mathematical Physics*, 257(3):725–771, 2005-08-01.

[61] I. F. Herbut. Zero-energy states and fragmentation of spin in the easy-plane antiferromagnet on a honeycomb lattice. *Phys. Rev. Lett.*, 99:206404, Nov 2007.

[62] C. Herring. Effect of time-reversal symmetry on energy bands of crystals. *Phys. Rev.*, 52:361–365, Aug 1937.

[63] H. Hopf. Über die abbildungen der dreidimensionalen sphäre auf die kugelfläche. *Mathematische Annalen*, 104(1):637–665, 1931-12-21.

[64] Y. S. Hor, J. G. Checkelsky, D. Qu, N. P. Ong, and R. J. Cava. Superconductivity and non-metallicity induced by doping the topological insulators Bi_2Se_3 and Bi_2Te_3. *Journal of Physics and Chemistry of Solids*, 72(5):572–576, 5 2011.

[65] Y. S. Hor, A. J. Williams, J. G. Checkelsky, P. Roushan, J. Seo, Q. Xu, H. W. Zandbergen, A. Yazdani, N. P. Ong, and R. J. Cava. Superconductivity in $Cu_xBi_2Se_3$ and its implications for pairing in the undoped topological insulator. *Phys. Rev. Lett.*, 104:057001, Feb 2010.

[66] P. Hosur, S. Ryu, and A. Vishwanath. Chiral topological insulators, superconductors, and other competing orders in three dimensions. *Phys. Rev. B*, 81(4):045120, 2010.

[67] C.-Y. Hou, C. Chamon, and C. Mudry. Electron fractionalization in two-dimensional graphenelike structures. *Phys. Rev. Lett.*, 98:186809, May 2007.

[68] D. Hsieh, D. Qian, L. A. Wray, Y. Xia, Y. S. Hor, R. J. Cava, and M. Z. Hasan. A topological Dirac insulator in a quantum spin Hall phase. 452:970–974, 2008.

[69] D. Hsieh, Y. Xia, D. Qian, L. A. Wray, J. H. Dil, F. Meier, J. Osterwalder, L. Patthey, J. G. Checkelsky, N. P. Ong, A. V. Fedorov, H. Lin, A. Bansil, D. Grauer, Y. S. Hor, R. J. Cava, and M. Z. Hasan. A tunable topological insulator in the spin helical Dirac transport regime. 460:1101–1105, 2009.

[70] D. Hsieh, Y. Xia, L. Wray, D. Qian, A. Pal, J. H. Dil, J. Osterwalder, F. Meier, G. Bihlmayer, C. L. Kane, Y. S. Hor, R. J. Cava, and M. Z. Hasan. Observation of Unconventional Quantum Spin Textures in Topological Insulators. 323(5916):919–922, 2009.

[71] R. Jackiw and S.-Y. Pi. Chiral gauge theory for graphene. *Phys. Rev. Lett.*, 98:266402, Jun 2007.

[72] R. Jackiw and C. Rebbi. Solitons with fermion number 1/2. *Phys. Rev. D*, 13(12):3398–3409, 1976.

[73] C. Kallin and A. J. Berlinsky. Is Sr_2RuO_4 a chiral p-wave superconductor? *Journal of Physics: Condensed Matter*, 21(16):164210, 2009.

[74] C. L. Kane and E. J. Mele. Quantum Spin Hall Effect in Graphene. *Phys. Rev. Lett.*, 95:226801, 2005.

[75] A. B. Kashuba. Conductivity of defectless graphene. *Phys. Rev. B*, 78:085415, Aug 2008.

[76] D. V. Khveshchenko. Ghost excitonic insulator transition in layered graphite. *Phys. Rev. Lett.*, 87:246802, Nov 2001.

[77] A. Kitaev. Periodic table for topological insulators and superconductors. volume 1134, pages 22–30. L. D. Landau Memorial Conference "Advances in Theoretical Physics", AIP, 2009.

[78] A. Y. Kitaev. Unpaired Majorana fermions in quantum wires. *Physics-Uspekhi*, 44(10S):131, 2001.

[79] F. R. Klinkhamer. Z-string global gauge anomaly and lorentz non-invariance. *Nuclear Physics B*, 535:233, 1998.

[80] M. Kohmoto, B. I. Halperin, and Y.-S. Wu. Diophantine equation for the three-dimensional quantum hall effect. *Phys. Rev. B*, 45:13488–13493, Jun 1992.

[81] M. König, S. Wiedmann, C. Brüne, A. Roth, H. Buhmann, L. W. Molenkamp, X.-L. Qi, and S.-C. Zhang. Quantum Spin Hall Insulator State in HgTe Quantum Wells. *Science*, 318:766–770, 2007.

[82] H. Leal and D. V. Khveshchenko. Excitonic instability in two-dimensional degenerate semimetals. *Nuclear Physics B*, 687:323, 2004.

[83] A. LeClair and D. J. Robinson. Super spin-charge separation for class a, c and d disorder. *Journal of Physics A: Mathematical and Theoretical*, 41(45):452002, 2008.

[84] D.-H. Lee and C. L. Kane. Boson-vortex-skyrmion duality, spin-singlet fractional quantum hall effect, and spin-1/2 anyon superconductivity. *Phys. Rev. Lett.*, 64:1313–1317, Mar 1990.

[85] H. Lin, R. S. Markiewicz, L. A. Wray, L. Fu, M. Z. Hasan, and A. Bansil. Single-dirac-cone topological surface states in the $tlbise_2$ class of topological semiconductors. *Phys. Rev. Lett.*, 105:036404, Jul 2010.

[86] H. Lin, L. A. Wray, Y. Xia, S. . Xu, S. Jia, R. J. Cava, A. Bansil, and M. Z. Hasan. Single-Dirac-cone Z_2 topological insulator phases in distorted Li_2AgSb-class and related quantum critical Li-based spin-orbit compounds. *ArXiv e-prints*, April 2010.

[87] H. Lin, L. A. Wray, Y. Xia, S. Xu, S. Jia, R. J. Cava, A. Bansil, and M. Z. Hasan. Half-Heusler ternary compounds as new multifunctional experimental platforms for topological quantum phenomena. *Nature Materials*, 9:546–549, 2010.

[88] C.-X. Liu, X.-L. Qi, H.-J. Zhang, X. Dai, Z. Fang, and S.-C. Zhang. Model hamiltonian for topological insulators. *Phys. Rev. B*, 82:045122, Jul 2010.

[89] H.-Z. Lu, W.-Y. Shan, W. Yao, Q. Niu, and S.-Q. Shen. Massive dirac fermions and spin physics in an ultrathin film of topological insulator. *Phys. Rev. B*, 81:115407, Mar 2010.

[90] A. W. W. Ludwig. A free field representation of the Osp(2|2) current algebra at level k=-2, and dirac fermions in a random SU(2) gauge potential, 2000.

[91] A. W. W. Ludwig, M. P. A. Fisher, R. Shankar, and G. Grinstein. Integer quantum hall transition: An alternative approach and exact results. *Phys. Rev. B*, 50:7526–7552, Sep 1994.

[92] R. M. Lutchyn, J. D. Sau, and S. Das Sarma. Majorana fermions and a topological phase transition in semiconductor-superconductor heterostructures. *Phys. Rev. Lett.*, 105(7):077001, 2010.

[93] L.M. Martelo, M. Dzierzawa, L. Siffert, and D. Baeriswyl. Mott-hubbard transition and antiferromagnetism on the honeycomb lattice. *Zeitschrift für Physik B Condensed Matter*, 103:335–338, 1997.

[94] Y. Matsushita, P. A. Wianecki, A. T. Sommer, T. H. Geballe, and I. R. Fisher. Type II superconducting parameters of Tl-doped PbTe determined from heat capacity and electronic transport measurements. *Phys. Rev. B*, 74:134512, Oct 2006.

[95] G Moore and N. Read. Nonabelions in the fractional quantum hall effect. *Nuc. Phys. B*, 360(2-3):362–396, 1991.

[96] J. E. Moore and L. Balents. Topological invariants of time-reversal-invariant band structures. *Phys. Rev. B*, 75(12):121306(R), 2007.

[97] J. E. Moore and J. Orenstein. Confinement-induced berry phase and helicity-dependent photocurrents. *Phys. Rev. Lett.*, 105:026805, Jul 2010.

[98] O. I. Motrunich and T. Senthil. Origin of artificial electrodynamics in three-dimensional bosonic models. *Phys. Rev. B*, 71:125102, Mar 2005.

[99] V. Mourik, K. Zuo, S. M. Frolov, S. R. Plissard, E. P. A. M. Bakkers, and L. P. Kouwenhoven. Signatures of Majorana Fermions in Hybrid Superconductor-Semiconductor Nanowire Devices. *Science*, 2012.

[100] L. Muñoz, E. Pérez, L. Viña, and K. Ploog. Spin relaxation in intrinsic gaas quantum wells: Influence of excitonic localization. *Phys. Rev. B*, 51:4247–4257, Feb 1995.

[101] M. Nakahara. *Geometry, topology, and physics*. Institute of Physics Publishing, 2003.

[102] C. Nayak, S. H. Simon, A. Stern, M. Freedman, and S. Das Sarma. Non-abelian anyons and topological quantum computation. *Rev. Mod. Phys.*, 80:1083–1159, Sep 2008.

[103] H. B. Nielsen and M. Ninomiya. Absence of neutrinos on a lattice: (II). Intuitive topological proof. *Nuclear Physics B*, 193(1):173–194, 12 1981.

[104] H. B. Nielsen and M. Ninomiya. The Adler-Bell-Jackiw anomaly and Weyl fermions in a crystal. *Physics Letters B*, 130(6):389 – 396, 1983.

[105] T. Oka and H. Aoki. Photovoltaic Hall effect in graphene. *Phys. Rev. B*, 79:081406, Feb 2009.

[106] Y. Oreg, G. Refael, and F. von Oppen. Helical Liquids and Majorana Bound States in Quantum Wires. *Phys. Rev. Lett.*, 105(17):177002, 2010.

[107] T. Paiva, R. T. Scalettar, W. Zheng, R. R. P. Singh, and J. Oitmaa. Ground-state and finite-temperature signatures of quantum phase transitions in the half-filled hubbard model on a honeycomb lattice. *Phys. Rev. B*, 72:085123, Aug 2005.

[108] A. C. Potter and P. A. Lee. Multichannel Generalization of Kitaev's Majorana End States and a Practical Route to Realize Them in Thin Films. *Phys. Rev. Lett.*, 105(22):227003, 2010.

[109] X.-L. Qi, T. L. Hughes, and S.-C. Zhang. Topological field theory of time-reversal invariant insulators. *Phys. Rev. B*, 78(19):195424, 2008.

[110] X.-L. Qi, R. Li, J. Zang, and S.-C. Zhang. Inducing a magnetic monopole with topological surface states. *Science*, 323(5918):1184–1187, 2009.

[111] X.-L. Qi and S.-C. Zhang. The quantum spin Hall effect and topological insulators. *Physics Today*, 63(1):33–38, 2010.

[112] Y. Ran, A. Vishwanath, and D.-H. Lee. Spin-charge separated solitons in a topological band insulator. *Phys. Rev. Lett.*, 101:086801, Aug 2008.

[113] Y. Ran, Y. Zhang, and A. Vishwanath. One-dimensional topologically protected modes in topological insulators with lattice dislocations. *Nature Physics*, 5:298–303, 2009.

[114] N. Read and D. Green. Paired states of fermions in two dimensions with breaking of parity and time-reversal symmetries and the fractional quantum hall effect. *Phys. Rev. B*, 61(15):10267–10297, 2000.

[115] N. Read and A. W. W. Ludwig. Absence of a metallic phase in random-bond ising models in two dimensions: Applications to disordered superconductors and paired quantum hall states. *Phys. Rev. B*, 63(2):024404, 2000.

[116] P. Roushan, J. Seo, C. V. Parker, Y. S. Hor, D. Hsieh, D. Qian, A. Richardella, M. Z. Hasan, R. J. Cava, and A. Yazdani. Topological surface states protected from backscattering by chiral spin texture. *Nature*, 460:1106–1109, 2009.

[117] R Roy. Topological phases and the quantum spin Hall effect in three dimensions. *Phys. Rev. B*, 79:195322, 2009.

[118] T. Sato, K. Segawa, H. Guo, K. Sugawara, S. Souma, T. Takahashi, and Y. Ando. Direct Evidence for the Dirac-Cone Topological Surface States in the Ternary Chalcogenide $TlBiSe_2$. *Phys. Rev. Lett.*, 105:136802, Sep 2010.

[119] A. P. Schnyder, S. Ryu, A. Furusaki, and A. W. W. Ludwig. Classification of topological insulators and superconductors in three spatial dimensions. *Phys. Rev. B*, 78(19):195125, 2008.

[120] T. Senthil, L. Balents, S. Sachdev, A. Vishwanath, and M. P. A. Fisher. Quantum criticality beyond the landau-ginzburg-wilson paradigm. *Phys. Rev. B*, 70:144407, Oct 2004.

[121] T. Senthil and M. P. A. Fisher. Competing orders, nonlinear sigma models, and topological terms in quantum magnets. *Phys. Rev. B*, 74:064405, Aug 2006.

[122] T. Senthil, A. Vishwanath, L. Balents, S. Sachdev, and M. P. A. Fisher. Deconfined quantum critical points. *Science*, 303(5663):1490–1494, 2004.

[123] S. L. Sondhi, A. Karlhede, S. A. Kivelson, and E. H. Rezayi. Skyrmions and the crossover from the integer to fractional quantum hall effect at small zeeman energies. *Phys. Rev. B*, 47:16419–16426, Jun 1993.

[124] S. Sorella and E. Tosatti. Semi-metal-insulator transition of the hubbard model in the honeycomb lattice. *EPL (Europhysics Letters)*, 19(8):699, 1992.

[125] T. D. Stanescu, V. Galitski, J. Y. Vaishnav, C. W. Clark, and S. Das Sarma. Topological insulators and metals in atomic optical lattices. *Phys. Rev. A*, 79:053639, May 2009.

[126] F. F. Tafti, J. J. Ishikawa, A. McCollam, S. Nakatsuji, and S. R. Julian. Pressure Tuned Insulator to Metal Transition in $Eu_2Ir_2O_7$. *ArXiv e-prints*, July 2011.

[127] A. Tanaka and X. Hu. Effective field theory with a θ-vacua structure for two-dimensional spin systems. *Phys. Rev. B*, 74:140407, Oct 2006.

[128] J. C. Y. Teo and C. L. Kane. Majorana fermions and non-abelian statistics in three dimensions. *Phys. Rev. Lett.*, 104:046401, Jan 2010.

[129] J. C. Y. Teo and C. L. Kane. Topological defects and gapless modes in insulators and superconductors. *Phys. Rev. B*, 82(11):115120, 2010.

[130] D. J. Thouless, M. Kohmoto, M. P. Nightingale, and M. den Nijs. Quantized Hall Conductance in a Two-Dimensional Periodic Potential. *Phys. Rev. Lett.*, 49(6):405–408, 1982.

[131] A. M. Tsvelik. Exactly solvable model of fermions with disorder. *Phys. Rev. B*, 51:9449–9454, Apr 1995.

[132] G.E. Volovik. *The Universe in a Helium Droplet*. International Series of Monographs on Physics. Oxford University Press, 2009.

[133] K. von Klitzing, G. Dorda, and M. Pepper. New Method for High-Accuracy Determination of the Fine-Structure Constant Based on Quantized Hall Resistance. *Phys. Rev. Lett.*, 45(6):494–497, 1980.

[134] X. Wan, A. M. Turner, A. Vishwanath, and S. Y. Savrasov. Topological semimetal and fermi-arc surface states in the electronic structure of pyrochlore iridates. *Phys. Rev. B*, 83:205101, May 2011.

[135] L.-L. Wang and D. D. Johnson. Ternary tetradymite compounds as topological insulators. *Phys. Rev. B*, 83:241309, Jun 2011.

[136] F. Wilczek. Two applications of axion electrodynamics. *Phys. Rev. Lett.*, 58:1799–1802, 1987.

[137] F. Wilczek and A. Zee. Linking numbers, spin, and statistics of solitons. *Phys. Rev. Lett.*, 51:2250–2252, Dec 1983.

[138] F. Wilczek and A. Zee. Appearance of gauge structure in simple dynamical systems. *Phys. Rev. Lett.*, 52(24):2111–2114, 1984.

[139] M. Wimmer, A. R. Akhmerov, M. V. Medvedyeva, J. Tworzydło, and C. W. J. Beenakker. Majorana bound states without vortices in topological superconductors with electrostatic defects. *Phys. Rev. Lett.*, 105:046803, Jul 2010.

[140] W. Witczak-Krempa and Y.-B. Kim. Topological and magnetic phases of interacting electrons in the pyrochlore iridates. *Phys. Rev. B*, 85:045124, Jan 2012.

[141] E. Witten. Current algebra, baryons, and quark confinement. *Nuclear Physics B*, 223(2):433–444, August 1983.

[142] B Wittmann, S N Danilov, V V Bel'kov, S A Tarasenko, E G Novik, H Buhmann, C Brüne, L W Molenkamp, Z D Kvon, N. NMikhailov, S. A. Dvoretsky, N. Q. Vinh, A. F. G. van der Meer, M. Murdin, and S. D. Ganichev. Circular photogalvanic effect in HgTe/CdHgTe quantum well structures. *Semiconductor Science and Technology*, 25(9):095005, 2010.

[143] L. A. Wray, S.-Y. Xu, Y. Xia, Y. S. Hor, D. Qian, A. V. Fedorov, H. Lin, A. Bansil, R. J. Cava, and M. Z. Hasan. Observation of topological order in a superconducting doped topological insulator. *Nature Physics*, 6(11):855–859, 11 2010.

[144] Y. Xia, D. Qian, D. Hsieh, L. Wray, A. Pal, H. Lin, A. Bansil, D. Grauer, Y. S. Hor, R. J. Cava, and M. Z. Hasan. Observation of a large-gap topological-insulator class with a single Dirac cone on the surface. *Nature Physics*, 5:398–402, 2009.

[145] D. Xiao, J. Shi, D. P. Clougherty, and Q. Niu. Polarization and adiabatic pumping in inhomogeneous crystals. *Phys. Rev. Lett.*, 102:087602, Feb 2009.

[146] G. Xu, H. M. Weng, Z. Wang, X. Dai, and Z. Fang. Chern Semimetal and the Quantized Anomalous Hall Effect in $HgCr_2Se_4$. *Phys. Rev. Lett.*, 107:186806, Oct 2011.

[147] B. H. Yan, C.-X. Liu, H.-J. Zhang, C.-Y. Yam, X.-L. Qi, T. Frauenheim, and S.-C. Zhang. Theoretical prediction of topological insulators in thallium-based III-V-VI 2 ternary chalcogenides. *EPL (Europhysics Letters)*, 90(3):37002, 2010.

[148] B. H. Yan, H.-J. Zhang, C.-X. Liu, X.-L. Qi, T. Frauenheim, and S.-C. Zhang. Theoretical prediction of topological insulator in ternary rare earth chalcogenides. *Phys. Rev. B*, 82:161108, Oct 2010.

[149] D. Yanagishima and Y. Maeno. Metal-nonmetal changeover in pyrochlore iridates. *Journal of the Physical Society of Japan*, 70(10):2880–2883, 2001.

[150] K.-Y. Yang, Y.-M. Lu, and Y. Ran. Quantum hall effects in a weyl semimetal: Possible application in pyrochlore iridates. *Phys. Rev. B*, 84:075129, Aug 2011.

[151] R. C. Yu, W. Zhang, H.-J. Zhang, S.-C. Zhang, X. Dai, and Z. Fang. Quantized anomalous hall effect in magnetic topological insulators. *Science*, 329(5987):61–64, 2010.

[152] H. Zhang, C.-X. Liu, X.-L. Qi, X. Dai, Z. Fang, and S.-C. Zhang. Topological insulators in Bi_2Se_3, Bi_2Te_3 and Sb_2Te_3 with a single Dirac cone on the surface. *Nat Phys*, 5(6):438–442, 06 2009.

[153] H. Zhang, C.-X. Liu, X.-L. Qi, X. Dai, Z. Fang, and S.-C. Zhang. Topological insulators in bi2se3, bi2te3 and sb2te3 with a single dirac cone on the surface. *Nat Phys*, 5(6):438–442, 06 2009.

[154] J. L. Zhang, S. J. Zhang, H. M. Weng, W. Zhang, L. X. Yang, Q. Q. Liu, S. M. Feng, X. C. Wang, R. C. Yu, L. Z. Cao, L. Wang, W. G. Yang, H. Z. Liu, W. Y. Zhao, S. C. Zhang, X. Dai, Z. Fang, and C. Q. Jin. Pressure-induced superconductivity in topological parent compound Bi_2Te_3. *Proceedings of the National Academy of Sciences*, 108(1):24–28, 2011.

[155] M. R. Zirnbauer. Riemannian symmetric superspaces and their origin in random matrix theory. *J.MATH.PHYS.*, 37:4986, 1996.